

The Pennsylvania State University

The Graduate School

College of Engineering

**EXPLORING MICROCHANNEL COOLING DESIGNS THROUGH THE USES OF  
NUMERICAL OPTIMIZATION AND ADDITIVE MANUFACTURING**

A Dissertation in

Mechanical Engineering

by

Kathryn L. Kirsch

© 2017 Kathryn L. Kirsch

Submitted in Partial Fulfillment  
of the Requirements  
for the Degree of

Doctor of Philosophy

December 2017

The dissertation of Kathryn L. Kirsch was reviewed and approved\* by the following:

Karen A. Thole  
Distinguished Professor  
Department Head of Mechanical and Nuclear Engineering  
Dissertation Advisor  
Chair of Committee

Stephen P. Lynch  
Assistant Professor of Mechanical Engineering

Robert F. Kunz  
Professor of Mechanical Engineering

Edward W. Reutzel  
Head of the Laser Process Technology Department at Penn State Applied Research Laboratory  
Associate Professor of Engineering Science and Mechanics

Reid A. Berdanier  
Research Associate at the Penn State Steady Thermal Aero Research Turbine Laboratory  
Special Member

Mary I. Frecker  
Associate Department Head for Graduate Programs of Mechanical and Nuclear Engineering  
Professor of Mechanical Engineering and Biomedical Engineering

\*Signatures are on file in the Graduate School.

## ABSTRACT

Advancing the performance of heat exchangers beyond their current capabilities requires a fresh look into the relationship between design methodologies and manufacturing techniques. Progress in design tools can lead to the efficient generation of unique geometries optimized for a given application; progress in manufacturing capabilities can turn those unique geometries into reality. Currently, however, the translation from computational design to as-built manufactured part is rarely one to one.

This work seeks to highlight the effects of both nontraditional and traditional design methodologies on microchannels manufactured using Laser Powder Bed Fusion. The nontraditional design approach made use of an adjoint-based sensitivity analysis to optimize the shape of four baseline microchannel designs for three different objective functions. The sensitivity analysis was coupled with a conventional flow solver, and identified regions of the baseline designs that exerted the strongest influence on the objective function. The shape of those most sensitive regions were then morphed to achieve the optimization goal. The resultant microchannel geometries were largely reproduced in the Laser Powder Bed Fusion process, though contained a much higher surface roughness than was modeled. Even still, some of the objective functions were achieved experimentally.

A follow-up study was conceived to delve deeper into the efficacy of the design tool, and to isolate the effects of the optimized features from the effects of high surface roughness in the as-built metal parts. A stereolithography process was used to build the optimized channels in plastic, and allowed for experimentation on the true, intended optimized designs. In general, the adjoint-based sensitivity analysis was successful: experiments on the plastic optimized channels yielded analogous performance to the numerical simulation. The influence of surface roughness in the metal parts varied depending on the shape changes.

Another study was performed that applied a traditional design approach to microchannels containing pin fins. These arrays were also built using Laser Powder Bed Fusion. Results from this study highlighted the differences in performance between conventionally and additively manufactured pin fin arrays. Additionally, the study identified in the additive process a dependence on surface roughness that was based on pin density in the channels; such a manufacturing consideration need not be taken into account with a conventional method.

## TABLE OF CONTENTS

List of Figures .....	viii
List of Tables .....	xv
Nomenclature .....	xvi
Acknowledgements .....	xviii
1 Introduction .....	1
1.1 Micro Scale Cooling .....	1
Electronics Cooling .....	1
Gas Turbine Cooling .....	3
1.2 Laser Powder Bed Fusion .....	4
1.3 Optimization Methods .....	6
1.4 Research Objectives .....	8
1.5 Dissertation Outline .....	8
2 Heat Transfer and Pressure Loss Measurements in Additively Manufactured Wavy Microchannels .....	10
2.1 Abstract .....	10
2.2 Introduction .....	10
2.3 Literature Review .....	11
2.4 Description of Test Coupons .....	13
2.5 Geometric Characterization .....	15
2.6 Experimental and Computational Methods .....	17
Experimental Setup .....	17
Uncertainty Analysis .....	19
Computational Setup .....	20
2.7 Results and Discussion .....	21
Pressure Loss Results .....	21
Heat Transfer Results .....	24
Augmentation Results .....	26
2.8 Conclusions .....	27
3 Experimental Investigation of Numerically Optimized Microchannels Created through Additive Manufacturing .....	29
3.1 Abstract .....	29
3.2 Introduction .....	29
3.3 Literature Review .....	30
3.4 Numerical Setup .....	32
Adjoint Method .....	34

Optimized Geometries .....	35
3.5 Geometric Characterization.....	40
3.6 Experimental Setup .....	43
Uncertainty Analysis .....	45
3.7 Results and Discussion.....	45
Pressure Loss Performance.....	46
Heat Transfer Performance.....	48
Augmentation Results.....	49
3.8 Conclusions .....	50
4 Pressure Loss and Heat Transfer Performance for Additively and Conventionally Manufactured Pin Fin Arrays.....	52
4.1 Abstract .....	52
4.2 Introduction .....	52
4.3 Literature Review .....	53
4.4 Fabrication of Test Coupons .....	56
4.5 Geometric Characterization of the Test Coupons.....	58
4.6 Experimental Facility .....	63
Experimental Uncertainty .....	65
4.7 Results and Discussion.....	66
Pressure Loss Results .....	67
Heat Transfer Results .....	70
Overall Augmentation Results.....	73
4.8 Conclusions .....	75
5 Numerical Optimization, Characterization, and Experimental Investigation of Additively Manufactured Communicating Microchannels .....	77
5.1 Abstract .....	77
5.2 Introduction .....	77
5.3 Literature Review .....	78
5.4 Channel Design .....	80
5.5 Numerical Setup.....	81
Adjoint-Based Shape Optimization .....	82
5.6 Numerical Results .....	83
5.7 Geometric Characterization.....	90
5.8 Experimental Setup .....	94
Experimental Uncertainty .....	95
5.9 Results and Discussion.....	95
Pressure Loss Test Results .....	95
Heat Transfer Results .....	98

5.10 Communicating vs. Non-Communicating Channel Performance .....	100
5.11 Conclusions .....	102
6 Isolating the Effects of Surface Roughness versus Wall Shape in Numerically Optimized, Additively Manufactured Micro Cooling Channels .....	104
6.1 Abstract .....	104
6.2 Introduction .....	104
6.3 Review of Relevant Literature.....	105
6.4 Channel Design .....	107
6.5 Simulation Setup .....	108
6.6 Test Coupon Manufacture .....	111
Plastic Stereolithography Process.....	111
Metal Additive Process.....	111
Non-Destructive Evaluation .....	112
Experimental Setup.....	114
Uncertainty Analysis .....	115
6.7 Experimental Results and Discussion .....	115
SLA Test Coupons vs. Numerical Simulation.....	116
Non-communicating Channels .....	116
Communicating Channels.....	120
SLA Test Coupons vs. L-PBF Coupons .....	122
Non-communicating Channels .....	122
Communicating Channels.....	123
6.8 Conclusions .....	125
7 Conclusions.....	126
7.1 Flow and Heat Transfer Performance of Wavy Microchannels .....	126
7.2 Pin Fin Arrays .....	128
7.3 Design Considerations for Additive Manufacturing .....	129
7.4 Recommendations for Future Work .....	130
References.....	132
A Appendix A: Detailed description of geometries .....	140
A.1 Variable cross-section versus constant cross-section .....	140
A.2 Addition of branches between primary channels.....	141
A.3 Optimized Shape Changes: Peaks and Troughs .....	143
A.4 Nondestructive Evaluation .....	144
B Appendix B: Further Discussion on Numerical Model and Adjoint Method .....	145
B.1 Adjoint Method.....	145
B.2 Implicit constraints on optimization method .....	146

B.3 Side wall boundary conditions.....	147
--	-----

## LIST OF FIGURES

Figure 1-1. Stereolithography (SLA) build process. A photoreactive resin is cured layer-by-layer to build a part.....	3
Figure 1-2. Depiction of skin cooling with mini serpentine cooling channels [11]. (a) Top down view of turbine airfoil. Cooling passages are denoted as 21. (b) Cross section of skin cooling scheme, taken from section AA in (a). The serpentine path is created using pin fins. (c) Isometric view of turbine airfoil, with the outer skin removed and the cooling passages highlighted. Coolant is routed up through the base of the airfoil, through the serpentine passages (b), into collector cavities denoted as 13 and 14, then out through the showerhead holes (denoted as 17), or out through the trailing edge of the airfoil (denoted as 16). ....	4
Figure 1-3. Depiction of the Laser Powder Bed Fusion (L-PBF) process [12]. ....	5
Figure 2-1. Description of the coupon build, with pertinent dimensions included. Flow direction is normal to the normal to the flange face. ....	13
Figure 2-2. Change in flow area through one period of the each of the wavy channel cases. ....	14
Figure 2-3. Visual representation of the test matrix used for this study. Flow goes left to right. ....	14
Figure 2-4. Description of the wavy formulation. Flow goes left to right. ....	14
Figure 2-5. 2D CT scan image. The surface determination algorithm outlined both external and internal coupon surfaces. The dark gray color represents the material and the light gray areas represent the open channels. Overlaid on the CT scan image is the design intent. The channels were 0.5 mm wide, and 1 mm high. ....	16
Figure 2-6. Line plots of surface roughness on two surfaces from one channel. The line is the curve fit to the surface; the scatter in the plot represents the points on the surface that deviate from the fit. ....	17
Figure 2-7. Rendering of the test section setup for both pressure loss and heat transfer measurements. Thermocouples were embedded in the rigid foam, PEEK plastic pieces, and the copper blocks. The LFE is located well upstream of the test coupon and is not pictured here. ....	18
Figure 2-8. Slice of the structured grid for a segment of the $\lambda=0.2L$ case. ....	21
Figure 2-9. Friction factor vs. Reynolds number. Included in the plot are data from additively manufactured straight rectangular channels or comparable size [16]. ....	22
Figure 2-10. Velocity vectors, colored by normalized velocity, of slices through each of the wavy channel cases with $Re=5000$ . Slices were taken at the second full peak in the wave, as indicated above the contour slices. Note that fluid next to the left wall of the $\lambda=0.1L$ case is near zero and that a full dean vortex forms in the $\lambda=0.4L$ case. ....	23



Figure 2-11. Top-down view of the normalized velocity through each of the wavy channel cases with $Re=5000$ . Flow goes from left to right. Note the pockets of low velocity in each peak and trough of the $\lambda=0.1L$ case.....	24
Figure 2-12. Friction factor augmentation vs. Reynolds number. ....	24
Figure 2-13. Nusselt number vs. Reynolds number.....	25
Figure 2-14. Nusselt number augmentation vs. Reynolds number. ....	26
Figure 2-15. Friction factor augmentation vs. heat transfer augmentation. ....	27
Figure 3-1. Four $45^\circ$ arcs formed the path along which a rectangle was swept to create the channel. Flow goes left to right [55].....	32
Figure 3-2. The two baseline cases of wavy channels used in the optimization study. Forty percent of the coupon length is shown. Flow is from left to right [55]. ....	33
Figure 3-3. Optimization results for the $\lambda=0.1L$ case. (a) Top down view of channel outlines at 50% channel height. (b) Change in cross sectional area through each optimized channel, normalized by the baseline cross sectional area. (c) and (d) In-plane velocity vectors superimposed on nondimensional contours near the beginning of the channels. (e) and (f) Secondary velocity vectors superimposed on nondimensional temperature contours near the end of the channels. ....	37
Figure 3-4. Optimization results for the $\lambda=0.4L$ case. (a) Top down view of channel outlines at 50% channel height. (b) Change in cross sectional area through each optimized, normalized by the baseline cross sectional area. (c) and (d) Secondary velocity vectors superimposed on nondimensional temperature contours near the beginning of the channels. (e) and (f) Secondary velocity vectors superimposed on nondimensional temperature contours near the end of the channels. ....	39
Figure 3-5. Build orientation and dimensions of test coupons.....	41
Figure 3-6. CT scan results from the $\lambda=0.1L$ optimized DMLS channels. (a) Change in cross sectional area of the optimized DMLS channels, normalized by the baseline DMLS channel. Only 50% of the coupon length is shown. (b) Channel wall outlines of each of the DMLS channels, at the same location as in Figure 3-3d. ....	42
Figure 3-7. CT scan results from the $\lambda=0.4L$ optimized DMLS channels. (a) Change in cross sectional area of the optimized DMLS channels, normalized by the baseline DMLS channel. Only 50% of the coupon length is shown. (b) Channel wall outlines of each of the DMLS channels, at the same location as in Figure 3-4d. ....	42
Figure 3-8. Test facility used for pressure loss and heat transfer measurements for the optimized wavy channel test coupons. ....	44

Figure 3-9. Friction factor vs. Reynolds number for all optimized coupons, plus the baseline coupons.....	47
Figure 3-10. Friction factor augmentation from the optimized channels relative to their baseline cases. (a) $\lambda=0.1L$ cases, (b) $\lambda=0.4L$ cases. ....	47
Figure 3-11. Nusselt number vs. Reynolds number for all optimized coupons, plus the baseline coupons.....	48
Figure 3-12. Nusselt number augmentation from the optimized channels relative to their baseline cases. (a) $\lambda=0.1L$ cases, (b) $\lambda=0.4L$ cases. ....	49
Figure 3-13. Heat transfer augmentation vs. friction factor augmentation to the one third power.	50
Figure 4-1. Pin fin spacing nomenclature .....	57
Figure 4-2. Test coupon build direction, with support structures. Flow direction into the page, normal to flanges. ....	57
Figure 4-3. Picture of L-PBF coupon showing smoothed flange and all support structures removed. ....	57
Figure 4-4. Point cloud data from the CT scan on a small section (2.5 mm long) of a representative bottom surface and its corresponding surface fit, shown in 2D as a curve fit. ....	59
Figure 4-5. View from inside the pin fin channel; image generated by the CT scan. Flow direction is into the page. The image in the lower left corner shows the location in the test coupon at which the CT scan image was taken.....	59
Figure 4-6. CT scan slice of top down view of the $S/D=2.0$ , $X/D=2.6$ coupon, with one pin fin magnified.....	60
Figure 4-7. Top down view of the 3D rendering of as-built test coupons. (a) $S/D=4.0$ , $X/D=2.6$ . (b) $S/D=1.5$ , $X/D=1.3$ . ....	61
Figure 4-8. Laser exposure area for one layer. (a) Top-down view of laser exposure area for two pin spacings. (b) Location of layer slice.....	61
Figure 4-9. Build direction and nomenclature for L-PBF multichannel coupons [16] .....	62
Figure 4-10. Cross section of experimental test facility .....	65
Figure 4-11. Friction factor results for the four L-PBF pin fin arrays, along with the results from the benchmarking coupon. ....	67
Figure 4-12. Friction factor augmentation from both L-PBF and smooth walled pin in arrays, along with L-PBF straight microchannels, with $S/D_h=2.0$ [16]. ....	69
Figure 4-13. Friction factor augmentation from both L-PBF and smooth walled pin fin arrays with $S/D=4.0$ . ....	70

Figure 4-14. Nusselt number vs. Reynolds number for the four L-PBF pin fin arrays and two baseline, multichannel L-PBF coupons, along with the results from the benchmarking coupon. ....	71
Figure 4-15. Nusselt number augmentation of L-PBF and smooth walled arrays with $S/D=2.0$ . .	71
Figure 4-16. Nusselt number augmentation of L-PBF and smooth walled arrays with $S/D=4.0$ . .	72
Figure 4-17. Direct comparison of friction factor augmentation and Nusselt number augmentation of smooth walled and L-PBF pin fin arrays with $S/D=2.0$ and $S/D=4.0$ at $Re=5000$ . ....	73
Figure 4-18. Direction comparison of friction factor augmentation and Nusselt number of augmentation of smooth walled and L-PBF pin fin arrays with $S/D=2.0$ and $S/D=4.0$ at $Re=20000$ . ....	73
Figure 4-19. Nusselt number augmentation vs. friction factor augmentation for the four L-PBF pin fin arrays from the present study, select smooth walled pin fin arrays and other L-PBF internal cooling schemes. ....	75
Figure 5-1. Depiction of communicating wavy channel design. The branches repeated every other period in the streamwise direction and every other channel in the spanwise direction. Flow goes left to right. ....	81
Figure 5-2. Two variations in baseline communicating wavy channel design. (a) $\lambda=0.1L$ ; (b) $\lambda=0.4L$ . Flow goes left to right. ....	81
Figure 5-3. Top-down view at 50% channel height of wall-resolved, structured mesh for the $\lambda=0.1L$ case. ....	82
Figure 5-4. Channel wall outlines from a top-down view at 50% channel height for $\lambda=0.1L$ baseline and optimized shapes. The gray color shows the location of the walls for the baseline case. (a) Zoomed-in view of middle branch, (b) and (c) zoomed-in view of branches subject to the periodic boundary condition. ....	84
Figure 5-5. Contours of normalized axial velocity at one slice location, immediately after the branch exit shown in Figure 5-4c. ....	85
Figure 5-6. Contours of non-dimensional temperature with secondary velocity vectors overlaid. ....	86
Figure 5-7. Channel wall outlines from a top-down view at 50% channel height for $\lambda=0.4L$ baseline and optimized shapes. The gray color shows the location of the walls for the baseline case. (a) Zoomed-in view of middle branch, (b) and (c) zoomed-in view of branches subject to the periodic boundary condition. ....	88
Figure 5-8. Contours of normalized axial velocity at one slice location. ....	88
Figure 5-9. Contours of non-dimensional temperature with velocity vectors overlaid. ....	89

Figure 5-10. Coupon orientation on the build plate. On the left view, flow is into the page; on the right view, flow is left to right.....	90
Figure 5-11. Channel wall outlines from a top-down view at 50% channel height for the as-built $\lambda=0.1L$ baseline and optimized shapes. The gray color shows the location of the walls for the baseline case. The dotted lines show the intended baseline design for comparison. (a) Zoomed-in view of a middle branch, same location as in Figure 5-4a, (b) and (c) zoomed-in view of branches at same locations as in Figure 5-4b and c.....	91
Figure 5-12. Channel wall outlines from a top-down view at 50% channel height for the as-built $\lambda=0.4L$ baseline and optimized shapes. The gray color shows the location of the walls for the baseline case. The dotted lines show the intended baseline design for comparison. (a) Zoomed-in view of a middle branch, same location as in Figure 5-7a, (b) and (c) zoomed-in view of branches at same locations as in Figure 5-7b and c.....	93
Figure 5-13. Experimental test rig for flow and heat transfer measurements .....	94
Figure 5-14. Friction factor augmentation versus Reynolds number for the $\lambda=0.1L$ case.....	96
Figure 5-15. Friction factor augmentation versus Reynolds number for the $\lambda=0.4L$ case.....	98
Figure 5-16. Top-down view at 25% channel height of the baseline and $J_1$ configurations. Contours are normalized axial velocity, with velocity vectors overlaid to highlight flow direction. ....	98
Figure 5-17. Nusselt number augmentation versus Reynolds number for the $\lambda=0.1L$ case. ....	99
Figure 5-18. Nusselt number augmentation versus Reynolds number for the $\lambda=0.4L$ case. ....	100
Figure 5-19. Friction factor augmentation vs. Nusselt number augmentation at a Reynolds number of 5000. Open markers indicate data from Kirsch and Thole [109], where microchannels were non-communicating (denoted in legend as ‘wavy’). Closed markers indicate data from the current study (denoted as ‘branched’). ....	101
Figure 6-1. Isolated wavy channel construction. To create the channels, a rectangle was swept along the path created by the four $45^\circ$ arcs. (a) $\lambda=0.4L$ case, (b) $\lambda=0.1L$ case, (c) description of wavy channel construction.....	108
Figure 6-2. Communicating wavy channel configuration. The primary channels were created in the same manner as shown in Figure 6-1, but branches were included to encourage fluid mixing. Branches emerged from the primary channels at a $45^\circ$ angle to the horizontal. (a) $\lambda=0.4L$ case, (b) $\lambda=0.1L$ case, (c) description of wavy channel construction. Note the sharp corner at the branch exit, which was included to encourage jet penetration. ....	108
Figure 6-3. Top-down view at 50% channel height of the computational mesh used for the $\lambda=0.1L$ communicating channel configuration. In the case of the isolated channels, only one channel was included in the simulation. Not shown in this figure is the heat input into the simulation,	

which was accomplished through a constant temperature boundary condition on the top and bottom endwalls. ....	109
Figure 6-4. Build direction for L-PBF coupons.....	112
Figure 6-5. Deviation from the design intent for the (a) 6.5X scale SLA test coupon and (b) the 1X scale L-PBF test coupon. The channels shown are for the objective to minimize pressure loss. The as-built channel outlines at the location specified at the top of the image are colored by their deviation from the design intent; the black outline shows the slice of the CAD model. The contour scales for the different manufacturing processes reflect the difference in scale between the two test coupons. ....	113
Figure 6-6. Cross-section of experimental setup for friction factor tests.....	115
Figure 6-7. Benchmarking data from straight, smooth, rectangular channels atop friction factor correlations for laminar flow ( $64/Re$ ) and turbulent flow (Colebrook Formula) .....	115
Figure 6-8. Friction factor augmentation for the $\lambda=0.1L$ non-communicating (isolated) channel case .....	116
Figure 6-9. 2D slices taken at 17.5% of the channel length of the $\lambda=0.1L$ Baseline and $\min(\Delta P)$ cases. Contours are colored with normalized axial velocity. Note that contours colored blue showcase flow moving in the negative x direction.....	117
Figure 6-10. 2D slices taken at 55% of the channel length of the $\lambda=0.1L$ Baseline and $\max(Q)$ cases. Contours are colored with nondimensional temperature; secondary velocity vectors are overlaid. Note the direction of the secondary velocity vectors in the $\max(Q)$ case relative to the baseline case.....	118
Figure 6-11. Friction factor augmentation for the $\lambda=0.4L$ non-communicating (isolated) channel case.....	119
Figure 6-12. 2D slices taken at 60% the channel length of the $\lambda=0.4L$ design. The baseline and all three optimized cases are shown. Contours are colored with nondimensional temperature; secondary velocity vectors are overlaid. ....	120
Figure 6-13. Friction factor augmentation for the $\lambda=0.1L$ communicating channel case. ....	120
Figure 6-14. 2D slices taken at 65% of the channel length of the $\lambda=0.1L$ communicating design. The baseline and all three optimized cases are shown. Contours are colored with non-dimensional temperature; secondary velocity vectors are overlaid. ....	121
Figure 6-15. Friction factor augmentation for the $\lambda=0.4L$ communicating channel case. ....	122
Figure 6-16. Friction factor from the $\lambda=0.1L$ non-communicating L-PBF and SLA test coupons, as well as the realizable $k-\epsilon$ model, normalized by each configuration's respective baseline channel. ....	123

Figure 6-17. Friction factor from the $\lambda=0.1L$ communicating L-PBF and SLA test coupons, as well as the realizable k- $\epsilon$ model, normalized by each configuration's respective baseline channel. ....	124
Figure A-1. Change in cross-sectional area for each of the wavelengths from the study in Chapter 2 through one wavelength of each channel. The longer the wavelength, the more significant deviation from the inlet cross-sectional area. This figure is a reproduction of Figure 2-2....	140
Figure A-2. Communicating channel design from Singh et al. [8]. ....	141
Figure A-3. Top-down view at 50% channel height of the as-manufactured initial communicating wavy channel design. ....	142
Figure A-4. Fillet radii for the communicating wavy channels. The radii were the same for the $\lambda=0.4L$ communicating channels. ....	142
Figure A-5. Contours of normalized static pressure from the isolated wavy channel simulations; contours were duplicated to include two channels. The outline of the communicating wavy channels are laid atop the two isolated channel contours. The inlet to the branch is centered on the high pressure region of one channel, and exits into the lower pressure region of the neighboring channel. ....	143
Figure A-6. Change in shape among all three optimized cases, plus the baseline, for the $\lambda=0.1L$ wavy channel design. Slice location was taken at the peak of the wave; the optimized designs show slight deviations from the baseline's pure rectangular cross-sectional area. ....	144
Figure B-1. Shape changes as dictated by different imposed changes to the objective function. The baseline design is shown for comparison. ....	147
Figure B-2. Comparison of shape changes at one slice location for different wall boundary conditions. Contours are colored by non-dimensional temperature. ....	148
Figure B-3. Comparison of flow structures at one peak in the wavy channel design. Contours are colored by normalized axial velocity, and secondary velocity vectors are overlaid. ....	149

## LIST OF TABLES

Table 2-1. DMLS Machine Settings [41].....	15
Table 2-2. Design vs. Actual Dimensions.....	17
Table 3-1. Change in observables relative to the baseline for $\lambda=0.1L$ .....	36
Table 3-2. Change in observables relative to the baseline for $\lambda=0.4L$ .....	36
Table 3-3. Measured dimensions of as-built channels .....	43
Table 4-1. Test matrix.....	56
Table 4-2. L-PBF pin fin microchannel coupon dimensions and roughness values .....	62
Table 4-3. L-PBF baseline multichannel coupon dimensions and roughness values [16] .....	63
Table 4-4. Studies from the literature to be included in results discussion.....	67
Table 5-1. Changes in $\Delta P$ , $Q$ , and $Q/\Delta P^{1/3}$ relative to $\lambda=0.1L$ Baseline .....	83
Table 5-2. Changes in $\Delta P$ , $Q$ , and $Q/\Delta P^{1/3}$ relative to $\lambda=0.4L$ Baseline .....	83
Table 5-3. Changes in $\Delta P$ and $Q$ relative to non-communicating channels.....	89
Table 5-4. Inlet dimensions of the CAD and as-built channels for $\lambda=0.1L$ .....	93
Table 5-5. Inlet dimensions of the CAD and as-built channels for $\lambda=0.4L$ .....	94
Table 6-1 Changes in $\Delta P$ , $Q$ , and $Q/\Delta P^{1/3}$ in non-communicating optimized channels relative to each respective baseline .....	110
Table 6-2. Changes in $\Delta P$ , $Q$ , and $Q/\Delta P^{1/3}$ in communicating optimized channels relative to each respective baseline.....	111

## NOMENCLATURE

$A_c$	cross sectional area
$A_f$	surface area of fin
AM	additive manufacturing
$A_s$	wetted surface area
$A_t$	total surface area
<b>b</b>	design variables
CFD	computational fluid dynamics
CT	computed x-ray tomography
D	pin diameter
$D_h$	hydraulic diameter
F	mathematical description of geometry
f	Friction factor
$f_0$	Empty duct friction factor, $f_0^{1/2} = -2.0 \cdot \log \left( \frac{\epsilon/D}{3.7} + 2.51 \cdot (\text{Re}_{Dh} \cdot \sqrt{f_0})^{-1} \right)$
h	convective heat transfer coefficient
H	channel height or pin fin height
HIP	Hot Isostatic Pressing
J	objective function or observable
k	thermal conductivity
L	coupon length
$L_c$	characteristic length
L-PBF	Laser Powder Bed Fusion
m	$\sqrt{(h \cdot p \cdot (k \cdot A_c)^{-1})}$
N	Number of pin fin rows
$N_{\text{pins}}$	Number of pin fins in array
Nu	Nusselt number, $h \cdot D_h \cdot k_{\text{air}}^{-1}$
$Nu_0$	Empty duct Nusselt number, $Nu_0 = (f/8 \cdot (\text{Re}_{Dh} \cdot 1000) \cdot \text{Pr}) \cdot \left( 1 + 12.7 \cdot (f/8)^{1/2} \cdot (\text{Pr}^{2/3} - 1) \right)^{-1}$
p	perimeter
P	Static pressure
pf	performance factor
q	flow variables
Q	Heat transfer rate
<b>R</b>	conservation laws
$R_a$	Surface roughness, $\frac{1}{n} \sum_{i=1}^n  z_{\text{surf}} - z_{\text{meas}} $
$\text{Re}_D$	pin Reynolds number, $U_{\text{max}} \cdot D \cdot \nu^{-1}$
$\text{Re}_{Dh}$	Reynolds number, $U \cdot D_h \cdot \nu^{-1}$
S	channel pitch or spanwise spacing
SLA	stereolithography
t	Thickness
T	Static temperature
U	Fluid axial velocity



$U_m$	mean channel velocity
$U_{max}$	maximum channel velocity
$u_\tau$	friction velocity
$w_b$	branch width
$W$	Channel width
$X$	streamwise spacing
$y^+$	Inner wall coordinate, $y^+=y \cdot u_\tau \cdot \nu^{-1}$

### Greek

$\Delta$	differential
$\epsilon$	sand grain roughness
$\lambda$	channel wavelength
$\Lambda$	adjoint variable
$\nu$	kinematic viscosity
$\rho$	density
$\eta_f$	fin efficiency, $\eta_f = \tanh(m \cdot L_c) \cdot (m \cdot L_c)^{-1}$
$\eta_o$	overall surface efficiency, $\eta_o = 1 - (N_{pins} \cdot A_f) \cdot (1 - \eta_f) \cdot A_t^{-1}$
$\theta$	nondimensional temperature, $\theta = (T_s - T(z, y)) \cdot (T_s - T_m)^{-1}$

### Subscripts

0	reference condition
1	inlet
2	exit
m	mean
meas	measured
s, surf	surface
Ch	channel
lm	log mean

## ACKNOWLEDGEMENTS

To Karen, who has so generously played the simultaneous roles of academic, personal, and professional advisor and mentor since I first walked into her office as a sophomore—thank you for your support and guidance. Working with you is the sole reason I was ever interested in graduate school in the first place, and I will forever be grateful for your monumental role in my growth as a person. Thank you for setting the bar for technical excellence and professionalism so high, and thank you for your faith in me.

To Michael, who has worked so diligently with me to improve my communication skills—thank you for opening up so many incredible opportunities for me. Traveling around the world with (or because of) you is the source of many a bright spot during my PhD.

To my committee members Steve, Rob, Ted, and Reid—thank you for your technical and professional guidance. Your input has been invaluable to the technical quality of my work. Thank you for all of your efforts to strengthen the impact of my work, and all of the time you have dedicated to helping me.

To my labmates, both at Penn State and at Karlsruhe, who made coming into the lab each day something I always looked forward to—thank you for your cheery demeanors, the fun conversations, and the help with homework, candidacy studying, and running experiments. Johannes, Franz, and Corina—thanks for so willingly accepting a crazy American into your lab. Amy, Jeff, Ken, Curtis, Robert, Molly, and Chris—thanks for casting my time as a graduate student as such a positive time in my life.

To Pratt and Whitney, who has maintained such a valuable relationship with me even after I no longer worked with them directly—thank you for your friendship and mentorship throughout my degree. Also, many thanks to the National Science Foundation, whose financial support allowed me the freedom to take risks in choosing my project.

To Jake, an unending source of joy and fulfillment in my life—thank you for teaching me something new every day. Life with you is a beautiful adventure. Thank you for keeping me motivated when I needed extra support, and for distracting me when I needed a break.

To my family, most especially Mom, Dad, and MJ, who didn't know quite what they were getting themselves into when I decided to go for a PhD—thank you for taking on this journey with me anyway. My PhD is a testament to the love and support you've given me since day one. Thank you for always being there for me in capacities that ranged from life advice to retail therapy. I love you.

# 1 INTRODUCTION

An important advantage inherent to the additive manufacturing (AM) process is the ability to lift many design constraints imposed by conventional manufacturing techniques, such as casting. The choice as to what exactly should be designed is one that is wisely handed to numerics; a long list of optimization schemes have been developed over the years to inform designers of the best possible architecture for the job. However, until recently, optimization schemes have generally only been able to provide guidance to designers; complex, organic geometries are difficult, if not impossible, to create using conventional means. Additionally, creating organic geometries can be difficult to create using conventional CAD tools.

The ideal heat exchanger is one that can be designed without regard for manufacturing limitations, and takes the form most optimized for its end use. Significant research efforts are required before that ideal is achieved, but understanding the link between different designs and their as-built counterparts is a step forward. This document contains five papers that investigate the current state of the relationship between computational designs and their additively-manufactured counterparts. Four of the papers contain experimental results on test coupons manufactured using Laser Powder Bed Fusion (L-PBF), one type of metal-based additive manufacturing. Internal surface roughness, a well-known consequence of L-PBF, played a large role in the aerothermal performance of these test coupons. In an effort to understand the influence of surface roughness better, the fifth paper presents experimental results of test coupons manufactured using a stereolithography (SLA) process, which yielded smooth walls.

## 1.1 Micro Scale Cooling

In electronics and gas turbine industries, the demand for high efficiency necessitates smaller components and, as a consequence, the cooling mechanisms trend toward the micro scale. Cooling on a small scale has many advantages. For one, as the size of cooling channels shrinks, the amount of coolant that comes into contact with the channel walls increases. The high surface area to volume ratio of microchannel heat sinks is appealing for situations where a high heat load needs to be dissipated with a small amount of coolant. Additionally, decreasing the size of cooling channels allows them to be placed closer to the heat source, making them a more efficient method of removing the heat.

### *Electronics Cooling*

The electronics industry canonically moves at a swift pace, with devices becoming outdated mere months after their initial release. A large driver for this rapid development is the

large-scale integration of circuits [1] and the three dimensional stacking of storage elements for increased memory capacity [2]. Both initiatives require efficient thermal management. The International Technology Roadmap for Semiconductors cites thermal constraints as a limiter for the large-scale integration and packaging of circuits [3].

A common method to achieve the required high heat removal rates is to use two-phase flow systems. Boiling flow, for example, is an excellent way to manage high heat fluxes; a study performed by Sadaghiani et al. [4] investigated micro and nano structures to enhance boiling for small-scale cooling, and achieved heat transfer coefficients well in excess of 3000 W/m<sup>2</sup>K. However, for many applications, two-phase flows are not an option, and could degrade the components that need to be cooled. For such applications, where air-cooled heat exchangers are generally preferred [1], the cooling channels must be small in order to achieve the required heat flux removal. In a study by Jung et al. [5], the authors found that micro-channel flows are capable of providing the same heat transfer coefficients as two-phase flow systems used for semiconductor applications.

The amount of mass flow available for cooling electronics is ordinarily quite limited. Typical heat exchangers for electronics are finned, which perform well for low mass flows. Additionally, recent efforts have focused on metal foams as potential solutions to the challenge of high heat removal [1,6,7]. Small, internal cooling channels are also actively studied [5]. One channel architecture of note is a wavy configuration [8], which promotes mixing in the channels due to the centripetal forces that act on the fluid particles as they navigate the waves.

A variety of manufacturing techniques are available to construct the micro (<100  $\mu\text{m}$ ) cooling features of interest to the electronics industry, such as LIGA (*Lithographie, Galvanoformung, Abformung*), chemical etching, diffusion bonding, stereolithography and micro-machining [9]. Stereolithography and LIGA are both additive processes, as opposed to subtractive processes, and are widely used to manufacture pin fin arrays or micro mixers, as examples [9].

In the current study, a stereolithography (SLA) process was used to build test coupons for friction factor experiments. The SLA process used a photoreactive resin, which is cured layer-by-layer using a high precision laser. Figure 1-1 depicts the type of SLA system used for the current study. The build platform is dropped into the resin tray, and the first layer of the part is cured directly to the build platform. Once the layer is complete, the build platform lifts, a wiper blade agitates the resin, and the build platform lowers into the resin tray again, one layer height above its initial dip. SLA processes can generally create very smooth surfaces and, when scaled appropriately, can build parts extremely close to their intended designs. One consideration when using SLA processes is the viscosity of the resin itself; when attempting to build small, internal

channels, liquid resin can get stuck in internal features and can be difficult to remove. As such, internal channels must either be scaled up, or be built in multiple pieces.

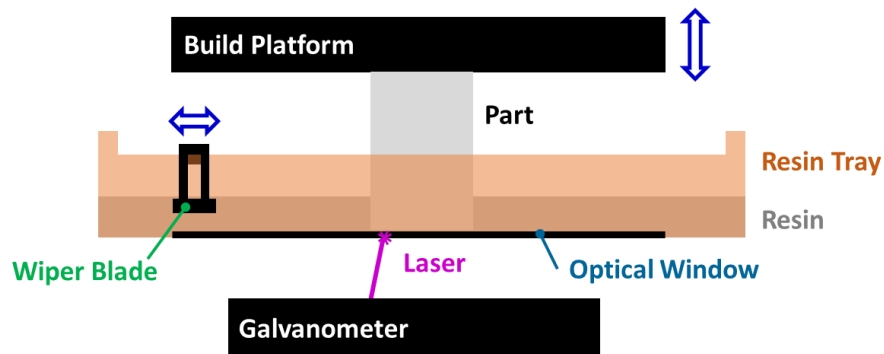


Figure 1-1. Stereolithography (SLA) build process. A photoreactive resin is cured layer-by-layer to build a part.

### *Gas Turbine Cooling*

Turbine components are exposed to combustion gases that far exceed their melting temperature. To maintain their durability, therefore, hot sections components must be cooled both internally and externally. Coolant air is bled from the compressor, which is routed around the combustor. As modern engines become more efficient, the compressor exit temperature increases; the higher the compressor exit temperature, the lower the cooling capacity of the air.

Internal cooling schemes can include turbulators, such as pin fins or ribs in serpentine channels, or impingement cooling. External cooling is accomplished through film cooling. Coolant flow passes through the components' internal passageways and exits through film holes that spread coolant over the exterior surface, thereby providing a barrier between the hot combustion gases and the component itself. Both methods of cooling represent a loss to the overall efficiency of the engine; any fluid used for cooling is not used to generate work in the turbine. However, film cooling specifically leads to a decrease in the turbine adiabatic efficiency because it empties the coolant into the main gas path, resulting in the non-isentropic mixing of the coolant with the main gas path air. Efforts in the industry are focused on methods to improve internal cooling schemes such that film cooling is no longer necessary.

Improvements in thermal management will require improved cooling designs that can perform well with less coolant; skin cooling serves as a viable medium for such a goal. Bunker et al. [10] cites an inevitable move from conventional internal cooling schemes to skin cooling, where designs are directly built into the exterior walls of an airfoil: a heat exchanger that is located closer to the hot gas path is more effective than one located internally.

Figure 1-2 shows an example of skin cooling using mini serpentine passages as the cooling mechanism. Coolant is routed up through the base of the airfoil and through the mini channels, the

serpentine nature of which is created using pin fins, to provide a heat sink to the outer skin of the airfoil. The coolant is then dumped into collector cavities, then exits through the trailing edge. Such small cooling mechanisms are restricted by current manufacturing techniques in that they cannot take forms that deviate from conventional pin fin shapes or straight-walled channels. Advances in current manufacturing technologies, along with the development of new manufacturing techniques, are essential to forward progress in the design and implementation of future mini or micro cooling channels.

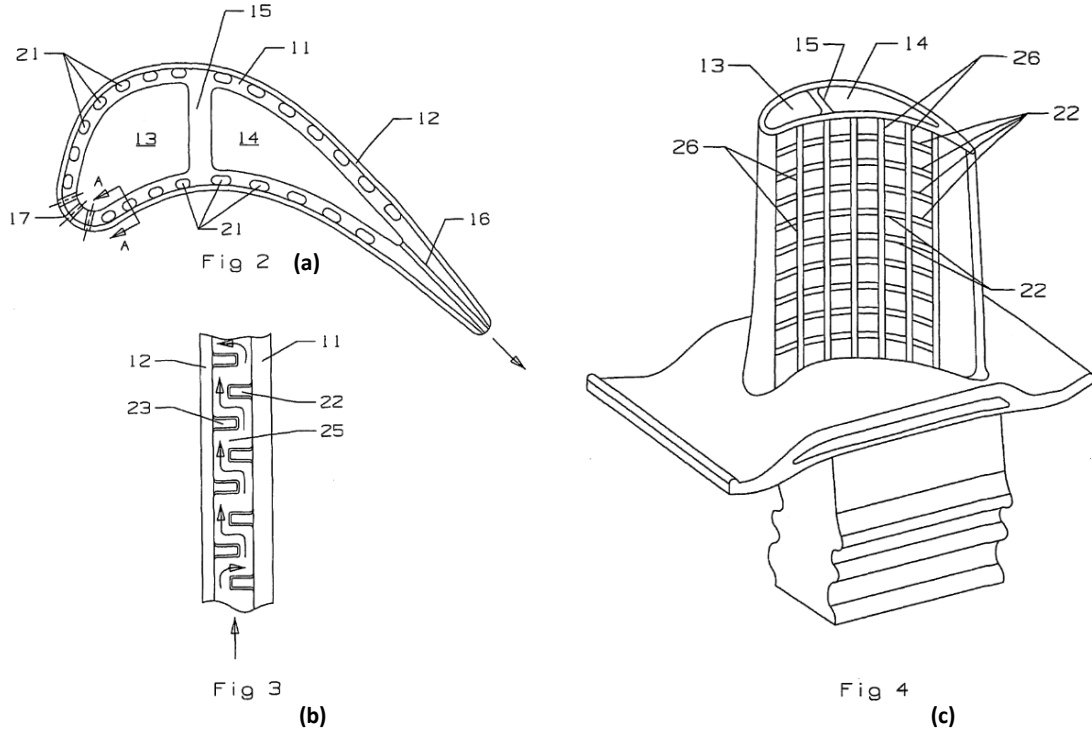


**Figure 1-2. Depiction of skin cooling with mini serpentine cooling channels [11]. (a) Top down view of turbine airfoil. Cooling passages are denoted as 21. (b) Cross section of skin cooling scheme, taken from section AA in (a). The serpentine path is created using pin fins. (c) Isometric view of turbine airfoil, with the outer skin removed and the cooling passages highlighted. Coolant is routed up through the base of the airfoil, through the serpentine passages (b), into collector cavities denoted as 13 and 14, then out through the showerhead holes (denoted as 17), or out through the trailing edge of the airfoil (denoted as 16).**

## 1.2 Laser Powder Bed Fusion

The umbrella term L-PBF encompasses all AM methods that employ a laser as the energy source to selectively melt regions of a metal powder bed. Various trade names for this process exist, such as Direct Metal Laser Sintering (DMLS), Selective Laser Melting (SLM) or Direct Metal Printing (DMP), but all L-PBF processes work in a similar manner, which is depicted in Figure 1-3 [12]. Metal powder is spread from the powder delivery chamber over the build area. A laser selectively fuses the powder particles together as instructed by machine software, which contains the part's geometric description in sliced format, among other pertinent machine

parameters. Once the layer is complete, the powder delivery piston raises, the fabrication piston lowers, and a new layer of powder is spread over the build area. The process repeats until all layers of the part have been manufactured. Unused powder is shaken from the part and can be sieved for reuse in the next build.

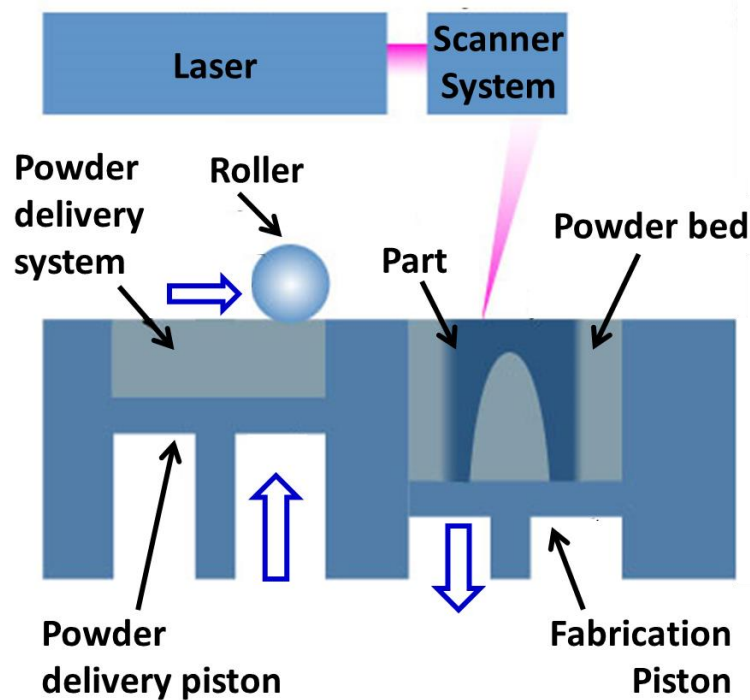


**Figure 1-3. Depiction of the Laser Powder Bed Fusion (L-PBF) process [12].**

Post-processing of L-PBF parts include stress relief, heat treatment, hot isostatic pressing (HIP) and surface finishing techniques, as select examples. Stress relieving parts is generally required for all L-PBF processes due to the locally high temperatures experienced by the part during a build; heat treatment and HIP procedures, on the other hand, are generally of interest only where improved mechanical properties are desired. Surface finishing techniques can be applied to all external surfaces of a part and include removing roughness features that form during the build and improving geometric tolerances. In some cases, internal surfaces can be smoothed as well. However, the length to diameter (L/D) ratios of the internal channels play a significant role. Abrasive materials traveling through channels with large L/D can create a bell-mouth effect, where more material is removed at the beginning of the channel than in the middle. Therefore, maintaining channel dimensions during the finishing process is difficult when the diameter is small or the length is long. As a consequence, internal surfaces generally remain untouched. Microchannels, therefore, are subject to issues in geometric tolerancing and contain large, irregular roughness features on all internal surfaces.

Surface roughness is a hallmark of the L-PBF process. Roughness can result from any number of consequences of the build process, such as the adhesion of loose powder particles, weld sputtering, stair-stepping effects or balling formation [13]. A key driver in the surface roughness formation is an artefact of the process itself, namely that fully-dense components are constructed from loose powder particles. The thermal conductivity of powder is driven by the powder density, and can be up to three hundred times less than the thermal conductivity of bulk metal [14]. Therefore, whether the current layer is to be built atop solid, fully-melted material (upward-facing surface), or atop loose powder (downward-facing surface) strongly affects the roughness levels that form. When melting material on an upward-facing surface, heat from the laser can conduct through the solid and away from the melt pool. For downward-facing surfaces, however, the heat from the laser cannot conduct away from the melt pool as quickly or as uniformly as it can through solid material. This different set of boundary conditions incurs two main penalties to surface finish. For one, the inconsistent conduction rate makes the melt pool more difficult to control, which can lead to instabilities that induce balling. The second consequence is that the melted material cannot cool as quickly. As a consequence, the adhesion of powder particles on unsupported surfaces occurs more readily. Additionally, the layerwise build process incurs what is known as a stair-stepping effect on slanted or rounded surfaces, which also contributes to the roughness levels.

In the case of microchannels, roughness features can serve as significant blockages to the flow, which has negative implications for the pressure loss through the channels. Snyder et al. [15] and Stimpson et al. [16] found that the friction factor through straight L-PBF microchannels was sensitive to the relative roughness, or the size of the roughness features relative to the channel hydraulic diameter. Heat transfer, on the other hand, was less sensitive to relative roughness; beyond a friction factor augmentation of four, the heat transfer no longer increased. However, the heat transfer performance of these simple, straight L-PBF microchannels was similar to that from common internal cooling schemes from the literature, such as pin fins [17,18] or ribs [19].

### **1.3 Optimization Methods**

Design inspiration can stem from any number of sources, but one popular and well-regarded tool comes in optimization analyses. Optimization procedures can be categorized into either gradient-based methods (first order methods) or nongradient-based methods (direct, or zero order methods) [20]. Gradient methods were first proposed in 1847 by Cauchy, but developments of direct methods only began in the 1960s, when digital computers became capable of solving the required calculations [20,21]. The aerospace industry quickly latched on to optimization methods



as powerful design tools and began using optimization techniques in tandem with computational fluid dynamics starting in the 1970s [21].

All optimization functions are posed to find a minimum (or maximum) solution to the problem at hand, subject to various constraints. The choice as to which optimization method to use is dependent on factors such as the size of problem, whether the objective function is continuous and/or smoothly differentiable, and whether the problem is subject to multiple local minima.

Direct methods, also known as zero-order methods, are applicable when the first or second derivative of the objective function is unavailable or when design variables are discontinuous. Examples of direct optimization methods include simulated annealing, genetic algorithms and differential evolution algorithms, among others [20]. Design variables are perturbed systematically, and the objective function is solved for each change in the design variables that is introduced. The results of each objective function solution can then be analyzed, and the most successful perturbation in design variables can be identified. Direct methods are generally robust and, in some cases, are capable of finding the problem's global minimum. However, the methods can require a prohibitively large number of solver iterations before achieving its goal. Additionally, the requirement that the objective function be solved for every change in design variable limits the number of design variables that can be reasonably introduced into a problem. Strategies such as Design of Experiments or parameterization of design variables can be used to circumvent this issue.

Gradient-based methods, or first-order methods, on the other hand, require the evaluation of the objective function's derivative. They can only guarantee a local minimum, as opposed to a global minimum, but are generally more efficient than direct optimization methods. Select examples of gradient methods include steepest descent, Newton's method, and nonlinear least squares [20,22]. Once a gradient-based optimization scheme has been executed, a sensitivity analysis can be performed to perturb the solution and identify how sensitive the solution is to changes in a design variable. Additionally, a sensitivity analysis can inform a researcher as to which of the design variables exhibits the strongest influence on the end result; such information is powerful in determining the smallest amount of change that will yield the largest benefit.

By definition, a sensitivity analysis requires knowledge of the derivative of the objective function with respect to all design variables. In even moderately complex problems, such a determination may quickly become cumbersome and require a large amount of computational resources. A computationally efficient way to perform a sensitivity analysis is to employ an adjoint solver. An adjoint approach can be either continuous or discrete; the difference between the approaches lies in whether the solver is derived from the continuous or discretized form of the differential equations that define the physics of the problem at hand. For the current studies, the

governing equations are the Navier-Stokes equations and the discrete adjoint solver was chosen to accomplish the sensitivity analysis [23]; the results from the adjoint solver were used in informing shape optimization for the wavy microchannels in Chapter 3, the results of which are presented in Chapter 4. Chapter 5 also presents results from the adjoint solver, though for a slightly different baseline configuration.

A brief mathematical description of the adjoint method is given in section 3.4. The advantage of the adjoint solver is that any coupling between the flow field and the design variables is eliminated, meaning that the flow solver need not run for every perturbation in every design variable. The approach is a key component of the current research: an efficient sensitivity analysis coupled with a low-fidelity flow solver can generate organic microchannel shapes that can then be reproduced using L-PBF.

#### **1.4 Research Objectives**

The primary objective of this dissertation is to explore the consequences of design decisions on a variety of micro cooling configurations built using additive manufacturing. In many cases, design tools and manufacturing techniques are studied in isolation. However, the two fields are intrinsically tied, and advances in one field can open up possibilities in the other.

The use of an adjoint-based sensitivity analysis has not yet been applied to microchannels manufactured using L-PBF. In fact, very few studies exist in the literature that have applied a shape optimization scheme so unconstrained to parts that could be manufactured. In using the adjoint method, the shape changes were relatively unconstrained; over one million degrees of freedom existed in the study, which resulted in shapes that would not have been achievable by parameterizing design variables. The potential of this design tool is vast. However, a key divide currently exists between the numerical simulation and the experimentation of L-PBF parts: the current inability of commercial codes to model large, irregular roughness features decouples the numerical design tools from the as-built geometries.

The results from the studies in this dissertation show that, despite this known disconnect, numerical tools can be used with some success in improving the design of micro cooling channels. Certain optimized shape changes can induce flow features that interact with surface roughness in different ways. For example, the goals of a shape change that encourages the formation of vortices will be augmented by the addition of surface roughness.

#### **1.5 Dissertation Outline**

Each chapter in this dissertation is an independent research paper. The papers that comprise chapters 2-4 have been peer-reviewed and are currently published; chapters 2 and 3 were

originally submitted to the 2016 and 2017 ASME Turbo Expo conferences, respectively. Chapter 2 is currently published in the Journal of Turbomachinery, while chapter 3 is in press with the Journal of Turbomachinery. Chapter 2 presents experimental results from wavy microchannels manufactured using L-PBF. Chapter 3 details the application of the adjoint-based shape optimization method on the channels from Chapter 2. The paper from chapter 4 is published in the International Journal of Heat and Mass Transfer, and presents the results from four L-PBF microchannel pin fin arrays for comparison to conventionally-manufactured pin fin arrays.

Chapters 5 and 6 contain papers that are not yet peer-reviewed or published. The paper in Chapter 5 will be submitted to the 2018 ASME Turbo Expo conference, and details results from a different set of microchannel designs optimized using the same method as in Chapter 3. Chapter 6 contains the results from the SLA optimized test coupons, and highlights the effects that the optimized shape changes had on the friction factor through the channels.

The final chapter of this dissertation contains a summary of the general findings from the previous five chapters, and provides suggestions for future work in the area that overlaps both design and additive manufacturing. Appendices provide some additional information on both the wavy channel geometry, as well as the optimization method used.

## **2 HEAT TRANSFER AND PRESSURE LOSS MEASUREMENTS IN ADDITIVELY MANUFACTURED WAVY MICROCHANNELS<sup>1</sup>**

### **2.1 Abstract**

The role of additive manufacturing for the hot section components of gas turbine engines grows ever larger as progress in the industry continues. The opportunity for the heat transfer community is to exploit the use of additive manufacturing in developing nontraditional cooling schemes to be built directly into components. This study investigates the heat transfer and pressure loss performance of additively manufactured wavy channels. Three coupons, each containing channels of a specified wavelength (length of one wave period), were manufactured via Direct Metal Laser Sintering and tested at a range of Reynolds numbers. Results show that short wavelength channels yield high pressure losses, without corresponding increases in heat transfer, due to the flow structure promoted by the waves. Longer wavelength channels offer less of a penalty in pressure drop with good heat transfer performance.

### **2.2 Introduction**

Advancements in additive manufacturing technology continuously prove and further secure the technique's place in the manufacturing world. The use of additive manufacturing, also generally known as 3-D printing, eliminates geometric design constraints imposed by conventional manufacturing techniques. Many different layer-by-layer additive processes fall under the umbrella term 3-D printing, but additively manufacturing metals is achieved through three processes: Electron Beam Melting (EBM), Selective Laser Melting (SLM) and Selective Laser Sintering (SLS). SLS methods or, more specifically Direct Metal Laser Sintering (DMLS) methods, are especially appropriate for building production-grade parts due to the ability to use high temperature alloys in the process. This advantage makes the DMLS process ideal for producing gas turbine components that must perform well under high thermal stresses.

Freedom from geometric constraints imposed by conventional manufacturing significantly opens up the design space. The internal cooling channels of gas turbine airfoils can assume shapes based not on their ability to be manufactured but on their ability to perform well from a heat transfer and pressure loss standpoint. To that end, this paper examines the heat transfer and pressure loss performance of microchannels whose design was motivated by the induction of vortical mixing, a benefit to heat transfer. These microchannels are members of a class of cooling channel designs

---

<sup>1</sup> Kirsch, K.L. and Thole, K.A., 2016, "Heat Transfer and Pressure Loss Measurements in Additively Manufactured Wavy Microchannels", *Journal of Turbomachinery*, vol. 139(1), pp. 011007

previously presented in the literature that have shown promise in other fields, such as electronics cooling [8,24–26].

Three variations of wavy microchannels were manufactured through DMLS and investigated both computationally and experimentally. Experimental results will be presented for a range of Reynolds numbers and will be compared to the computational predictions. The uniqueness of this study comes in both the manufacturing of these wavy channels and the experimental procedure; the performance of complex DMLS channels at engine-relevant Reynolds numbers has not been previously reported.

## **2.3 Literature Review**

Because the DMLS process is relatively new, many previous studies have sought to characterize the parts that the process yields. Khaing et al. [27] evaluated the roughness and tolerance of DMLS parts through manufacturing cylinders, cones, rectangular ribs and other small features; the authors fabricated parts using a state of the art laser sintering machine [27]. Dimensional errors for these specific parts were found to vary between 0.003 mm and 0.082 mm. Ning et al. [28] reported that smaller geometries are more susceptible to dimensional errors due to the inherent shrinkage in DMLS parts. Dimensional errors are dependent on material, machine properties and the geometry of the part and are critical to know for cooling of turbine components. Delgado et al. [29] investigated the influence of process parameters, namely laser scan speed, layer thickness and build direction, on the final part. The authors reported that build direction had the largest effect on the quality of the final part, where quality was evaluated from both dimensional accuracy and mechanical properties of the part.

The surfaces of DMLS parts are intrinsically rough; while outward-facing surfaces can be smoothed via machining, internal features, such as microchannels, cannot be post-processed easily. Kandlikar et al [30] argued the need for nontraditional parameters, such as constricted flow area, to describe surface roughness more accurately for internal passages. The authors found that, especially in microchannels, the waviness and three dimensionality of surface irregularities have a large effect on the flow structure. Huang et al. [31] studied flow through pipes of very high relative roughness, up to 42%. The authors found that the friction factor in laminar flow yielded higher values than the theoretical  $64/Re$  and the transition to turbulent flow occurred below Reynolds numbers of 2000 when relative roughness exceeded 7%. Dai et al. [32] independently reported similar findings through examining liquid flow through mini channels. The authors found that channels whose relative roughness surpassed 2% exhibited higher friction factor at low Reynolds numbers than laminar theory predicted.

Stimpson et al. [16] examined the effects of surface roughness on flow structures in DMLS parts containing microchannels. In a related study, Snyder et al. [15] analyzed the effect that build direction had on flow structures in similar DMLS parts, paying particular attention to the different roughness features generated by the different build orientations. The authors of both studies reported relative roughness values ranging between 20% and 38% of the channel hydraulic diameters and proved that correlations for friction factor and heat transfer no longer hold true for surfaces with such high roughness values. Both studies confirmed the findings of Norris [33] in showing that the rough DMLS surfaces augment the heat transfer only to a point; when the friction factor augmentation exceeds four, heat transfer augmentation is no longer affected by increasing surface roughness.

Few other studies examined heat transfer and pressure loss measurements for DMLS parts, though focused on external surfaces only. Ventola et al. [34] provided an in-depth investigation of heat transfer and pressure loss measurements on DMLS parts, but only examined external finned surfaces. Wong et al. [35] and Manglik et al. [36] both used SLM to create novel designs for heat sinks.

Investigations on microchannel heat sinks, using internal cooling passageways as opposed to finned surfaces, is another field in which additive manufacturing and 3D printing is gaining much interest. Numerous studies [8,24–26,36,37] have looked at wavy channels as a way to cool electronics, in situations where large pressure losses or high mass flow rates are not applicable. A class of studies [26,38,39] investigated wavy channels whose walls aligned such that the flow navigated converging-diverging passages. A key finding from these studies was that a high pressure loss through these channels was seen due flow separation from the wall, which led to vortices forming in the cavities of the waves. Additional studies examined wavy channels whose cross-sectional area was kept the same. Snyder et al. [40] performed an experimental study on wavy channels and reported increased heat transfer with a minimal increase in friction factor. However, only one wall was heated in the authors' experiment. Sui et al. [25] performed a numerical study on wavy microchannels and showed that vortical structures move along the flow direction and continuously change as they move downstream, thus providing good heat transfer over the length of the channel. Singh et al. [8] also performed a numerical study on wavy channels and wavy channels connected via branches. The authors demonstrated that the wavy channels exhibited high heat transfer performance, without a large penalty in pressure drop. The study focused on low Reynolds numbers. This study by Singh et al. provided the motivation for the current study: the design of the current wavy channels mimicked that of the study by Singh et al.

This review of relevant literatures sets up the motivation behind this study and exposes a research area that remains unexplored: the marriage of knowledge on additive manufacturing capabilities with ideas of successful cooling schemes from across thermal management disciplines. This study is unique in that it considers the potential of wavy channels, a method used in small-scale electronics cooling, for use in cooling gas turbine components and assesses the channels' performance at high Reynolds numbers when manufactured additively.

## 2.4 Description of Test Coupons

Three different test coupons were designed and additively manufactured using Inconel 718 for this study. Each coupon was designed to be 25.4 mm in length and in width, with the height of the coupon set to 1.52 mm. The coupon wall thickness neared the lower limit of the manufacturing capability at 0.25 mm. Flanges were manufactured on each test coupon for ease of experimental investigation and also served as anchors for the part's support structures in the build, as can be seen in Figure 2-1. The coupons were built at 45° relative to the build direction.

The waves of all three wavelengths investigated were drawn from four 45° arcs, whose connecting tangents were set to be equal. The channels were formed by sweeping a rectangle along the resulting curve; the rectangle was kept normal to the wave beginning and end. Thus, the flow saw a slight reduction in cross-sectional area as it moved through the channels that was dependent on the waviness of the channel. The change in cross-sectional area was periodic and is shown for one period of each of the cases in Figure 2-2. The minimum hydraulic diameter was used as the length scale in all friction factor and heat transfer calculations.

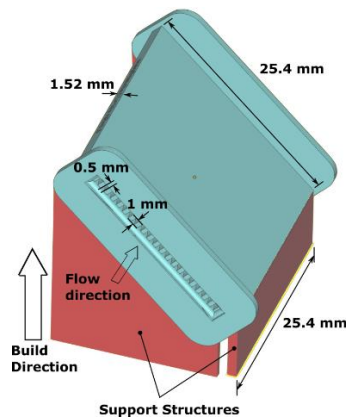


**Figure 2-1. Description of the coupon build, with pertinent dimensions included. Flow direction is normal to the normal to the flange face.**

Figure 2-3 displays a visual representation of the test matrix used in this study. Waviness of the channels was quantified by setting the ratio of wavelength,  $\lambda$ , to coupon length,  $L$ . Three ratios of 0.1, 0.2 and 0.4 were used, whereby a ratio of 0.1 represented the highest frequency wave

and a ratio of 0.4 represented the lowest frequency wave. Equal-length segments (40% of the coupon length) of each wavelength investigated are shown in Figure 2-3; that is, one period of the  $\lambda=0.4L$  case, two periods of the  $\lambda=0.2L$  case and four periods of the  $\lambda=0.1L$  case. Figure 2-4 illustrates the four  $45^\circ$  arcs and the channel construction around the resulting wavy line.

The coupons were manufactured using a state of the art DMLS machine, using the process parameters (material scaling, layer thickness and beam offset) outlined in the manufacturer's specifications [41] and given in Table 2-1 for Inconel 718. Adjusting process parameters to obtain final parts that matched the original design more closely was outside of the scope of this study.

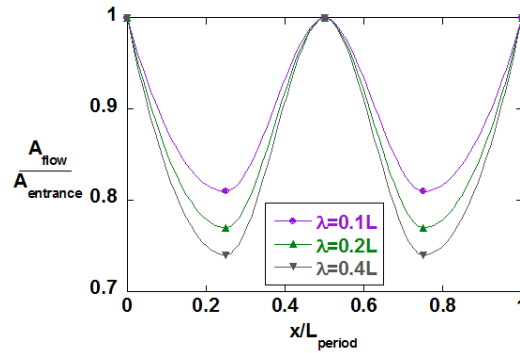


Figure 2-2. Change in flow area through one period of the each of the wavy channel cases.

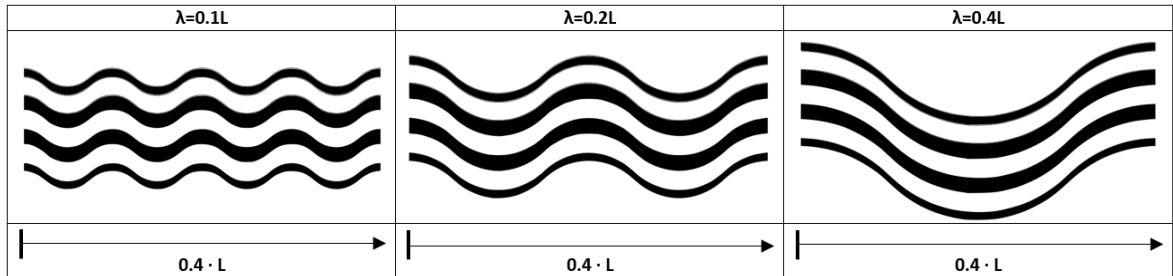


Figure 2-3. Visual representation of the test matrix used for this study. Flow goes left to right.

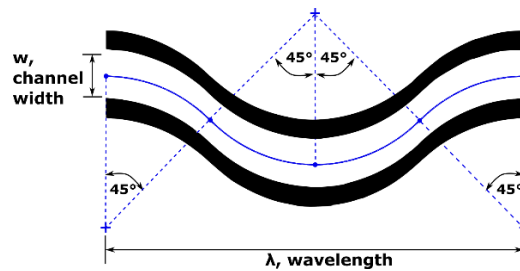


Figure 2-4. Description of the wavy formulation. Flow goes left to right.



**Table 2-1. DMLS Machine Settings [41]**

<b>Parameter</b>	<b>Value</b>
Material Setting	IN718 040 Performance
Material Scaling X	0.045%
Material Scaling Y	0.16%
Beam Offset	0.11 mm
Layer Thickness	0.04 mm

## **2.5 Geometric Characterization**

In the DMLS process, metal powder is sintered together via a high powered laser beam. To ensure adequate contact between the layers, the laser sinters powder deeper than the top-most layer. Where layers do not form directly atop one another, for example on downward facing surfaces, sintered powder particles can form beneath the top-most layer. For this reason, all downward facing surfaces, including internal downward facing surfaces, of DMLS parts are inherently and irregularly rough [15]. An important part of analyzing the experimental data came in properly characterizing the internal surfaces of the part, which included determining the roughness of each surface and, equivalently, the true cross-sectional area and wetted surface area.

Parts and supports were removed from the DMLS build plate via wire electro discharge machining (EDM). Outer faces of the parts were able to be machined and smoothed, but inner surfaces remained untouched. To determine the internal surface characteristics in each coupon, Computed X-Ray Tomography (CT scan) was used. A CT scan takes a series of 2D images of an object that can later be combined to form a 3D reconstruction of that object. The virtually reconstructed object forms as varying levels of grayscale, which correspond to varying levels of material density. In the case of these coupon scans, the resolution (voxel size) achievable by the CT scanner was 35  $\mu\text{m}$ .

To analyze the coupon scans, a commercial software was used to combine the 2D images into the reconstructed coupon [42]. An example of a 2D CT scan image is shown in Figure 2-5, with the CAD model superimposed on the image. Both internal and external coupon surfaces were determined using the software's algorithms; surface determinations allowed for the measurement of each channel's cross-sectional area and perimeter, from which a hydraulic diameter could be calculated.

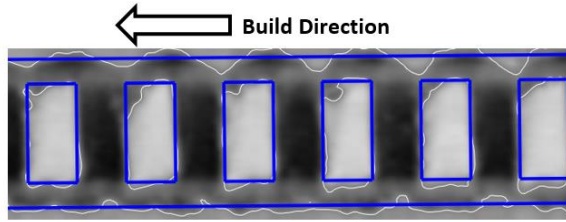


**Figure 2-5. 2D CT scan image. The surface determination algorithm outlined both external and internal coupon surfaces. The dark gray color represents the material and the light gray areas represent the open channels. Overlaid on the CT scan image is the design intent. The channels were 0.5 mm wide, and 1 mm high.**

Essential in determining the surface area of each channel was the need to characterize the channel roughness. As was to be expected, each of the channel walls exhibited varying levels of roughness due to the build direction that was chosen; the top and left walls of each channel, from the perspective of Figure 2-5, were always unsupported during the build. The consequence of these unsupported walls was most visible in the top left of each channel, where the corner was rounded.

To calculate channel roughness, a point cloud of geometric data was exported from the CT scan software. Using an in-house code, a surface was fit to the channel walls and roughness features were deduced based on their deviations from the surface fit. Figure 2-6 shows line plots of surface roughness along the length of a representative channel at 50% of the channel height for the  $\lambda=0.1L$  case. To note, the number of data points in each plot was the same; in the upward facing surface, data points overlapped one another. The difference in the scatter plots is clear; the upward facing surface was much smoother than the downward facing surface, which exhibited larger deviations from the fit. The roughness levels on the downward facing surface were a result of the DMLS build process, as previously shown by Stimpson et al. [16] and Snyder et al. [15]. An arithmetic roughness average,  $R_a$ , was calculated using the height differences between the CT scan data and the channel wall surface fits for each of the coupons. The  $R_a/D_h$  values are shown in Table 2-2, along with the measured hydraulic diameter, cross-sectional area and surface area of each coupon. For reference, the design dimensions are also included. The surface roughness for all coupons, which were averaged over all channels and all surfaces, was similar, which is not surprising given the same build direction for each coupon. All coupons showed an increase in  $D_h$  over the design value.

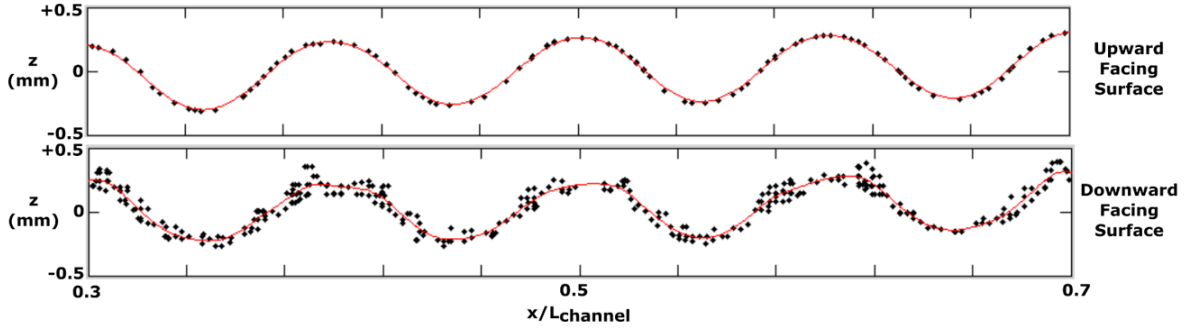


Figure 2-6. Line plots of surface roughness on two surfaces from one channel. The line is the curve fit to the surface; the scatter in the plot represents the points on the surface that deviate from the fit.

Table 2-2. Design vs. Actual Dimensions

Coupon	Number of	Design	Actual	Design	Actual $A_s$	Design	Actual $A_c$	$R_a/D_h$
n	Channels	$D_h$ (mm)	$D_h$ (mm)	$A_s$ (mm <sup>2</sup> )	(mm <sup>2</sup> )	$A_c$ (mm <sup>2</sup> )	(mm <sup>2</sup> )	
$\lambda=0.1L$	20	0.58	0.64	1717	1825	10.3	10	0.018
$\lambda=0.2L$	20	0.565	0.63	1717	1849	10.3	9	0.015
$\lambda=0.4L$	18	0.55	0.60	1548	1645	9.3	8.1	0.016

## 2.6 Experimental and Computational Methods

### *Experimental Setup*

A cross-section of the test facility used for these experiments is shown in Figure 2-7. This facility has been benchmarked and used by numerous investigators in our laboratory [15,16,43]. Air flow through the coupon emanated from a constant pressure inlet; the flow rate was then controlled via a ball valve located downstream of the test section. The mass flow rate through the system was measured using a laminar flow element (LFE) [44]. To measure the pressure drop through the coupon, pressure taps were installed upstream of the inlet contraction and downstream of the outlet expansion. Both contraction and expansion were constructed of a combination of polyether ether ketone (PEEK) plastic and nylon, as can be seen in Figure 2-7. The choice of PEEK plastic and nylon was motivated by their low thermal conductivities, which were important in mitigating heat losses during heat transfer tests. Thermocouples were located upstream and downstream of the coupon to measure the inlet and outlet air flow temperatures. The test section was compressed vertically, by way of the longer bolts shown in Figure 2-7 to ensure no air leaked out of any test section interfaces. The friction factor for each coupon was obtained using Equation 2-1, where  $\Delta P$  was the pressure drop across each coupon. To account for the extra working length between the pressure taps, as well as for the loss associated with a sharp expansion at the coupon outlet, a loss coefficient of one was assumed at the coupon exit in order to calculate the pressure at

the coupon exit. The value for the hydraulic diameter in Equation 2-1 was taken to be the measured hydraulic diameter, which was obtained from the CT scans. The characteristic velocity was calculated from the mass flow rate, as measured by the LFE, where the value for cross-sectional area was measured from the CT scans. To calculate the density, the ideal gas law was used.

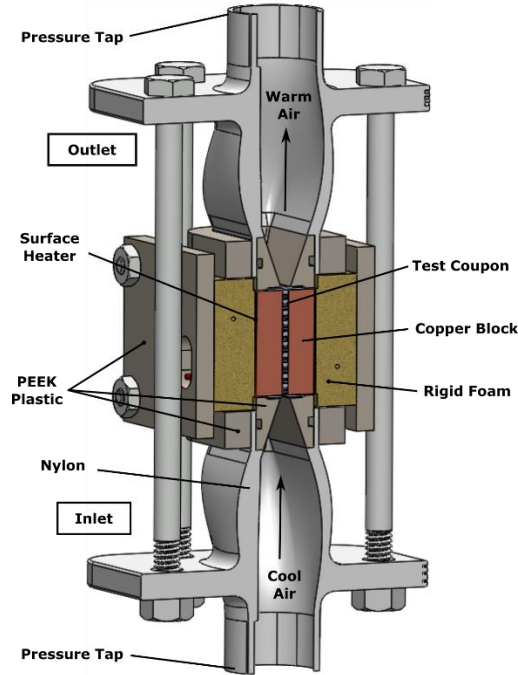


**Figure 2-7. Rendering of the test section setup for both pressure loss and heat transfer measurements. Thermocouples were embedded in the rigid foam, PEEK plastic pieces, and the copper blocks. The LFE is located well upstream of the test coupon and is not pictured here.**

$$f = \Delta P \cdot \frac{D_h}{L_{ch}} \cdot \frac{2}{\rho \cdot U^2} \quad 2-1$$

In the case of the heat transfer experiments, a constant temperature boundary condition was imposed on the test coupon from a heated copper block. A very thin layer of thermally conductive paste adhered a surface heater to the copper block; the same paste was also used in ensuring good contact between the copper block and the test coupon. Rigid foam surrounded the heated system to reduce the heat losses and was sandwiched between two pieces of PEEK plastic. Thermocouples were embedded in the copper block and in the rigid foam, in addition to being adhered to the surface heater and to the outside of the rigid foam to quantify the conduction losses through the system. A detailed description of the conduction loss calculations, which were performed using a 1D approximation and the above-mentioned thermocouples, can be found in [16]. The most significant losses were through the rigid foam surrounding the copper blocks. In the worst case scenarios, which occurred at low Reynolds numbers, conduction losses amounted to 8% of the total

heat transfer; at Reynolds numbers above 3000, conduction losses amounted to under 5% of the total heat transfer. The measured conduction losses were relatively constant over the range of Reynolds numbers tested. Therefore, at higher Reynolds numbers where higher heat input was required, the percentage of conduction losses with respect to the total heat transfer was low.

The temperature of the coupon surface,  $T_s$ , was calculated using a one-dimensional heat transfer analysis, which is described in detail in [16]. The temperature of the copper block,  $T_{Cu}$ , was measured using thermocouples embedded halfway between the coupon surface and the rigid foam block. Previous research using this experimental setup showed the assumption of constant temperature boundary condition was validated [43]. The vendor ensured a dense final part with very little porosity [45], which was important for heat transfer calculations; the thermal conductivity of the test coupon was taken to be equal to that of stock Inconel 718.

Heat into the system was set via power supplies connected to the surface heaters. The log mean temperature difference was calculated using Equation 2-2, which was needed in calculating the heat transfer coefficient, obtained from Equation 2-3. The subscripts 1 and 2 refer to the entrance and exit of the coupon, respectively, and the subscript  $s$  refers to the surface temperature. The surface area,  $A_s$ , in Equation 2-3 was calculated from the CT scan data for each coupon.

The heat into the system was confirmed via redundant measurements: (1) direct measure of the heat from the electric heaters minus the estimated conduction losses, as previously mentioned, and (2) a first law energy balance. For each experiment, these two measurement methods were compared and agreed to within 7% except for the low Re cases (below 2000) in which the agreement was better than 15%.

$$\Delta T_{lm} = \frac{\Delta T_1 - \Delta T_2}{\ln \left( \frac{T_s - T_1}{T_s - T_2} \right)} \quad 2-2$$

$$h = \frac{Q_{in} - \Sigma Q_{loss}}{A_s \cdot \Delta T_{lm}} \quad 2-3$$

### *Uncertainty Analysis*

Measurement uncertainty was quantified using the method outlined by Kline and McClintock [46]. Uncertainty in friction factor measurements was dominated by the range of differential pressure transducers used to measure pressure drops across the LFE and across the coupon. The uncertainty in the LFE itself was 0.8% of the reading, with a repeatability of 0.1% [44]. The low Reynolds numbers in these experiments approached the lower limit of even the smallest pressure transducers. For this reason, uncertainty in friction factor at low Reynolds

numbers approached 23%. However, for Reynolds numbers above 2000, friction factor uncertainty for all cases was below 10%.

Uncertainty in Nusselt number was dominated by the uncertainty in obtaining accurate geometric dimensions. The accuracy in measuring channel height and width via the CT scanner was within 3.5  $\mu\text{m}$ , the resolution achievable by the CT scan software. Uncertainty in geometric measurements also affected the calculation of the coupon wall temperature, which required the measurement of the coupon thickness; the log mean temperature difference, therefore, was the second largest contributor to the Nusselt number uncertainty. Overall relative uncertainty in Nusselt number ranged from 2% to 7% for all cases.

### *Computational Setup*

Computational simulations for each of the three wavy channel cases were performed via a commercial computational fluid dynamics (CFD) software [47]. The simulations were run as conjugate calculations, with the steady RANS and energy equations solved using the realizable  $k$ - $\varepsilon$  turbulence model and the SIMPLE algorithm. Roughness effects were not included in the numerical simulation, despite the magnitude of their effect on both pressure loss and heat transfer results. The interest in the computational study revolved more around understanding the major flow features.

The computational grid was set up in a commercial grid generation software [48]. The grid in each case was set up in a multi-block configuration with structured domains; spacing near the wall was refined such that  $y^+$  values remained near or below one, as is appropriate for the sublayer resolved turbulence model used. The number of cells in each case was 1.6 million. Given that both fluid and solid domains were modeled, the heat transfer analysis was conjugate.

The computational domain included one full-length channel, with the side walls of the channel modeled as periodic. A mass flow inlet, at a specified pressure chosen to match the experimental inlet pressure, was applied at the entrance of each channel. The length of each channel was just under 42 times the channel hydraulic diameter and depended on the waviness of the channel; the flow was therefore taken to be fully developed over the majority of the channel length.

A pressure outlet was imposed at the channel exit. For each case at each Reynolds number, the outlet pressure value was iterated upon until the inlet pressure remained at its specified value. Constant temperature boundary conditions were applied at the top and bottom walls to mimic the experimental setup. Figure 2-8 shows a slice through the center of a channel segment of the mesh for the  $\lambda=0.2L$  case.

A grid sensitivity study was performed for the  $\lambda=0.2L$  case, where the initial number of grid cells were doubled. At a mid Reynolds number of 5000, the change in friction factor was -0.1%

and the change in Nusselt number was 0.1% from the initial grid to the refined grid. Therefore, the initial grid size was deemed to have a high enough resolution for acceptable results. Sufficient convergence was determined when the normalized residuals reached  $1 \times 10^{-6}$  and typically required near 4000 iterations.

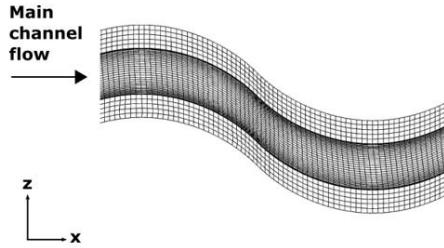


Figure 2-8. Slice of the structured grid for a segment of the  $\lambda=0.2L$  case.

## 2.7 Results and Discussion

Results will be presented for the wavy channels at varying Reynolds numbers. The pressure loss through each coupon will be discussed first, followed by a discussion on the heat transfer performance.

### *Pressure Loss Results*

To ensure accurate measurements, the test facility was benchmarked with a coupon containing smooth cylindrical channels, manufactured conventionally from aluminum; the channels were drilled then reamed to achieve adequately smooth surfaces. The results from the smooth channel test are shown in Figure 2-9, plotted atop friction factor correlations for laminar flow (Laminar Theory,  $f=64/Re$ ) and turbulent flow (Colebrook formula). The Colebrook formula is given in Equation 2-4; the term  $\epsilon/D$  was taken to be zero for the smooth coupon [49], where  $D$  represented the diameter of the smooth cylindrical channel and  $\epsilon$  represented the channel roughness.

$$\frac{1}{\sqrt{f}} = -2.0 \cdot \log \left( \frac{\epsilon/D}{3.7} + \frac{2.51}{Re \cdot \sqrt{f}} \right) \quad 2-4$$

Good agreement between the experimental data and the correlations was seen. Deviation from the correlations in the region between  $700 \leq Re \leq 2000$  can be explained by entrance effects; with channel  $L/D_h$  ratios between 20 and 63, entrance effects play a significant role on friction factor in the laminar region. However, entrance effects are not a factor in the turbulent regime due to the shorter length required to obtain fully developed flow.

Data from the wavy channel coupons are shown in Figure 2-9, as well as data from similarly-sized additively manufactured straight rectangular channels taken from Stimpson et al. [16]. The measured hydraulic diameter of the Stimpson et al. rectangular channels was 0.626 mm

and the ratio of roughness average to hydraulic diameter was 0.017. Stimpson et al. showed that the roughness levels resulting from the DMLS process increased the friction factors significantly, as can be seen in Figure 2-9. Not surprisingly, the wavy channels exhibited higher friction factors than their straight channel counterpart. The highest friction factor was seen in the channels with the shortest wavelength,  $\lambda=0.1L$ , and decreased with increasing wavelength.

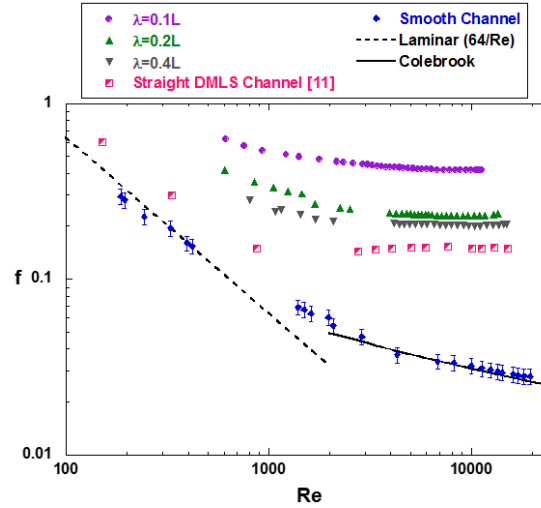


**Figure 2-9. Friction factor vs. Reynolds number. Included in the plot are data from additively manufactured straight rectangular channels or comparable size [16].**

In wavy channels, the flow velocity periodically increases and decreases as the fluid navigates the waves; in the case of these wavy channels, this behavior was exaggerated by the changing flow area, shown in Figure 2-2. As the channel turns, higher velocity fluid hugs the inner wall while fluid near the outer wall travels more slowly. When given enough flow length, this difference in velocity creates shear stresses that can cause the formation of Dean vortices [50].

Figure 2-10 shows results from the numerical study; slices of velocity vectors through each of the wavy channel cases are shown, colored by velocity magnitude. A full Dean vortex was seen to form in the  $\lambda=0.4L$  case, with a smaller one shown in the  $\lambda=0.2L$  case and only smaller vortical structures in the  $\lambda=0.1L$  case. At such short wavelengths, the length between turns in the channel was not enough for the formation of the Dean vortices.

The strongest difference in velocity magnitude across the channel width was seen at the shortest wavelength  $\lambda=0.1L$ . As a consequence of the strongly accelerated flow, areas of separation from the channel wall were seen in the  $\lambda=0.1L$  case. Figure 2-10 shows regions of near zero velocity along the left wall, indicating separation from the wall. These pockets of low momentum velocity caused substantial increases in the friction factor at all Reynolds numbers studied as was shown in Figure 2-9.



Pockets of low velocity are also quite clear from Figure 2-11, which shows a top-down view of normalized velocity in a slice through the channels at 50% channel height. The highest magnitude velocity travels through the channel in a nearly straight line, bypassing the areas bounded by the peaks and troughs. Smaller pockets of low velocity were seen in the  $\lambda=0.2L$  case and none are visible in the  $\lambda=0.4L$  case.

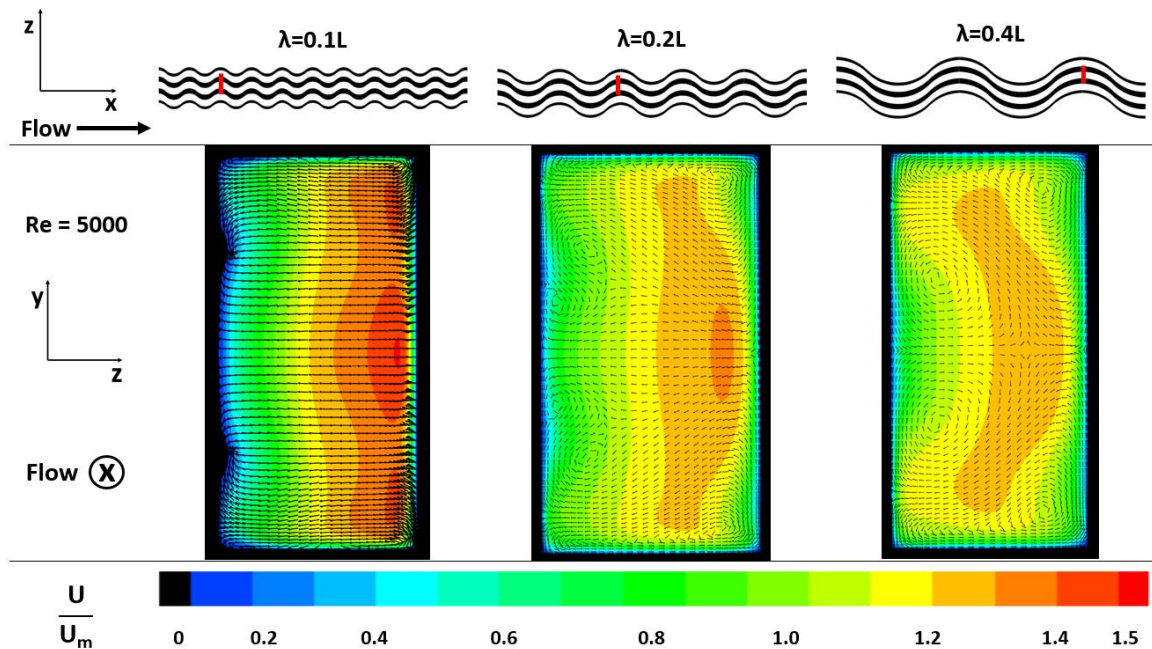


Figure 2-10. Velocity vectors, colored by normalized velocity, of slices through each of the wavy channel cases with  $Re=5000$ . Slices were taken at the second full peak in the wave, as indicated above the contour slices. Note that fluid next to the left wall of the  $\lambda=0.1L$  case is near zero and that a full dean vortex forms in the  $\lambda=0.4L$  case.

Despite the difference in channel construction and roughness values between this study and other wavy channel studies, these results are consistent with those seen in literature [26,28,38–40]; given enough momentum, high velocity fluid hugs the leeward wall and separates from the far wall, causing pockets of low momentum fluid and an overall higher pressure loss through the channel. The friction factors were not as high for the  $\lambda=0.2L$  and  $\lambda=0.4L$  as the  $\lambda=0.1L$  case, which is also expected based on the velocity contours in Figure 2-10 and in Figure 2-11. These results are also expected due to the fact that the longer wavelength channels also had higher area contraction ratios.

Figure 2-12 shows friction factor augmentation versus Reynolds number for each of the cases. The  $\lambda=0.1L$  case shows a high penalty in friction factor over a straight smooth channel, with augmentation values between 8 and 15. The  $\lambda=0.2L$  and  $\lambda=0.4L$  cases, however, show augmentation values closer to those from the straight additively manufactured channel. The results from the numerical analysis suggest that the dominant flow feature contributing to the friction

factor, outside of the high surface roughness, was the formation of low momentum pockets in the wavy channels particularly for  $\lambda=0.1L$ . The Dean vortex formation's contribution to the friction factor was minimal; the  $\lambda=0.4L$  case showed only a relatively smaller increase in friction factor over the additively manufactured straight channel.

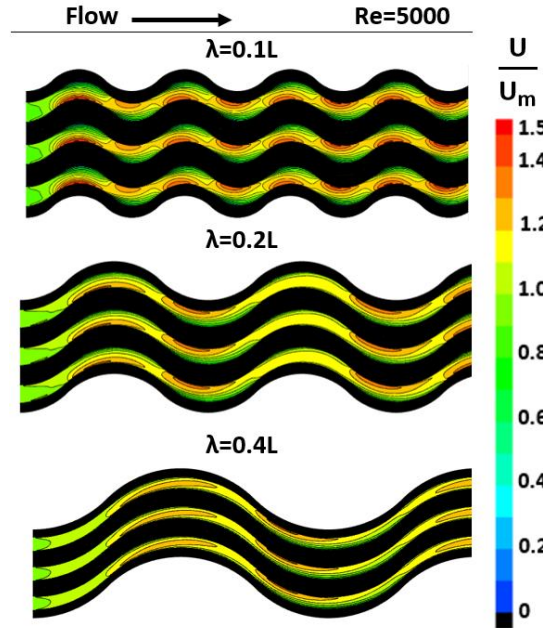


Figure 2-11. Top-down view of the normalized velocity through each of the wavy channel cases with  $Re=5000$ . Flow goes from left to right. Note the pockets of low velocity in each peak and trough of the  $\lambda=0.1L$  case.

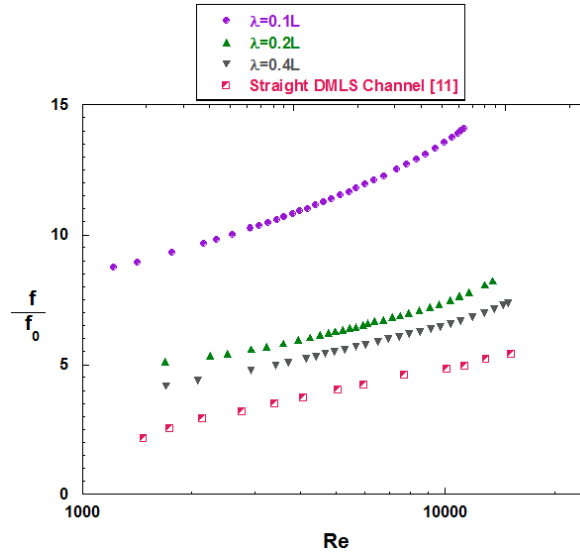


Figure 2-12. Friction factor augmentation vs. Reynolds number.

### Heat Transfer Results

Similar to the friction factor measurements, heat transfer measurements were validated using the same smooth, conventionally-manufactured coupon. Shown in Figure 2-13, the smooth

channel heat transfer results match well to the heat transfer correlation given by Gnielinski [51], shown in Equation 2-5.

Results in Figure 2-13 show that at low Reynolds numbers (<4000), the heat transfer data from the wavy channels exhibited higher heat transfer augmentation than the straight DMLS channels, but as Reynolds number increased, data from all four cases merged. The difference in wavelength appeared to have minimal impact on the heat transfer performance of the channels, despite the large differences in flow structure.

As previously mentioned, an upper limit to heat transfer performance in extremely rough straight channels was reported by Stimpson et al. [16]. These findings corroborated those from Norris [33], who found that beyond a friction factor augmentation of four, a corresponding heat transfer augmentation was not seen. However, as was seen in Figure 2-12, the friction factor augmentation from all wavy channel cases surpassed four for all Reynolds numbers tested. The results from Figure 2-13 indicate that the wavy channel construction, combined with the high channel roughness, yielded higher heat transfer augmentation levels. As previously discussed, wavy channels generate large differences in fluid velocity as the flow moves through the channel. Where high momentum fluid runs near a leeward wall, high heat transfer occurs; where low momentum fluid lags near the opposite wall, low heat transfer is to be expected.

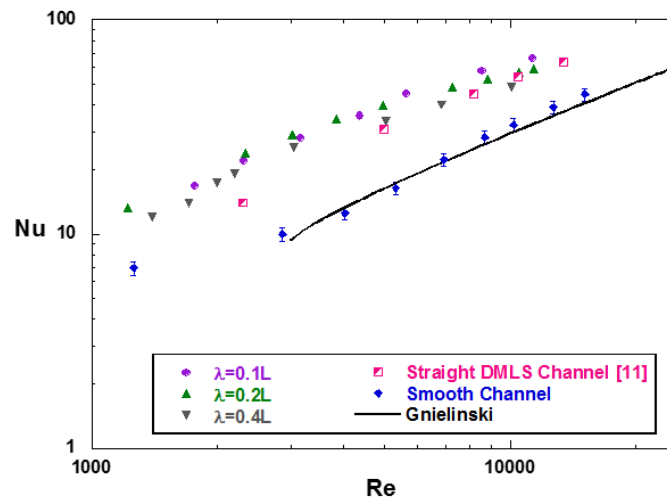


Figure 2-13. Nusselt number vs. Reynolds number.

$$Nu_D = \frac{\left(\frac{f}{8}\right) \cdot (Re - 1000) \cdot Pr}{1 + 12.7 \cdot \left(\frac{f}{8}\right)^{\frac{1}{2}} \cdot (Pr^{\frac{2}{3}} - 1)}$$

2-5

Figure 2-14 shows the Nusselt number augmentation versus Reynolds number. At low Reynolds numbers, the heat transfer augmentation of the wavy channels is 50% higher than that from the straight DMLS channel. Using the results from the numerical study, two contributors to the heat transfer can be deduced: the difference in fluid momentum as the flow navigates the waves and the roughness. At lower Reynolds number, the dominant mechanism appeared to be the flow structure while at higher Reynolds numbers, the channel roughness prevailed.

#### *Augmentation Results*

A comparison of the relative performance of these wavy channels is given in Figure 2-15, where friction factor augmentation is plotted versus Nusselt number augmentation. Also included on the plot are data from various other internal heat transfer schemes [19,52–54]. Consistent with the previous discussions, the  $\lambda=0.1L$  case exhibited much higher friction factor augmentation than most other cases for the same heat transfer augmentation levels. However, both the  $\lambda=0.2L$  and the  $\lambda=0.4L$  cases showed a much increased Nusselt number augmentation for a similar friction factor augmentation over the straight DMLS channel case for Reynolds numbers under 4000.

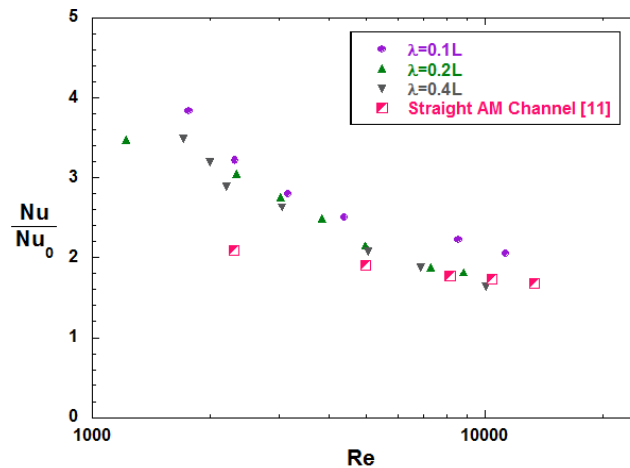


**Figure 2-14. Nusselt number augmentation vs. Reynolds number.**

In comparing the wavy channels to conventional internal cooling geometries, the  $\lambda=0.2L$  and  $\lambda=0.4L$  wavy channels offered similar heat transfer performance with decreased pressure loss. In the case of the pin fin studies, the wake behind a pin fin is detrimental to the friction factor, which is a similar flow characteristic seen in the  $\lambda=0.1L$  case; separated flow only yields high heat transfer at a high cost of pressure loss.

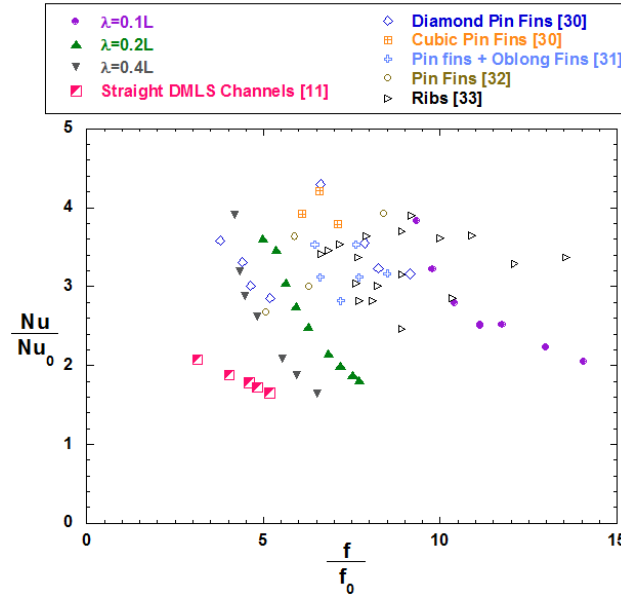


Figure 2-15. Friction factor augmentation vs. heat transfer augmentation.

## 2.8 Conclusions

Three wavy channel coupons, each containing channels of varying wavelength, were designed and additively manufactured to evaluate pressure loss and heat transfer performance of the channels. Three channel wavelengths of  $\lambda=0.1L$ ,  $\lambda=0.2L$  and  $\lambda=0.4L$  were investigated. Additionally, each of the channels were evaluated numerically to gain a better understanding of the flow features. Both the experimental and numerical analyses were performed over a range of Reynolds numbers. For comparison, data from an additively manufactured straight rectangular channel were included in the discussion.

The wavy channels with the longer wavelengths,  $\lambda=0.2L$  and  $\lambda=0.4L$ , performed well from both a heat transfer and friction factor standpoint. The long wavelength, in addition to a periodic decrease in cross-sectional area seen by the flow, allowed the flow to remain attached to the channel walls. In the case of the  $\lambda=0.1L$  wavelength, the flow acceleration through the channels caused separation from the walls. Consequently, the friction factor seen by the  $\lambda=0.1L$  case was significantly higher than the other two cases. These flowfield and, where applicable, friction factor results were consistent with findings from previous wavy channel experiments and numerical analyses; where flow is forced past the peaks and troughs of the waves, pockets of low momentum ensue and a penalty in friction factor is seen.

Nusselt number augmentation seen by all geometries was good, especially at lower Reynolds numbers ( $<4000$ ). When compared to the straight DMLS channel case, the heat transfer augmentation from the wavy channels of wavelengths  $\lambda=0.2L$  and  $\lambda=0.4L$  was much higher for similar friction factor augmentation values. Previous studies have shown that in wavy channels,

the flow remains unsteady throughout the entire channel length, which proves to be a benefit to heat transfer. In the case of the  $\lambda=0.1L$  channels, the heat transfer augmentation was similar to the other two wavelength cases, but the friction factor augmentation was substantially higher.

Based on these results, more research is needed to determine effective DMLS microchannel design and construction. As the technology behind the DMLS process becomes better understood, researchers can take advantage of the vast, open design space available to them. While roughness in DMLS parts has been shown to increase the pressure loss, it has also been shown to increase the heat transfer. The ability to capture the heat transfer benefits while minimizing the pressure loss detriments will come with continued research and exploration beyond conventional designs.

### **3 EXPERIMENTAL INVESTIGATION OF NUMERICALLY OPTIMIZED MICROCHANNELS CREATED THROUGH ADDITIVE MANUFACTURING<sup>2</sup>**

#### **3.1 Abstract**

The increased design space offered by additive manufacturing can inspire unique ideas and different modeling approaches. One tool for generating complex yet effective designs is found in numerical optimization schemes, but until relatively recently, the capability to physically produce such a design had been limited by manufacturing constraints.

In this study, a commercial adjoint optimization solver was used in conjunction with a conventional flow solver to optimize the design of wavy microchannels. Three objective functions were chosen for two baseline wavy channel designs: minimize the pressure drop between channel inlet and outlet, maximize the heat transfer on the channel walls and maximize the ratio between heat transfer and pressure drop. The optimizer was successful in achieving each objective and generated significant geometric variations from the baseline study.

The optimized channels were additively manufactured using Direct Metal Laser Sintering and printed reasonably true to the design intent. Experimental results showed that the high surface roughness in the channels prevented the objective to minimize pressure loss from being fulfilled. However, where heat transfer was to be maximized, the optimized channels showed a corresponding increase in Nusselt number.

#### **3.2 Introduction**

Growth in the manufacturing industry has encouraged a new design methodology across a variety of disciplines. Where product design was previously dictated by manufacturing constraints, design for high performance can now dominate. In the case of internal cooling schemes for gas turbine components, effective designs minimize the pressure loss while maximizing the heat transfer.

Additive manufacturing (AM), specifically Direct Metal Laser Sintering (DMLS), is an attractive manufacturing process for certain components in the hot section of gas turbines: the method can utilize aerospace-grade materials to create geometries unattainable by conventional manufacturing techniques. Such complex geometries can be conceived in myriad ways, but one quantitative way is through numerical optimization algorithms.

---

<sup>2</sup> Kirsch, K.L. and Thole, K.A., 2017, "Experimental Investigation of Numerically Optimized Microchannels Created through Additive Manufacturing", *Journal of Turbomachinery*, **140**(2), 021002 (11 pages)

Many different optimization techniques exist and can vary greatly in complexity, but all require an objective function to be minimized or maximized. For this study, a commercially available adjoint optimization solver was used and three different objective functions were posed. The initial geometries were derived from Kirsch and Thole [55], who designed and additively manufactured wavy microchannels of varying wavelengths; two of the wavelengths were chosen for this optimization study whereby the inlet and exit areas of the microchannels remained constant. The three objectives were to (1) minimize the pressure loss through the channels, (2) maximize the heat transfer on the channel walls and (3) maximize the ratio of heat transfer to pressure loss. To that end, a total of six test coupons were manufactured via DMLS for the two wavelengths.

This study aims to provide some insight into the ability to reproduce numerically optimized geometries and to assess the performance of those optimized geometries in the physical domain. First, a detailed analysis of the optimization results will be provided. Next, the as-manufactured channels will be evaluated and compared to the design intent, and to the baseline designs. Lastly, motivated by the insights gathered from the numerical results and the knowledge of the as-manufactured geometries, a discussion on the experimental pressure loss and heat transfer results will follow.

### **3.3 Literature Review**

The design of microchannel heat exchangers varies greatly depending on the end use. Wavy channel designs are primarily used for electronics cooling or other low flow rate applications due to the fluid mixing generated by the waves. Wavy channels can be constructed as sinusoidal waves [37,38], converging-diverging periodic sections [24,56,57], variable amplitude and/or wavelength sections [25,26] or as a series of circular arcs [8]. Each of these designs promote large vortical structures, which increase the heat transfer, yet the penalty in pressure loss is relatively low.

Most wavy channel studies have been performed at Reynolds numbers well into the laminar regime. For that reason, the study by Kirsch and Thole [55] was conceived to test the potential of wavy channels at flow rates more relevant to gas turbine engines. At Reynolds numbers below 5000, the heat transfer was more of a function of the wavelength than of the channels' high surface roughness, indicating the flow structures promoted by the wavy channels were the dominant heat transfer mechanism in that flow regime.

High surface roughness is a hallmark of most metal additive manufacturing processes [15,16]; where external surfaces can be post-processed and smoothed, internal surfaces remain rough. The roughness features that form are dependent on the machine process parameters, such



as laser power, hatch distance, layer thickness and laser scan speed [27,29,58–60]. Bacchewar et al. [60] isolated laser power as a strong contributor to surface roughness on downward facing surfaces, or down skins; decreasing the power on those surfaces yielded smoother features. In a similar vein, Wegner et al. [59] reported that increasing the laser energy density on up skins yielded a smoother face due to evening out the characteristic stair-stepping effect on inclined surfaces.

Characterizing the as-built DMLS part is essential, especially where tight tolerances are required. In the case of microchannels or other small ( $<3 \text{ mm}^3$ ) features, the natural shrinkage that occurs from the DMLS process can be up to 10% of the part's initial dimensions [28]. A common method for investigating AM parts is to use a Computed X-Ray Tomography (CT) scan because it is non-destructive in nature. Multiple studies have used this technique [15,16,55,61,62] with success; Stimpson et al. [63] confirmed via scanning electron microscopy (SEM) that the resolution of the scans was high enough to resolve large roughness features at the scale of the present study.

The AM process represents a powerful tool for building parts whose architecture is unrealizable by conventional manufacturing techniques. Designing for AM requires a completely different methodology, one in which optimization may play a pivotal role. Martinelli and Jameson [21] provided a detailed overview of the natural link between optimization and computational aerodynamics; shape optimization for airfoil design, for example, began in the 1970s.

Most optimization techniques can be grouped into either direct methods (zero order methods) or into gradient based methods (first order methods) [20]. Direct methods include approaches such as simulated annealing, differential evolution and genetic algorithms [64–67]. Verstaete et al. [65] combined a conjugate heat transfer analysis and a finite element analysis to perform a parameterized study on the shape of a high pressure turbine blade, including its internal cooling channels. This combination of analysis capabilities provided a robust means of finding the optimum result. However, direct methods can be computationally expensive, especially when the number of design parameters is large.

A sensitivity analysis, the category under which an adjoint optimization solver belongs, is an example of a first order method. Efficient calculation of the gradient of the objective function can reduce the computational effort required to find an optimum, when compared to the effort required from zero order methods [68]; the adjoint method was specifically derived for this efficient calculation and is widely used for a variety of shape optimization goals [68–70]. Wang et al. [71] researched the adjoint method as it applied to finned heat exchangers; fin parameters to be optimized included the width, pitch, height and length.

Topology optimization, as opposed to shape optimization, changes the distribution of material and not simply its shape [20]. Dede et al. [72] used topology optimization to additively

manufacture a heat sink for electronics cooling; the authors' optimized heat sink showed higher heat transfer performance than their baseline. Other topology optimization studies [73,74] have been numerical in nature, but show great promise for future production.

With the exception of the study performed by Dede et al. [72], the combination of numerical optimization schemes with additive manufacturing has not been widely reported in the literature. Our study aims to showcase the capabilities of AM as they relate to a powerful numerical optimization method.

### 3.4 Numerical Setup

The wavy channel design from which the current study derives was developed such that a constant radius of curvature in the channel prevailed; the sign of the radius of curvature switched every period [55]. A top-down image of the channel construction is shown in Figure 3-1. A rectangle was swept along the path created by the four circular arcs to form a channel and was kept normal to the channel inlet at all times. The channels were characterized by their wavelength,  $\lambda$ , relative to the length of the test coupon,  $L$ . Two wavelengths from the initial study in [55] were chosen to be optimized for the current study:  $\lambda=0.1L$  (Figure 3-2a) and  $\lambda=0.4L$  (Figure 3-2b). To note, Figure 3-2 shows only 40% of the coupon length. Ten periods of the  $\lambda=0.1L$  case and 2.5 periods of the  $\lambda=0.4L$  case fit in the length of the test coupon.

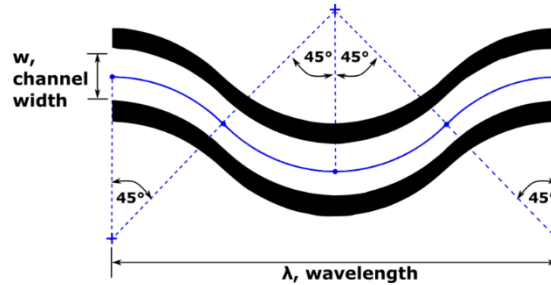
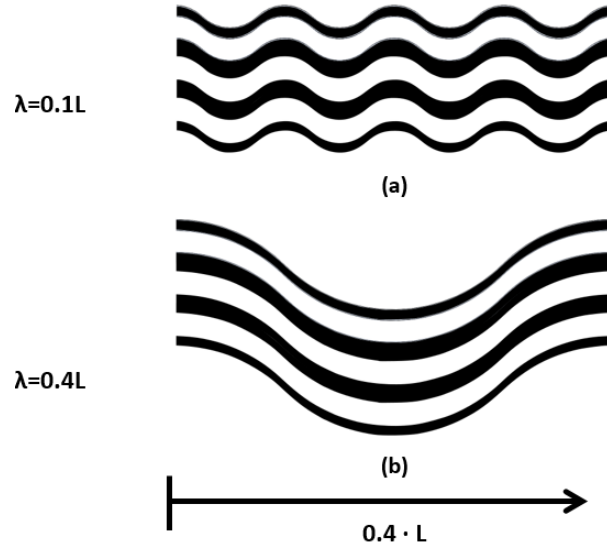


Figure 3-1. Four 45° arcs formed the path along which a rectangle was swept to create the channel. Flow goes left to right [55].

A commercial computational fluid dynamics (CFD) solver [47] was used to simulate the pressure loss and heat transfer through the two chosen wavy channel cases. The structured grids were composed in a multi-block pattern using a commercial grid generation program [48]; cell  $y^+$  values remained near or below one throughout the entire domain, as is appropriate for the sublayer resolved turbulence model used. Each model contained one channel and was made up of 1.1 million cells. The steady RANS and energy equations were solved using the realizable  $k-\epsilon$  turbulence model and the SIMPLE algorithm.

A velocity boundary condition was imposed at the inlet to the channel and a pressure boundary condition was imposed at the outlet. To mimic the experimental setup, a constant

pressure was held at the inlet to the channel and the channel top and bottom walls were heated via constant temperature boundary condition. Each simulation contained only one channel.



**Figure 3-2. The two baseline cases of wavy channels used in the optimization study. Forty percent of the coupon length is shown. Flow is from left to right [55].**

The adjoint optimization solver was run for three different objective functions, also known as observables and denoted here as  $J$ , for each of the two wavelength channels. Equations 3-1a – c show each of the observables. Equation 3-1c was chosen due to its proportionality to a commonly used performance factor, shown in Equation 3-2.

$$J_1 = \min(\Delta P) \quad \text{3-1a}$$

$$J_2 = \max(Q) \quad \text{3-1b}$$

$$J_3 = \max\left(\frac{Q}{\Delta P^{1/3}}\right) \quad \text{3-1c}$$

$$pf = \frac{Nu/Nu_0}{(f/f_0)^{1/3}} \quad \text{3-2}$$

The following section will describe the adjoint formulation and its connection to the flow solver, which was a key component to this study. The sensitivity analysis generated by the adjoint solver encouraged a geometric change that would have been difficult to achieve by a user-controlled parametric study. The inlet and exit cross sectional areas of the channels were held constant, but each one of the 1 million nodes outside the inlet and exit represented a degree of freedom. The resulting channel geometries were highly complex and aperiodic. To note, the sensitivities calculated by the adjoint solver were used to inform shape optimization, as opposed to topology optimization; the general trend of the wavy channel composition did not change.

### Adjoint Method

In a typical engineering optimization problem, the goal is to minimize (or maximize) some objective function by changing a set of design variables; constraints on the problem come in the form of both geometric bounds and fluid dynamic boundary conditions [20,75]. A common means of finding an optimum solution is to employ a gradient based method, which involves taking the derivative of the objective function with respect to the design variables. One such way to determine this gradient is to perform a sensitivity analysis.

Let  $J$  represent the objective function.  $J$  is a function of both the flow variables,  $\mathbf{q}$ , and the geometry,  $F$ , both of which are a function of the design variables,  $\mathbf{b}$ . The gradient of  $J$  with respect to the design variables is written in Equation 3-3 its expanded form using the chain rule.

$$\frac{\partial J}{\partial \mathbf{b}} = \frac{\partial J}{\partial \mathbf{q}} \cdot \frac{\partial \mathbf{q}}{\partial \mathbf{b}} + \frac{\partial J}{\partial F} \cdot \frac{\partial F}{\partial \mathbf{b}} \quad 3-3$$

The quantity  $\partial \mathbf{q} / \partial \mathbf{b}$  represents the sensitivity of the flow field to the design variables, which is not easily determined without running the flow solver for every perturbation in every design variable; the number of required simulations, therefore, becomes prohibitive in even moderately complex problems. The advantage of the adjoint method comes in its ability to eliminate this high computational cost. The mathematical approach to the adjoint method will be laid out here briefly.

Let  $\mathbf{R}$  denote the conservation laws governing the fluid behavior.  $\mathbf{R}$  are also a function of the flow variables,  $\mathbf{q}$ , and the geometry,  $F$ , and are identically equal to zero; the first derivative of  $\mathbf{R}$  takes a form similar to that in Equation 3-3 and is shown in simplified form in Equation 3-4.

$$\delta \mathbf{R} = \frac{\partial \mathbf{R}}{\partial \mathbf{q}} \cdot \delta \mathbf{q} + \frac{\partial \mathbf{R}}{\partial F} \cdot \delta F = 0 \quad 3-4$$

At this point, the adjoint variable, denoted as  $\Lambda$ , is introduced in the form of an arbitrary vector and is multiplied through Equation 3-4. Because the goal is to eliminate the quantity  $\partial \mathbf{q} / \partial \mathbf{b}$  from Equation 3-3, the value for  $\Lambda$  is chosen such that Equation 3-5 is satisfied.

$$\Lambda \cdot \frac{\partial \mathbf{R}}{\partial \mathbf{q}} = - \frac{\partial J}{\partial \mathbf{q}} \quad 3-5$$

The set of equations in 3-5 are known as the adjoint equations; these equations are solved to convergence in the adjoint solver to obtain values for  $\Lambda$ . Once  $\Lambda$  is known (and after some rearranging of the terms from Equations 3-3 and 3-4), the change in objective function with respect to the design variables can be written as

$$\delta J = \left[ \frac{\partial J}{\partial F} - \Lambda \cdot \frac{\partial \mathbf{R}}{\partial F} \right] \cdot \delta F \quad 3-6$$

In Equation 3-6 the sensitivity of the flow field to the design variables is removed and the change in  $J$  becomes a function of the geometric sensitivity, which is relatively straightforward to calculate, and the adjoint variable. The adjoint variable contains the sensitivity of the flow variables to changes in the geometry, which can be used to inform the design change necessary to achieve the objective function.

In this study, the flow solver and adjoint solver were contained in the same program [47]. While the discretization of the flow equations and the formation of the discretized adjoint equations were handled by the program, the steps taken by the user are outlined here:

- (1) Run the flow solver to convergence: obtain the flow variables,  $\mathbf{q}$ , by solving the conservation laws,  $\mathbf{R}$ .
- (2) Run the adjoint solver to convergence: obtain the sensitivity of the flow field to geometric variations by solving Equation 3-5, the adjoint equations.
- (3) Modify the geometry based on the sensitivity results to improve the objective function
- (4) Rerun the flow solver and compare the objective function to that from the previous flow solution.
- (5) Repeat until the flow variables show no more sensitivity to geometric changes.

For observable  $J_1$ , these five steps were repeated 14 times; for  $J_2$ , 5 times; and for  $J_3$ , 7 times. The adjoint and flow solvers were run for a Reynolds number of 5000 for both wavelength geometries. Typically, the adjoint solver converged near 15000 iterations, while the flow solver converged in 6000 iterations, where the threshold for convergence was set at  $1e-9$ .

For the  $\lambda=0.1L$  case, the observable  $J_1$  was also optimized at a Reynolds number of 15000. The difference between the optimized geometries at the two Reynolds numbers was small. The following discussion on the optimization results, and the subsequent discussion on the experimental results, assumes that the optimized shape changes roughly apply across a range of Reynolds numbers.

### *Optimized Geometries*

The final observables from the six optimization studies are shown in Table 3-1 and Table 3-2 for the  $\lambda=0.1L$  and  $\lambda=0.4L$  cases. The percentage difference values are relative to the respective baseline cases. Outlined boxes show the results of the quantity for which the adjoint solver was used to optimize; for comparison, the other two quantities are listed as well. In general, larger differences from the baseline cases were seen for the  $\lambda=0.1L$  case than for the  $\lambda=0.4L$  case.

**Table 3-1. Change in observables relative to the baseline for  $\lambda=0.1L$** 

	$\Delta P$	$Q$	$Q/\Delta P^{1/3}$
$J_1 = \min(\Delta P)$	-8.4%	-0.5%	+2.5%
$J_2 = \max(Q)$	+28.5%	+26%	+16%
$J_3 = \max(Q/\Delta P^{1/3})$	+1.7%	+23.8%	+17.5%

**Table 3-2. Change in observables relative to the baseline for  $\lambda=0.4L$** 

	$\Delta P$	$Q$	$Q/\Delta P^{1/3}$
$J_1 = \min(\Delta P)$	-5.5%	-3.5%	-1.6%
$J_2 = \max(Q)$	+7%	+5.3%	+3%
$J_3 = \max(Q/\Delta P^{1/3})$	+4.8%	+4.8%	+3.2%

Figure 3-3 shows samples of the geometric changes to the channels as a result of the sensitivity study for the  $\lambda=0.1L$  case. The outlines of the channels in Figure 3-3a are at 50% the channel height; a line plot showing the change in cross sectional area through the optimized channels is in Figure 3-3b; and the contours in Figure 3-3c-f are colored by nondimensional temperature, with velocity vectors overlaid. Nondimensional temperature,  $\theta$ , is defined such that  $\theta$  is equaled to one when the fluid and wall temperatures are equal, thereby making it a measure of heat transfer performance.

The most dramatic changes in wall shape came in the streamwise middle of the channel, with the inlet and exit of the channels showing only slight deviations from the baseline, which can be seen in Figure 3-3b. In general, the changes in cross sectional area between the  $J_1$  ( $\min(\Delta P)$ ) and  $J_2$  ( $\max(Q)$ ) observables mirrored each other: where the  $J_1$  case showed an increase in the cross sectional area,  $J_2$  showed a decrease, and vice versa. The  $J_3$  shapes struck a balance between  $J_1$  and  $J_2$ .

A different shape change occurred for each of the ten periods in the channel and occurred predominantly between peaks and troughs in the channels, where the radius of curvature defining the wave switched signs (Figure 3-3c and d). At the peaks and troughs, all the optimized channel shapes were nearly the same as the baseline shape (Figure 3-3e and f). See Section A.3 for more details. For the observables  $J_2$  and  $J_3$ , where heat transfer was to be maximized, higher angular velocity was seen throughout the channel as compared to the baseline. The walls tended to bow outward (Figure 3-3c), then bow inward immediately after rounding a peak or a trough in the channel (Figure 3-3d). This alternating pattern worked to draw flow from the center of the channel toward the upper and lower endwalls. The consequences of these shape changes can be seen at locations (e) and (f), where the secondary velocity vectors showed coherent flow patterns in the  $J_2$  and  $J_3$  cases that differed considerably from the flow patterns in the baseline case.

In looking at the nondimensional temperature contours in Figure 3-3c-f, the highest non dimensional temperatures were found where the vortices met the side walls. The fluid motion caused by the channel waviness created an impingement-like effect for every turn in the channel; this effect was exacerbated in the  $J_2$  and  $J_3$  cases, where the walls' protrusions into the channel provided a larger impingement surface. Figure 3-3d shows this event most clearly. Near the end of the channel (Figure 3-3e, f), the heat transfer performance at the channel midspan was notably higher for the  $J_2$  and  $J_3$  cases than for the baseline and  $J_1$  cases.

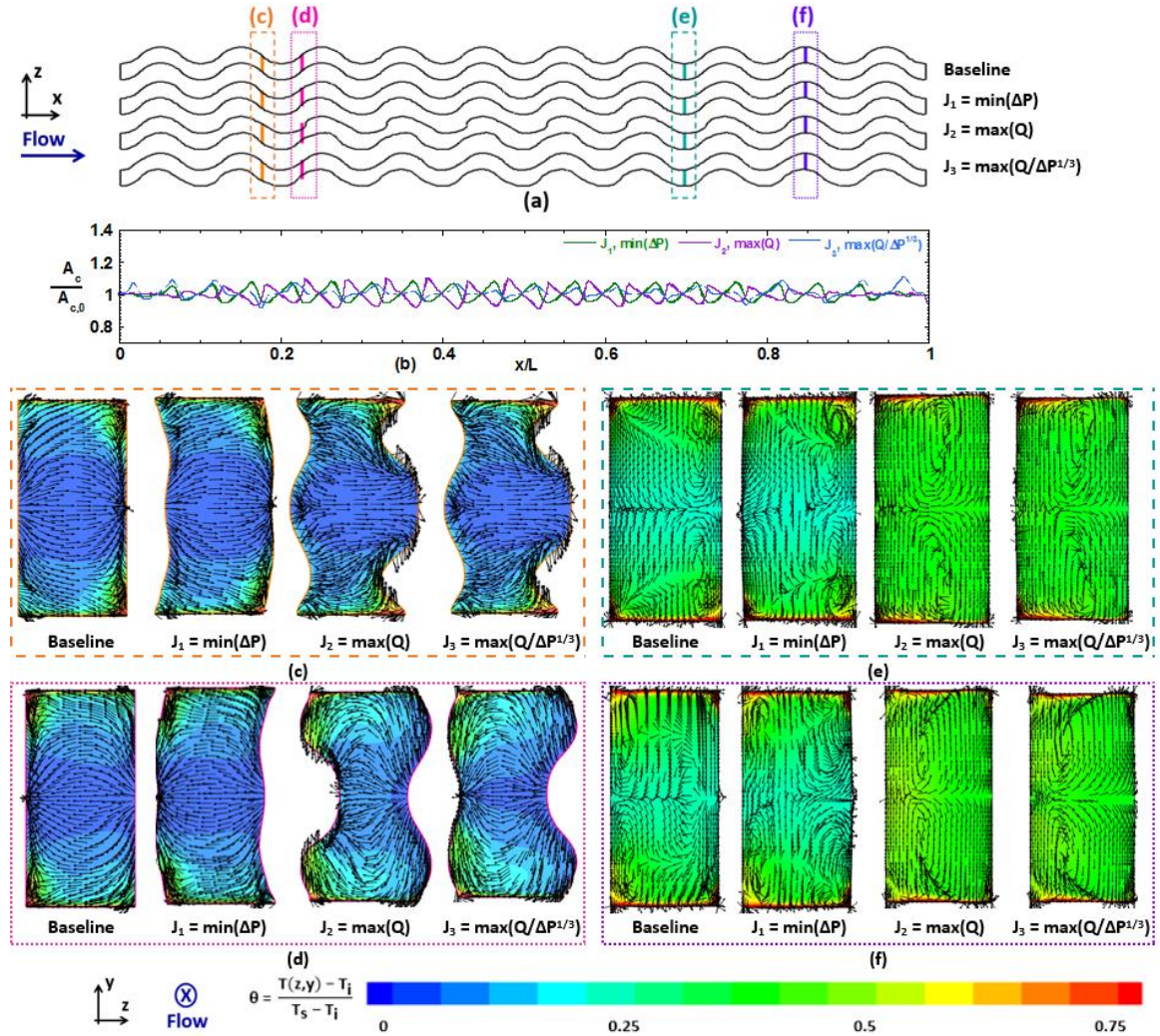


Figure 3-3. Optimization results for the  $\lambda=0.1L$  case. (a) Top down view of channel outlines at 50% channel height. (b) Change in cross sectional area through each optimized channel, normalized by the baseline cross sectional area. (c) and (d) In-plane velocity vectors superimposed on nondimensional contours near the beginning of the channels. (e) and (f) Secondary velocity vectors superimposed on nondimensional temperature contours near the end of the channels.

The solution to minimizing pressure loss, observable  $J_1$ , came in minimizing the amount of backflow in the channel. As the flow navigated the channel waves, the direction of centripetal

force exerted on the fluid particles switched signs every period. As the force direction changed, the direction of the vortices in the channel switched as well, which caused a small amount of flow to move backward. This behavior is evident in Figure 3-3d in looking at the in-plane velocity vectors for the baseline study; note these velocity vectors are not representative of the true secondary flow pattern and are, instead, based upon the Cartesian velocity components. The cluster of vectors seen in the slice of the baseline study was not present for the  $J_1$  case; the movement of the walls for  $J_1$  eased the transition for the vortical structures through each subsequent period. However, the difference in secondary velocity vector patterns for the  $J_1$  and baseline channels at locations (e) and (f) was small, indicating that the optimizer was more closely focused on the locations between channel peaks and troughs. Note that these velocity vector patterns do show the secondary flow patterns, given that the slice locations were taken normal to the local flow direction. The wall shape changes were not as significant for the  $J_1$  case and indeed, the degree to which  $J_1$  was satisfied was less than  $J_2$  and  $J_3$  (Table 3-1).

Figure 3-4 shows the optimization results for the  $\lambda=0.4L$  case in a manner similar to Figure 3-3; Figure 3-4a shows a top-down view of the channel outlines, taken at 50% the channel height, Figure 3-4 shows the change in cross sectional area through the optimized channels, normalized by the baseline cross sectional area, and the contours in Figure 3-4c-f show nondimensional temperature with velocity vectors overlaid; much like in Figure 3-3, the vector patterns shown at locations c and d are in-plane velocity vectors, while those shown at locations e and f are indicative of the secondary flows to the local normal. Much like the shorter wavelength channels, the most significant shape changes came between the peaks and troughs in the channels (Figure 3-4c and d); the shape of all three optimized channels matched the baseline channel at each peak and trough (Figure 3-4e and f).

For the same observable at any streamwise location, the general shape transformations between the  $\lambda=0.1L$  case and  $\lambda=0.4L$  case were markedly different, as were the changes in cross sectional area through the optimized channels relative to the baseline channels. Unlike for the  $\lambda=0.1L$  baseline case, the  $\lambda=0.4L$  baseline channel structure allowed for the formation of Dean vortices, which are characteristic in flows through curved channels [50]. The shape changes induced by the optimizer, therefore, revolved around either enhancing those vortical structures (in the  $J_2$  and  $J_3$  observables) or diminishing them (in the  $J_1$  observable).

Comparing the contours in Figure 3-4c and Figure 3-4d shows that the shape changes for each of the observables were similar, but occurred in different streamwise locations depending on the main objective. For example, the  $J_1$  slice at location (b) exhibited a similar shape as the  $J_2$  and  $J_3$  slices at location (c). Where heat transfer was to be maximized, in observables  $J_2$  and  $J_3$ , the



leeward wall bowed outward, in the direction of the fluid motion (Figure 3-4c); following the peak in the channel, that same wall curved inward, again in the direction of the fluid motion (Figure 3-4d). This wall movement facilitated the formation of vortices, the result of which can be seen at locations (e) and (f) for the  $J_2$  and  $J_3$  cases. When compared to the baseline flow structure at those locations, the vortex patterns for  $J_2$  and  $J_3$  showed fuller vortical structures that were more centered in the spanwise ( $z$ ) dimension. The temperature contours in Figure 3-4 confirmed that the shape changes related to maximizing heat transfer achieved the objective: from location (d) until the end of the channel, the  $J_2$  and  $J_3$  cases showed higher heat transfer performance than the  $J_1$  and baseline cases. However, instead of providing an impingement surface to maximize the heat transfer, like in the  $\lambda=0.1L$  geometry, the wall movements simply relocated and strengthened the vortical structures that were already present in the baseline case.

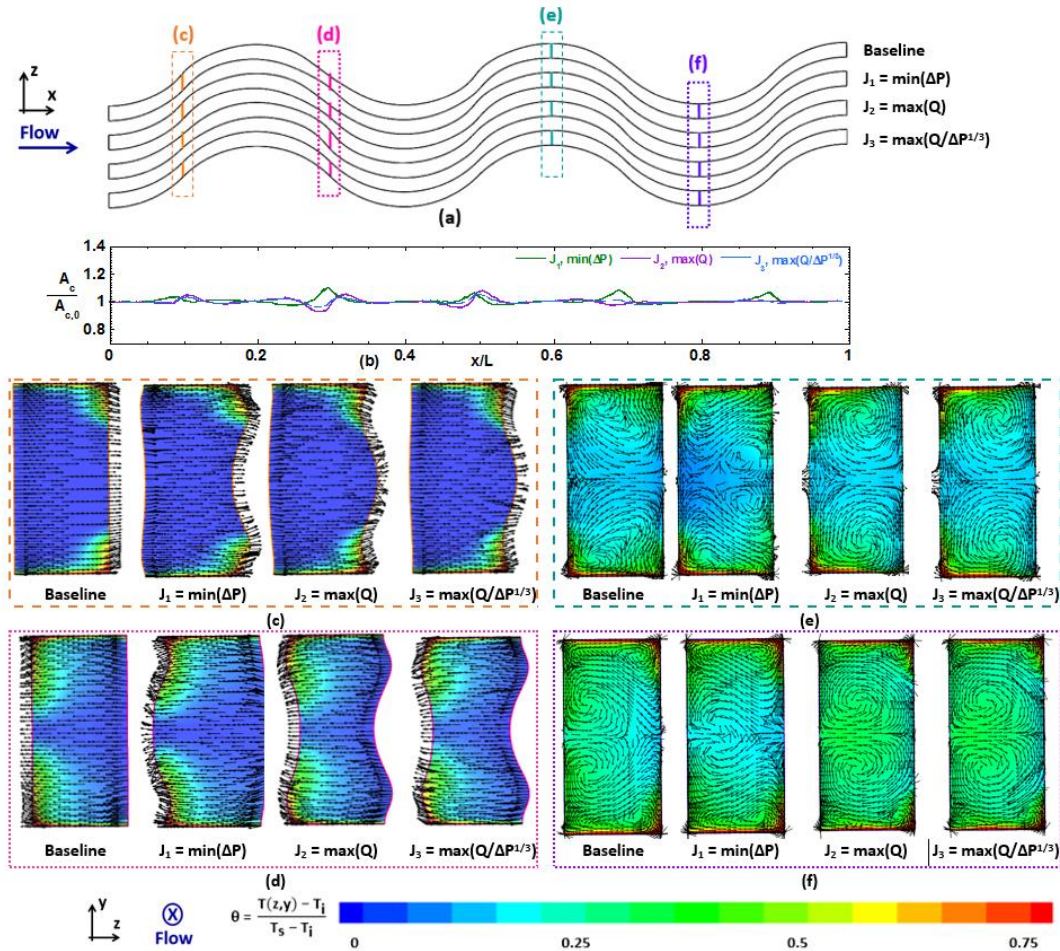


Figure 3-4. Optimization results for the  $\lambda=0.4L$  case. (a) Top down view of channel outlines at 50% channel height. (b) Change in cross sectional area through each optimized, normalized by the baseline cross sectional area. (c) and (d) Secondary velocity vectors superimposed on nondimensional temperature contours near the beginning of the channels. (e) and (f) Secondary velocity vectors superimposed on nondimensional temperature contours near the end of the channels.

An analysis of the results for the  $J_1$  observable shows that the leeward wall bowed inward at location (b) in Figure 3-4, then outward at location (c), which was the exact opposite behavior seen for the  $J_2$  and  $J_3$  cases. Increasing the cross sectional area of the channel after the fluid rounded the peak lowered the flow momentum and discouraged the formation of vortices. In Figure 3-4e and f, the size of the vortices in the  $J_1$  channel was much smaller than in the baseline, suggesting that diminishing the vortical structures was the key to achieving the pressure loss objective. The temperature contours show the lowest heat transfer effectiveness for the  $J_1$  case, consistent with the results seen in Table 3-2.

### 3.5 Geometric Characterization

The optimized channels from the numerical study were duplicated to fill a test coupon; 20 channels for the  $\lambda=0.1L$  case and 18 channels for the  $\lambda=0.4L$  case fit in the spanwise dimension of the test coupons. All coupons, including both baseline studies, were built layerwise at a  $45^\circ$  angle using DMLS; the machine parameters were set to those recommended for the chosen material [45], which was stock Inconel 718 powder. The baseline coupons were included on the same build plate in order that the performance of the optimized geometries could be directly compared to the baseline; any effects from variabilities in the DMLS process were therefore negated.

Figure 3-5 shows the build orientation of the test coupons, along with relevant dimensions. The test coupons were 25.4 x 25.4 x 1.5 mm in size; the aspect ratio of the rectangular channels was two, with the channels spaced in the spanwise direction at  $S/D_h=2.0$ . Channel hydraulic diameter was nominally 0.68 mm and the aspect ratio of the channels was two. Support structures were fixated on the coupon flanges, as well as on the bottom-most coupon wall and served not only to provide physical support for the build layers, but also to conduct heat away from the part toward the build plate during the build.

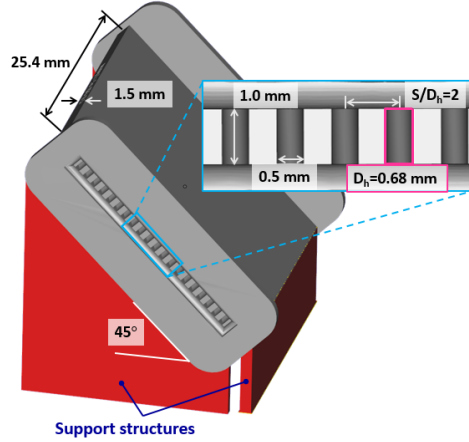


**Figure 3-5. Build orientation and dimensions of test coupons.**

To determine how well the optimized features were produced, the internal surfaces of each coupon were evaluated using a CT scanner. The resolution, or voxel size, of the CT scan image was  $35\text{ }\mu\text{m}$ , although the software used to analyze the CT scan data allowed for the determination of a part's surface to be resolved within  $3.5\text{ }\mu\text{m}$ . The internal and external surfaces of each coupon were determined using algorithms within the software, which compared local grayscale values in each voxel to distinguish between material and background. Once the surfaces were identified, 2D slices from the CT scan were analyzed to determine the cross sectional area, perimeter and surface area of each channel.

Figure 3-6 shows select results from the DMLS channels for  $\lambda=0.1L$ ; Figure 3-6a shows the change in cross sectional area of the DMLS optimized channels, normalized by the DMLS baseline channel cross sectional area, for half of the coupon length ( $0.1 < x/L < 0.6$ ). Figure 3-6b shows a 2D slice of all DMLS channels atop one another at the same streamwise location as in Figure 3-3d.

A comparison between Figure 3-6b and Figure 3-3d shows that the wall shapes for all cases stayed relatively true to the optimized design: the flow constriction called for by the optimizer in the  $J_2$  and  $J_3$  cases was achieved, as was the slight curve in both channel side walls for the  $J_1$  case. Additionally, in looking at Figure 3-6a, the trend in cross-sectional area at  $x/L \approx 0.23$  for the three optimized cases resembled the design intent (Figure 3-3b). The cross sectional area measured for the  $J_2$  case was much smaller than the  $J_1$  and  $J_3$  cases, whose measured cross sectional areas were nearly equal. However, the ordinate extrema of the line plots in Figure 3-6a are far greater than in Figure 3-3b, which indicates that the DMLS process was unable to reproduce the nuanced differences between the CAD baseline and optimized channels.

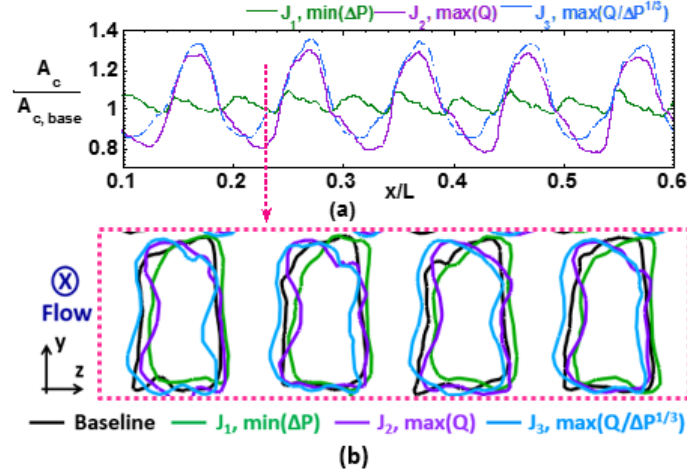


Figure 3-6. CT scan results from the  $\lambda=0.1L$  optimized DMLS channels. (a) Change in cross sectional area of the optimized DMLS channels, normalized by the baseline DMLS channel. Only 50% of the coupon length is shown. (b) Channel wall outlines of each of the DMLS channels, at the same location as in Figure 3-3d.

Figure 3-7 shows select results from the CT scans of the  $\lambda=0.4L$  DMLS channels. Figure 3-7a shows the change in cross sectional area through the DMLS optimized coupons, normalized by the DMLS baseline channels (for  $0.1 < x/L < 0.6$ ), and Figure 3-7b shows a 2D slice of all DMLS channels at the same location as in Figure 3-4d. Unlike for Figure 3-6a, both the magnitude and the general trend in cross sectional area of the optimized channels relative to the baseline were similar to the plot from Figure 3-4b. At  $x/L \approx 0.3$ , the cross sectional area of the  $J_1$  case was the largest of the three cases, followed by the  $J_3$  case, then by the  $J_2$  case. The channel outlines in Figure 3-7b support this trend and largely match those seen in Figure 3-4d; the large negative feature of the  $J_1$  optimized result built well, as did the large positive features called for by  $J_2$  and  $J_3$  optimized results.

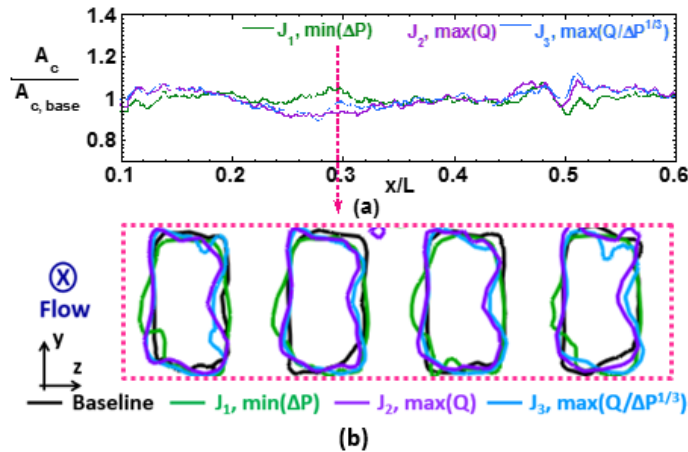


Figure 3-7. CT scan results from the  $\lambda=0.4L$  optimized DMLS channels. (a) Change in cross sectional area of the optimized DMLS channels, normalized by the baseline DMLS channel. Only 50% of the coupon length is shown. (b) Channel wall outlines of each of the DMLS channels, at the same location as in Figure 3-4d.

Table 3-3 shows relevant measured dimensions of the eight channels from this study, compared with the dimensions from the design intent. The measured hydraulic diameters and inlet cross sectional areas built slightly smaller than the intended CAD, but the surface area of the channels nearly matched the intent.

Roughness levels in each coupon, denoted as  $R_a$ , are also included in Table 3-3 and were quantified by measuring the distance between each point on the CT scanned model and surfaces fit to the model. In general, the  $\lambda=0.1L$  cases exhibited larger roughness features than the  $\lambda=0.4L$  cases. However, the difference among the optimized channels for the same wavelength was minimal; the optimized features did not affect the levels of roughness in the channels relative to the baseline.

As expected, neither the baseline nor the optimized DMLS matched their corresponding CAD models perfectly. Overall, however, optimized features as small as 50  $\mu\text{m}$  (10% of the channel width) built successfully, which is on the order of the build layer thickness. Additionally, both positive and negative features were built with equal success on both upward and downward facing surfaces. The failure of optimized features to build was related to their location on the channel walls. Given that the DMLS process could not produce sharp corners, as evidenced by the 2D slices in Figure 3-6b and Figure 3-7b, any optimized features near the corners were not able to be resolved.

**Table 3-3. Measured dimensions of as-built channels**

	Inlet Hydraulic Diameter [mm]		Inlet Cross Sectional Area [mm <sup>2</sup> ]		Surface Area [mm <sup>2</sup> ]		$R_a/D_h$
	Design	Actual	Design	Actual	Design	Actual	
Baseline	0.68	0.62	0.52	0.43	2.7	2.5	0.023
$J_1, \min(\Delta P)$		0.62		0.43	2.6	2.6	0.026
$J_2, \max(Q)$		0.61		0.44	2.6	2.5	0.022
$J_3, \max(Q/\Delta P^{1/3})$		0.62		0.44	2.6	2.65	0.018
Baseline		0.64		0.43	2.4	2.4	0.016
$J_1, \min(\Delta P)$		0.65		0.44	2.35	2.5	0.011
$J_2, \max(Q)$		0.65		0.44	2.35	2.4	0.016
$J_3, \max(Q/\Delta P^{1/3})$		0.65		0.44	2.35	2.49	0.013

### 3.6 Experimental Setup

A bench-top rig, a cross section of which is shown in Figure 3-8, was used to measure the pressure loss and heat transfer performance of the eight DMLS coupons. Flow was governed by a commercial mass flow controller [76] and air was used as the working fluid. A constant pressure

was held at the inlet to the test section; to achieve target Reynolds numbers between 300 and 15000, the pressure downstream of the test section was adjusted.

Static pressure taps were located in the upstream and downstream Nylon pieces of the test facility to measure the pressure drop through the channels. A loss coefficient of zero was assumed at the coupon inlet, while a loss coefficient of one was assumed at the outlet to account for the test section expansion. In the friction factor calculation, the fluid density was obtained via the ideal gas law and the channel velocity,  $U$ , was calculated from the known mass flow rate through the system. The channel length was measured as the length that the fluid navigated.

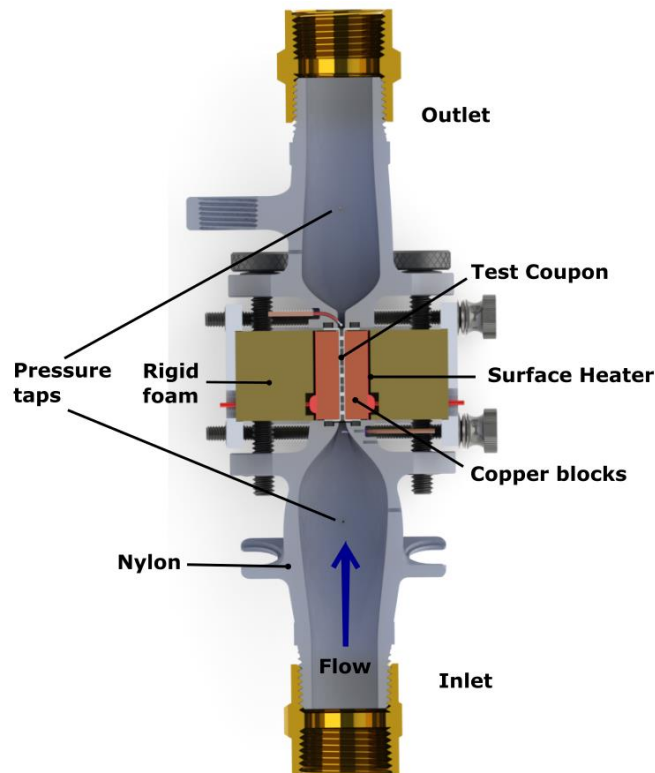


**Figure 3-8. Test facility used for pressure loss and heat transfer measurements for the optimized wavy channel test coupons.**

For heat transfer tests, a heated copper block provided a constant temperature boundary condition on the test coupon walls. Heat into the system was set by power supplies connected to electrical resistance surface heaters, which were adhered to the copper blocks. The coupon surface temperature was calculated using a 1D conduction analysis, a full description of which can be found in [16]; for each test, the power supply voltages were set such that the temperature on both top and bottom walls of the test coupon were equal. Using the coupon surface temperature, as well as thermocouple measurements at the inlet and outlet of the test section, a log mean temperature difference could be calculated and the convective heat transfer coefficient was then obtained using Equation 3-7.

$$h = \frac{Q - \sum Q_{\text{loss}}}{A_s \cdot \Delta T_{\text{lm}}} \quad 3-7$$

The term  $\sum Q_{\text{loss}}$  from Equation 3-7 represented the combined conduction losses through the test facility. Conduction losses were quantified by placing thermocouples in the copper blocks, the rigid foam, and the Nylon test pieces; at low Reynolds numbers, conduction losses neared 15% of the total heat into the system but decreased to 2% for Reynolds numbers over 8000. For each test, an energy balance was performed and matched to within 15% of the measured net heat input to the test rig; for Reynolds numbers above 4000, the energy balance was within 11% of the calculated heat input.

This test facility has been used by numerous studies from our laboratory [15,16,55] and has been validated by testing a conventionally manufactured coupon containing cylindrical channels that were reamed smooth. For both pressure loss and heat transfer tests, the benchmarking coupon matched the applicable friction factor and Nusselt number correlations for smooth channels to within 8% at all Reynolds numbers of interest in the current study.

#### *Uncertainty Analysis*

To quantify experimental uncertainty, the methods proposed by Kline and McClintock [46] were applied to all measured and calculated quantities. The largest source of overall uncertainty for friction factor tests came in the size of the pressure transducer used to measure the pressure drop across the coupon. At low Reynolds numbers (<500) for the  $\lambda=0.4L$  cases, which represented the worst case scenario for the entire test matrix, friction factor uncertainty neared 17%. However, for all flow tests above a Reynolds number of 4000, overall friction factor uncertainty was below 7%. The precision uncertainty, calculated using a 95% confidence level, ranged between 1.5% and 2% across the entire extent of Reynolds numbers.

Uncertainty in Nusselt number was driven by the calculation of the coupons' surface temperatures. Uncertainty in the thickness of the thermal paste was a contributing factor, as was the uncertainty in the thickness of the coupon top and bottom walls. Both the uncertainty in surface temperature and Nusselt number were below 6% for all coupons. Precision uncertainty for Nusselt number was 3% across all Reynolds numbers.

### **3.7 Results and Discussion**

Results will be presented first in the form of a pressure loss analysis, followed by a discussion on the heat transfer performance of the optimized channels relative to their respective baselines. Due to the large number of DMLS process parameters, and the high sensitivity of microchannels to small variations in those process parameters, the data to be presented in this paper

come only from coupons manufactured on the same build plate. While the design of the baseline wavy channels originated in Kirsch et al. [55], data from that initial study will not be presented here.

Additionally, the channel dimensions used in the upcoming discussions will be those at the inlet to each coupon, as calculated from the CT scan data. The optimizer worked to achieve each objective relative to the bulk channel properties because the inlet and exit areas were kept constant during the simulations. Therefore, to most accurately understand how well the optimized DMLS channels achieved their intended goals, the aperiodic changes in cross sectional area that occurred beyond the channel inlet will not be taken into account in the geometric scaling parameters.

To validate the results from the test facility, an aluminum test coupon containing cylindrical channels was machined; the channels were reamed smooth to achieve nearly zero relative roughness. Data from the smooth channels will be presented in the upcoming results, along with smooth channel correlations: laminar theory ( $64/Re$ ) and the Colebrook formula for the friction factor tests, and the Gnielinski correlation for the heat transfer tests.

#### *Pressure Loss Performance*

Figure 3-9 shows friction factor for each of the DMLS optimized channels, along with the DMLS baseline coupons and smooth benchmarking coupon, versus Reynolds number. Consistent with results from Kirsch et al. [55], all  $\lambda=0.1L$  cases showed a higher friction factor than the  $\lambda=0.4L$  cases due to the channel construction; the shorter wavelength and smaller radii of curvature created a stronger propensity for flow separation and yielded a higher pressure loss over the longer wavelength channels, even when pressure loss was to be minimized.

For a given wavelength, the trends among the optimized channels relative to their baseline differed considerably. The stark increase in friction factor from the  $\lambda=0.1L$   $J_2$  case was prominent in Figure 3-9, averaging a 50% increase over the baseline. Both the  $J_1$  and  $J_3$  observables, however, showed nearly equal friction factor to the baseline study. These results indicate that while the  $J_1$  objective was not achieved, the  $J_3$  objective showed promise. Requesting that the numerical optimizer account for both pressure loss and heat transfer translated well to the physical domain. By contrast, the  $J_1$  objective was wholly unfulfilled for the  $\lambda=0.4L$  case, with the  $J_1$  coupon yielding a measurably higher friction factor than its baseline coupon. Both the  $J_2$  and  $J_3$  cases also showed increased friction factors over their baseline coupon, as was predicted by the optimizer.



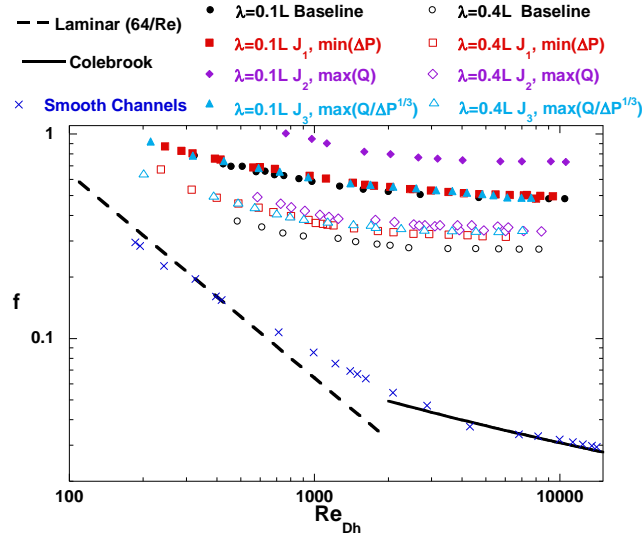


Figure 3-9. Friction factor vs. Reynolds number for all optimized coupons, plus the baseline coupons.

To highlight the performance of each of the optimized channels relative to their baseline designs, Figure 3-10 shows the friction factor augmentation from the optimized channels over their baselines. An augmentation of one is specified in Figure 3-10 with a dotted line. The failure to achieve the  $J_1$  objectives is explicitly discernable in the augmentation plots. Additionally, the performance of the  $J_3$  objective relative to the  $J_2$  objective is clear: when the optimizer sought to increase the ratio of heat transfer to pressure drop, the resulting friction factor was measurably lower than when only heat transfer was to be maximized.

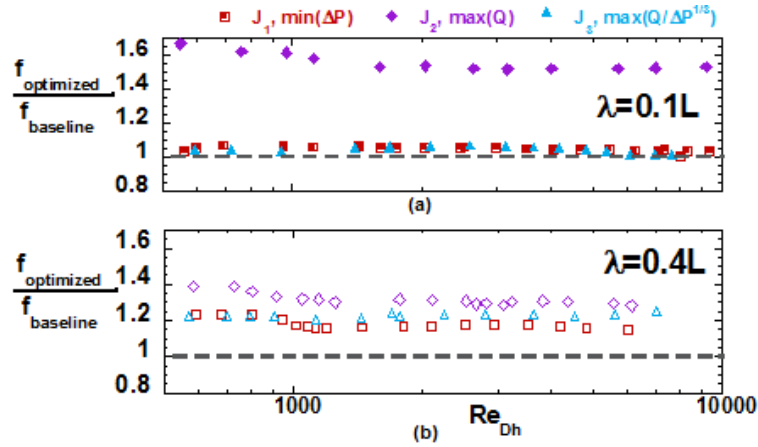


Figure 3-10. Friction factor augmentation from the optimized channels relative to their baseline cases. (a)  $\lambda=0.1L$  cases, (b)  $\lambda=0.4L$  cases.

As previously discussed, each of the optimized geometries built relatively true to their optimized design. While not all optimized wall features were reproduced perfectly, distinctly different geometries emerged from the DMLS build process that largely resembled their numerically-generated counterparts. The fact that neither wavelength's  $J_1$  objective was achieved implies that the large roughness features inside the channel were the more dominant effect on flow

structure, instead of the wall shape. Channel wall movements that worked to reduce the backflow in the channel ( $\lambda=0.1L$  case) or to diminish vortical structures ( $\lambda=0.4L$  case) failed to work as the optimizer had predicted due to the large, irregular roughness features in the channel.

However, where the vortical structures were to be strengthened without regard to flow losses, in the  $J_2$  cases, the resultant friction factors were measurably higher than the other two objectives. Especially for the shorter wavelength, the dramatic changes in wall shape for the  $J_2$  objective undoubtedly complicated the flowfield relative to the channels from the baseline and the  $J_1$  objective, which negatively impacted the friction factor.

### Heat Transfer Performance

Heat transfer results are shown in Figure 3-11 for all DMLS coupons, along with the results from the smooth benchmarking coupon. The spread in Nusselt number across the optimized channels was much less than the spread in friction factor seen from Figure 3-9. In fact, the heat transfer performance of all  $\lambda=0.4L$  cases were within 9% of each other, with the  $J_2$  case marginally outperforming the others.

The  $J_2$  case for the  $\lambda=0.1L$  wavelength, however, showed heat transfer performance around 20% higher than the baseline channels. These results implied that the shape changes induced by the optimizer achieved their goals; creating stronger vortical structures would positively influence the heat transfer while negatively affecting the pressure loss, which is what the results support.

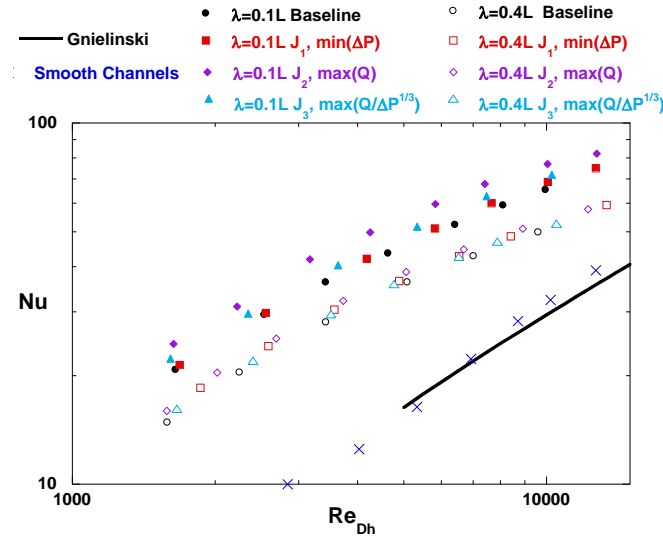
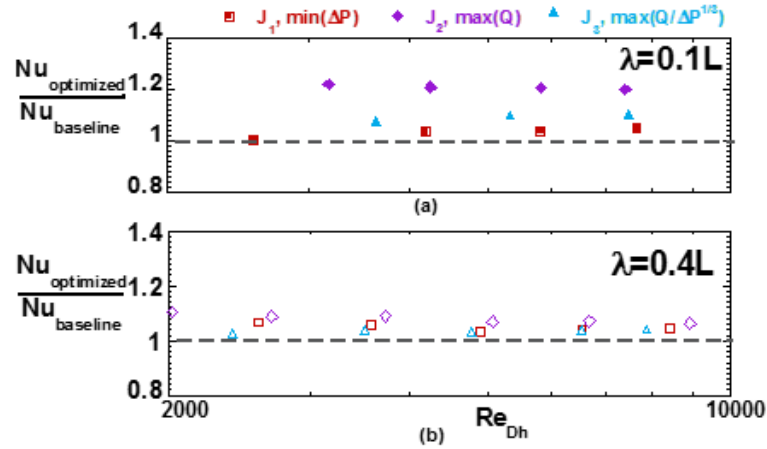


Figure 3-11. Nusselt number vs. Reynolds number for all optimized coupons, plus the baseline coupons.

Figure 3-12 more clearly shows the difference between the optimized channels and the baseline channels; Figure 3-12a shows heat transfer augmentation from the optimized over the baseline channels for the  $\lambda=0.1L$  cases, while Figure 3-12b shows the same augmentation for the

$\lambda=0.4L$  cases. Much like the friction factor results, the  $J_3$  objectives performed more similar to the  $J_1$  cases than to the  $J_2$  cases. This observation further supports the claim that the DMLS build process was able to reproduce the geometric differences between the  $J_2$  and  $J_3$  cases aimed at mitigating the strength of the vortical structures.



**Figure 3-12. Nusselt number augmentation from the optimized channels relative to their baseline cases. (a)  $\lambda=0.1L$  cases, (b)  $\lambda=0.4L$  cases.**

#### *Augmentation Results*

To fully interpret the impact of the numerical optimizer on the experimental results, the following discussion will focus on the combined friction factor and heat transfer augmentation. Figure 3-13 shows heat transfer augmentation against friction factor augmentation to the one third power, representative of the performance factor mimicked by the objective  $J_3, \max(Q/\Delta P^{1/3})$ . As anticipated from the isolated friction factor and heat transfer results in the previous sections, the high friction factor seen by the  $J_2$  objectives was not offset by a high heat transfer augmentation; the  $J_2$  cases, therefore, showed poor overall performance in Figure 3-13. Additionally, the  $J_1$  and  $J_3$  cases for the  $\lambda=0.4L$  wavelength show a higher penalty in friction factor augmentation than benefit to heat transfer when compared with the  $\lambda=0.4L$  baseline.

Successful representations of the intended optimized goals were seen for the  $\lambda=0.1L$   $J_1$  and  $J_3$  objectives. Both observables yielded a higher heat transfer augmentation for the same friction factor augmentation as their baseline channel. Specifically for the  $J_3$  observable, the heat transfer augmentation was consistently 15% higher than the baseline study.

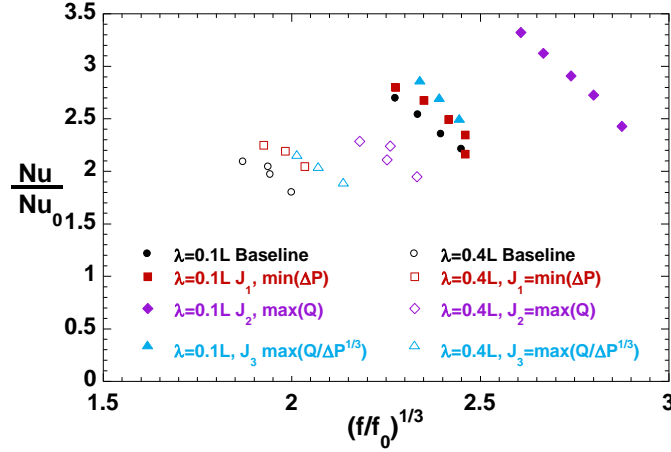


Figure 3-13. Heat transfer augmentation vs. friction factor augmentation to the one third power.

### 3.8 Conclusions

A numerical optimization study was performed on two different configurations of wavy microchannels characterized by their wavelengths:  $\lambda=0.1L$  and  $\lambda=0.4L$ . Three objective functions were posed for each channel that reflected common goals across internal cooling schemes: (1) minimize the pressure loss, (2) maximize the heat transfer and (3) maximize the ratio of heat transfer to pressure loss. Computational results showed that each of the objective functions was successfully realized.

The channel shapes that resulted from the optimizer differed considerably depending on the objective function and on the wavelength of the channel. Where pressure loss was to be minimized for the  $\lambda=0.1L$  case, the channel walls sought to decrease the flow separation that occurred in the baseline design. For the  $\lambda=0.4L$  case, the optimizer worked to mitigate the strength of the vortices that formed in the baseline. To maximize the heat transfer for both wavelengths, the optimizer generated channel wall shapes that encouraged the formation of and strengthened the vortical structures.

Each of the numerically optimized channels, along with their baseline channels, were built using DMLS. The channels were evaluated non-destructively to understand how well the optimized channel shapes were able to be reproduced. In general, the success or failure of an optimized feature to be built lied with its location in the channel. Near the sharp corners, which are difficult to resolve at the scale of these channels, optimized features did not build. However, any features greater than the build layer thickness near midheight of the channel were reproduced successfully, regardless of whether the surface were upward- or downward-facing.

Experimental results showed that the objective to minimize pressure loss was not achieved for either wavelength. The large roughness features that are characteristic of the DMLS process

dominated the flow structure more than the shapes of the walls. On the other hand, where heat transfer was to be maximized without regard for channel losses, the wall shapes successfully enhanced the strength of the vortical structures in the channel and strongly influenced the flowfield in the channels. Both wavelength channels saw an increase in both the friction factor and the heat transfer in the channels whose shape was aimed at maximizing heat transfer. However, the penalty in pressure loss was far higher than the benefit in heat transfer.

The best overall performance was seen by the objective to maximize the ratio of heat transfer to pressure loss. While the objective to minimize pressure loss itself was not accomplished, forcing the optimizer to account for pressure loss while maximizing the heat transfer had strong implications for the experimental results. For the same friction factor augmentation as the  $\lambda=0.1L$  baseline channel, the  $\lambda=0.1L$  channels optimized for heat transfer and pressure loss exhibited a 15% increase in heat transfer augmentation.

Much work still needs to be done to understand the role that shape optimization has in additively manufactured microchannels. While these experiments represent an extremely small segment of possible internal cooling schemes, lessons learned from these results can be applied more broadly. Surface roughness strongly affects the pressure loss and heat transfer performance of DMLS microchannels, but the wall shape also exerts an unmistakable influence. Both heat transfer and pressure loss should be taken into account for any internal cooling optimization scheme. As progress continues in both the manufacturing industry and in numerical optimization methods, further research can continue to delve into the natural link between numerical optimization and additive manufacturing.

## **4 PRESSURE LOSS AND HEAT TRANSFER PERFORMANCE FOR ADDITIVELY AND CONVENTIONALLY MANUFACTURED PIN FIN ARRAYS<sup>3</sup>**

### **4.1 Abstract**

Pin fin heat exchangers represent a common, viable means of keeping components cool and are widely used for electronics cooling and turbine airfoil cooling. Advancements in manufacturing technology will allow these heat exchangers to be built using new methods, such as laser powder bed fusion, a form of additive manufacturing. New manufacturing approaches, however, render a direct comparison between newly and conventionally manufactured parts meaningless without a good understanding of the difference in the performance.

This research study investigated microchannel pin fin arrays that were manufactured using Laser Powder Bed Fusion and compared them to studies of pin fin arrays from the literature, which are representative of traditionally-manufactured pin fin arrays, where the pin and endwall surfaces exhibited much lower surface roughness. Pin fin arrays with four different spacings were manufactured and tested over a range of Reynolds numbers; pressure loss and heat transfer measurements were taken. Additionally, the test coupons were evaluated non-destructively and the as-built geometric features were analyzed.

Measured surface roughness was found to be extremely high in each one of the microchannel pin fin arrays and was found to be a function of the pin spacing in the array, as was the shape of the pin itself; with more pins in the array came higher surface roughness and more distorted pin shapes. Comparisons between the smooth pin fin arrays from literature and the rough pin fin arrays from the current study showed that the high surface roughness more strongly affected the friction factor augmentation than it did the heat transfer augmentation relative to the smooth pin fin arrays.

### **4.2 Introduction**

Additive manufacturing (AM), more generically known as 3-D printing, has emerged as a viable manufacturing technique for heat exchangers in a variety of applications. While the nature of AM relaxes many design restrictions imposed by conventional manufacturing techniques, the specific application of the heat exchanger may heavily dictate its final form.

---

<sup>3</sup> Kirsch, K.L. and Thole, K.A., 2017, "Pressure Loss and Heat Transfer Performance for Additively and Conventionally Manufactured Pin Fin Arrays", *International Journal of Heat and Mass Transfer*, **108**(2017), pp. 2502-2513

In thin cross-sectional areas, for example, the cooling method must provide structural support in addition to removing the heat, which is the case in the trailing edge of turbine airfoils. Pin fin arrays are the conventional solution for such scenarios because of the additional convective surface area and because of the increased turbulent mixing in the flow. Pin fin arrays are a widespread and effective cooling technology, most commonly employed to cool electronic and gas turbine components. Even as manufacturing processes evolve and increasingly complex heat exchanger designs become physically realizable, pin fins will remain relevant to the durability of components where high thermal and mechanical stresses are present and where high heat transfer is required.

Certain types of AM are especially applicable to harsh thermal environments. Laser Powder Bed Fusion (L-PBF) methods employ aerospace-grade materials and yield final parts that can endure in gas turbine engines. This paper examines the performance of pin fin arrays produced using L-PBF, where pin and endwall surfaces were extremely rough, and compares them to pin fin arrays produced using conventional methods, where both pin and endwall surfaces are much smoother, hereon simply referred to as smooth.

Four pin fin arrays with different spacings were manufactured additively and will be discussed in the context of geometric reproducibility, surface roughness and trends in pressure loss and heat transfer performance when compared to smooth walled pin fin arrays placed in a microchannel.

### **4.3 Literature Review**

Pin fin arrays have been studied extensively and reports on their performance abound in the literature. Many early pin fin studies focused on pin height-to-diameter ( $H/D$ ) ratios and on pin spacing, in both streamwise ( $X$ ) and spanwise ( $S$ ) directions. Chyu et al. [77] varied pin  $H/D$  ratios and found that for  $H/D=1$ , the pin surface contributed to 40% of the total array heat transfer. Metzger et al. [78] performed a row-resolved heat transfer analysis on pin arrays of varying  $X/D$  and  $S/D$ , in addition to varying array orientation [79]; VanFossen and associates [80,81] also studied staggered pin fin arrays and determined an effect of pins' locations in the array on the heat transfer. These studies showed that decreasing  $X/D$  and  $S/D$  increased the heat transfer, but yielded a corresponding penalty in pressure drop. Armstrong and Winstanley [82] compiled much of this early research and developed power law correlations based on Reynolds numbers; the authors noted that  $S/D$  had a stronger influence on friction factor than did  $X/D$ . More recently, Ostanek [83] developed correlations using Artificial Neural Networks that also took into account array geometry. Lyall et al. [84] and Lawson et al. [18] contributed discussions on Reynolds number effects on both

the heat transfer and the pressure drop; an increase in Reynolds number generated higher heat transfer. Siw et al. [85] investigated narrow pin fin channels, where wall effects were influential, and found much increased heat transfer performance when compared to a conventional, wide pin fin array.

Numerous studies on micro pin fin arrays have also been performed, made possible by new manufacturing techniques such as diffusion bonding, stereolithography, chemical etching and LIGA [9]. Some of the studies were motivated by an interest in 1X scale performance for gas turbine airfoil skin cooling [86] and others were focused on small electronics cooling [87–89]. In general, these true scale experiments performed similarly to their scaled-up counterparts in terms of both pressure loss and heat transfer performance, with one exception shown by Heo et al. [89]. Heo et al. manufactured rough pin surfaces and saw an increase in convective heat transfer from the roughened surfaces as compared to the smooth surfaces. The authors tested Reynolds numbers only up to 750. In a similar vein, Chang et al. [90] artificially roughened the endwall surfaces of a pin fin array and reported higher heat transfer from the roughened channel than a smooth channel at all Reynolds numbers studied,  $1000 < Re < 30000$ . Both studies [89,90] also reported correspondingly high pressure losses from their roughened pin fin arrays.

The additive manufacturing process yields extremely rough surfaces [15], a consequence of the sintering process. One group of studies led by Jodoin [91–93] examined arrays of aluminum pyramidal pin fins that were manufactured additively via Cold Gas Dynamic Spraying. The authors collected bulk heat transfer data and reported good thermal performance coupled with high pressure losses. The authors also performed  $\mu$ -Particle Image Velocimetry ( $\mu$ PIV) measurements and saw turbulence intensities of up to 25% at  $Re_{Dh}=500$  [93]; the high surface roughness caused an early transition to turbulence.

Other studies that have taken into consideration the pressure loss and heat transfer performance of additively manufactured finned heat exchangers include those by Ventola et al. [34], Wong et al. [35] and Dede et al. [72], who all used Selective Laser Melting (SLM). The three studies investigated external surfaces only. To note, external surfaces can often be post-processed to reduce the roughness; however, internal surfaces of microchannels prove challenging to post process, especially when the microchannel is filled with objects such as pin fins.

Characterizing surface roughness, among other part features, is important in AM parts and especially so in mini or micro geometries. Ning et al. [28] found that dimensional variances in L-PBF parts are a function of the machine parameters and that smaller geometries are especially prone to such variances due to the natural shrinkage of L-PBF parts, which can reduce the size of small parts (defined as less than  $3 \text{ mm}^3$ ) by up to 90%. The surface finish of AM parts is a strong function



of the process parameters, such as laser scan speed, hatch distance, laser energy density and layer thickness [27,29,58,59,94]. Wegner et al. [59] found that increasing the laser energy density smooths the part surface and mitigates the stair-stepping effect seen on inclined upward facing surfaces. Similarly, Yadroitsev et al. [94] advocated for smaller layer thicknesses to improve surface finish.

Snyder et al. [15], Stimpson et al. [16] and Kirsch and Thole [55] performed detailed pressure loss and heat transfer experiments on L-PBF open microchannels and characterized the surface roughness through the use of a Computed X-Ray Tomography (CT) scanner. Roughness features were found to protrude deep into open channel space and corresponded to relative sand grain roughness values between 20% and 38% the channel hydraulic diameters [15,16]. The authors found that the heat transfer augmentation caused by the roughened surfaces plateaued when the friction factor augmentation surpassed four, which corroborated the findings from Norris [33]. Snyder et al. [15] noted that the ability to reproduce a desired channel geometry was a strong function of the build direction, as was the final part's surface roughness. These findings were confirmed in multiple independent studies [29,60,95]. Bacchewar et al. [60] identified laser power as especially influential in the surface roughness of downward facing surfaces; for upward facing surfaces, the laser power had minimal impact on surface roughness. Jamshidinia and Kovacevic [96] found that the proximity of parts during the build process affects the heat accumulation in the part and therefore influences its surface roughness. In Stimpson et al. [63], they expanded upon their initial study in [16] develop a correlation to estimate friction factor given the parts' mean relative roughness, which the authors calculated from SEM images.

Surfaces with high relative roughness have also been the focus of studies by Huang et al. [31] and Dai et al. [32]. Huang et al. [31] investigated interior pipe walls with uniform surface roughness created by adhering acrylic spheres of a specified diameter to the pipe walls. The relative roughness, or the ratio of acrylic sphere diameter to pipe diameter, reached 42%; the authors found that friction factor for flow in the subcritical regime exceeded that predicted by laminar theory. Dai et al. [32] focused on liquid flow through mini and micro channels and reported similar results—when relative roughness surpassed 2%, laminar flow theory under predicted the friction factor. Kandlikar et al. [30] reported a transition to turbulent flow at Reynolds numbers as low as 350 and called for more accurate measures, such as constricted flow area, to represent surface roughness properly.

This summary of relevant work showcases the community's interest in finned heat exchangers and in understanding the additive manufacturing process as it relates to thermal performance. With the wealth of information available on the performance of smooth-walled pin

fin arrays and the recent knowledge gained on the surface roughness of AM parts, this paper aims to provide insights into the combined effects of high surface roughness with the complex flow structures so characteristic of pin fin arrays. While external surfaces can be machined or treated to remove roughness features, the internal surfaces of microchannels filled with pin fins are not easily accessible to remedy the surface roughness. The uniqueness of this paper is it is the first to evaluate the use of L-PBF for building microchannels containing pin fins.

#### 4.4 Fabrication of Test Coupons

Four pin fin test coupons were manufactured using L-PBF with its machine's stock Inconel 718 powder [45]. These coupons were constructed in a research laboratory using a commonly available L-PBF machine. The L-PBF machine manufacturer ensured a fully dense final part, so all coupon thermal properties were taken to be that of conventional Inconel 718. The material scaling parameters, beam offset and layer thickness used for the build were those recommended by the manufacturer for Inconel 718 [45]. The layer thickness was set to 40  $\mu\text{m}$ ; the laser focus diameter varied between 100 and 500  $\mu\text{m}$  [41].

The test coupons were 25.4 mm in length and in width, and 1.5 mm in height, which set the endwall thickness in the pin fin array to be 0.25 mm; the open channel hydraulic diameter for each coupon was 1.9 mm. All pin fins were designed to be cylindrical in shape with a diameter of 1 mm and an  $H/D=1$ . The test matrix is shown in Table 4-1; a visual description of the pin fin nomenclature used in this paper is shown in Figure 4-1.

. An important benefit of pin fin heat exchangers is their addition of surface area over which heat transfer can take place. Given that each of the arrays was confined to a constant volume duct, the number of pins in each test varied and therefore, the convective surface area varied accordingly. The third column in Table 4-1 shows the percent increase in convective surface area from each configuration compared to an open duct. Three variations in spanwise spacing and two variations in streamwise spacing were constructed and tested at a range of Reynolds numbers between 500 and 25000.

**Table 4-1. Test matrix**

$S/D$	$X/D$	Added surface area relative to open duct
2.0	2.6	50%
4.0	2.6	43%
1.5	2.6	58%
2.0	1.3	85%

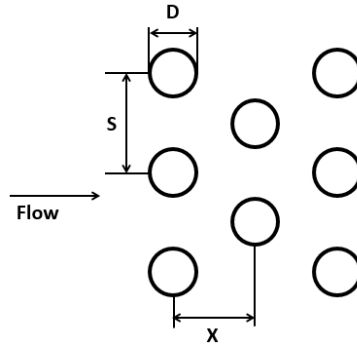


Figure 4-1. Pin fin spacing nomenclature

The L-PBF coupons were built layerwise at a  $45^\circ$  angle to the build plate, in the orientation shown in Figure 4-2. For the size of the coupon and the material used, an angle of  $45^\circ$  ensured that all features with downward facing surfaces would be partially supported [45]. The test section flanges served as anchors for the coupon's support structures during the build.

The coupons were removed from the build plate using a wire electro discharge machine (EDM). Support structures were removed manually from each test coupon and flange surfaces were smoothed to ensure a good seal in the test section as shown in Figure 4-3.

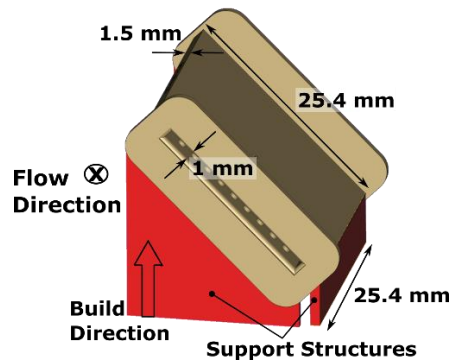


Figure 4-2. Test coupon build direction, with support structures. Flow direction into the page, normal to flanges.

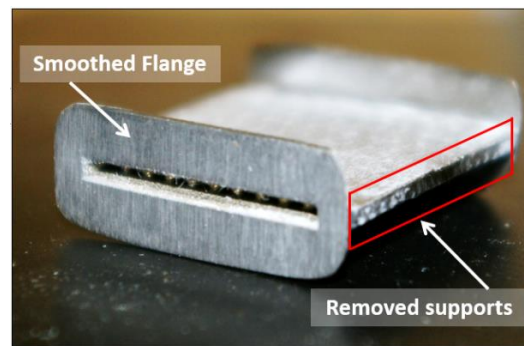


Figure 4-3. Picture of L-PBF coupon showing smoothed flange and all support structures removed.

## 4.5 Geometric Characterization of the Test Coupons

Due to the locally high temperatures experienced by the part during an L-PBF build, thermal distortion and shrinkage naturally occur. To account for the shrinkage, the L-PBF machine software imposes a geometric scaling factor, as well as a beam offset scalar, with the goal of achieving part dimensions close to that of the CAD model. Even still, evaluation of the part's true construction relative to the design intent is crucial for data analysis. To measure such small internal surfaces accurately, Computed X-Ray Tomography (CT Scan) was used.

The resolution, or voxel size, achievable by the CT scanner used for these experiments was 35  $\mu\text{m}$ . Data from the CT scan were output as 2D slices of the part, showing varying levels of grayscale that corresponded to varying material density. These 2D images were stitched together to form a 3D model of the as-built part using commercial software [42]. The software was able to achieve surface determinations within  $1/10^{\text{th}}$  the voxel size, or 3.5  $\mu\text{m}$ , by using algorithms that compared local grayscale values in each voxel. Therefore, only surface features larger than 3.5  $\mu\text{m}$ , or 0.35% of the pin fin diameter, were able to be resolved, which was deemed sufficient for determining the coupons' pertinent dimensions and for calculating the roughness on each of the internal surfaces.

The CT scan results showed unmistakably high surface roughness on the test coupon walls; by contrast, the pin surfaces were relatively smooth, though not necessarily circular in cross section. Surface roughness was quantified by fitting a polynomial surface to the top and bottom walls, then measuring the difference between each point on the coupon wall and that fitted surface. That difference was used in the calculation of the arithmetic mean roughness,  $R_a$ , the definition of which is shown in Equation 4-1. A 2D example of the surface fit (shown as a curve fit) of a small section on one coupon's bottom wall is shown in Figure 4-4. The roughness features skewed toward positive deviation because of the presence of the pins; the high temperature experienced by the solid pin fins may have caused loose powder particles to stick more readily around the pin base during the build [96]. Typical localized values of maximum peak to valley roughness values ranged between 25% and 35% of the channel hydraulic diameter.

$$R_a = \frac{1}{n} \sum_{i=1}^n |z_{\text{surf},i} - z_{\text{meas},i}| \quad 4-1$$

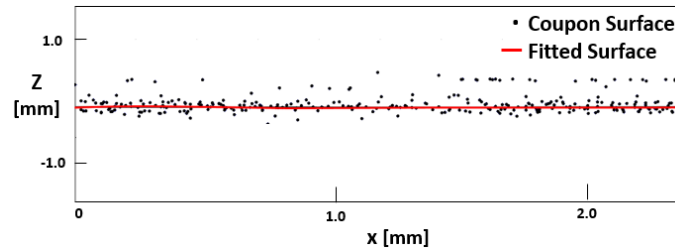


**Figure 4-4. Point cloud data form the CT scan on a small section (2.5 mm long) of a representative bottom surface and its corresponding surface fit, shown in 2D as a curve fit.**

Figure 4-5 shows an image generated by the CT scan from inside the pin fin array; the top wall was expectedly rough, given that it was largely unsupported during the build. In the powder bed fusion process, the laser power is set such that the laser penetrates deeper than the current layer, which ensures good adhesion between solid layers. However, on downward facing surfaces, under which no solid material exists to conduct away the heat generated by the laser, large roughness features form.

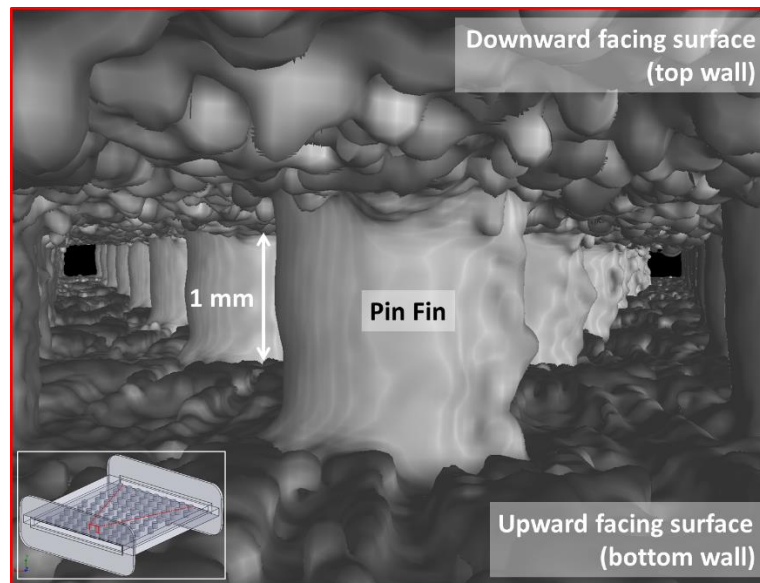


**Figure 4-5. View from inside the pin fin channel; image generated by the CT scan. Flow direction is into the page. The image in the lower left corner shows the location in the test coupon at which the CT scan image was taken.**

The bottom walls of the coupons were also extremely rough, the reason for which lies in both the high temperatures experienced by the discrete, solid pin fins, as previously discussed, and in the thickness of the walls themselves. A wall thickness of 0.25 mm neared the limits of the L-PBF process capabilities to produce a fully dense wall. As the bottom wall of the coupon was built, heat from the laser was not able to be conducted away and the wall remained at an elevated temperature, thus allowing powder particles to become partially sintered to the coupon surface.

Pertinent coupon dimensions were calculated using the 2D slices output from the CT scan. Figure 4-6 shows a mid-height slice from a top down view of the  $S/D=2.0$ ,  $X/D=2.6$  coupon. The build direction relative to the image is shown also, as is the flow direction; due to the build direction chosen, each pin fin had large roughness features that formed on its downward facing surface, consequently rendering the cross sectional shape of each pin not as circular as intended. This formation is visible in Figure 4-5 as well, on the right side of the pin from the vantage point of the figure. The pins' shapes appeared to be a function of the spacing in the channel.

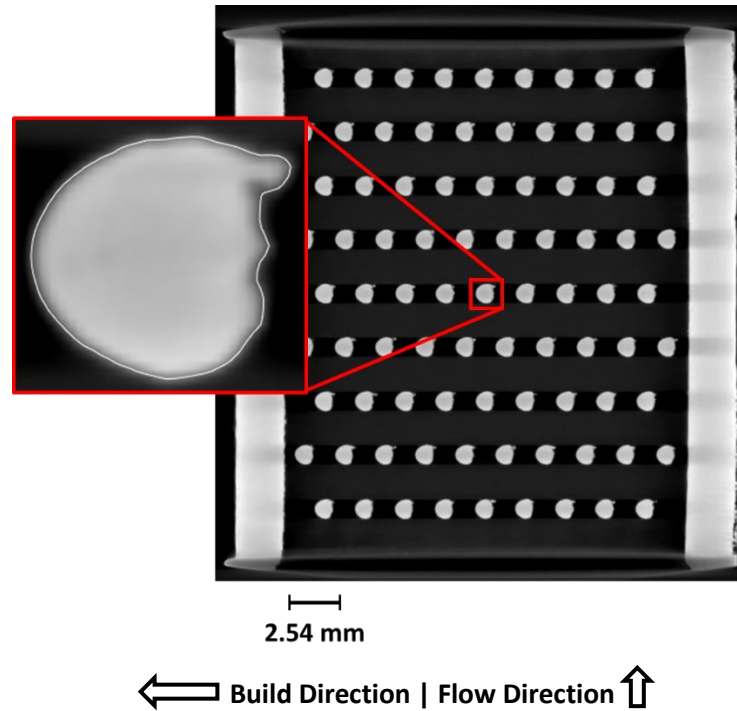


Figure 4-6. CT scan slice of top down view of the  $S/D=2.0$ ,  $X/D=2.6$  coupon, with one pin fin magnified.

Figure 4-7 shows a top down cutaway view of the 3D rendering of two coupons generated by the CT scan; Figure 4-7a shows the widest spaced array at  $S/D=4.0$  and  $X/D=2.6$  and Figure 4-7b shows the tightest spaced array at  $S/D=1.5$  and  $X/D=1.3$ . The view area in each figure is equal and the build direction and flow direction match those labeled in Figure 4-6. In Figure 4-7, the roughness features that formed on the downward facing surfaces of the pins. The increase in number and size of the roughness features that formed on the downward facing surfaces of the pins are evident in the tighter spaced array (Figure 4-7b). Additionally, the pin shape between the two arrays was noticeably different.

One hypothesis for the supposed correlation between pin density, surface roughness and pin shape lies in the amount of surface area exposed to the laser for each build layer. Figure 4-8 shows the exposure area, or the amount of material to be melted by the laser, for one layer of the build process for the widest ( $S/D=4.0$ ,  $X/D=2.6$ ) and tightest ( $S/D=1.5$ ,  $X/D=1.3$ ) spaced pin fin

arrays. A larger amount of surface area requires more time for the laser to melt the metal powder, causing the coupon to experience an elevated temperature for a longer period of time. Such an elevated temperature could cause loose powder particles to adhere to the solid surfaces, thereby incurring a higher surface roughness on the channel endwalls, as well as on the pin surfaces, distorting the pin shapes.

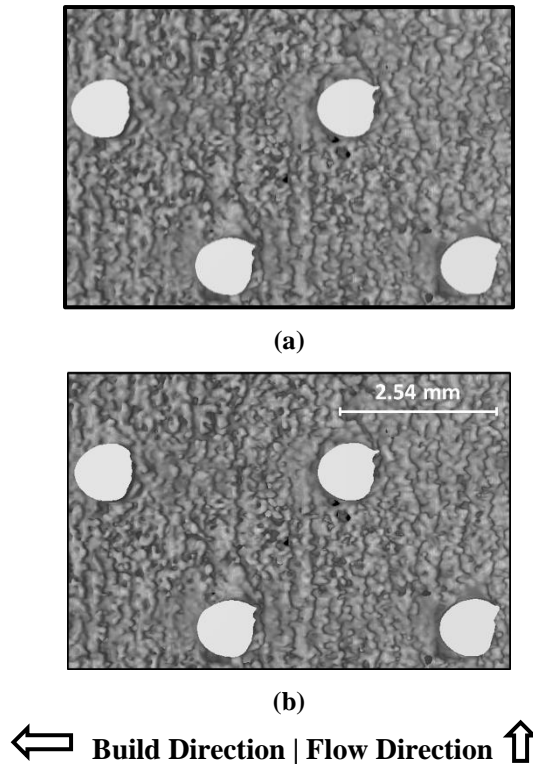


Figure 4-7. Top down view of the 3D rendering of as-built test coupons. (a)  $S/D=4.0$ ,  $X/D=2.6$ . (b)  $S/D=1.5$ ,  $X/D=1.3$ .

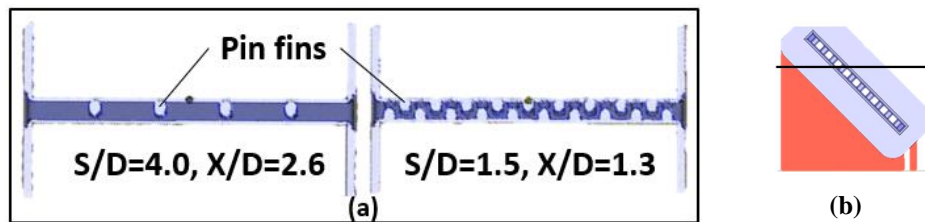


Figure 4-8. Laser exposure area for one layer. (a) Top-down view of laser exposure area for two pin spacings. (b) Location of layer slice.

Despite any small extra features on the pin, a pin diameter was calculated as if the cross section were circular by using an in-house image processing code. The cross-sectional area of each pin was calculated using the top-down 2D slices from the CT scan analysis software (Figure 4-6); from that calculation, an effective pin diameter was backed out. The pin diameter calculations are shown in Table 4-2, along with the channel hydraulic diameter and the relative roughness of the

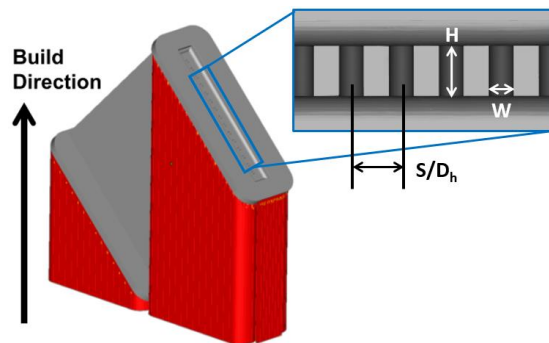
coupon surfaces normalized by the pin diameter and by the channel hydraulic diameter. The pin diameters were taken as the average of all slices over the entire height of the channel.

Table 4-2 also shows the fin efficiency ( $\eta_f$ ) and overall surface efficiency ( $\eta_o$ ) for each of the pin fin arrays, which were calculated using the methods described in [97]. The overall surface efficiencies were over 97% for all four arrays.

Two L-PBF baseline coupons containing multiple rectangular microchannels will be included in the results discussion and will be described briefly here; these microchannel test coupons were studied for friction factor and heat transfer in Stimpson et al. [16]. The coupons were built at a 45° angle to the build plate, though not in the same orientation as the pin fin arrays. Figure 4-9 shows the build orientation and the nomenclature to be used for the multichannel coupons. The coupons were manufactured from Inconel 718 and the machine parameters were the same as for the pin fin arrays [45]. Additionally, the coupon dimensions were the same as for the pin fin arrays.

**Table 4-2. L-PBF pin fin microchannel coupon dimensions and roughness values**

	$S/D=4.0, X/D=2.6$	$S/D=2.0, X/D=2.6$	$S/D=1.5, X/D=2.6$	$S/D=1.5, X/D=1.3$	Design Intent
Pin $D$	0.95 mm	0.93 mm	0.88 mm	0.90 mm	1.0 mm
Channel $D_h$	2.1 mm	2.0 mm	1.9 mm	1.9 mm	1.95 mm
$R_a/D$	0.074	0.088	0.09	0.10	--
$R_a/D_h$	0.039	0.046	0.047	0.053	--
$\eta_f$	89%	89%	89%	89%	--
$\eta_o$	99%	99%	98%	97%	--



**Figure 4-9. Build direction and nomenclature for L-PBF multichannel coupons [16]**

The baseline test coupons were characterized in the same manner described for the microchannels containing pin fins; a CT scanner was used to evaluate the internal surfaces, calculate the surface roughness and determine pertinent length scales. Table 4-3 shows the number of channels in each multichannel coupon from [16], as well as the hydraulic diameter from the design intent and as calculated from the CT scan results.



The channel spanwise spacing is included as well and will be used to distinguish between the two channels in the discussions of the experimental results, consistent with the nomenclature used for the pin fin arrays.

The arithmetic mean roughness, normalized by the channel hydraulic diameter, was significantly higher for the L-PBF pin fin arrays than for the L-PBF multichannel array. Where the pin fin arrays contained numerous unsupported surfaces throughout the entire test coupon, in the multichannel test pieces, unsupported surface were confined by continuous fins (walls). The discrete pin fins served as a less effective means to conduct away the heat from the build and consequently yielded higher surface roughness than the multichannel configuration.

Both fin efficiency,  $\eta_f$ , and overall surface efficiency,  $\eta_o$ , were also calculated for the two multichannel L-PBF coupons from Stimpson et al. [16] and are included in Table 4-3. Both fin and overall surface efficiencies were over 99% for the multichannel coupons.

**Table 4-3. L-PBF baseline multichannel coupon dimensions and roughness values [16]**

$D_h$	Design	As-built	Design	As-built
	0.41 mm	0.47 mm	0.83 mm	0.92 mm
Aspect ratio ( $H:W$ )	2.2		2.2	
No. of Channels	24		16	
$S/D_h$	<b>2.1</b>		<b>1.55</b>	
$R_a/D_h$	0.025		0.015	
$\eta_f$	>99%		>99%	
$\eta_o$	>99%		>99%	

#### 4.6 Experimental Facility

Figure 4-10 shows a cut-away of the test facility used for all pressure loss and heat transfer experiments. This facility has been benchmarked and used in numerous experiments from our laboratory [15,16,43,55,63]. The test section working fluid was air and was pressured to hold a constant inlet pressure of 670 kPa for each Reynolds number tested; the exit pressure was adjusted to attain target Reynolds numbers. All experiments remained in the incompressible flow regime. A commercial gas flow controller was used to control the mass flowrate [76]. The Reynolds number was calculated using the pin diameter and the maximum velocity in the channel, as shown in Equation 4-2. The maximum velocity was a function of the spanwise spacing of the pins and was calculated using Equation 4-3. The inlet and outlet sections were built from Nylon using Selective Laser Sintering to reduce the conductive losses. Static pressure taps were located in these inlet and outlet Nylon pieces to measure the pressure drop across the test coupon. A friction factor

was calculated per pin fin row for each experiment using Equation 4-4, where  $N$  is the number of rows in the array. This friction factor definition, sometimes referred to as a flow friction factor [82], is commonly employed among pin fin studies. Its definition is one quarter of the definition of friction factor through channels.

$$Re_D = \frac{U_{max} \cdot D}{\nu} \quad 4-2$$

$$U_{max} = \frac{W}{W - N_{span} \cdot D} \cdot U_m \quad 4-3$$

$$f = \Delta P \cdot \frac{1}{2 \cdot \rho \cdot U_{max}^2} \cdot \frac{1}{N} \quad 4-4$$

In the case of heat transfer tests, copper blocks were heated using a resistive surface heater and served as a constant temperature boundary condition on the coupon endwalls. The surface heaters were directly wired to power supplies that controlled the heat into the system. The assumption of constant temperature boundary condition was validated in a previous study [43]. Thermal paste adhered the surface heater to the copper blocks, as well as the copper blocks to the test coupon. By using a 1D conduction analysis that included both the measured coupon wall thickness and the thermal paste thickness, the temperature of the coupon wall was calculated for the log mean temperature difference. Rigid foam surrounded the copper blocks and provided insulation; additional insulation was inserted in crevices between the foam and nylon to mitigate conduction losses.

Conduction losses were quantified with thermocouples embedded throughout the test section: on the heater itself, in the copper blocks, in the rigid foam and in the Nylon inlet and outlet sections. The highest conduction losses, around 15% of the total heat into the system, were seen at low Reynolds numbers. For Reynolds numbers above 8000, conduction losses were relatively constant around 5%. These losses were accounted for in the definition of the heat transfer coefficient as shown in Equation 4-5. As a check on the heat transfer calculations, an energy balance was performed by measuring the inlet and outlet air temperatures for each test. Comparisons were made between the energy balance of the air passing through the coupon with that of the heat input from the heaters. In all cases, the energy balance matched to within 12% of the measured heat input, minus the conduction losses.

The heat transfer coefficient was based on the log mean temperature difference as shown in Equation 4-5, where  $A_s$  was the wetted surface area, calculated from Equation 4-6. In words, Equation 4-6 represents the surface area of the open channel plus the surface area of the pin fins, minus the pin fin footprints.

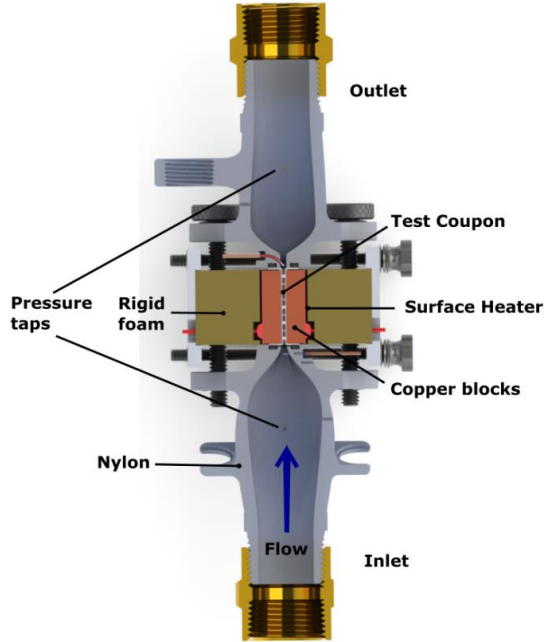


Figure 4-10. Cross section of experimental test facility

$$h = \frac{Q - \sum Q_{\text{losses}}}{A_s \cdot \Delta T_{\text{lm}}} \quad 4-5$$

$$A_s = 2 \cdot L \cdot (W + H) + N_{\text{pins}} \cdot \left( \pi D H - 2 \cdot \left( \frac{\pi D^2}{4} \right) \right) \quad 4-6$$

#### *Experimental Uncertainty*

Experimental uncertainty was calculated using the methods described in Kline & McClintock [46]. In the friction factor results, the largest source of uncertainty came in the measurement of the pressure drop across the test coupon. At low Reynolds numbers, the pressure loss was low especially in the array with the widest spacing. In those worst case scenarios with the widest spaced array, at Reynolds numbers below 500, uncertainty in the friction factor neared 30%, but quickly dropped to below 10% for Reynolds numbers greater than 1000. For the array with the tightest spacing of pins, uncertainty was below 10% in the friction factor for Reynolds numbers above 500. However, the repeatability of the datasets, calculated at a 95% confidence level, was between 1.5% and 2% for all Reynolds numbers of interest.

In the case of the heat transfer tests, Nusselt number uncertainty was relatively constant at 5%. The largest source of uncertainty came in the calculation of the coupon wall temperature using the 1D conduction analysis. Uncertainty in the thickness of the paste that adhered the copper block to the test coupon, along with the uncertainty in wall thickness measured by the CT scan,

contributed to the error in calculating the coupon wall temperature. Repeatability in Nusselt number, however, was under 3% for all Reynolds numbers.

#### **4.7 Results and Discussion**

Experiments were conducted on the four L-PBF pin fin coupons to obtain friction factors and Nusselt numbers across a range of Reynolds numbers. These values will be compared to smooth-walled pin fin arrays containing similar streamwise and spanwise spacings.

Additionally, where applicable, the following graphs will contain data points from an open (no pin fins), smooth, conventionally manufactured test coupon for benchmarking purposes. The smooth channel data points are plotted against common smooth channel correlations. Convention for pin fin array friction factor calculation involves the Fanning friction factor definition, or one quarter the friction factor definition for channel flow. Therefore, a factor of one quarter was applied to the smooth channel correlations: for the flow tests, Laminar Theory ( $f = 16/Re_{Dh}$ ) and the Colebrook formula [98] were used in the laminar and turbulent regimes, respectively. For the heat transfer tests, the turbulent Gnielinski correlation was used [51]. The benchmarking coupon was machined from aluminum and contained cylindrical channels that were reamed smooth. Data from the benchmarking coupon matched well to the smooth channel correlations as will be shown in the results.

Despite the deviation from the design intent in pertinent dimensions measured using the CT scan data, as shown in Table 4-2, the length scales (and consequently, the  $U_{max}$  calculations) for Reynolds number, friction factor and Nusselt number are those from the design intent. The trend in both friction factor and heat transfer results was the same regardless of whether the actual or the design intent length scales were used.

To compare the L-PBF micro pin fin arrays to studies from the literature, applicable previous work will be included in the following graphs. The majority of the comparison studies come from smooth pin fin arrays, but the studies by Stimpson et al. [16] containing L-PBF rectangular microchannels will be included as well; the spanwise spacing of those channels was  $S/D_h=1.55$  and  $S/D_h=2.1$ . Table 4-4 shows all previous studies that will be included in the upcoming graphs and notes whether those studies will be discussed in the context of friction factor tests, heat transfer tests, or both.

The following sections will be divided into discussions on (1) pressure loss performance, (2) heat transfer performance and (3) combined friction factor and heat transfer augmentation. Included in these discussions will be the influence of streamwise and spanwise spacing on the array's performance, as well as the effect of varying Reynolds number. Given that the relative

roughness in the channels was so high, the discussions will be motivated by the effect of the roughness features on the results when smooth and rough arrays are directly compared.

**Table 4-4. Studies from the literature to be included in results discussion**

	Baseline, Multichannel Coupon L-PBF Stimpson et al. [16]		Ostaneck, J.K. [99]		Lawson et al. [18]			Brigham et al. [100]
S/D	1.55	2.1	2.0	2.0	2.0	4.0	4.0	4.0
X/D	N/A	N/A	2.16	2.6	1.73	1.73	3.46	4.0
f		x	x	x	x	x	x	
Nu	x	x	x	x	x	x	x	x
$R_a/D_h$	0.015	0.025	Smooth		Smooth			Smooth

### Pressure Loss Results

Figure 4-11 shows the friction factor results for the four pin fin arrays in the present study for a range of Reynolds numbers; the friction factor correlations for laminar and turbulent flow are also given, along with the data points from the smooth benchmarking coupon.

Generally in pin fin arrays, friction factor is driven by the spanwise spacing of the pins because it dictates the blockage to the flow [18,78,82,84]. In fact, many correlations for friction factor in pin fin arrays omit any dependence on streamwise spacing and are a function of spanwise spacing, only. For example, Damerow [101] and Jacob [102] include only the spanwise spacing and Reynolds number in their correlations; Damerow [101] claimed that friction factor was not a function of row number. A friction factor correlation given by Metzger [78] is valid only for one spanwise spacing value of  $S/D=2.5$ , but over a wide range of  $X/D$  values,  $1.5 \leq X/D \leq 5.0$ .

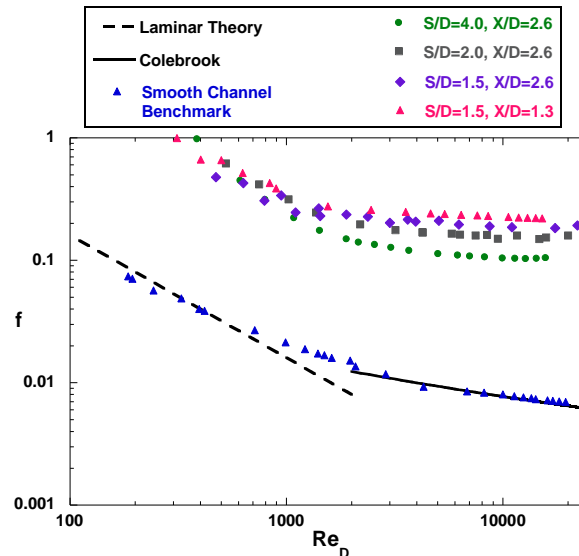


**Figure 4-11. Friction factor results for the four L-PBF pin fin arrays, along with the results from the benchmarking coupon.**

The trend in friction factor seen in Figure 4-11 does not match with the findings from these previous studies. Friction factor for the L-PBF pin fin arrays correlated with pin density, not solely with spanwise spacing; an increase in the numbers of pins in the coupon led to an increase in the pressure loss through the array. Surface roughness on the top and bottom walls was a function of the number of pins in the channel (Table 4-2). The coupon with the tightest streamwise and spanwise spacings ( $S/D=1.5$ ,  $X/D=1.3$ ) showed roughness values 35% higher than the coupon with the widest spacings ( $S/D=4.0$ ,  $X/D=2.6$ ) (Table 4-2). As a result of the larger number of pin fins in the array, loose powder particles more easily adhered to the test coupon inner walls, thereby increasing the overall surface roughness. Therefore, even coupons containing the same spanwise spacing ( $S/D=1.5$ ), but different streamwise spacings ( $X/D=2.6$  and  $X/D=1.3$ ) exhibited different friction factor values, which is not normally reported in the literature.

To isolate the effects of surface roughness, the friction factor from the L-PBF arrays can also be compared to studies of smooth-walled pin fin arrays of similar spacings [18,99]. To note, the studies from [18,99] were scaled up by an order of magnitude. However, the Reynolds numbers tested for the scaled up pin fin arrays match the Reynolds numbers tested in the current study.

Figure 4-12 shows the friction factor augmentation of the L-PBF coupon with spacing  $S/D=2.0$ ,  $X/D=2.6$ , along with three previous smooth walled pin fin studies with  $S/D=2.0$ , over a smooth channel; the three streamwise spacings of the smooth walled studies were  $1.73D$ ,  $2.16D$  and  $2.6D$  [18,99]. Additionally, friction factor augmentation from the L-PBF straight rectangular multichannel study with no pin fins but channel spacing  $S/D_h=2.1$  is included [16].

The friction factor augmentation values were calculated using the conventional definitions for the test coupon at hand. For the pin fin arrays,  $f_0$  was calculated using the same correlations applied in Figure 4-11 or one quarter the smooth channel correlations for channel flow. For the multichannel array, the smooth channel friction factor was calculated using traditional channel flow correlations, Laminar Theory ( $64/Re$ ) and the Colebrook formula [98]. The Reynolds number definition used for the augmentation plots was the duct Reynolds number, as opposed to the pin Reynolds number. The augmentation values, therefore, are comparable between the two types of microchannels.

Figure 4-12 shows that the augmentation values from the pin fin arrays, both L-PBF and smooth, were substantial. The difference in friction factor augmentation between the L-PBF and the smooth walled pin fin array grew with increasing Reynolds number; at low Reynolds numbers, the friction factor augmentation from the pin fin arrays was similar, regardless of surface finish. However, at higher Reynolds numbers, the L-PBF pin fin array showed nearly double the augmentation from the smooth walled arrays. Given that the average size of the roughness features

in the L-PBF coupon was 9% of the pin diameter (Table 4-2), the flowfield in the array was affected not only by the presence of the pins, but also by the large roughness features on the endwalls and the non-circular nature of the pins themselves.

In directly comparing the two L-PBF studies, the pin fin array showed substantially higher friction factor augmentation than the straight channels [16]. The disparity in friction factor augmentation can be explained primarily by the differences in the flowfields. While the pin fins produced high levels of turbulence and wake shedding, the multichannel coupon with no pin fins was similar to that of channel flow with very rough walls.

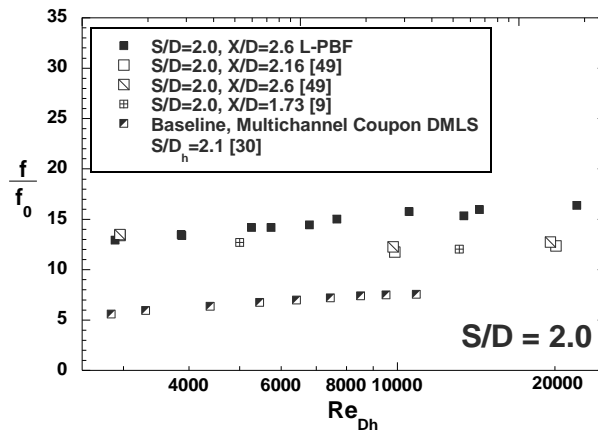


Figure 4-12. Friction factor augmentation from both L-PBF and smooth walled pin in arrays, along with L-PBF straight microchannels, with  $S/D_h=2.0$  [16].

In Figure 4-13, where spacings of  $S/D=4.0$  are compared, the friction factor augmentation showed a relatively consistent higher friction factor augmentation over their smooth-walled counterparts. However, much like the L-PBF pin fin array spaced at  $S/D=2.0$ , the roughness in the array with  $S/D=4.0$  more strongly affected the pressure loss through the array at Reynolds numbers above 10000. At a Reynolds number of 15000, the  $S/D=4.0$  L-PBF pin fin array showed friction factor augmentation around four times that of the  $S/D=4.0$  smooth walled arrays.

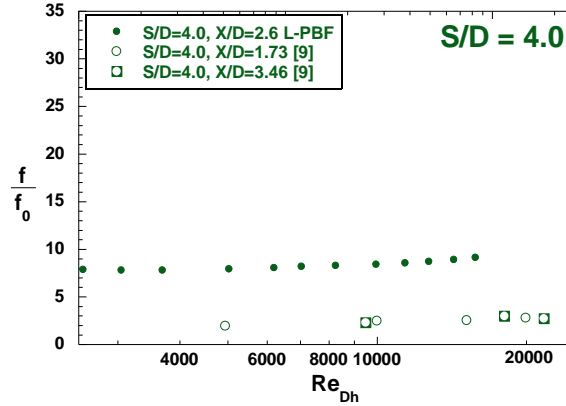


Figure 4-13. Friction factor augmentation from both L-PBF and smooth walled pin fin arrays with  $S/D=4.0$ .

### Heat Transfer Results

Figure 4-14 shows the Nusselt numbers for each of the four L-PBF coupons, along with the data points from the benchmarking coupon and the Gnielinski correlation. All four of the L-PBF coupons showed a considerable increase in the heat transfer as compared to the smooth channel correlation as well as the multichannel L-PBF baseline with no pin fins [16]. While the difference among the four L-PBF coupons was relatively small, two trends emerged that compared well to trends observed in the literature. Tighter spanwise spacing generally yields higher heat transfer than wider spanwise spacing [18,78], which was the case for the L-PBF coupons with  $S/D=4.0$  and  $S/D=2.0$ . However, the difference in Nusselt number is small when the difference in spanwise spacing is marginal [99], as was the case in the L-PBF coupons spaced at  $S/D=2.0$  and  $S/D=1.5$ . The second trend was that for a given spanwise spacing, a tighter streamwise spacing generally yields higher heat transfer [18,99]; that trend was evident in the L-PBF coupons with  $S/D=1.5$ ,  $X/D=2.6$  and  $S/D=1.5$ ,  $X/D=1.3$ .

The high surface roughness in the coupons affected the heat transfer of the L-PBF pins relative to their smooth walled counterparts, especially at higher Reynolds numbers and tighter spacings. Ostanek [99] found that turbulence on the endwalls of pin fin arrays provided the most significant contribution to the heat transfer from the arrays; increasing the roughness on the endwalls increased the turbulence and therefore increased the overall heat transfer. Figure 4-15 shows the Nusselt number augmentation over a smooth duct of the L-PBF coupon with  $S/D=2.0$ , along with smooth walled pin fin arrays from the literature also spaced at  $S/D=2.0$  [18,99]. While streamwise spacing exerts a minimal effect on the pressure drop through the array, it strongly affects the heat transfer because it influences the wake formation and wake interactions among the pins [18]. Both streamwise and spanwise spacing prove influential in the final heat transfer results of any pin fin array. The chosen combination of streamwise and spanwise spacings in the L-PBF



coupons with  $S/D=2.0$  led to strong wake interactions [17], which were presumably enhanced by the high surface roughness in the channel. As Reynolds number increased, that effect was magnified: the difference between the smooth walled and L-PBF pin fin arrays grew with increasing Reynolds number. Additionally, given that the cross sectional shape of the L-PBF pin fins was not perfectly circular, the wakes behind the L-PBF and smooth walled pin fins were assumed to be different.

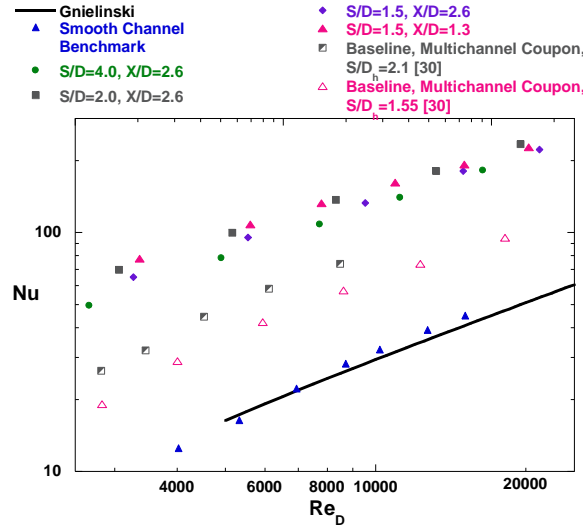


Figure 4-14. Nusselt number vs. Reynolds number for the four L-PBF pin fin arrays and two baseline, multichannel L-PBF coupons, along with the results from the benchmarking coupon.

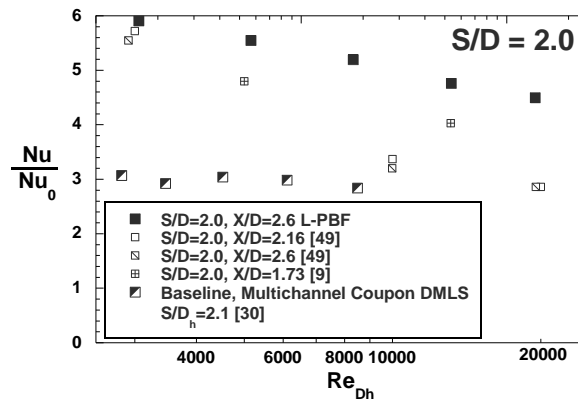


Figure 4-15. Nusselt number augmentation of L-PBF and smooth walled arrays with  $S/D=2.0$ .

Figure 4-16 shows the Nusselt numbers of both L-PBF and smooth walled pin fin arrays with  $S/D=4.0$  [18,100]. The L-PBF coupon showed similar performance to the smooth walled coupons. While the high surface roughness in the AM coupon undoubtedly added to the already turbulent flowfield in the array, the wide spanwise spacing in the array meant that the pin wake interactions were nevertheless limited [17]. Therefore, in directly comparing the L-PBF pin fin

arrays with the smooth walled arrays, the effect of surface roughness on the flowfield as it related to heat transfer was minimal for pins with relatively wide spacing  $S/D=4.0$ .

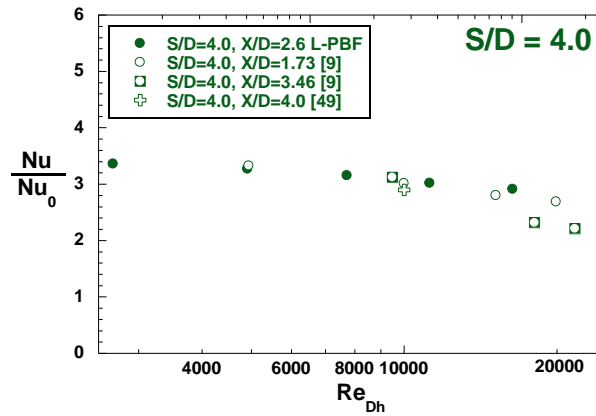


Figure 4-16. Nusselt number augmentation of L-PBF and smooth walled arrays with  $S/D=4.0$ .

In Figure 4-17 and Figure 4-18, the friction factor augmentation and heat transfer augmentation for pin fins made using L-PBF compared with those made using conventional methods are directly compared; a low Reynolds number case is shown in Figure 4-17 and a high Reynolds number case is shown in Figure 4-18. Both figures highlight the observation that the increase in friction factor augmentation far outweighed the increase in heat transfer augmentation for the  $S/D=4.0$  array. As previously discussed, the high surface roughness on the endwalls strongly affected the friction factor through the L-PBF array relative to its smooth counterpart; on the other hand, the wake interactions from the pins were limited by the wide spanwise spacing, which resulted in negligible differences in the heat transfer between smooth and rough arrays. These two effects accounted for the large discrepancy between friction factor augmentation and heat transfer augmentation seen in both Figure 4-17 and Figure 4-18.

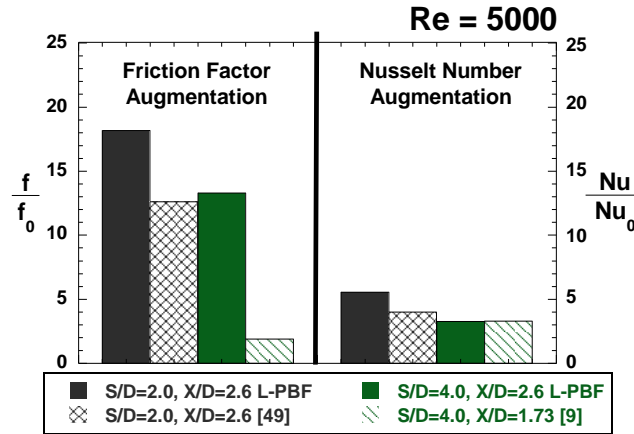


Figure 4-17. Direct comparison of friction factor augmentation and Nusselt number augmentation of smooth walled and L-PBF pin fin arrays with  $S/D=2.0$  and  $S/D=4.0$  at  $Re=5000$ .

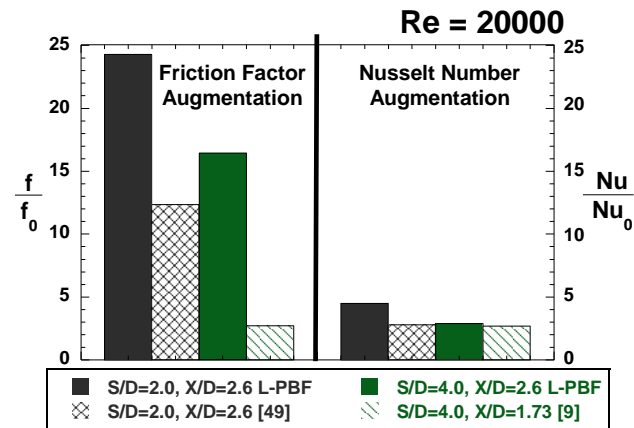


Figure 4-18. Direct comparison of friction factor augmentation and Nusselt number augmentation of smooth walled and L-PBF pin fin arrays with  $S/D=2.0$  and  $S/D=4.0$  at  $Re=20000$ .

#### Overall Augmentation Results

To gain a better understanding of how the data from the current study relates to the large amount of research available in the literature, friction factor and heat transfer performance can be analyzed concurrently. Figure 4-19 shows friction factor augmentation vs. Nusselt number augmentation for the four L-PBF coupons from the current study, along with six other studies from the literatures. Two of the previous studies [16,55] were also manufactured using L-PBF; the other four are representative of commonly-employed internal cooling schemes [18,19,79,99].

With the exception of the ribbed channel study [19], the friction factor augmentation of the four L-PBF pin fin arrays far surpassed most of the previous studies, with only a slight benefit in Nusselt number augmentation. In general, the L-PBF coupon with the widest spacing of pins ( $S/D=4.0$ ,  $X/D=2.6$ ) showed similar heat transfer performance as the other three spacings for less of a pressure loss.

Due to the roughness inherent in the L-PBF process, and the positive correlation between pin density and surface roughness, this result is important to understand for heat exchanger designers. The coupon with the widest spacing ( $S/D=4.0$ ,  $X/D=2.6$ ) had one sixth the number of pins as the coupon with the tightest spacing ( $S/D=1.5$ ,  $X/D=1.3$ ). The fact that the same heat transfer augmentation can be achieved with a reduction in the number of pins can lead to material and cost savings in engine components.

In comparing the multiple L-PBF microchannel studies, the pin fins exhibited a significantly higher friction factor augmentation than either the straight or wavy L-PBF multichannel coupons. The arithmetic mean roughness to hydraulic diameter ratio in the L-PBF channels was one quarter that seen in the pin fin arrays [16,55], which most likely contributed to the difference in friction factor augmentation seen in Figure 4-19. However, the different flowfields between the pin fin arrays and the channel flows were inherently different and were the predominant drivers of the difference in friction factor augmentation. Especially at low Reynolds numbers, the wavy microchannels show similar heat transfer performance to the pins, with considerably less of a penalty in pressure loss.

Given that flowrates in many applications are governed by fixed supply and exit pressures, a small study was done on the L-PBF pin fin arrays to determine the required mass flow at a given pressure ratio, as compared to a smooth duct. The mass flow through the smooth duct was calculated using a friction factor correlation and the target pressure ratio from the L-PBF coupon. For the tightest spacing of pins ( $S/D=1.5$ ,  $X/D=1.3$ ), the flowrate through the L-PBF array was reduced by 90% to achieve the same pressure ratio across a smooth duct. With the lower required mass flow came a corresponding decrease in the heat transfer, but only by 40% as compared to the smooth duct. By comparison, the widest spaced pin fin array ( $S/D=4.0$ ,  $X/D=2.6$ ) exhibited an 80% reduction in mass flow, with only a 30% decrease in the heat transfer. When analyzed with a constant pressure ratio, the high friction factor augmentation from the L-PBF pin fin arrays caused by the rough surface finish is redeemed by the high heat transfer augmentation.

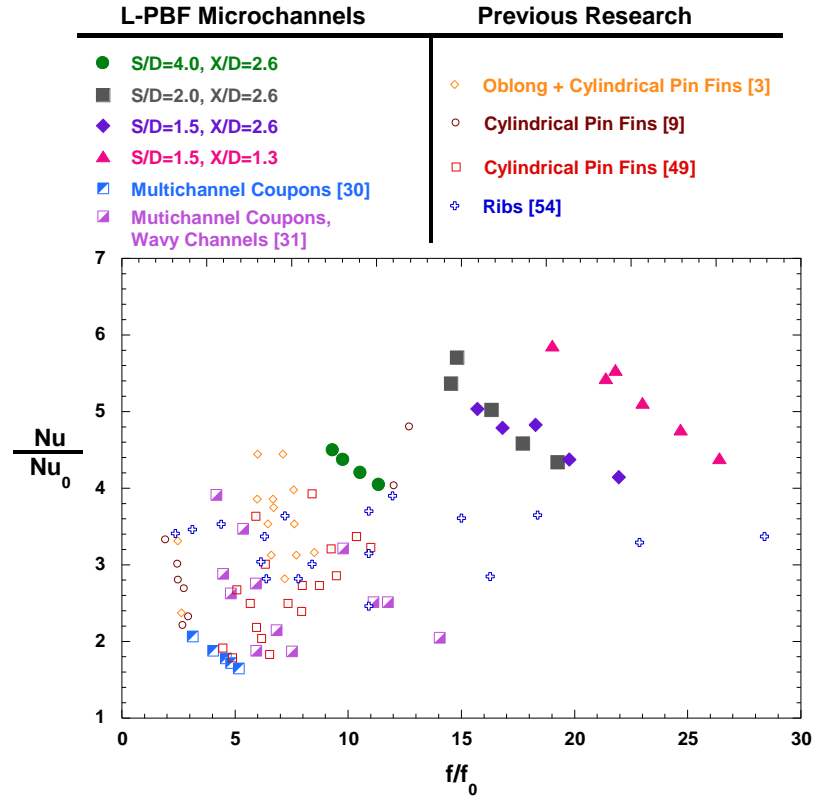


Figure 4-19. Nusselt number augmentation vs. friction factor augmentation for the four L-PBF pin fin arrays from the present study, select smooth walled pin fin arrays and other L-PBF internal cooling schemes.

#### 4.8 Conclusions

Four microchannel pin fin arrays were manufactured using L-PBF and experimentally investigated for pressure loss and heat transfer performance. Additionally, the test coupons were CT scanned and the internal features of the arrays were analyzed. The test coupons showed extremely high roughness on both top and bottom endwall surfaces. The surface roughness appeared to be a function of the number of pins in the array; as pin density increased, a corresponding increase in the roughness in the channel was seen due to the higher levels of heat accumulation during the build. With the larger amount of exposed surface area per build layer, more loose powder particles may have more readily adhered to the interior channel surfaces.

The positive trend in roughness correlated with the positive trend seen in the friction factor results, which does not agree with trends from previous studies in the literature. In smooth pin fin arrays, friction factor is generally influenced by spanwise spacing and not affected by variations in streamwise spacing. The increase in friction factor between two L-PBF coupons with the same spanwise spacing, but different streamwise spacing, was therefore attributed to the difference in surface roughness levels. When compared to their smooth pin fin array counterparts, the L-PBF

arrays showed an increase in friction factor of 20-80% (for a tighter spanwise spacing) and 60% (for a wider spanwise spacing) over smooth arrays with the same spanwise spacing.

The heat transfer augmentation of the L-PBF coupons far exceeded that of a smooth channel. Additionally, the heat transfer dependence on both streamwise and spanwise spacing in the L-PBF pin fin arrays agreed with reports from the literature; a significant decrease in the spanwise spacing led to a measureable increase in the heat transfer, while a slight decrease in spanwise spacing led to a marginal increase in the heat transfer. Decreasing the streamwise spacing also led to an increase in the heat transfer. The wake interactions in the arrays were beneficial to the heat transfer performance, regardless of surface finish.

In directly comparing the L-PBF coupons to their smooth array counterparts, the spanwise spacing proved to have a strong effect. At a close spanwise spacing, the L-PBF coupon outperformed other smooth arrays with the same spacing, especially at higher Reynolds numbers. With a wider spanwise spacing, however, the difference between the L-PBF and smooth arrays was small. An important mechanism in heat transfer from a pin fin array is the pin wake interactions; the rough surfaces work to exacerbate those interactions, but only for spanwise spacings close enough for the wakes to influence one another.

In comparing the four L-PBF pin fin arrays from the current study to other studies from the literature, the friction factor from the current test coupons was extremely high, with only a marginal benefit in heat transfer. The L-PBF coupon with a wide spanwise spacing showed the lowest friction factor of the four coupons, with a similar heat transfer performance. Put another way, the array with the fewest pins exhibited similar heat transfer performance to the array that contained six times the number of pins. Such a reduction in the number of pin fins could lead to measureable decrease in engine component weight and material requirements. If L-PBF becomes the chosen method for manufacturing pin arrays, this study has found that roughness levels and pin shape are intrinsically tied to the pin spacing in the array and prove equally influential in the performance of the array; fewer pins in an array can provide better overall performance than a densely-packed array.

Designing for additive manufacturing requires a different thought process and a full understanding of the benefits and drawbacks of the technique. With more fundamental research on what can be expected from the L-PBF process as it relates to conventional cooling schemes, the high surface roughness can be exploited to achieve more efficient heat exchangers.

## **5 NUMERICAL OPTIMIZATION, CHARACTERIZATION, AND EXPERIMENTAL INVESTIGATION OF ADDITIVELY MANUFACTURED COMMUNICATING MICROCHANNELS<sup>4</sup>**

### **5.1 Abstract**

The degree of complexity in internal cooling designs is tied to the capabilities of the manufacturing process. Additive manufacturing grants designers increased freedom while offering adequate reproducibility of micro-sized, unconventional features that can be used to cool the skin of gas turbine components. One such desirable feature can be sourced from nature; a common characteristic of natural transport systems is a network of communicating channels.

In an effort to create an engineered design that utilizes the benefits of those natural systems, the current study presents wavy microchannels that were connected using branches. Two different wavelength baseline configurations were designed, then each were numerically optimized using a commercial adjoint-based method. Three objective functions were posed to (1) minimize pressure loss, (2) maximize heat transfer, and (3) maximize the ratio of heat transfer to pressure loss. All baseline and optimized microchannels were manufactured using Laser Powder Bed Fusion for experimental investigation; pressure loss and heat transfer data were collected over a range of Reynolds numbers.

The additive manufacturing process reproduced the desired optimized geometries faithfully. Surface roughness, however, strongly influenced the experimental results; successful replication of the intended flow and heat transfer performance was tied to the optimized design intent. Even still, certain test coupons yielded performances that correlated well with the simulation results.

### **5.2 Introduction**

As the maturity of advanced manufacturing techniques grows, the heat transfer community is offered an opportunity to develop new, unique cooling designs. In hot section components of a gas turbine engine, those unique designs can find an end use in skin cooling, an inherently challenging technology to produce due to its necessarily small size.

Additive manufacturing (AM) represents a potentially viable method for achieving complex skin cooling schemes. Various metal AM processes exist, all of which are capable of using aerospace grade materials suitable for high temperature applications. Laser Powder Bed Fusion (L-

---

<sup>4</sup> Kirsch, K.L. and Thole, K.A., 2017, "Numerical Optimization, Characterization, and Experimental Investigation of Additively Manufactured Communicating Microchannels", submitted to the ASME Turbo Expo 2018 Conference, June 11-15, 2018, Lillestrøm, Norway

PBF) processes, as one example, can achieve the precision required to produce micro-sized features. Additionally, using techniques such as L-PBF widens the design possibilities.

One source of inspiration for new designs can be found in nature; intricate networks of communicating channels are ubiquitous in biological systems and provide an efficient means of transport. In the current study, a previously-conceived wavy microchannel design [55] was modified to include branches between neighboring channels, creating a complex array through which the cooling air would travel. The implementation of the branches was meant to augment heat transfer by disrupting the boundary layer formation on the primary channels' walls; the angle of the branches was chosen such that the penalty to the pressure loss would be minimized.

Two different variations of the communicating wavy channel design were conceived. Each design was then optimized for a given objective through an adjoint-based shape optimization method [47]. The three objective functions sought to (1) minimize the pressure loss between the channel inlet and exit, (2) maximize the heat transfer on the channel top and bottom endwalls, and (3) maximize the ratio of heat transfer to pressure drop. The baseline and optimized channels were then manufactured using L-PBF and non-destructively evaluated to determine the build success. Lastly, the test coupons were experimentally tested for pressure loss and heat transfer at a range of Reynolds numbers between 2000 and 15000.

### **5.3 Literature Review**

The origin of several aspects of the current study stems from the electronics cooling industry. Wavy channel studies from the literature have widely focused on low Reynolds number applications [8,25,26,37,56]; wavy channels promote mixing in the flow due to the vortical structures they generate, which is beneficial to the heat transfer. However, the pressure drop through wavy channels has been shown to be only marginally higher than that through straight channels [8].

A series of communicating channel studies has also been performed for use in electronics cooling [103–106]. In these studies, straight channels were connected via branches oriented perpendicular to the flow direction. A notable result from one such study by Herman et al. [103] was that an increase in both heat transfer and pressure drop was seen at a low Reynolds number ( $Re=366$ ), when compared to a straight, non-communicating channel. With an increase in Reynolds number ( $Re=593$ ), however, the authors cited higher heat transfer with no further penalty to pressure loss. Singh et al. [8] investigated communicating wavy microchannels in a numerical study and found that the branches increased the heat transfer; the branches were angled at  $45^\circ$  from the flow direction, making them a more aerodynamic feature than the studies in [103–106]. Peng



et al. [107] mimicked the branching structures found in leaf veins, including the porous walls that make up those veins. The porosity in their heat sink proved beneficial to the heat transfer, while exerting minimal influence on the friction factor augmentation.

Weaver et al. [108] studied wavy channels at engine-relevant Reynolds numbers; their concept incorporated a layered design, where the channel waves were derived from the layered weave of the channels. The design achieved uniform distribution of the cooling flow while minimizing both the pressure loss and the required mass flow through the weave. Kirsch and Thole [55,109] also investigated wavy channels at more realistic Reynolds numbers for gas turbine applications and manufactured the channels using L-PBF; in [109], the authors optimized the shape of the wavy microchannels based on the same objectives used in this current study. Experimental results showed that the wavy channels exhibited higher heat transfer than straight channels of the same aspect ratio and spacing [55]. Additionally, the as-built optimized shapes were reproduced fairly well, with the objective to maximize the ratio of heat transfer to pressure loss having yielded a performance akin to the simulation's.

Other studies that have used optimization in conjunction with L-PBF heat exchangers include Dede et al. [72], who used topology optimization, and Arie et al. [110], who performed a multi-objective optimization study. In both cases, the optimized design outperformed the conventional. Several numerical studies exist as well, with the goal of furthering design tools available to heat exchanger designers [66,68,73,111].

As a consequence of any powder bed fusion AM process, large, irregular surface roughness features form on all surfaces [15,16]. Bacchewar [60] identified laser power as the strongest contributor to surface roughness on downward facing surfaces, or surfaces that are unsupported by solid material. The build direction also has a heavy influence on the roughness features that form inside of a part [15,29,95], as well as the ability to reproduce a certain shape accurately [15,95]. Part placement and inert gas flow have also been found to influence the roughness [13,112], as have the laser scan speed and the hatch distance [27,58].

In the case of heat exchangers, surface finish has a large impact on the pressure loss and heat transfer. Wong et al. [35] and Ventola et al. [34] produced AM heat exchangers and found that the surface roughness positively influenced the heat transfer; the AM surfaces were all external flow features. Stimpson et al. [16] and Snyder et al. [15] found that the surface roughness in their internal L-PBF channels augmented the heat transfer only to a certain point. Relative roughness, or the size of the roughness features compared to the hydraulic diameter, played a large role in the performance of these microchannels; higher relative roughness more strongly affected the friction factor than the heat transfer. In fact, beyond a friction factor augmentation of four, surface

roughness no longer served to increase the heat transfer, a finding that confirmed results from Norris [33].

Part shrinkage or warpage can distort AM part features or cause the final dimensions to vary from the design intent. Ning et al. [28] found that parts less than 3 mm in size were susceptible to shrinkage up to 10% of the part's design dimensions. For this reason, properly characterizing the final part is a necessary step in analyzing the performance of AM parts. Computed X-Ray Tomography (CT) scans are a common method for determining internal features because the method is non-destructive and is capable of resolving large roughness features [15,16,55,61,62].

Effectively taking advantage of the open design space offered by AM requires thinking outside the conventional designs for heat exchangers [62,113]. The current study is unique in that it combines a conventional cooling channel design with an idea derived from transport systems in nature. Further, these baseline designs have been numerically optimized, thereby taking advantage of advanced, commercially-available design tools. The branches between the wavy channels create an intricate array of communicating cooling channels aimed to increase the heat transfer without substantially increasing the pressure loss.

#### **5.4 Channel Design**

The wavy channels were created by sweeping a rectangle along a path created using  $45^\circ$  arcs; each period in the channel contained four such arcs, whose edge tangents were equal. Figure 5-1 shows the design of the communicating channels. The white space is the channel area, while the gray represents the walls. The four  $45^\circ$  arcs in one wave period are shown, along with the branch angle, which was also at  $45^\circ$  to the tangent at the peak or trough of the channel wave.

The width of the channels was twice the width of the branches. The inlet to the branches was filleted to minimize losses while the exit of the branches was meant to encourage the flow to penetrate into the neighboring channel. The baseline designs were characterized by the ratio of their wavelength,  $\lambda$ , to the entire test coupon length,  $L$ . Two ratios were chosen for this study:  $\lambda=0.1L$  and  $\lambda=0.4L$ . The length of the coupon was such that 10 periods of the  $\lambda=0.1L$  case fit in the streamwise dimension of the coupon, while 2.5 periods were present in the  $\lambda=0.4L$  case.

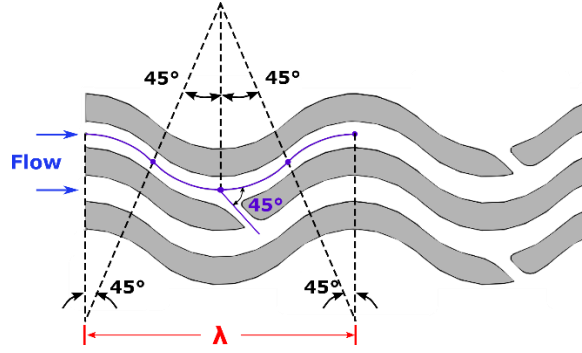


Figure 5-1. Depiction of communicating wavy channel design. The branches repeated every other period in the streamwise direction and every other channel in the spanwise direction. Flow goes left to right.

Figure 5-2 shows four channels for each case; white space represents the channel, while the gray color illustrates the walls. The branches repeated every other period in the streamwise direction and every other channel in the spanwise direction; this alternating pattern can be seen in Figure 5-2. A total of twenty channels fit in the spanwise dimension of the test coupon for the  $\lambda=0.1L$  case, while the test coupon for the  $\lambda=0.4L$  case contained eighteen channels. Spacing between the channels was two channel hydraulic diameters,  $D_h$ .

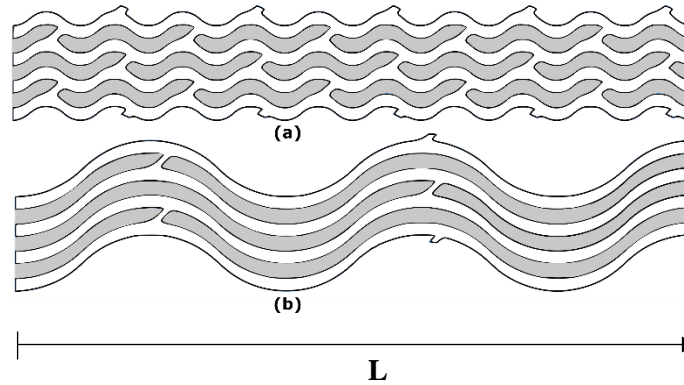


Figure 5-2. Two variations in baseline communicating wavy channel design. (a)  $\lambda=0.1L$ ; (b)  $\lambda=0.4L$ . Flow goes left to right.

## 5.5 Numerical Setup

The optimization portion of this study was reliant upon the results from an initial simulation of each baseline configuration. A high quality, wall-resolved, structured mesh of the fluid domain was created [48], which contained two neighboring channels with their corresponding branches. Only the fluid domains were modeled. To solve the steady RANS and energy equations, the realizable  $k-\epsilon$  turbulence model was chosen [47]; the boundary conditions in the model were set for a Reynolds number of 5000, and mimicked those from the experimental setup. Both the mesh and select boundary conditions are shown in Figure 5-3. Heat was introduced into the system from a

constant temperature boundary condition imposed on the top and bottom endwalls (not shown in Figure 5-3).

Each mesh contained 2.1 million cells, and the  $y^+$  values remained near or below one over the entire length of the domain, as is appropriate for the sublayer resolved turbulence model used. A grid-sensitivity study was performed on a similar geometry in a previous study [55]; doubling the number of cells in the mesh resulted in a -0.1% difference in friction factor, and a -0.1% difference in Nusselt number.

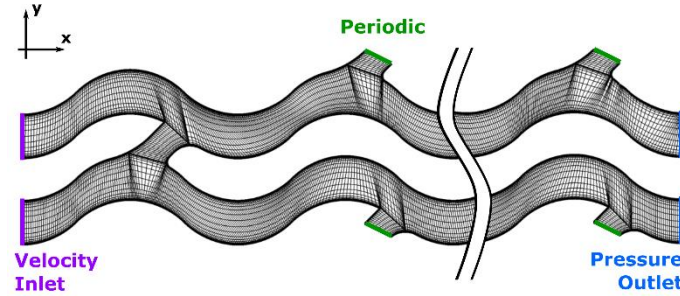


Figure 5-3. Top-down view at 50% channel height of wall-resolved, structured mesh for the  $\lambda=0.1L$  case.

#### *Adjoint-Based Shape Optimization*

The converged solutions to the steady RANS and energy equations provided input for the subsequent optimization analysis. Embedded within the flow solver [47] was a tool to perform a sensitivity analysis, which was equipped to inform shape change. The sensitivity analysis was accomplished using an adjoint method, whose computational efficiency is epitomized by its handling of numerous degrees of freedom. A full mathematical description of the adjoint method is given in Kirsch and Thole [109], but a brief description will be given here.

Three different objective functions were imposed on each of the baseline designs. The objective functions are denoted as  $J$ , and are shown in Equations 5-1a-c. The third objective function reflects a commonly-used performance factor in internal cooling studies [114].

$$J_1 = \min(\Delta P) \quad \text{5-1a}$$

$$J_2 = \max(Q) \quad \text{5-1b}$$

$$J_3 = \max(Q/\Delta P^{1/3}) \quad \text{5-1c}$$

The adjoint approach introduces a set of equations, known as the adjoint equations, to be solved to convergence, much like the governing equations for a flow simulation. Contained within the adjoint equations is the relation between the governing equations and the chosen objective function for a given flowfield. The results from the converged adjoint equations can be used to

determine the sensitivity of the design variables on the objective function. In the current study, each one of the nodes in the computational mesh represented a design variable.

Based on the results of the sensitivity analysis, the shape of the geometry at hand can be changed such that the most sensitive nodes are moved in an advantageous direction. The user defines the degree to which the shape is changed. The software [47] then morphs the mesh to reflect this shape change and ensures that the quality of the mesh remains the same as the original; additionally,  $y^+$  values from subsequent flow solutions are generally unaffected.

One design iteration encompasses running the flow solver, running the adjoint solver, and morphing the mesh. Design iterations continue until either no further changes to the shape are suggested, or the flow solution no longer converges given the latest shape change. In the current study, between five and ten design iterations were needed to reach the optimized result in the simulations. Constraints were imposed on the overall length of the channels such that they would fit into the same coupon dimensions. Additionally, the periodic boundary conditions for the branches were required to change in the same manner. However, beyond these constraints, all mesh nodes represented a degree of freedom, and the resulting shape changes were complex and aperiodic.

## 5.6 Numerical Results

All three objective functions for both wavelengths were achieved. While no specific target was set, each of the optimized observables differed from the baseline's accordingly. Table 5-1 and Table 5-2 show the change in the observables of interest relative to the respective baseline configurations for the  $\lambda=0.1L$  and  $\lambda=0.4L$  cases, respectively. Bolded values in the two tables showcase the end result of the target observable, while the other two observables are shown for comparison.

**Table 5-1. Changes in  $\Delta P$ ,  $Q$ , and  $Q/\Delta P^{1/3}$  relative to  $\lambda=0.1L$  Baseline**

	$\Delta P$	$Q$	$Q/\Delta P^{1/3}$
$J_1=\min(\Delta P)$	<b>-4.4%</b>	-3.9%	-2.5%
$J_2=\max(Q)$	+6.6%	<b>+6.6%</b>	+4.3%
$J_3=\max(Q/\Delta P^{1/3})$	+0.4%	+1.92%	<b>+1.8%</b>

**Table 5-2. Changes in  $\Delta P$ ,  $Q$ , and  $Q/\Delta P^{1/3}$  relative to  $\lambda=0.4L$  Baseline**

	$\Delta P$	$Q$	$Q/\Delta P^{1/3}$
$J_1=\min(\Delta P)$	<b>-3.2%</b>	+0.2%	+1.3%
$J_2=\max(Q)$	+11.7%	<b>+11.7%</b>	+6.6%
$J_3=\max(Q/\Delta P^{1/3})$	+3.3%	+3.8%	<b>+2.7%</b>

The majority of shape changes occurred in areas surrounding the branches. Figure 5-4 shows three zoomed-in locations from a top-down view of the channel outlines at 50% channel height. At the top of the figure is a top-down view of the entire channel length; the three locations of the zoomed-in images are outlined in bold rectangles. The walls are colored gray, and are colored based on the outline of the baseline geometry. Outlines of the optimized channels cutting through gray color, therefore, show that the channel area has expanded relative to the baseline, while any outlines in the white area (fluid domain) represent a contraction relative to the baseline.

A cursory glance at Figure 5-4 reveals a marked difference between the outlines of the  $J_1$  objective to minimize pressure loss and the two objectives with heat transfer as an observable,  $J_2$  and  $J_3$ . In general, where the walls of the objective to minimize pressure loss moved outward, the walls of the other two objectives moved inward, and vice versa. In specifically looking at the outline of the  $J_1$  objective in Figure 5-4c, the angle of the branch exit shifted closer to the direction of flow, and the opposite wall bowed outward slightly. This shape change served to decrease fluid momentum, and thus, reduced the extent to which fluid from the branches penetrated the neighboring channels. For scale, certain wall movements are shown with their deviation from the CAD model.

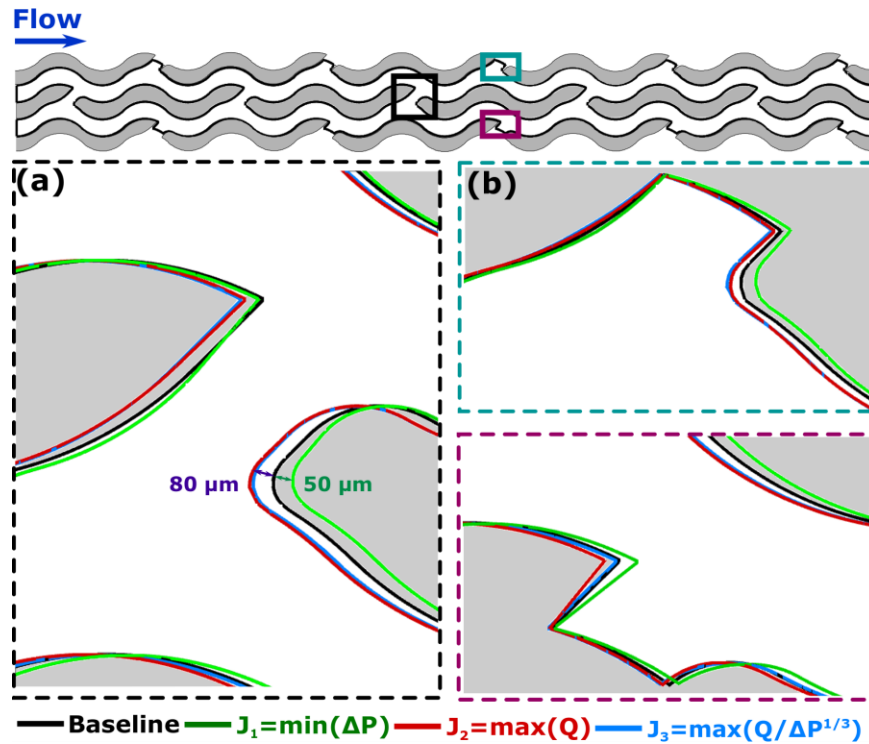


Figure 5-4. Channel wall outlines from a top-down view at 50% channel height for  $\lambda=0.1L$  baseline and optimized shapes. The gray color shows the location of the walls for the baseline case. (a) Zoomed-in view of middle branch, (b) and (c) zoomed-in view of branches subject to the periodic boundary condition.

Evidence for this claim can be seen in Figure 5-5, which shows normalized axial velocity contours from each of the baseline and optimized configurations; the slice location is immediately following the branch exit highlighted in Figure 5-4c. The  $J_1$  objective shows the lowest normalized velocity across the entire width of the channel. Perhaps most notably, the normalized velocity on the leeward wall (left wall, from the reader's point of view) is only marginally higher than the mean velocity,  $U_m$ . This result suggests that fluid from the branches barely penetrated to the far wall, an assuredly intended consequence of the shape changes in the channels and branches. By contrast, the baseline,  $J_2$ , and  $J_3$  cases all showed high normalized velocity on both the windward and leeward walls, thus validating the original design intent to enable jet formation.

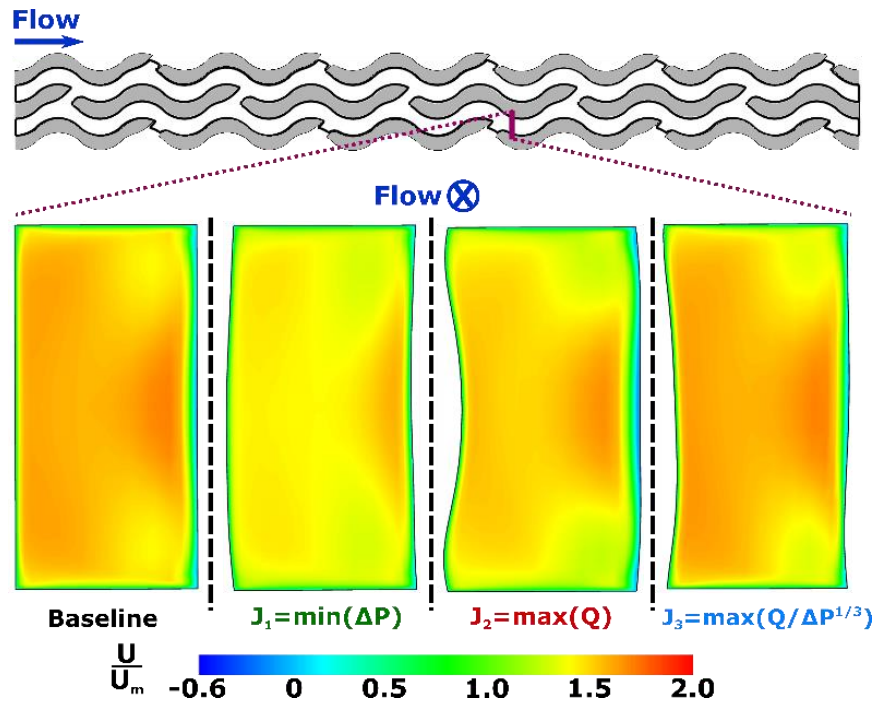


Figure 5-5. Contours of normalized axial velocity at one slice location, immediately after the branch exit shown in Figure 5-4c.

Moving slightly downstream from Figure 5-5, Figure 5-6 shows non-dimensional temperature contours, with secondary velocity vectors overlaid, at the trough of the wave. Immediately visible in Figure 5-6 for the baseline,  $J_2$ , and  $J_3$  cases are the presence of Dean vortices, flow features that are commonly found in wavy channels due to the centripetal forces experienced by the fluid particles [8,50]. To note, Kirsch and Thole [109] found no such vortical formation in the baseline design of the non-communicating  $\lambda=0.1L$  wavy microchannels; insufficient flow development length was posited to explain the absence of the Dean vortices. The introduction of the branches in the current study, however, appeared to have increased the fluid momentum enough to form the characteristic vortical pattern.

Given the velocity contour of the  $J_1$  objective function in Figure 5-5, the lack of fully formed vortical structures in the  $J_1$  slice in Figure 5-6 is unsurprising. The secondary flows present in the  $J_1$  slice are weaker than those seen for any of the three other geometries. The shape changes that prevented jet-like flow from the branches led to the inability of Dean vortices to form. These observations in flow patterns are consistent with the overall numerical results (Table 5-1), which showed a 4.4% decrease in pressure loss from the  $J_1$  objective relative to the baseline.

Contours of non-dimensional temperature also support the findings from the objective to maximize heat transfer shown in Table 5-1: the highest non-dimensional temperature can be seen in the  $J_2$  slice in Figure 5-6, especially at the channel mid-height. The vortices are strongest in the  $J_2$  slice, confirming that the stronger vortices are more effective at removing heat from the channel endwalls.

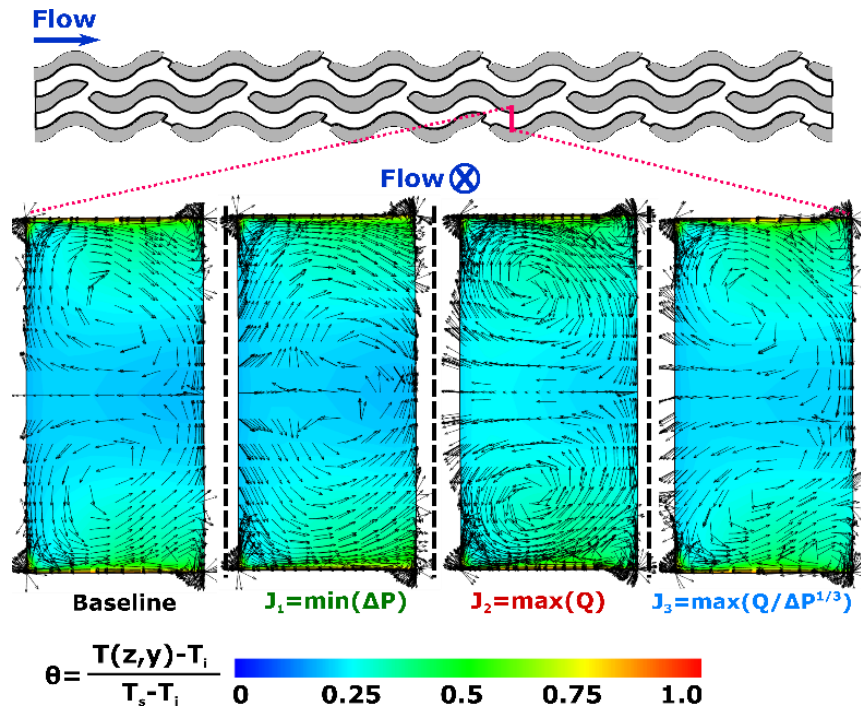


Figure 5-6. Contours of non-dimensional temperature with secondary velocity vectors overlaid.

Figure 5-7 presents the outlines of the baseline and optimized channels for the  $\lambda=0.4L$  configuration in a similar manner to Figure 5-4; the channel outlines were taken at 50% the channel height, and the gray color illustrates the walls, while the white color is the fluid domain. The walls are again colored to the edge of the baseline design.

Striking differences between the optimized and baseline branch locations can be seen in Figure 5-7, most notably in Figure 5-7a. To note, the outlines of the optimized branches do not reflect a translation of the branch locations; instead, the outlines show how far the branch had arched at the channel mid-height. At the top and bottom endwalls, all four cases' branch locations



matched. Where heat transfer was to be maximized ( $J_2$  and  $J_3$  objective functions), the branch shape at 50% channel height jutted forward, in the direction of the channel inlet. By contrast, the mid-height branch shape for the objective to minimize pressure loss ( $J_1$ ) extended aft. This behavior strongly affected the interaction between flow emanating from the branches and the main channel flow.

Slightly downstream of the branch location highlighted in Figure 5-7a came further notable shape changes. The location of the slices shown in Figure 5-8 was taken to be where the radius of curvature in the wave design switched signs (Figure 5-1). The slices are shown with contours of normalized axial velocity. Figure 5-8 reveals stark differences in the patterns of the shape changes; objective functions  $J_2$  and  $J_3$  showed a sharp inward bow of the leeward wall, whereas the leeward wall of the  $J_1$  objective function bowed outward. Additionally, the contour levels in each of the slices varied among the objectives. The arched nature of the branch shapes, along with the shape changes downstream of the branches, either encouraged ( $J_2$  and  $J_3$  objectives) or suppressed ( $J_1$  objective) the intended jet formation.

The downstream effect of the jet penetration (or lack thereof) can be seen in Figure 5-9, where non-dimensional temperature contours are shown for a slice location at the trough of the channel; secondary velocity vectors are overlaid. For the  $J_2$  and  $J_3$  objectives, where a windward bend in channel shape resulted in higher normalized axial velocity (seen in Figure 5-8), Figure 5-9 shows characteristic Dean vortex formation. Additionally, non-dimensional temperature is visibly higher on the windward (right side from the reader's point of view) walls of the  $J_2$  and  $J_3$  objectives than for either the baseline or  $J_1$  cases.

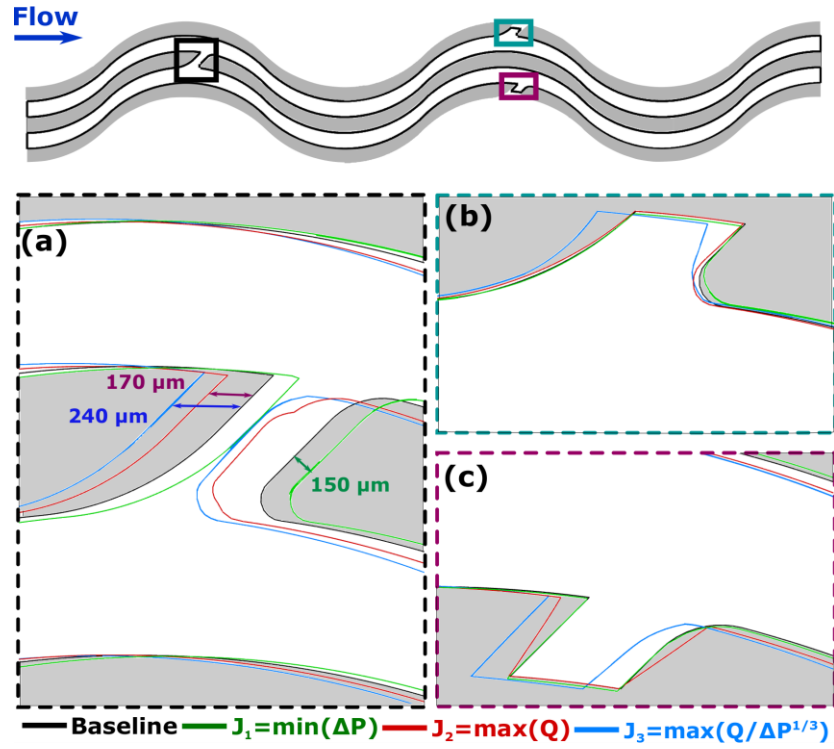


Figure 5-7. Channel wall outlines from a top-down view at 50% channel height for  $\lambda=0.4L$  baseline and optimized shapes. The gray color shows the location of the walls for the baseline case. (a) Zoomed-in view of middle branch, (b) and (c) zoomed-in view of branches subject to the periodic boundary condition.

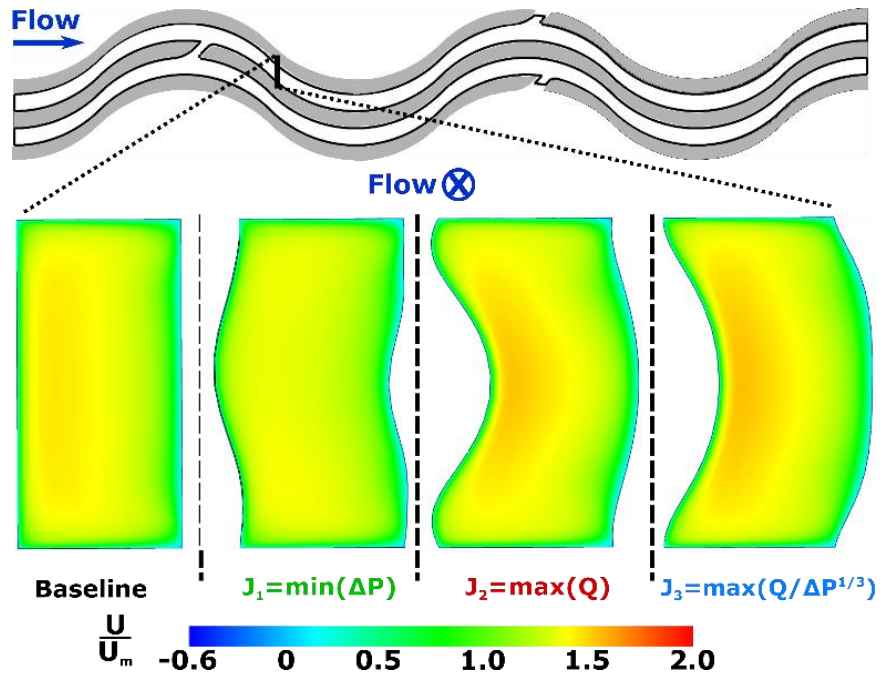


Figure 5-8. Contours of normalized axial velocity at one slice location.

By contrast, no vortical structures were seen in the slice for the  $J_1$  objective; expanding the leeward wall at the location highlighted in Figure 5-8 lowered the fluid momentum, which resulted in a lack of vortex formation in the channel trough. The vector patterns in Figure 5-9 support the results shown in Table 5-2. Pressure loss was decreased for the  $J_1$  case relative to the baseline by 3.2%, due most likely to the lack of Dean vortices, while heat transfer was increased by 11.7% and 3.8%, respectively, in both the  $J_2$  and  $J_3$  cases due to increased fluid mixing.

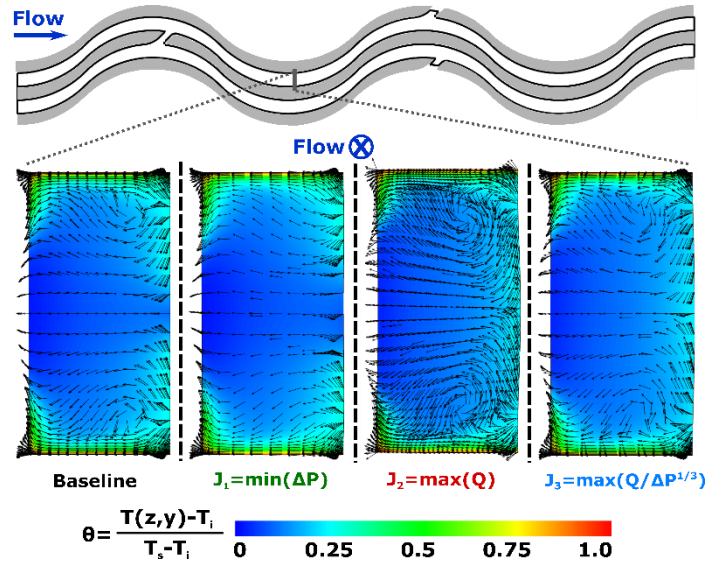


Figure 5-9. Contours of non-dimensional temperature with velocity vectors overlaid.

The intent of the communicating nature of the microchannels was to increase the heat transfer while mitigating any increase in the frictional losses. As such, the communicating channel simulation results can be compared to the simulation results from the non-communicating channels [109]. Table 5-3 shows the difference in  $\Delta P$  and  $Q$  between the communicating wavy channels relative to their respective non-communicating counterpart. In general, the design intent was successful. For both cases, the benefit to heat transfer outweighed the detriment to pressure loss. Further exploration into the differences between communicating and non-communicating channels will occur in the experimental results section.

Table 5-3. Changes in  $\Delta P$  and  $Q$  relative to non-communicating channels

	$\lambda=0.1L$		$\lambda=0.4L$	
	$\Delta P$	$Q$	$\Delta P$	$Q$
$J_1=\min(\Delta P)$	-4%	+5%	-3%	+2%
$J_2=\max(Q)$	+7%	+16%	+12%	+13%
$J_3=\max(Q/\Delta P^{1/3})$	+0.4%	+11%	+3%	+6%

## 5.7 Geometric Characterization

Once the optimization analysis was complete, each set of channels was duplicated to fit into a test coupon for experimentation. Each coupon was manufactured using L-PBF [41] with Inconel 718 powder, and were built layerwise at a  $45^\circ$  angle to the build plate. The machine specifications were set to the default for Inconel 718 [45]. Figure 5-10 shows two views of the same coupon on the build plate, with one view looking into the flow direction and another looking at the front face of the test coupon. Pertinent dimensions are given for scale. Support structures were located on the coupon flanges, as well as the downward-facing sidewall of the test coupon itself.

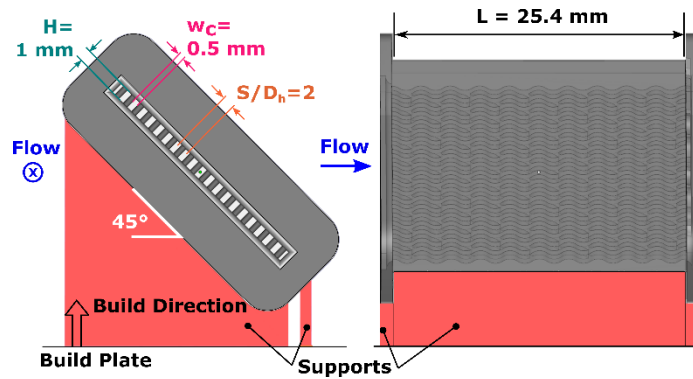


Figure 5-10. Coupon orientation on the build plate. On the left view, flow is into the page; on the right view, flow is left to right.

Once the build was complete, the parts were heat treated to remove any residual stresses that accumulated during the build process. The parts were then removed from the build plate using a wire electro-discharge machine, and any other remaining support pieces were manually removed from the parts. The flange surfaces of the test coupons were smoothed to ensure good contact between the coupon and test section, but all other surfaces remained untouched.

A critical step in analyzing the experimental results lies in measuring the internal channel dimensions. Non-destructive evaluation of the test coupons was accomplished using CT scans, which allowed for a voxel size (resolution) of  $35\text{ }\mu\text{m}$ . Analysis of the CT scan data can be performed in a similar manner to the numerical results analysis, by visualizing 2D slices of the as-built test coupon.

Figure 5-11 shows a top-down view at 50% channel height of the as-built baseline and optimized channels. The format of Figure 5-11 mimics that of Figure 5-4, with all three zoomed-in locations in Figure 5-11 matching those from Figure 5-4. Additionally, for reference, a dotted line showing the intended baseline design is included, as is one key dimension for scale.

A few notable features in Figure 5-11 stand out, perhaps the first of which is the large protrusion in the  $J_2$  outline (red) seen at location (a), in addition to the smaller protrusions visible

at location (c). These protrusions are roughness elements, a natural consequence of the L-PBF process. These roughness elements can extend into the flow as far as 25% of the channel width, and are highly irregular; as such, comparable protrusions are seen across all four cases, most especially on unsupported surfaces. The unsupported surfaces can be identified in Figure 5-11 by any outlines that are jagged in nature. By contrast, smooth outlines indicate a supported surface.

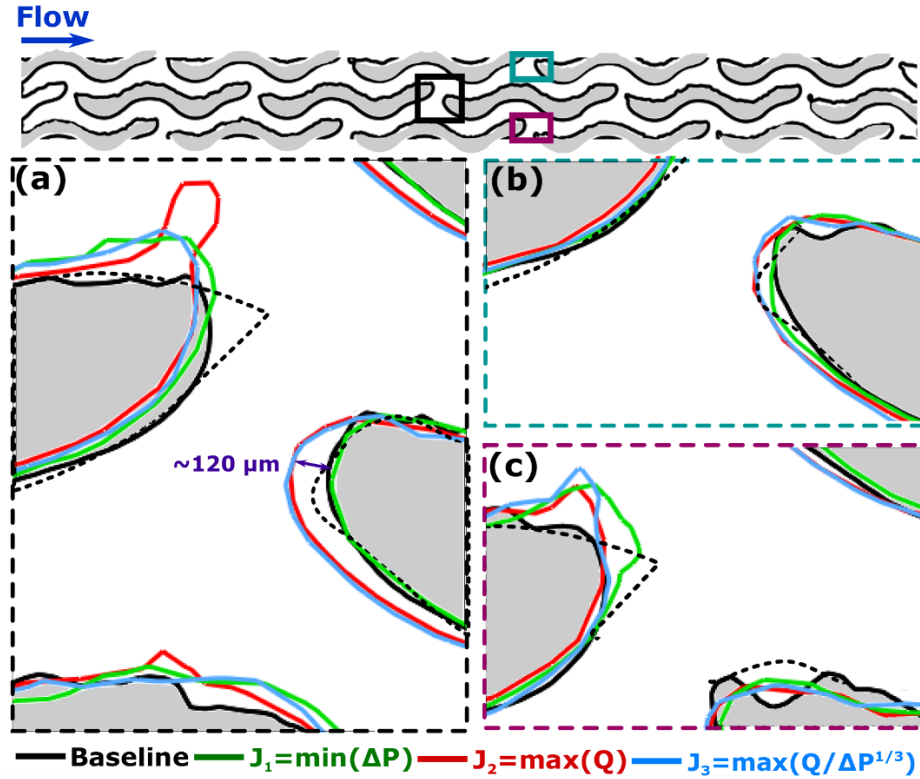


Figure 5-11. Channel wall outlines from a top-down view at 50% channel height for the as-built  $\lambda=0.1\text{L}$  baseline and optimized shapes. The gray color shows the location of the walls for the baseline case. The dotted lines show the intended baseline design for comparison. (a) Zoomed-in view of a middle branch, same location as in Figure 5-4a, (b) and (c) zoomed-in view of branches at same locations as in Figure 5-4b and c.

A second notable feature in Figure 5-11 can be seen in the inability of the L-PBF process to reproduce the branch feature designed to encourage jet penetration. Specifically at locations (a) and (c), the dotted line depicting the intended baseline design lies isolated from the as-built outlines, and extends farther into the channel than any of the as-built channels. Due to the chosen build direction, this particular design feature was unsupported and, because of its small size, did not build properly. Given the complicated nature of these channel designs, however, no one build direction could have fully supported all internal features.

The dimension emphasized in Figure 5-11 highlights the capability of the L-PBF process to produce the intended inward bow in the  $J_2$  and  $J_3$  objectives. As shown in Figure 5-4, the intended geometric feature was to bow inward by approximately  $80\text{ }\mu\text{m}$ ; the as-built dimension was closer

to 120  $\mu\text{m}$ . By contrast, the outward bow intended in the  $J_1$  design was not successfully reproduced. Figure 5-4 shows that the difference between outlines of the baseline and  $J_1$  objective was to be around 50  $\mu\text{m}$  at 50% channel height. Such a deviation was not enough to be captured by the L-PBF process faithfully.

A number of other design intentions, however, were also successfully reproduced in the build. For example, the optimizer created a slight contraction in flow area in the branch for the  $J_2$  and  $J_3$  objectives (Figure 5-4a), and indeed, the as-built branch outlines for the  $J_2$  and  $J_3$  objectives followed suit (Figure 5-11a). By contrast, the intended feature for the location (b) shows a similar trend in branch flow area. Additionally, the main channel flow area was to contract where the fluid exited the branch and entered the main channel for objectives  $J_2$  and  $J_3$  (Figure 5-4a), a behavior that was also reproduced in the as-built channels (Figure 5-11a).

Figure 5-12 shows select CT scan results for the  $\lambda=0.4L$  case, presented in the same manner as Figure 5-11; all locations outlined in Figure 5-12 are the same as those highlighted in Figure 5-7. The outlines of the baseline intended designs are also included for reference and are shown in dotted lines in the figure. The outlines of the baseline intended designs are also included for reference and are shown in dotted lines in the figure; notable deviations of the optimized designs from the baseline are quantified as well.

Much like Figure 5-11, Figure 5-12 shows large roughness features that formed on the unsupported surfaces in the channels. Especially visible at locations (a) and (c), these roughness features are concentrated near the branch feature intended to encourage jet penetration. Just as for the  $\lambda=0.1L$  case, this small feature was not built successfully because it was unsupported throughout the build.

However, the general geometric trends seen in Figure 5-7 were largely reproduced in the as-built test coupons. In the case of the  $J_3$  objective, the L-PBF channels showed the most significant deviation from the baseline L-PBF channel, as was the intent; at all three highlighted locations, the channel bowed sharply toward the inlet. Similarly, for objectives  $J_2$  and  $J_3$ , the main channel was to contract in area where the fluid exited the branch. Such a characteristic is seen in Figure 5-12 at locations (a) and (c).

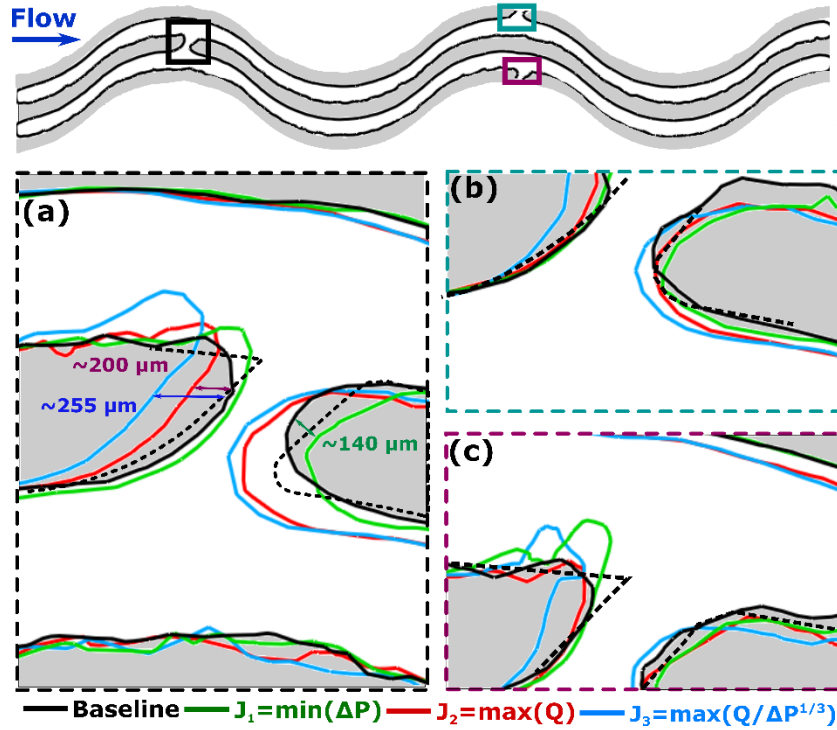


Figure 5-12. Channel wall outlines from a top-down view at 50% channel height for the as-built  $\lambda=0.4\text{L}$  baseline and optimized shapes. The gray color shows the location of the walls for the baseline case. The dotted lines show the intended baseline design for comparison. (a) Zoomed-in view of a middle branch, same location as in Figure 5-7a, (b) and (c) zoomed-in view of branches at same locations as in Figure 5-7b and c.

The CT scan data were also used to quantify the as-built channel dimensions. An in-house code was written to analyze 2D slices of the L-PBF coupons sweeping through the coupon in the axial dimension; the cross-sectional area and perimeter were calculated, which were then used to calculate a hydraulic diameter. To achieve a meaningful comparison among all baseline and optimized channels, the dimensions used in the subsequent results analyses were measured using the CT scan data at the entrance to each of the channels. As such, dimensions given in Table 5-4 and Table 5-5 are for the entrance to each of the channels. For comparison, data from Kirsch et al. [14] are included as well, denoted as ‘isolated.’ In general, the communicating channels built to within 10% of the intended dimensions.

Table 5-4. Inlet dimensions of the CAD and as-built channels for  $\lambda=0.1\text{L}$

	Communicating		Isolated [109]		CAD	
	$A_c (\text{mm}^2)$	$D_h (\text{mm})$	$A_c (\text{mm}^2)$	$D_h (\text{mm})$	$A_c (\text{mm}^2)$	$D_h (\text{mm})$
Baseline	0.5	0.63	0.43	0.62	0.52	0.68
$J_1 [\min(\Delta P)]$	0.48	0.63	0.43	0.62		
$J_2 [\max(Q)]$	0.5	0.64	0.44	0.61		
$J_3 [\max(Q/\Delta P^{1/3})]$	0.46	0.62	0.44	0.62		

Table 5-5. Inlet dimensions of the CAD and as-built channels for  $\lambda=0.4L$

	Communicating		Isolated [109]		CAD	
	$A_c$ (mm <sup>2</sup> )	$D_h$ (mm)	$A_c$ (mm <sup>2</sup> )	$D_h$ (mm)	$A_c$ (mm <sup>2</sup> )	$D_h$ (mm)
Baseline	0.54	0.68	0.43	0.67	0.52	0.68
$J_1$ [min( $\Delta P$ )]	0.54	0.69	0.44	0.65		
$J_2$ [max( $Q$ )]	0.55	0.69	0.44	0.65		
$J_3$ [max( $Q/\Delta P^{1/3}$ )]	0.52	0.68	0.44	0.65		

## 5.8 Experimental Setup

All pressure loss and heat transfer experiments were performed on a bench-top rig, using air as the working fluid; Figure 5-13 shows a cross-section of the facility, which has been used in numerous previous studies [15,16,43,55,109]. Flow into the rig was controlled using a commercial mass flow controller [76]. The inlet to test section was pressurized, and was held at a constant pressure over the range of Reynolds numbers of interest in this study. A needle valve downstream of the test coupon was adjusted to achieve the different Reynolds numbers, while maintaining the inlet pressure.

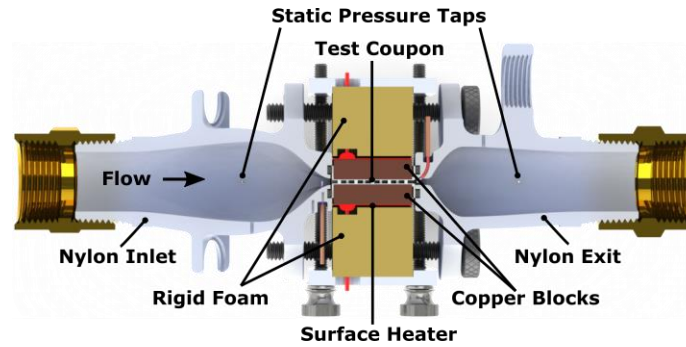


Figure 5-13. Experimental test rig for flow and heat transfer measurements

Static pressure taps were located upstream of the nylon inlet contraction and downstream of the nylon exit contraction to measure the pressure drop across each test coupon. The fluid velocity was calculated by using the inlet cross-sectional area calculated from the CT scans, along with the calculated fluid density and measured mass flow rate. Channel length was taken to be the length that the fluid traveled, taking into account the wavy nature of the channels.

For heat transfer tests, a copper block was adhered to the test coupon faces using a high thermal conductivity paste. The copper block was heated through the use of a resistive surface heater connected to power supplies. Thermocouples were located in the copper blocks, as well as throughout the test section to quantify conduction losses. To calculate the test coupon surface temperature, a one dimensional conduction analysis was performed.



Heat transfer was calculated using two different methods. The first took the total heat into the system, less the conduction losses, as the net heat input. The second method was the result of an energy balance, using thermocouples at the inlet and exit of the test coupon. The two methods agreed to within 11% of each other.

#### *Experimental Uncertainty*

Experimental uncertainty was evaluated using the methods proposed by Kline and McClintock [46]. In the flow tests, the pressure transducers used to measure the pressure drop across the coupons governed the uncertainty. For Reynolds numbers above 4000, the overall uncertainty was below 7%, while for Reynolds numbers below 4000, the overall uncertainty was below 9%. Repeatability among tests, however, was between 1.5% and 2% for all Reynolds numbers.

Calculation of the test coupon surface temperature introduced the largest source of uncertainty in the heat transfer tests. The one dimensional conduction analysis used to calculate the surface temperature takes into consideration the thickness of the copper block and the thickness of the paste adhering the block to the coupon; the measurement of the thin layer of paste contributed the most to the heat transfer calculations. Nusselt number overall uncertainty, therefore, was below 6% for all coupons, with precision uncertainty below 3%.

### **5.9 Results and Discussion**

Experimental results will be presented first in terms of friction factor augmentation, then in terms of Nusselt number augmentation. The Colebrook equation [98] will be used for the smooth, empty duct friction factor,  $f_0$ , whereas the Gnielinski correlation [51] will be used for the empty duct Nusselt number,  $Nu_0$ . Where applicable, results from the numerical simulations will be included, as will experimental results from Kirsch and Thole [109]. All experimental data were analyzed using the channel inlet hydraulic diameter and cross-sectional area measured from the CT scan data.

#### *Pressure Loss Test Results*

Figure 5-14 shows friction factor augmentation for the communicating  $\lambda=0.1L$  case. Markers for the experimental results are labeled 'AM,' while the numerical results are labeled as 'k- $\epsilon$ .' The trend in experimental data is upward because flow through the microchannels reaches the fully rough flow regime [109], where friction factor no longer changes as Reynolds number increases; the baseline friction factor,  $f_0$ , however, continues to decrease with increases in Reynolds number.

Immediately apparent in Figure 5-14 is the difference in magnitude of friction factor augmentation between the numerical and experimental results. This difference can be attributed to the high surface roughness in the channels, which was not modeled in the simulation. Additionally, the spread of data across the experimental results is wider than that for the numerical results.

The objectives to minimize pressure loss ( $J_1$  objective) and to maximize heat transfer ( $J_2$  objective) exhibited analogous performance to the numerical predictions. In the  $J_1$  case, the shape changes sought to decrease the fluid momentum and thus, decreased the propensity for jet-like flow from the branches into the channels. Such shape changes translated well to the physical domain; the L-PBF process was able to reproduce these nuanced shape changes successfully, as evidenced by the results in Figure 5-14. Additionally, as observed in Figure 5-11, the branch feature that was designed to encourage jet penetration did not build exactly as intended. The lack of jet penetration, therefore, may have furthered the optimizer's intent to decrease pressure loss. Similarly, in the  $J_2$  case, the goal of the geometric changes was to increase the fluid velocity in the branches, thereby creating stronger jets to enter the main channels. Despite not closely replicating the intended branch geometry, other shape changes in the channels sought to encourage Dean vortex formation in the main channels. Therefore, as expected, the friction factor augmentation from the  $J_2$  case was higher than that from the baseline.

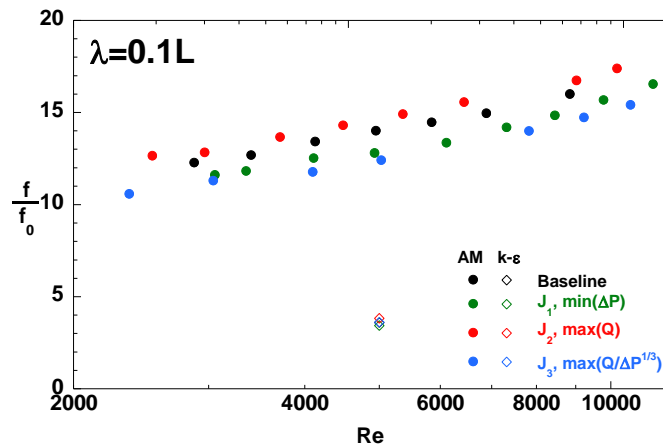


Figure 5-14. Friction factor augmentation versus Reynolds number for the  $\lambda=0.1L$  case.

On the other hand, the shape changes that occurred for the  $J_3$  case created weaker vortical structures than in the  $J_2$  case (Figure 5-6). Such a design intent, coupled with the as-built branch shape, may explain the results from the  $J_3$  objective, which deviated from the expected: the friction factor augmentation for the  $J_3$  objective was the lowest among all cases (Figure 5-14).

Figure 5-15 shows friction factor augmentation for the  $\lambda=0.4L$  case, and also includes both experimental and numerical results. A similar disparity existed between the magnitude of friction

factor augmentation in the experimental and numerical results for the  $\lambda=0.4L$  case as did for the  $\lambda=0.1L$  case. Additionally, the augmentation values varied greatly across the experimental results, whereas limited variation was seen for the numerical results. These differences can be explained by the high surface roughness in the L-PBF microchannels, which was not accounted for in the simulation.

The lowest friction factor augmentation values were seen for the baseline case in Figure 5-15. Even where pressure drop was to be minimized, in the  $J_1$  objective, the friction factor augmentation exceeded its non-optimized counterpart. As was seen in the Numerical Results section, the shape changes for the  $\lambda=0.4L$  design were considerable, especially in the branch itself (Figure 5-7). As previously mentioned, in the case of the  $J_1$  objective, the arch of the branch shape in the aft direction lowered the fluid momentum, thereby causing lower fluid velocity downstream (Figure 5-8); the arch was reproduced fairly well in the as-built channels (Figure 5-12).

However, such a shape change also resulted in stronger recirculation zones in the branch itself, specifically near the top and bottom of the channel. Figure 5-16 shows a top-down view at 25% channel height of the baseline and  $J_1$  configurations. The view location is the same as in Figure 5-7a. Secondary velocity vectors are laid atop normalized axial velocity contours to highlight the direction of the flow. For the  $J_1$  objective, the direction of the vectors moving through the branch is noticeably different than the direction of the vectors in the baseline design. Given the friction factor results in Figure 5-15, this recirculation zone is hypothesized to have negatively affected the frictional losses through the coupon. In L-PBF microchannels, where roughness plays a large role in the flow development, the negative effects of this recirculation zone may have been amplified and thus, yielded a higher friction factor augmentation than the baseline.

As predicted, both the  $J_2$  and  $J_3$  objectives also exhibited a higher friction factor augmentation than the baseline design, as seen in Figure 5-15. The shape changes that generated higher velocity in the branches were successfully reproduced in the L-PBF test coupon. The branch shapes, especially, were replicated faithfully (Figure 5-12) and the roughness features most likely enhanced the optimizer's intent.

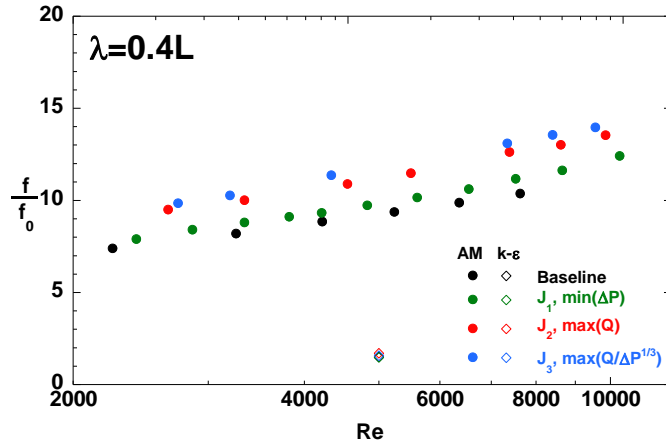


Figure 5-15. Friction factor augmentation versus Reynolds number for the  $\lambda=0.4L$  case.

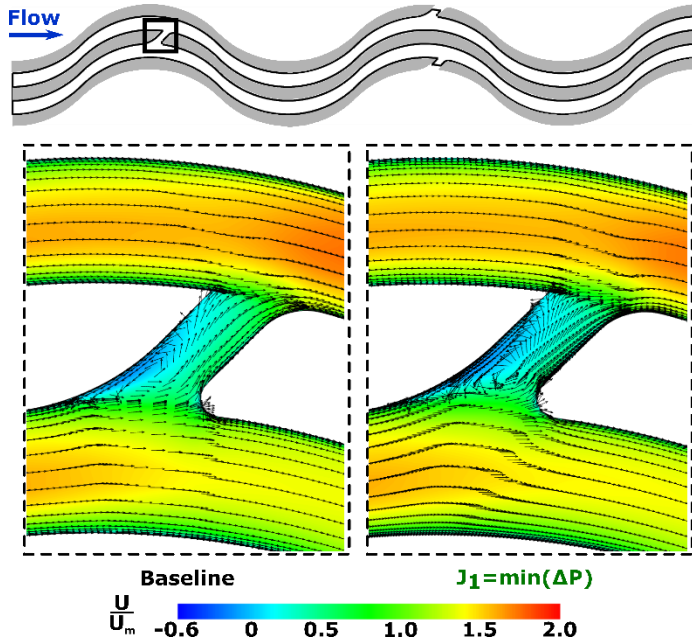


Figure 5-16. Top-down view at 25% channel height of the baseline and  $J_1$  configurations. Contours are normalized axial velocity, with velocity vectors overlaid to highlight flow direction.

### Heat Transfer Results

Much like the friction factor results, heat transfer results will be presented in the form of an augmentation over a smooth baseline channel. Experimental and numerical heat transfer results for the  $\lambda=0.1L$  case are shown in Figure 5-17. Heat transfer performance mimics the friction factor results: the objective to maximize heat transfer ( $J_2$ ) yielded the highest heat transfer augmentation, as was predicted by the simulation. Similarly, the objective to minimize pressure loss ( $J_1$ ) yielded the lowest augmentation values.

Over the Reynolds number range tested, the  $J_2$  objective showed about a 10% increase in heat transfer augmentation over the baseline design, which was slightly higher than expected based on the simulation's prediction (Table 5-1). Given that the shape of the  $J_2$  microchannels were meant to promote jet formation and encourage Dean vortex development, the addition of surface roughness most likely augmented these goals.

A notable result from Figure 5-17 is the heat transfer performance for the  $J_3$  case relative to the  $J_1$  case. Figure 5-14 showed that the  $J_3$  case exhibited lower friction factor augmentation than the  $J_1$  case, which deviated from the expectation, but Figure 5-17 shows similar heat transfer performance between the two geometries. These results suggest that the optimized geometry achieved its goals, at least partially: an attempt to maintain good heat transfer performance did so without a substantial increase in pressure loss.

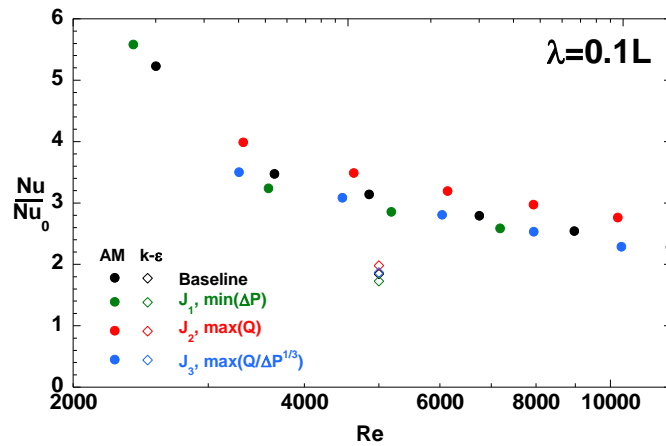


Figure 5-17. Nusselt number augmentation versus Reynolds number for the  $\lambda=0.1L$  case.

Figure 5-18 presents heat transfer augmentation values for the  $\lambda=0.4L$  case, and contains both experimental and numerical results. The heat transfer augmentation for all four L-PBF test coupons was similar; the  $J_1$  objective yielded the lowest heat transfer augmentation, which was to be expected, but the two objectives with heat transfer as the observable yielded results nearly on top of the baseline results. Despite the higher friction factor augmentation seen for the  $J_2$  and  $J_3$  cases in Figure 5-15, the heat transfer performance appeared to be unaffected. The features that were successfully reproduced in the build served less to increase the heat transfer than they did to augment the frictional losses.

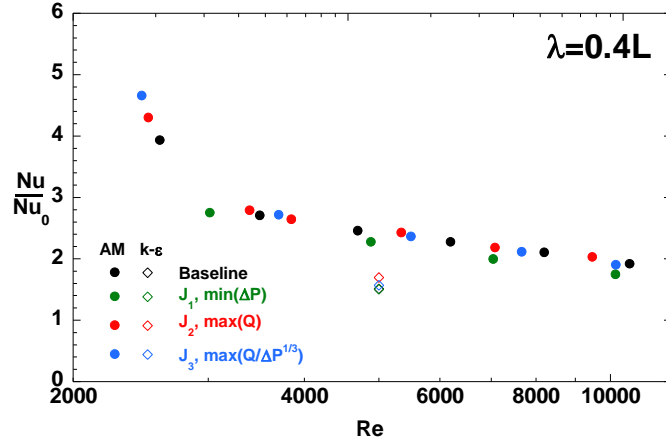


Figure 5-18. Nusselt number augmentation versus Reynolds number for the  $\lambda=0.4L$  case.

### 5.10 Communicating vs. Non-Communicating Channel Performance

To gain a better understanding of how the addition of the branches in wavy microchannels affected performance, we can directly compare the friction factor and heat transfer augmentation between the communicating and non-communicating (isolated) channels from Kirsch and Thole [109]. Figure 5-19 shows the friction factor augmentation versus Nusselt number augmentation at a Reynolds number of 5000 for communicating and non-communicating channels. Data from both wavelengths are included.

The first element of Figure 5-19 that stands out is the notably high friction factor augmentation shown by the  $\lambda=0.1L$  wavy channel with the objective to maximize heat transfer. By contrast, the  $\lambda=0.1L$  communicating case to maximize heat transfer shows a much decreased friction factor augmentation, with a comparable heat transfer augmentation. In the case of the non-communicating channels, the objective to maximize heat transfer was achieved in the simulation by creating large vortical structures in the channels [14]. Given the high surface roughness in the as-manufactured channels, this intended flow feature was enhanced, and, as a consequence, a significant increase in the frictional losses was measured. On the other hand, the objective to maximize heat transfer in the communicating case revolved around encouraging jet penetration from the branches into neighboring channels. While such jet penetration may have been tempered given the results of the as-built channels (Figure 5-11), this design intent incurred less of a penalty to the friction factor, and was less affected by the roughness in channels.

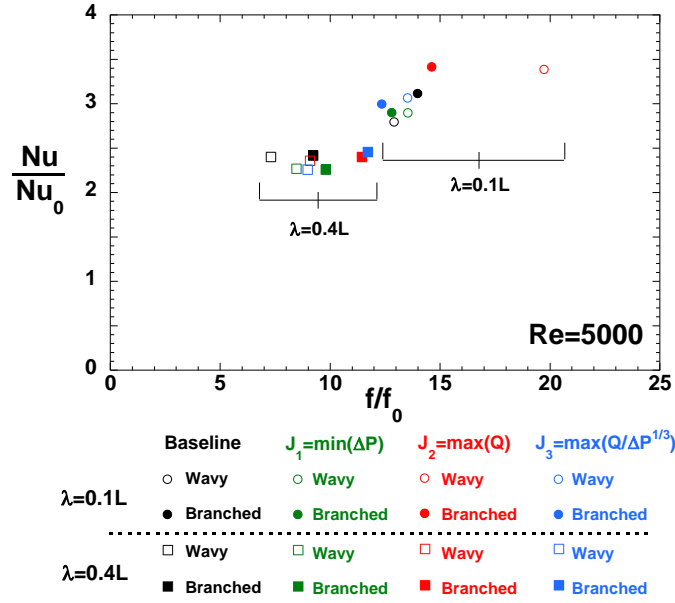


Figure 5-19. Friction factor augmentation vs. Nusselt number augmentation at a Reynolds number of 5000. Open markers indicate data from Kirsch and Thole [109], where microchannels were non-communicating (denoted in legend as ‘wavy’). Closed markers indicate data from the current study (denoted as ‘branched’).

In a similar vein, the objective to minimize pressure loss for the communicating and non-communicating channels yielded differences in terms of the success of the design intent. In the case of the isolated channels, the objective was achieved numerically by reducing the amount of backflow in the channels, which occurred where the radius of curvature switched signs (Figure 5-1) [109]. Due to the surface roughness in the channels, this objective was not achieved experimentally; the  $J_1$  geometry for the wavy case exhibited a higher friction factor augmentation than the baseline. However, the objective to minimize pressure loss in the communicating case was achieved in the as-built microchannels. The design intent revolved around reducing the fluid momentum in the branches, thus limiting the extent to which fluid penetrated into neighboring branches. Such a design intent translated to the physical domain much better than the intent to mitigate any backflow.

In looking at the  $\lambda = 0.4L$  geometry, the wavy channel objectives to increase the heat transfer ( $J_2$  and  $J_3$ ) matched the performance of the same objectives in the communicating case. The addition of the branches in the longer wavelength did little to increase the heat transfer. Fewer branches existed in the  $\lambda = 0.4L$  case than in the  $\lambda = 0.1L$  case (Figure 5-2), so their effect on the flow and heat transfer performance was less pronounced. In the as-built test coupons, the presence of the surface roughness may have exerted a much more significant effect on the flow features than the presence of the branches. As such, the optimizer’s shape changes surrounding the branches

may not have been enough to achieve the heat transfer objective experimentally; differences between the communicating and non-communicating channels were seen only in the friction factor.

### **5.11 Conclusions**

The current study was created to push the limits of the additive manufacturing process. The baseline microchannel configurations borrowed a key element from many transport systems found in nature, namely secondary branches that connect primary channels; two different wavelengths of a communicating wavy channel design were chosen for a baseline configuration. Each were numerically optimized with three different goals to (1) minimize the pressure loss, (2) maximize the heat transfer, and (3) maximize the ratio of heat transfer to pressure loss. The resultant geometries were complex, with cross-sectional shapes that were far from rectangular.

Each of the objectives functions was achieved numerically, with the majority of shape changes occurring near the branches themselves. Where pressure loss was to be minimized, the branches morphed such the flow exited the branches a shallower angle into its neighboring main channel. Other shape changes in the objective to minimize pressure loss sought to decrease the fluid momentum, which lessened the formation of Dean vortices in the channel. On the other hand, where heat transfer was to be maximized, the shape of the branches encouraged jet penetration into neighboring channels, thereby enhancing the formation of Dean vortices and increasing the fluid mixing.

The numerically optimized channels were duplicated to fit in test coupons, and were additively manufactured using a Laser Powder Bed Fusion process. The as-built test coupons built relatively true to their design intents. However, a natural consequence of the additive manufacturing process is the surface roughness; the presence of large roughness features, especially on any unsupported surfaces, most assuredly affected the flow through the channels, and also influenced how well the design of the branch exit was replicated.

Experimental results showed that, in the shorter wavelength configuration, the objective to minimize pressure loss was achieved. The optimizer's goal to decrease the fluid momentum translated well to the as-built microchannels, with the friction factor augmentation of the optimized channels around 6% less than the baseline. Similarly, the objective to maximize heat transfer was achieved as well, with an increase in the heat transfer augmentation from the optimized channels at around 9% over the baseline.

In the longer wavelength channels, the presence of the branches did not strongly influence the channels' heat transfer performance. While objectives to maximize heat transfer resulted in an increase in the pressure loss, heat transfer remained unaffected. The effects of surface roughness



may have outweighed the effects of the shape changes surrounding the branches due to the fact that the branch additions were sparse.

This study represents only an initial foray into the relationship between design tools and additive manufacturing. While additive manufacturing lifts many design constraints imposed by conventional means, the manufacturing process is less than perfect. Different concerns, such as build direction and surface roughness, must be taken into consideration. Until a tool that more closely integrates design decisions and build consequences exists, the numerical tools currently available for optimization methods should be explored. Additionally, detailed investigation into the current capabilities of the additive manufacturing process are critical in furthering the technology. With continued research into both the design tools and the manufacturing technology, the full potential of additive manufacturing can be realized, and more effective microchannel cooling configurations can be created.

## **6 ISOLATING THE EFFECTS OF SURFACE ROUGHNESS VERSUS WALL SHAPE IN NUMERICALLY OPTIMIZED, ADDITIVELY MANUFACTURED MICRO COOLING CHANNELS<sup>5</sup>**

### **6.1 Abstract**

Metal-based additive manufacturing is a disruptive technology with the capability to transform industries. The increased design space the technology offers is enticing to designers, who are given an opportunity to develop components that exceed prior performance levels; optimization tools can be used to provide guidance. However, the nature of surface roughness in additively manufactured parts is highly irregular, and computational models generally cannot properly capture the surface morphology. How, then, can current numerical tools predict the performance of additively manufactured components, or aid designers in developing products that meet their needs?

The current study aims to provide insight into the current capabilities of both design tools and the additive manufacturing process for microchannels intended for cooling components. A commercially-available optimization scheme was used to improve the design of four microchannel cooling configurations. These optimized geometries were printed using a metal-based additive manufacturing process; only some objective functions were achieved experimentally. In the current study, the same optimized geometries were printed using a stereolithography process, which built smooth channels as simulated in the optimization scheme. Experiments were performed to gather friction factor data, and results showed that the design intents were largely validated. Analyses of the metal test coupons alongside the plastic coupons showcase the direct effects of surface roughness: the influence of surface roughness was predominantly tied to the goal of the shape change.

### **6.2 Introduction**

Additive manufacturing (AM) has generated widespread excitement for a variety of applications. The advanced manufacturing technique can create near net shape geometries, including at the micro-scale, and its applications range from prototypes to production-level components.

Building parts layer-by-layer lifts many design constraints imposed by conventional, subtractive manufacturing techniques. As such, the true potential of AM can only be realized when

---

<sup>5</sup> Kirsch, K.L. and Thole, K.A., 2017, “Isolating the Effects of Surface Roughness versus Wall Shape in Numerically Optimized, Additively Manufactured Micro Cooling Channels”, to be submitted to *Experimental Thermal and Fluid Science*

this more open design space is fully exploited: numerical design tools are a necessary component in the ever-evolving field of AM. However, the current connection between computational models and their as-built counterparts can be weak, depending on the manufacturing method used.

Metal-based AM, for example, is one such process that produces parts that can deviate from their design intent given the complexity of the manufacturing process. Especially at the micro-scale, poor surface finish in metal AM parts affects not only the success of the build to replicate the intended design accurately, but also the ability of the part to function as desired. Evaluating the effectiveness of design tools for metal AM, therefore, can be difficult; upon analyzing the performance of the as-built parts, a natural question arises as to whether the performance can be attributed to the design features, or simply to the resultant geometry.

The current study seeks to isolate the effects of design features from surface roughness in parts created through Laser Powder Bed Fusion (L-PBF), one type of metal AM. The medium through which this study will be presented is through microchannel heat exchangers. Previous work by Kirsch and Thole [109,115] found mixed success in the ability of optimized L-PBF wavy microchannel designs to perform as intended. To probe deeper into those findings, the current study presents the same baseline and optimized wavy channel designs from Kirsch and Thole, but built using a Stereolithography (SLA) process, which faithfully reproduced the optimized geometries with relatively smooth surfaces. The SLA test coupons were then tested for friction factor over a range of Reynolds numbers. The results of the current study aim to interrogate the chosen optimization method, an efficient and simple design tool, as well as to gain a better understanding of the effects of surface roughness in complex channels.

### **6.3 Review of Relevant Literature**

The use of numerical tools to guide design decisions has become an integral step in the modern design process. Optimization schemes, in particular, are of distinct interest in cases where the most effective design may not be obvious, or where an acceptable compromise between competing objectives is desired. Martinelli and Jameson [21] published a detailed review of the natural relation between shape optimization and aerodynamics, the first foray into which occurred once computational fluid dynamics (CFD) became well-established.

Shape and topology optimization methods have been the focus of a number of recent studies in the field of heat exchangers [65,68,69,72–74,109,116,117]. Both schemes are accomplished through gradient-based optimization, meaning that the gradient of the objective function with respect to any design variables must be calculable. An efficient way to calculate this

gradient for a large number of design variables is through the adjoint method, which decouples any perturbations to design variables from the flow solver.

Many studies on optimization schemes are numerical in nature [65,68,69,73,74,116,117]; some studies, however, have experimentally investigated their numerically optimized designs [72,109]. Dede et al. [72] used topology optimization for a finned, external-flow heat exchanger; Kirsch and Thole [109] used shape optimization in internal micro cooling channels. In both studies, the heat exchangers were built using L-PBF, and both authors reported that the surface finish affected their aerothermal performance. In Dede et al. [72], the optimized heat exchanger outperformed the baseline, while in Kirsch and Thole [109], the optimized channels showed mixed success relative to their baselines.

In general, external flow features can be smoothed, but internal cooling channels with large L/D are difficult to smooth while maintaining nominal channel dimensions. Seminal studies by Snyder et al. [15] and Stimpson et al. [16] reported on the effects of roughness in L-PBF microchannels. The authors found that the size of the roughness features relative to the channel hydraulic diameter played a key role in the channels' performance. Higher relative roughness directly correlated with higher friction factors, but only proved beneficial to the heat transfer to a point; once the friction factor augmentation in the channel surpassed a value of four, no further benefit to the heat transfer was seen. These results corroborated the findings from Norris [33].

The type of surface roughness that results from the L-PBF process is irregular in shape and size [60,94]. Build direction exerts a strong influence on the roughness levels [29,95], as well as the likelihood that a part will build close to its intended design [15]. Modeling such surface roughness, however, is difficult. Results from studies on the effects of uniform roughness [30–32] cannot be applied to channels in which the surface morphology is so complex. In one study by Stimpson et al. [63], however, the authors developed a correlation for predicting the friction factor and heat transfer from straight L-PBF microchannels; a key finding was that randomly roughened surfaces correlate best with the measured arithmetic mean roughness.

The channel design in the current study is one commonly used in low mass flow applications, such as those for fluid mixing or small electronics cooling. Wavy channels promote mixing in the flow through to characteristic vortical structures that form because of the centripetal force enacted on the fluid particles [8]. Common methods to create the channel waviness can be through sinusoidal waves [37,38], or from circular arcs [8]. The most common variables to change in wavy channels are the wavelength and amplitude [25,26], which affect the vortex characteristics in the channels.

Most wavy channels from the literature were performed at low Reynolds numbers ( $Re < 1000$ ). However, studies by Kirsch and Thole [55] and Weaver et al. [108] investigated wavy channels at higher ( $2000 < Re < 20000$ ) Reynolds numbers, and found that the benefits of the wavy channel design transferred well to higher Reynolds number applications.

The current study is unique in that it delves into the flow physics of complex, optimized microchannel cooling designs. Until a closer tie between numerical optimization techniques and manufacturing capabilities exists, fundamental studies like the current one are crucial in bridging the gap between simulations and experiments. This study aims to explore the current capabilities of a simple, computationally-inexpensive design tool, as well as lend insight into key differences to expect between smooth and roughened channels.

#### **6.4 Channel Design**

The wavy channels in the current study were created by sweeping a rectangle along a path constructed with four  $45^\circ$  arcs. This design was chosen such that the fluid particles in the channels traveled through the same radius of curvature, and thus experienced the same magnitude of centripetal force; the direction of that centripetal force switched signs from positive to negative twice in every period.

In two of the baseline configurations, the channels were isolated from one another. In the other two baseline designs, branches connected the primary channels in an effort to increase fluid mixing. Each of the isolated and communicating channel designs contained two different wavelengths,  $\lambda$ , relative to the entire test coupon channel length,  $L$ :  $\lambda=0.1L$  and  $\lambda=0.4L$ .

Figure 6-1 explains how the isolated wavy channel was created in the  $\lambda=0.1L$  case; the method was the same for the  $\lambda=0.4L$  case, therefore creating a larger amplitude wave. Ten periods were present in the  $\lambda=0.1L$  case, while 2.5 were present for the  $\lambda=0.4L$  case. The direction of the radius of curvature switched signs in between the peaks and troughs of the channels.

Figure 6-2 shows the channel construction for the communicating wavy channels. The branches between primary channels in Figure 6-2 emanated at a  $45^\circ$  angle to the horizontal. Branches were included in every other period in the axial dimension, and between every other channel in the spanwise dimension. This alternating pattern can be seen in the full-length image of the channels. The entrance to the branches was filleted to minimize losses, while the exit from the branch was sharper to encourage jet penetration.

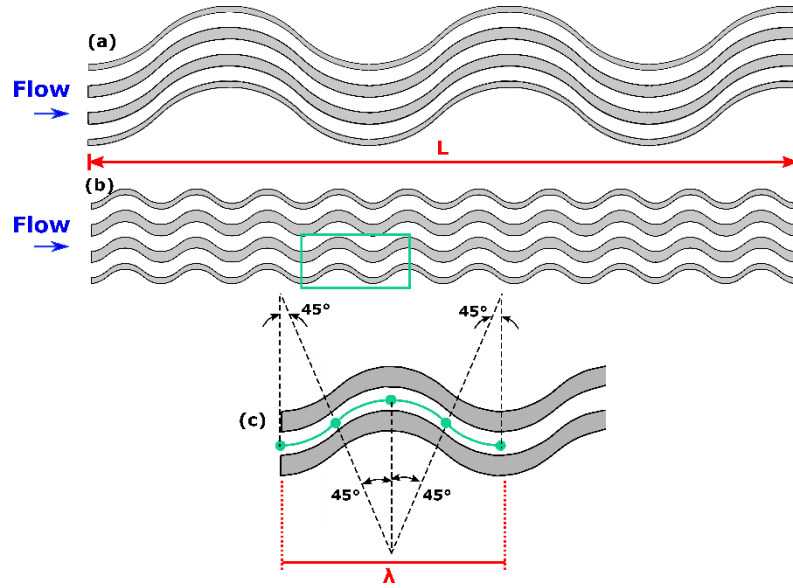


Figure 6-1. Isolated wavy channel construction. To create the channels, a rectangle was swept along the path created by the four  $45^\circ$  arcs. (a)  $\lambda=0.4L$  case, (b)  $\lambda=0.1L$  case, (c) description of wavy channel construction.

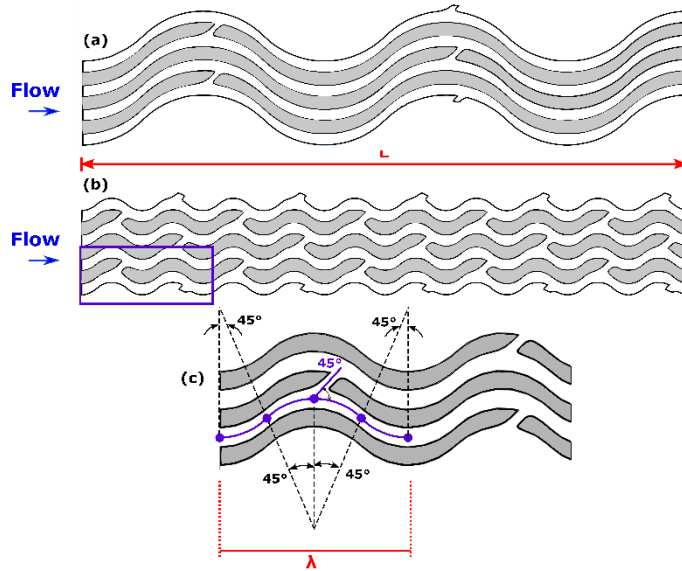


Figure 6-2. Communicating wavy channel configuration. The primary channels were created in the same manner as shown in Figure 6-1, but branches were included to encourage fluid mixing. Branches emerged from the primary channels at a  $45^\circ$  angle to the horizontal. (a)  $\lambda=0.4L$  case, (b)  $\lambda=0.1L$  case, (c) description of wavy channel construction. Note the sharp corner at the branch exit, which was included to encourage jet penetration.

## 6.5 Simulation Setup

A wall-resolved, structured mesh was created for each of the four baseline configurations. The steady RANS and energy equations were solved using the realizable  $k-\epsilon$  turbulence model; only the fluid domains were included in the simulation. The boundary conditions mimicked those from the experimental setup in Kirsch and Thole [55,109]; a constant temperature boundary

condition was imposed on the channel top and bottom endwalls, and the flow conditions were for a Reynolds number of 5000.

In the case of the isolated channels, the mesh contained 1.1 million nodes. For the communicating channels, two neighboring channels were modeled with their corresponding branches, and thus contained double the number nodes. For the communicating channels, the exterior branches were subject to periodic boundary conditions.

Figure 6-3 shows a slice of the computational mesh for the  $\lambda=0.1L$  communicating case, along with certain boundary conditions highlighted. Note that the other computational meshes were similar. The results from the numerical simulation fed into a shape optimization analysis, which was embedded within the same program as the flow solver. Shape optimization was accomplished through a sensitivity analysis, which was calculated by solving a set of equations known as the adjoint equations. The adjoint method is a highly efficient means of calculating the sensitivity of a large number of design variables on a given objective function. In the current simulation, each one of the nodes in the computational mesh represented a design variable.

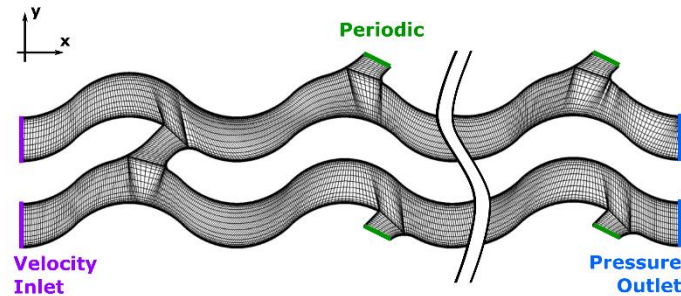


**Figure 6-3. Top-down view at 50% channel height of the computational mesh used for the  $\lambda=0.1L$  communicating channel configuration. In the case of the isolated channels, only one channel was included in the simulation. Not shown in this figure is the heat input into the simulation, which was accomplished through a constant temperature boundary condition on the top and bottom endwalls.**

Each of the four baseline configurations were subjected to three different objective functions, denoted as  $J$  and shown in Equations 1-3. The first objective was to minimize the pressure loss between channel inlet and outlet, the second objective was to maximize the heat transfer on the top and bottom endwalls, and the third objective sought to maximize the ratio of heat transfer to pressure loss. The form of the third objective function mirrors a commonly-used performance factor in internal cooling channels, originally derived in Gee and Web [114].

$$J_1 = \min(\Delta P) \quad 6-1$$

$$J_2 = \max(Q) \quad 6-2$$

$$J_3 = \max\left(\frac{Q}{\Delta P^{1/3}}\right) \quad 6-3$$

A full, mathematical description of the adjoint method is given in Kirsch and Thole [55]; the derivation and discretization of the adjoint equations, however, were accomplished within the program [47]. The adjoint equations are solved to convergence much like the governing equations for the flow solver. Once converged, the sensitivity of each one of the design variables (mesh nodes) on the objective at hand can be determined. The user defines the degree to which the shape should change, then the mesh is morphed as directed by the sensitivity results. The resultant mesh retains its original quality and its original  $y^+$  values. The flow solver governing equations are then solved to convergence with the new geometry, and the objective function can be compared to the results from the previous flow solution.

One design iteration includes solving the governing equations to convergence, solving the adjoint equation to convergence, morphing the mesh, and re-running the flow solver. In all, between six and fourteen design iterations were performed for each of the objective functions on each of the baseline designs. A final design was chosen when either the objective function no longer changed, or the flow solver no longer converged.

Each of the shape changes achieved their intended objective function. Table 6-1 shows the results from the numerical study of the non-communicating channels as a percentage of the baseline value; Table 6-2 shows the same data, but from the communicating channel configuration. The bolded values show the results from the objective function at hand, while the other two values are shown for comparison.

In general, the objective to maximize heat transfer was the most successful. Perhaps because the wavy channel configuration already promoted such strong mixing in the flow, this objective was easiest to satisfy. The most significant deviation from the baseline was seen in the  $\lambda=0.1L$  non-communicating channel to maximize heat transfer (+26%). By contrast, the least significant deviations from the baseline were seen in the objectives to maximize the ratio of heat transfer to pressure loss for both wavelengths in Table 6-2, which shows the communicating channels. The conflict between increasing the heat transfer and decreasing the pressure loss was not well-resolved by the optimizer in the communicating channels.

**Table 6-1 Changes in  $\Delta P$ ,  $Q$ , and  $Q/\Delta P^{1/3}$  in non-communicating optimized channels relative to each respective baseline**

	$\lambda=0.1L$			$\lambda=0.4L$		
	$\Delta P$	$Q$	$Q/\Delta P^{1/3}$	$\Delta P$	$Q$	$Q/\Delta P^{1/3}$
J <sub>1</sub>	<b>-8.4%</b>	-0.5%	+2.5%	<b>-5.5%</b>	-3.5%	-1.6%
J <sub>2</sub>	+28.5%	<b>+26%</b>	+16%	+7%	<b>+5.3%</b>	+3%
J <sub>3</sub>	+1.7%	+23.8%	<b>+17.5%</b>	+4.8%	+4.8%	<b>+3.2%</b>



**Table 6-2. Changes in  $\Delta P$ ,  $Q$ , and  $Q/\Delta P^{1/3}$  in communicating optimized channels relative to each respective baseline**

	$\lambda=0.1L$			$\lambda=0.4L$		
	$\Delta P$	$Q$	$Q/\Delta P^{1/3}$	$\Delta P$	$Q$	$Q/\Delta P^{1/3}$
J <sub>1</sub>	<b>-4.4%</b>	-3.9%	-2.5%	<b>-3.2%</b>	+0.2%	+1.3%
J <sub>2</sub>	+6.6%	<b>+6.6%</b>	+4.3%	+11.7%	<b>+11.7%</b>	+6.6%
J <sub>3</sub>	+0.4%	1.9%	<b>+1.8%</b>	+3.3%	+1.8%	<b>+2.7%</b>

## 6.6 Test Coupon Manufacture

### *Plastic Stereolithography Process*

Once the optimization procedure was complete, the baseline and optimized channels were duplicated in order to fit in a test coupon. In the current study, six channels were included in the test coupons, and the scale of the coupons was chosen such that the channels could be built in one, solid piece. A commercially-available SLA machine was used for the build [118]. Once a build has completed, the parts are removed from the build platform, cleaned using isopropyl alcohol, and cured in a UV oven. Once cured, support structures are easily broken off.

The layer thickness (resolution in the z-dimension) was 50 microns; the laser spot size (resolution in the x- and y-dimensions) was 140  $\mu\text{m}$ . Multiple test pieces were built at the same time, but in all, five builds were required to manufacture all pieces and took approximately 200 hours to complete.

The SLA test pieces were designed such that the tops of the channels were open. Therefore, any residual resin could be cleaned out, and the internal surfaces of the channels could cure evenly. During testing, a lid was placed atop the channels to seal the test section. The channels were 6.5 mm in height, and 3.25 mm in width at the entrance, which was scaled up 6.5X from the manufactured channels in Kirsch and Thole [115,119]. The L/D for all channels was 41.

### *Metal Additive Process*

The test coupons for the previous studies from Kirsch and Thole [115,119] were meant to replicate heat transfer properties of the intended production-level micro-sized heat exchanger. As such, the test pieces were manufactured from stock Inconel 718 powder [45] using default parameters in the L-PBF process [27]. In any L-PBF process, metal powder is melted together layer-by-layer until the part is complete.

For the test coupons from Kirsch and Thole [115,119], the layer thickness was 40  $\mu\text{m}$ . The x-y resolution in L-PBF processes is driven by many different process parameters and, as such, difficult to quantify. However, a typical resolution can be assumed to be within a few hundred microns [41]. The total build time for the test coupons was near 40 hours; the build plate, however, contained coupons other than the sixteen test coupons from Kirsch and Thole [115,119].

The L-PBF process is comparable to a welding process, and imparts significant thermal stress in each of the parts. Therefore, parts must be heat treated to eliminate any residual stresses before being removed from the build plate. A wire electro-discharge machine (EDM) is used to remove parts from the build plate. Any other support structures not removed by the EDM must be manually machined off.

As previously mentioned, a natural consequence of the L-PBF process is high surface roughness. As the laser traces each subsequent slice of the part and melts the metal powder, nearby loose powder particles can become sintered to the fully-melted regions. This behavior occurs more readily on unsupported surfaces, or those in which the current layer has no solid material directly underneath. These unsupported surfaces can also deviate from the CAD model more than supported surfaces; intricate features are more difficult to replicate when loose powder, instead of fully melted material, lies directly beneath the current layer.

The build direction for the L-PBF test coupons is shown in Figure 6-4, and was chosen such that most internal surfaces would build appropriately. However, given the complicated nature of the channel designs, unsupported surfaces were unavoidable and, as a result, the L-PBF test coupons deviated from the design intent in both surface finish and geometric tolerance.

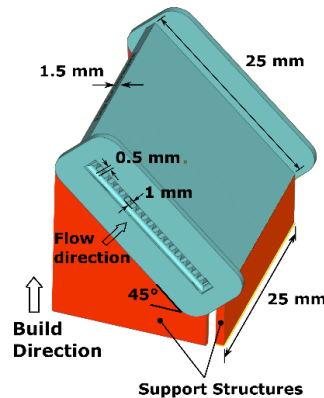


Figure 6-4. Build direction for L-PBF coupons

#### *Non-Destructive Evaluation*

A critical part of any AM or 3D printing study comes in properly characterizing the resultant part. Two SLA test coupons were scanned using X-Ray Computed Tomography (CT) to evaluate how closely the printed designs matched the optimized intent. The resolution of the scan was 90  $\mu\text{m}$ , which was more than sufficient to capture all design features. For both SLA test coupons, 95% of the geometry matched the CAD model to within 140  $\mu\text{m}$ , the laser spot size.

Each of the L-PBF test coupons was CT scanned as well, at a resolution of 35  $\mu\text{m}$ . The rough internal surfaces of the L-PBF microchannels were determined using proprietary software [42] that computed the gradient between solid material and open space. Deviations from the design

were primarily driven by the roughness, although certain features such as sharp corners were difficult to reproduce.

Figure 6-5 shows a 2D slice taken at an L/D close to 7, or 17.5% the channel length for both the SLA and L-PBF channels; the intended design is shown in a black outline, while the as-built channel outlines are colored by their deviation from the CAD model. Figure 6-5a shows the outline for the SLA test coupon, which was 6.5 times larger than the L-PBF test coupon, from which one channel's cross-section is shown in Figure 6-5b. As such, the deviation color bar for the SLA test coupon is 6.5 times greater in magnitude than the deviation color bar for the L-PBF channels.

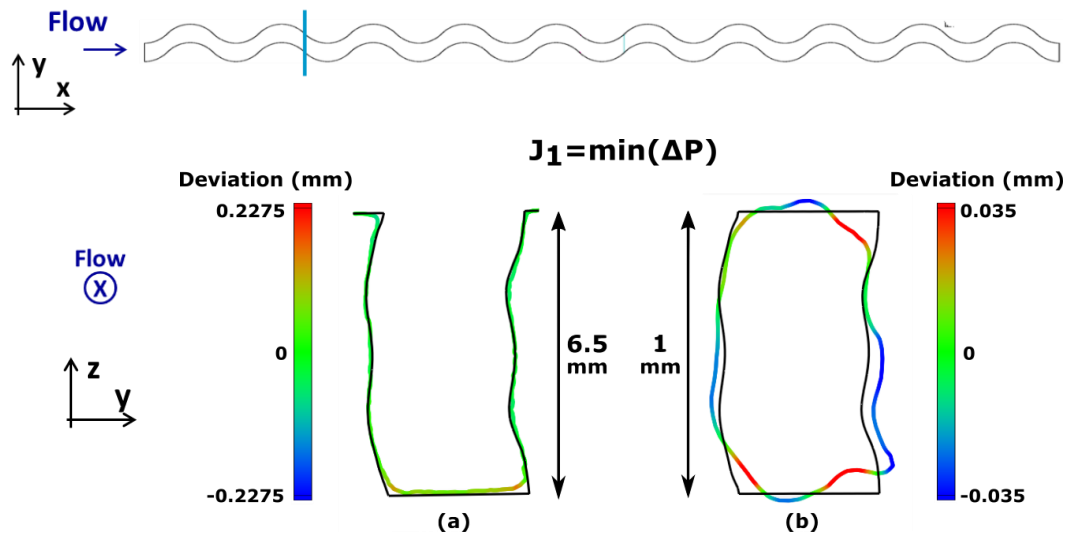


Figure 6-5. Deviation from the design intent for the (a) 6.5X scale SLA test coupon and (b) the 1X scale L-PBF test coupon. The channels shown are for the objective to minimize pressure loss. The as-built channel outlines at the location specified at the top of the image are colored by their deviation from the design intent; the black outline shows the slice of the CAD model. The contour scales for the different manufacturing processes reflect the difference in scale between the two test coupons.

The deviation from the CAD model is visually much more significant in the L-PBF test coupon than in the SLA test coupon. This result is expected, given the small size of the channels. The corners of the channels in the L-PBF process did not build quite as intended, yielding much more rounded intersections between channel endwalls. However, certain design features from the optimizer were generally reproduced.

The SLA test coupon, on the other hand, built nearly identical to the design intent. The largest deviation, seen at the corners of the channel, was less than the laser spot size of 140  $\mu\text{m}$ . Much of this success can be attributed to the fact that the channels were scaled up 6.5X. Given that the intent of this study was to understand how the numerical shape changes performed experimentally, the CT scan results of the SLA test coupons validated the study's premise; the SLA test coupons were deemed a sufficient representation of the optimized channel design.

### *Experimental Setup*

A bench-top rig was used to calculate the friction factor for each of the test coupons. A mass flow controller [76] governed the air flow through the test rig; the Reynolds number ranged between 2000 and 18000. A static pressure tap was located upstream of the channels; the channels emptied to atmosphere. During testing, vacuum grease was used to seal the interface between test piece and test section, as well as seal the contact between the channels and their lids. Figure 6-6 shows a cross-section of the experimental setup. An example test piece containing the  $\lambda=0.4L$  channels is shown for reference. The test piece sits inside a lip in the test section, and the channels and their lids are clamped together to ensure no leaks occur during testing.

Mean fluid velocity was calculated from the measured mass flow rate using the cross-sectional area at the entrance to the channels; given that the SLA test pieces built so close to the design intent, the dimensions were taken to be the CAD dimensions.

To validate the test rig, a test piece containing six straight, smooth, rectangular channels was printed along with the wavy channels to test for friction factor. Figure 6-7 shows the friction factor from this benchmark test coupon; outside of Reynolds numbers between 700 and 2000, the friction factor from the test coupon was within 5% of the correlations. In the laminar-to-turbulent transition region, the influence from entrance effects was measurable because of the channel  $L/D$ ; Langhaar [120] found that for  $L/D$  between 20 and 63, entrance effects influenced the friction factor in the transition region.

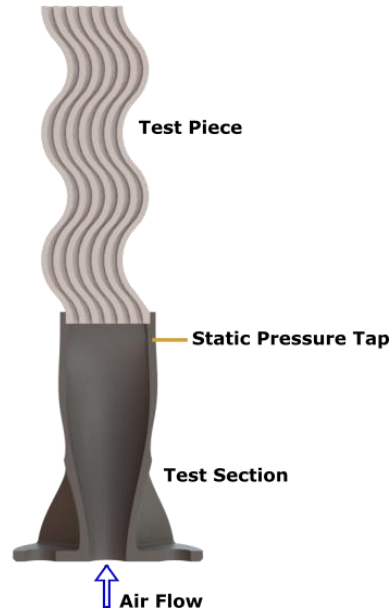


Figure 6-6. Cross-section of experimental setup for friction factor tests.

#### Uncertainty Analysis

Uncertainty was quantified using the methods proposed in Kline and McClintock [46]. Overall uncertainty in measuring friction factor was under 5% for all conditions; the largest source of uncertainty came in the calculation of the mean velocity used in the friction factor calculations. The uncertainty in measuring the pressure drop was under 0.5%, and the uncertainty in Reynolds number measurements was under 1%. Repeatability in friction factor among tests was under 4%.

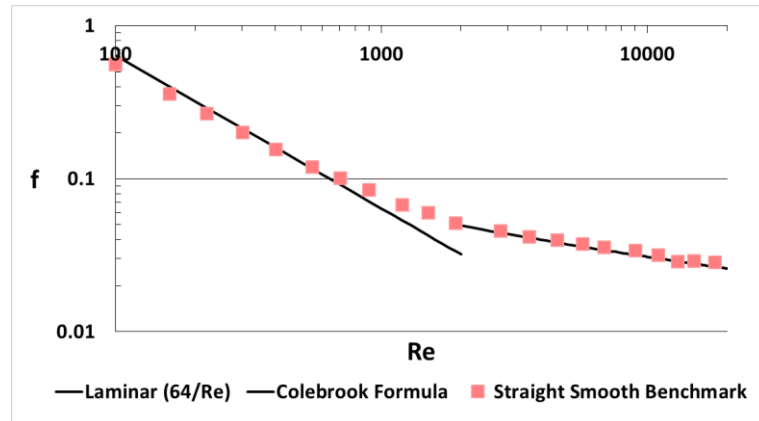


Figure 6-7. Benchmarking data from straight, smooth, rectangular channels atop friction factor correlations for laminar flow ( $64/Re$ ) and turbulent flow (Colebrook Formula)

### 6.7 Experimental Results and Discussion

Friction factor results will be presented in terms of an augmentation over a smooth baseline, calculated using the Colebrook formula [98]; both experimental and numerical data points will be

included. Where applicable, flowfield results from the numerical simulations will be included to explain the experimental results.

### *SLA Test Coupons vs. Numerical Simulation*

#### *Non-communicating Channels*

Figure 6-8 shows the friction factor augmentation for the SLA test coupons and the numerical results for the  $\lambda=0.1L$  non-communicating (isolated) case. The trend with Reynolds number is constant, meaning that the friction factor from the SLA coupons decreases with Reynolds number at the same rate as a perfectly smooth channel.

The magnitude of the experimental results differs from the numerical results by between 35 and 50%, which may be attributed to the inability of the flow solver to capture all secondary flows; the realizable  $k-\epsilon$  turbulence model is known to fall short in capturing complex flows accurately [121].

However, the trends between experimental and numerical results were similar. For example, the channels optimized for a decrease in pressure loss showed a 5-9% decrease in friction factor augmentation experimentally. The numerical results predicted a 6% decrease in friction factor augmentation. In the simulation, the objective to minimize pressure loss was achieved by mitigating backflow in the channel. Where the radius of curvature switched signs (shown in Figure 6-1), the flow solver showed signs of backflow in the baseline case. Figure 6-9 shows 2D slices at 20% of the channel length colored by normalized axial velocity. Two specific locations of backflow can be seen in the baseline contour, denoted by any dark blue color. In contrast, all fluid in the slice through the optimized channel is moving in the positive  $x$  direction. These shape changes translated well to the experimental results, which indeed showed a decreased pressure loss relative to the baseline design.

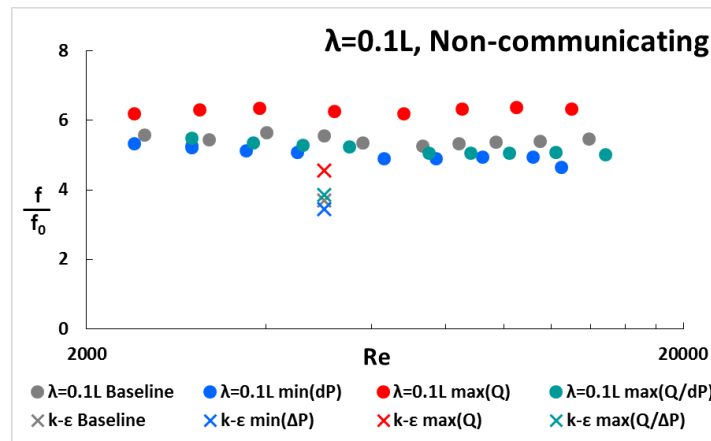


Figure 6-8. Friction factor augmentation for the  $\lambda=0.1L$  non-communicating (isolated) channel case

The objective to maximize heat transfer also yielded similar friction factor augmentation trends in both experimental and numerical results. In the experimental results, the objective to maximize heat transfer showed a friction factor augmentation between 10 and 20% higher than the baseline; in the numerical results, the optimized channel showed a 25% increase in friction factor augmentation over the baseline.

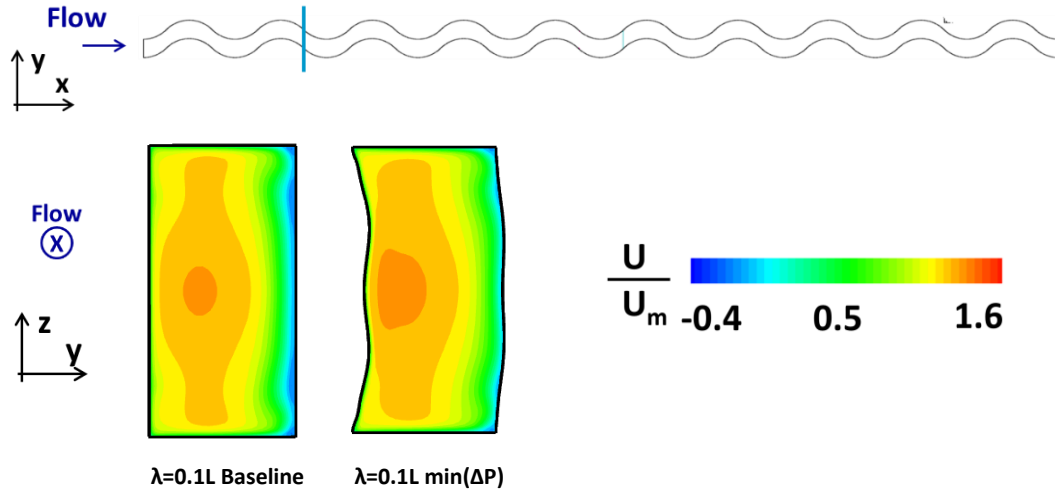


Figure 6-9. 2D slices taken at 17.5% of the channel length of the  $\lambda=0.1L$  Baseline and  $\min(\Delta P)$  cases. Contours are colored with normalized axial velocity. Note that contours colored blue showcase flow moving in the negative x direction.

The intent of the shape optimization to increase the heat transfer revolved around creating stronger vortices in the channels [55]. Figure 6-10 shows 2D slices taken from the numerical results at 55% of the channel length from the  $\lambda=0.1L$  baseline and  $\lambda=0.1L \max(Q)$  geometries. Note that slice locations Figure 6-10 do not showcase any shape changes. All shape changes occurred in between the peaks and troughs of the wavy channels, where the radius of curvature switched signs, which strongly affected the flow structures in the peaks and troughs.

The contours in Figure 6-10 are colored by non-dimensional temperature; secondary velocity vectors are included as well. The contour levels in the baseline case are noticeably darker (lower non-dimensional temperature) than in the case to maximize heat transfer. Additionally, the velocity vector directions differ significantly. Where heat transfer was to be maximized, velocity vectors pointed directly vertical, showing that fluid was forced toward the top and bottom endwalls to remove the heat. These vortical structures undoubtedly played a role in the friction factor increase over the baseline case, and their creation translated well to the experimental results.

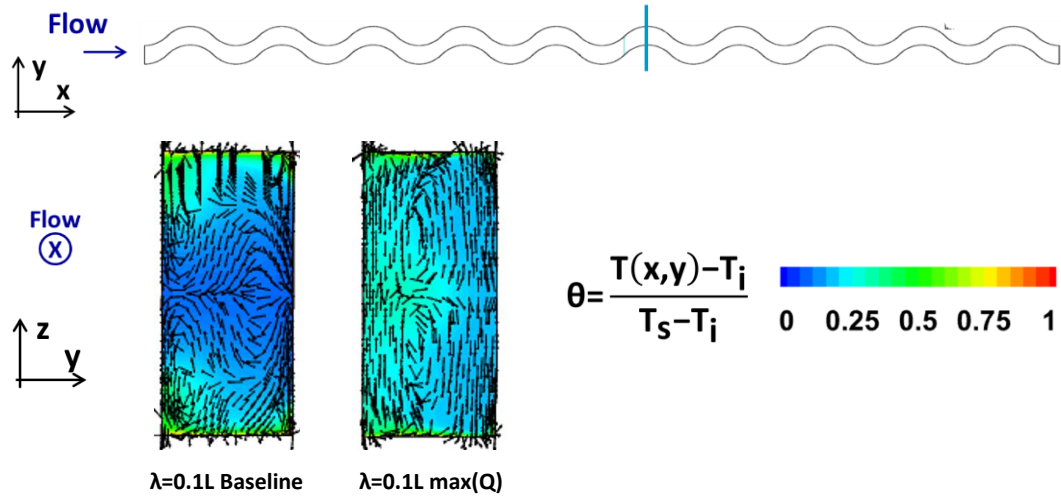
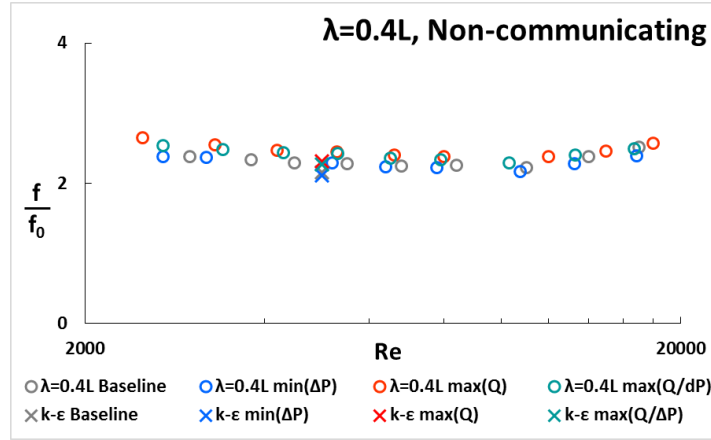


Figure 6-10. 2D slices taken at 55% of the channel length of the  $\lambda=0.1L$  Baseline and  $\max(Q)$  cases. Contours are colored with nondimensional temperature; secondary velocity vectors are overlaid. Note the direction of the secondary velocity vectors in the  $\max(Q)$  case relative to the baseline case.

The objective to maximize the ratio of heat transfer to pressure loss performed differently than predicted, in that the friction factor augmentation in the experimental results was lower than the baseline. The numerical simulation predicted a higher friction factor augmentation than the baseline. This discrepancy may be attributed to the flow solution's ill prediction of the vortex strength. In general, the shape changes for the objective to maximize the ratio of heat transfer to pressure loss were a compromise between those for the objective to maximize heat transfer and the objective to minimize pressure loss. In the experimental results, the strength of the vortices induced by the shape changes are hypothesized to have exerted a weaker effect on the friction factor than predicted; the shape changes that reduced backflow outweighed those that promoted stronger vortices.

Figure 6-11 shows friction factor augmentation for both numerical and experimental results from the  $\lambda=0.4L$  configuration. Note that the abscissa is half that from Figure 6-8; the friction factor augmentation in the longer wavelength was much less than for the shorter wavelength. Additionally, the difference in magnitude between the numerical and experimental results in Figure 6-11 was significantly smaller than in Figure 6-8. Given the longer distance the fluid traveled before reaching a sign change in the radius of curvature, the flow incurred fewer losses and was prone to fewer secondary flows. Characteristic Dean vortices form most fully in the peaks and troughs of the channels, fewer of which were present in the  $\lambda=0.4L$  case than in the  $\lambda=0.1L$  case. As such, the realizable  $k-\epsilon$  model was able to capture the flow features more accurately than in the shorter wavelength.





**Figure 6-11. Friction factor augmentation for the  $\lambda=0.4L$  non-communicating (isolated) channel case.**

The goals of the optimizer in the  $\lambda=0.4L$  case were structured around the secondary flows in the channels. Where pressure drop was to be minimized, the size of these vortices was diminished; where heat transfer was to be maximized, the size of these vortices was enhanced. Figure 6-12 supports these claims. 2D slices are shown at the axial location specified in the figure, and show non-dimensional temperature contours with secondary velocity vectors overlaid. The fullest vortices are seen for the objective to maximize heat transfer, while the smallest are seen for the objective to minimize pressure loss. Given the longer flow development length, the amount of backflow in the  $\lambda=0.4L$  channels was negligible. Therefore, the predominant flow features to be targeted by the shape changes were the vortices. The non-dimensional temperature contour levels reflect the flowfield shown from the vectors. Stronger mixing, and therefore higher non-dimensional temperatures, were seen where the vortices are strongest.

The objective to maximize the ratio of heat transfer to pressure loss exhibited shape changes that closely mimicked those for the objective to maximize heat transfer. Figure 6-12 shows very similar vortical structures in the objective to maximize the ratio of heat transfer to pressure loss as those seen in the objective to maximize heat transfer solely. The objective to maximize the ratio of heat transfer to pressure loss resulted in an increase in friction factor augmentation of 6% over the baseline, which matched the simulation results.

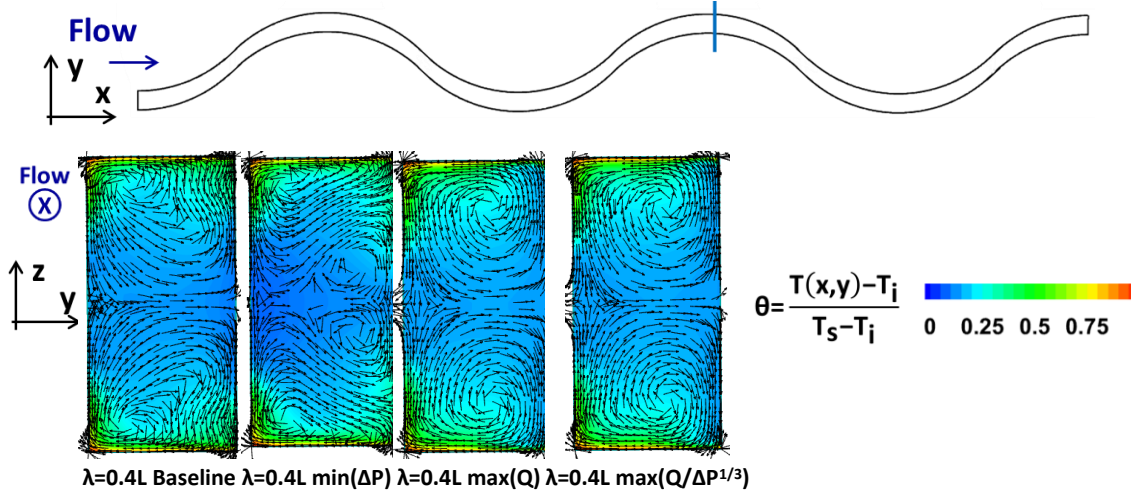


Figure 6-12. 2D slices taken at 60% the channel length of the  $\lambda=0.4L$  design. The baseline and all three optimized cases are shown. Contours are colored with nondimensional temperature; secondary velocity vectors are overlaid.

### Communicating Channels

Figure 6-13 shows the friction factor augmentation for the communicating channels at the  $\lambda=0.1L$  wavelength. Much like in Figure 6-8, the magnitude between the numerical and experimental results differed by 40-50%. However, the trends predicted by the simulations were again captured in the experimental results. The experimental results for the objective to maximize heat transfer showed a 4% increase in friction factor augmentation over the baseline, which was similar to the prediction of an increase by 5%. Additionally, the objective to minimize pressure loss yielded a friction factor 5% under the baseline, which again was markedly close to the simulation's result of a decrease by 4%.

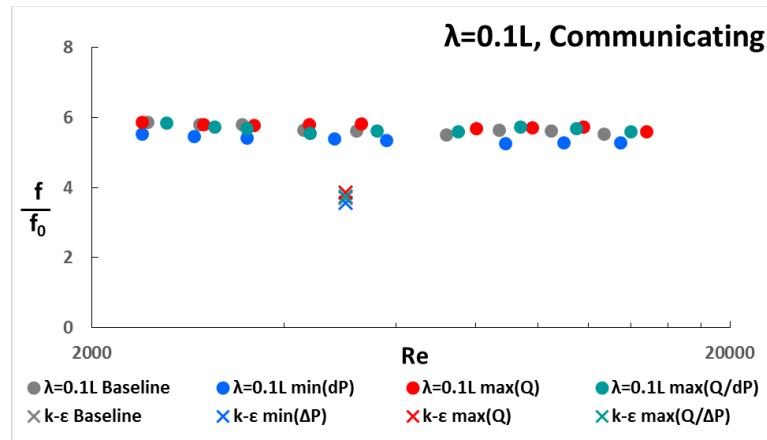


Figure 6-13. Friction factor augmentation for the  $\lambda=0.1L$  communicating channel case.

The inclusion of the branches between wavy channels strongly influenced the formation of vortical structures in the primary channels. As such, the majority of shape changes in the communicating channels came in the vicinity of the branches. Figure 6-14 shows 2D slices of all

four  $\lambda=0.1L$  communicating channel cases at a axial distance of 65% the channel length. Unsurprisingly, the largest vortices are seen for the objective to maximize heat transfer, as are the lowest non-dimensional temperatures. In looking at the objective to maximize the ratio of heat transfer to pressure loss, the vortices are present, but smaller in magnitude than those for the objective to maximize heat transfer only. By contrast, the secondary flows for the objective to minimize pressure loss are minimal. The shape changes generated by the optimizer can be hypothesized to have generated similar flow structures in SLA test coupons, given the similar trends seen in Figure 6-13.

As was the case for the  $\lambda=0.4L$  non-communicating channels, the difference in friction factor augmentation between the numerical and experimental results for the  $\lambda=0.4L$  communicating channels was small. Figure 6-15 shows the experimental and numerical friction factor augmentation results for the  $\lambda=0.4L$  communicating channels. Due to the branch pattern and the long wavelength of the primary channels, the number of branches in the test coupon was significantly smaller than in the  $\lambda=0.1L$  case (Figure 6-2). Therefore, the increase in fluid mixing due to the branches, and thus an increase in the requirement for the realizable  $k-\epsilon$  model to model stronger secondary flows, was nominal. The objective to minimize pressure loss was achieved in the experimental results, as was the objective to maximize heat transfer. The objective to maximize the ratio of heat transfer to pressure drop, however, deviated from the intended result. The strength of the vortices in the  $\lambda=0.4L$  communicating channels is hypothesized to be stronger than predicted, and thus yielded a higher friction factor augmentation than the baseline.

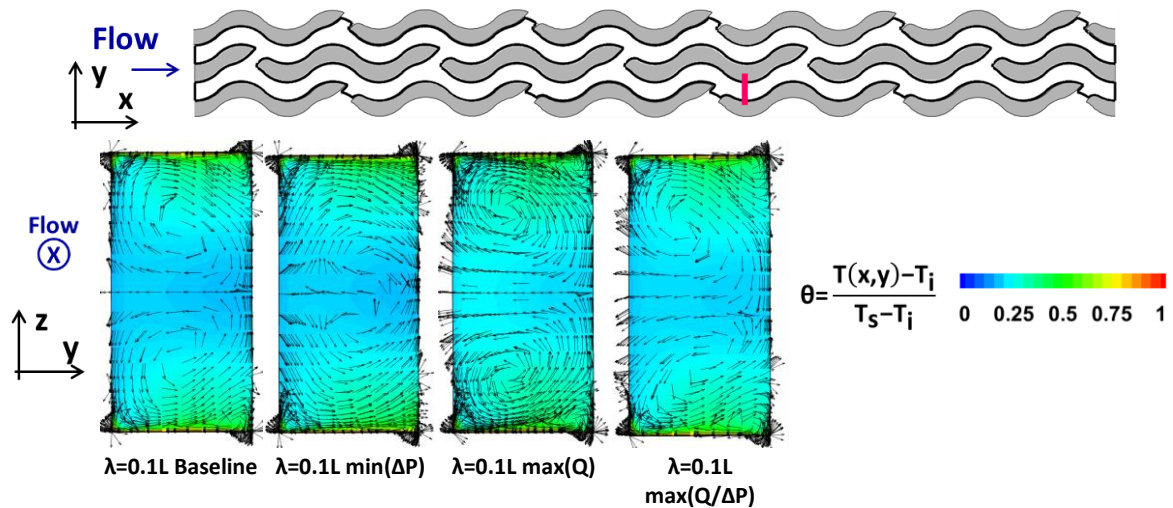


Figure 6-14. 2D slices taken at 65% of the channel length of the  $\lambda=0.1L$  communicating design. The baseline and all three optimized cases are shown. Contours are colored with non-dimensional temperature; secondary velocity vectors are overlaid.

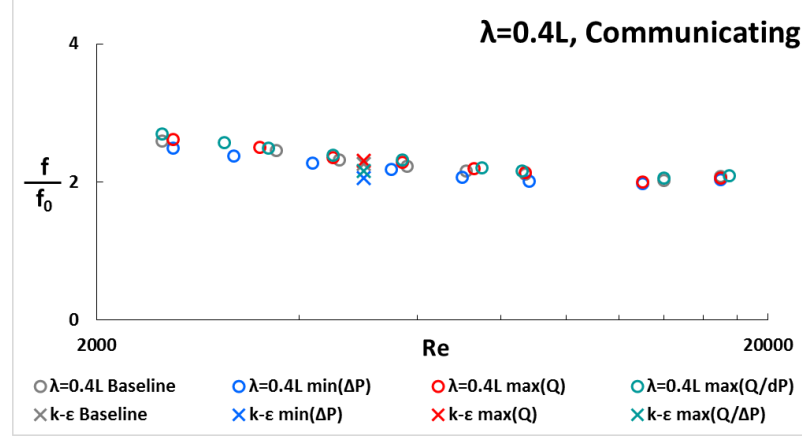


Figure 6-15. Friction factor augmentation for the  $\lambda=0.4L$  communicating channel case.

#### *SLA Test Coupons vs. L-PBF Coupons*

As previously mentioned, the experimental results from the optimized L-PBF channels showed mixed success in terms of replicating the trends predicted by the simulation. The following discussion will delve into these discrepancies, and examine the influence of high surface roughness on the channels' performance by focusing on the  $\lambda=0.1L$  wavelength.

#### *Non-communicating Channels*

Figure 6-16 shows normalized friction factor from each of the optimized channels of the  $\lambda=0.1L$  non-communicating configuration. Experimental data from the L-PBF and SLA test coupons are included, as well as the results from the realizable k- $\epsilon$  simulation. Each data point is normalized by its respective baseline design.

The L-PBF test coupons failed at the objective to minimize pressure loss: the optimized channels showed a higher friction factor than the baseline design. The shape changes aimed to minimize the backflow in the channels, which did not work in the L-PBF channels. The high surface roughness on the internal channel walls negated any effect that the wall shape had on mitigating backflow; roughness features that protruded into the flow undoubtedly disturbed the flow, rendering the shape changes ineffective in reducing pressure loss. However, for smooth-walled channels, the design intent was successfully achieved.

Where heat transfer was to be maximized, the optimized L-PBF microchannels showed a friction factor over 50% higher than the L-PBF baseline microchannels. The shape of the optimized channels was meant to encourage stronger vortex formation. Given the rough channel walls, this shape change in the L-PBF channels most likely augmented the design intent; the combination of larger-scale vortices, induced by the shape change, and smaller-scale vortices, induced by the roughness features, contributed to a friction factor well above the baseline.

The SLA coupon optimized for heat transfer, however, showed a lower normalized friction factor than the numerical model. This result supports the aforementioned claim that the flow solution most likely under predicted the strength of the vortices. The discrepancy between the realizable  $k-\epsilon$  model and the SLA test coupon showcases just how much the roughness in the L-PBF microchannels amplified the design intent.

For the final objective to maximize the ratio of heat transfer to pressure loss, the L-PBF microchannel performance matched almost exactly that of the numerical model; the performance of the SLA coupon, on the other hand, showed a lower normalized friction factor. An explanation for these results can take a similar form to that given for the results to maximize heat transfer: the numerical model under predicted the strength of the secondary flows in the channel. However, the surface roughness in the L-PBF channels enhanced vortex formation, which increased the friction factor. This design intent was, in fact, helped by the surface roughness because the goal to increase the fluid mixing was tempered by the goal to mitigate pressure loss. The optimized shape changes, in tandem with the surface roughness, led to the achievement of the design goal.

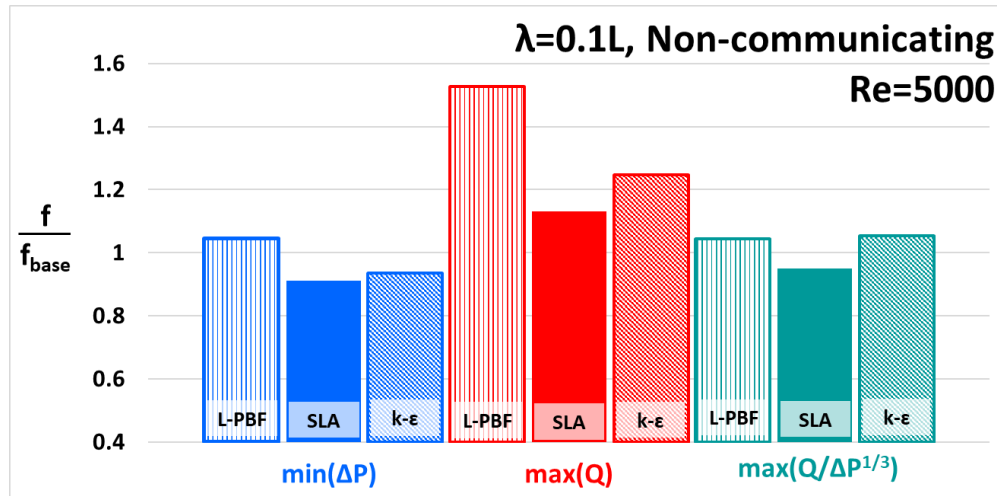


Figure 6-16. Friction factor from the  $\lambda=0.1L$  non-communicating L-PBF and SLA test coupons, as well as the realizable  $k-\epsilon$  model, normalized by each configuration's respective baseline channel.

### Communicating Channels

The shape changes in the communicating channels were focused on the areas surrounding the branches, and as a result, generated different shape changes than in the non-communicating cases. As such, an analysis into the performance of the L-PBF communicating channels can lend further insight into the efficacy of the design tool.

Figure 6-17 shows the friction factor from each of the optimized  $\lambda=0.1L$  communicating channels, normalized by the baseline. As in Figure 6-16, experimental results from the L-PBF and SLA test coupons are included, along with the results from the numerical simulation.

An unexpected result shown in Figure 6-17 is that the L-PBF test coupon outperformed its numerical goal: the L-PBF coupon yielded a lower normalized friction factor than the realizable  $k-\epsilon$  model predicted. In the optimized channels, the branch shapes were morphed such that they introduced flow into the neighboring branch at a shallow angle, thereby mitigating jet penetration. This shape change was much more transferable to the L-PBF manufacturing process than that to mitigate backflow, and proved much less sensitive to the addition of high surface roughness.

Additionally, the sharp exit of the branch in the initial design (seen in Figure 6-2) did not build exactly as intended in the L-PBF test coupons due to its small size, and to the build angle chosen [115]. Figure 6-17 supports a hypothesis that the more easily-manufactured shape change, combined with the lack of intended jet penetration, led to a more successful representation of the optimized goal in the L-PBF channels. A similar hypothesis can be applied to the objective to maximize the ratio of heat transfer to pressure loss; the intended and unintended shape changes that mitigated jet penetration eclipsed those that sought to encourage fluid mixing.

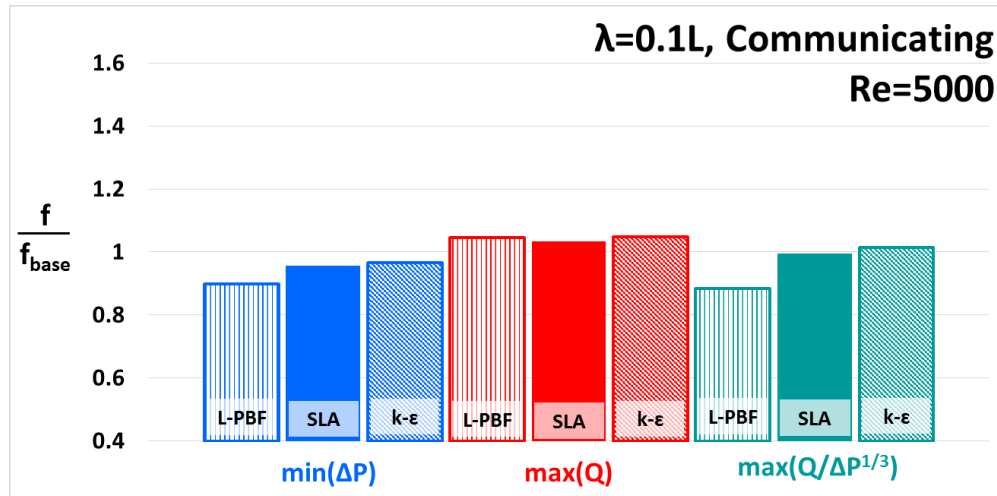


Figure 6-17. Friction factor from the  $\lambda=0.1L$  communicating L-PBF and SLA test coupons, as well as the realizable  $k-\epsilon$  model, normalized by each configuration's respective baseline channel.

The L-PBF microchannels optimized for heat transfer exhibited the same performance as intended. Again, most shape changes occurred near the branches, and served to intensify jet penetration. This shape change appeared to be less sensitive to the surface roughness than shape changes to promote stronger vortices. Due to the lack of sharp branch exit in the L-PBF coupons, the experimental results show that the surface roughness did not augment the intent to maximize heat transfer to the same magnitude as the non-communicating channels.

## 6.8 Conclusions

The genesis of the current study derived from a fundamental disconnect between numerical design tools and manufacturing processes. As additive manufacturing continues to generate excitement, the need for design tools that fully exploit its many capabilities will grow.

The current study used microchannel heat exchanger designs as the medium through which to investigate a simple, computationally-efficient optimization tool. The tool made of an adjoint-based sensitivity analysis, which informed shape change. Sensitivities of the design variables, which were comprised of every computational mesh node, were calculated using a steady flow solver, which was chosen to minimize the computational load. The optimization objectives were to (1) minimize the pressure loss between channel inlet and exit, (2) maximize the heat transfer on the top and bottom endwalls, and (3) maximize the ratio of heat transfer to pressure loss. Each objective was achieved numerically, and the resulting geometries were complex.

The four baseline and optimized wavy cooling channels were printed using a Stereolithography process that accurately replicated the designs. Two different wavelengths were studied; half of the test coupons contained channels that were isolated from one another, while the other contained communicating channels

Experimental results showed that the design tool worked well. Despite the sensitivity analysis having been calculated from a steady flow solution, the chosen turbulence model captured enough flow features to generate a shape change that accomplished its goals experimentally. General weak points of the flow solver were found in its ability to capture the strengths of the vortices accurately.

This study also aimed to delve deeper into the results from previous studies in which the same optimized channels were manufactured using Laser Powder Bed Fusion. High surface roughness in these test coupons introduced flow features that were not taken into account in the simulation. Due to the surface roughness, shape changes that were particularly sensitive to surface roughness enhanced the friction factor well beyond its intended value. However, shape changes that were not as sensitive to roughness generated results that were comparable to the intent.

The fields of design and manufacturing are rapidly evolving. Tandem advances in both fields will lead to a closer link between an intended design and its manufactured part. Integrating the consequences of the additive process into design tools is an integral step in fully realizing the potential of the advanced manufacturing process. However, until such technology exists, an in-depth analysis of the current design tools can prove useful to those aiming for better, more efficient designs.

## 7 CONCLUSIONS

The relationship between additive manufacturing and design methodologies is an area with much left to explore. The previous five chapters shed some light into the intrinsic ties between design decisions and the resultant manufactured part. In general, the L-PBF process was able to reproduce a set of wavy microchannel designs that all differed depending on whether the design intent was to minimize pressure loss or maximize heat transfer. The performance of those microchannels relative to their intended design was influenced by the surface roughness in the channels; some channel designs performed as intended, while others did not. Surface roughness was also a factor in the L-PBF microchannel pin fin arrays. High surface roughness on the top and bottom endwalls, along with roughness on the pin surfaces itself, undoubtedly generated a complicated flowfield that promoted significant mixing.

The results from Chapters 3, 5, and 6 proved true an initial hypothesis that micro cooling channels, despite their small size, were an appropriate medium for an optimization analyses. Slight changes to the channel shapes affected the pressure loss and heat transfer measurements. Additionally, the adjoint-based shape optimization method was computationally efficient, justifying the use of a low-fidelity CFD solver as a viable component in generating improved designs. The following sections will summarize in more detail the primary findings from the studies in this dissertation.

### 7.1 Flow and Heat Transfer Performance of Wavy Microchannels

A key benefit to wavy channels is that they promote fluid mixing due to the centripetal forces that are enacted on the fluid particles. Wavy channels are not typically used in high mass flow applications, like those for gas turbine component cooling, but results from Chapter 3 proved that they perform well; especially at Reynolds numbers below 4000, wavy channels showed higher heat transfer than straight L-PBF channels of the same aspect ratio for the same frictional losses.

Two different wavelength channels from Chapter 3 were subjected to three different objective functions that sought to (1) minimize the pressure drop, (2) maximize the heat transfer, and (3) maximize the ratio of heat transfer to pressure drop. The sensitivity analyses that resulted from these objective functions identified important areas of the baseline designs that influenced the objective functions. The final, optimized shapes of these wavy channels were all distinctly different. These differences were captured well in the L-PBF manufacturing process; experimental results showed different flow and heat transfer properties of the microchannels.

However, not all objective functions were achieved. For example, the objective to minimize pressure loss in the shorter wavelength failed. Chapter 6 showed that this failure can be



attributed to the surface roughness, and not the intended design. The smooth, scaled-up SLA test coupons showed analogous results to the numerical simulations in that the objective to minimize pressure loss was achieved. The intent of the shape changes were to prevent backflow near the channel walls. The presence of the surface roughness rendered this shape change ineffective in the L-PBF coupons; the roughness features that protruded into the flow created most likely created secondary flows that increased the frictional losses.

The objective to maximize heat transfer, however, was achieved in the L-PBF coupons. Indeed, the SLA test coupons also showed a higher friction factor, which was indicative of stronger vortical structures, and implied a successful design intent. The shape changes achieved their goal to increase fluid mixing in order to increase the heat transfer. In the L-PBF coupons, the larger vortices encouraged by the shape changes most likely interacted with the smaller vortices generated from the roughness features. As such, the friction factor suffered immensely. The L-PBF channels optimized for heat transfer yielded a friction factor over 50% higher than the baseline. However, the heat transfer performance in the L-PBF channels exceeded that from the baseline by over 20%.

Chapter 5 presented a similar study as in Chapter 3, but with a different baseline configuration. The channels in Chapter 5 were still wavy in nature, at the same two wavelengths studied in Chapter 3, but were connected using branches that were designed to pull fluid from higher pressure regions in one channel to lower pressure regions in the neighboring channel. The branch entrance was filleted to minimize losses, while the exit was sharp to encourage jet penetration. The network of channels was created to mimic transport systems found in nature. Additionally, the addition of the branches was meant to encourage fluid mixing between the channels.

The majority of shape changes that occurred in the communicating channels took place around the branches themselves. For example, the objective to minimize pressure loss in the shorter wavelength led to a shallower angle at which the fluid from the branches was introduced into the primary branch. This design intent was replicated well in the L-PBF test coupons; the optimized channels showed a 10% decrease in friction factor relative to the L-PBF baseline design. This performance, in fact, exceeded that from both the simulation and the optimized SLA test coupons, which both showed a 5% decrease in friction factor relative to the baseline channels.

The L-PBF optimized channels are hypothesized to have outperformed the simulation because the branch feature designed to encourage jet penetration did not build quite as intended. The small size of the feature, combined with the chosen build direction, resulted in a rounded branch exit, instead of the intended sharp exit. The intent of the optimized branch shape, therefore, was helped by the build process's inability to generate the geometric feature to encourage jet

penetration. Additionally, the optimizer's design intent was less affected by the surface roughness. Unlike in the non-communicating channels, where the objective to minimize pressure loss was focused on near-wall backflow, the communicating channels focused on branch angle, which was a goal more easily achieved in the L-PBF process.

The objective to maximize heat transfer in the communicating channels also resulted in a performance akin to the simulation's. The increase in heat transfer from the optimized channels relative to the baseline was near 10%; the simulation predicted an increase in heat transfer by 8%. The penalty to friction factor, however, was substantially lower than in the non-communicating case. The optimized channels showed a 5% increase in friction factor over the baseline, which matched that predicted by the simulation. The hypothesized reduction in jet penetration in the L-PBF channels may explain this result; the lack of sharp exit from the branches may have negatively influenced the channels' ability to promote fluid mixing. However, other shape changes throughout the channel sought to increase the strength of the vortices in the channels. Those shape changes can be assumed to be successful, given the increased heat transfer performance by the optimized channels.

## **7.2 Pin Fin Arrays**

Pin fins are commonly used in situations in which high heat removal is necessary and structural integrity is required. Cylindrical pin fin arrays are ubiquitous in both the gas turbine and electronics cooling industries. As excitement for additive manufacturing grows, knowledge of how the process affect pin fin array cooling will help designers make informed decisions.

As was the case for the wavy microchannels, surface roughness played a significant role in the performance of the AM pin fin arrays. The rough top and bottom endwalls most likely interacted with the wakes generated by the pin fins, which increased the heat transfer. Additionally, the wakes from the L-PBF pin fins can be assumed to be slightly larger than those manufactured conventionally; roughness features form on the pins themselves, making them more ovalar than intended. As such, fewer pins are need in AM pin fin arrays than in conventional arrays.

Surface roughness was found to be a function of the pin density. More pins to be melted per layer during a build is hypothesized to have resulted in accumulated heat in the part, which attracted more loose powder particles. After a point, the higher roughness levels ceased to increase the heat transfer. Results from Chapter 4 showed the same heat transfer performance for two pin fin arrays with vastly different number of pins; the array with one sixth fewer pins showed about a 30% decrease in frictional losses. Therefore, the recommendation to use fewer pins in an array has two implications: (1) fewer pins are required to attain the same heat transfer because of the

inherently high surface roughness from the L-PBF process, and (2) fewer pins will keep the roughness levels in check.

### 7.3 Design Considerations for Additive Manufacturing

Future design tools will incorporate the effects of all additive manufacturing parameters on the performance of the design. Higher surface roughness can be intentionally added in areas that require better heat removal, for example, or smoother surfaces can be achieved on either up- or downskins by changing the laser power. Material properties can be considered in the heat transfer performance. The build direction can be factored into the design, as well, ensuring that the design does not contain any features that cannot build properly. Simply put, the possibilities are exciting. However, until such a close tie exists between modeled and manufactured parts, designers are left to improvise with the tools available now.

Designing for additive manufacturing requires a complete revamp in design procedures. Thinking in three dimensions is crucial, as is beginning to source design ideas from nature. Sharp corners or straight lines are rare in nature; future designs should borrow trends that mirror evolutionary successes. Mathematical tools, such as optimization strategies, can help immensely. The final output from an optimization study, however, should be critically analyzed. Some specific considerations are given below.

1. **Choose a baseline design wisely.** When using shape optimization, choose a baseline design that is complex enough to contain flow features that the sensitivity analysis can target, but not so complex that a RANS solution will lose key flow features. As previously mentioned, gradient-based methods (into which a sensitivity analysis can be categorized) are subject to local minima. Therefore, the starting point of a shape optimization is important. In topology optimization, on the other hand, the starting point is not important. In topology optimization, an open design volume, constrained only by a maximum possible volume, is filled with material in such a way that best achieves the optimization goal. However, options for commercially-available topology optimization methods that incorporate both flow and heat transfer are not available currently. Endeavors into exploring shape optimization, therefore, are worth the effort.
2. **Validate the chosen turbulence model.** A sensitivity analysis can only be as good as its input data. Spend a significant amount of time choosing the turbulence model that best captures the flowfield for the geometry of interest. In the current study, a variety of turbulence models were tested on a straight, rectangular channel of the same cross-

sectional area and length as the wavy channels. The realizable  $k-\epsilon$  model yielded results that most closely matched friction factor and heat transfer correlations from the literature. When applied to the wavy channels, the realizable  $k-\epsilon$  model was then assumed to aptly capture various flow features that affected both friction factor and heat transfer. The results from the SLA test coupon experiments validated this assumption.

3. **Closely investigate the intent of the shape changes.** How will these shape changes be affected by roughness? Roughness features from the walls protruding into the flow undoubtedly cause smaller, secondary flows that interact with the main channel flow. If the goal is to increase fluid mixing, for example, these roughness features will most likely augment the goal.

#### **7.4 Recommendations for Future Work**

The novelty and future potential of AM sustains widespread interest amongst researchers, with no dearth of motivating interests, proposed research topics or opportunities for collaborative efforts. While the AM process incurs some limitations, progress in the manufacturing industry is continuous and challenges related to surface finish, geometric tolerances, and tuning process parameters for different materials are actively being addressed by the research community. Materials that are developed specifically for AM will also introduce a step-change in the field, as will more integrated design procedures that take into consideration build direction, material properties, and process parameters.

Numerical work to gain a deeper understanding of the L-PBF process will be crucial. Modeling the complex physics of the process will allow for the development of more effective process parameters for desired as-built features. Additionally, the ability to model the large, complex, and irregular roughness features in commercially-available codes will be a huge boon to the industry. Current roughness modeling generally cannot apply to micro-sized channels; uniform, sand grain roughness, for example, is most effective in external flow applications. A deeper investigation into the possibility of applying discrete element roughness models, for example, to micro cooling channels will benefit designers immensely.

Another worthy goal may be to investigate multi-objective shape optimization schemes. Objectives to decrease pressure loss or increase heat transfer are useful, but the ability to find a balance between features that achieve such performance goals and features that can be built successfully will prove more useful. Incorporating the sensitivities of manufacturability may be lead to different shapes depending on the build direction chosen for the specific geometry.

Continued fundamental work in the flow and heat transfer properties of rough heat exchangers is necessary. Flow visualization studies on scaled-up roughness will be important in understanding its effects on flow through microchannels; Laser Doppler Velocimetry or Particle Image Velocimetry experiments to understand the size and influence of vortices shed from large and small roughness features will contribute much to the field. Such studies would be of equal interest for channels containing pin fins as for channels containing wavy features. Understanding the different levels of interaction could be useful when determining the build direction of the channels, or which process parameters to use in the manufacturing process.

## REFERENCES

- [1] Bhattacharya, A., and Mahajan, R. L., 2002, "Metal Foam and Finned Metal Foam Heat Sinks for Electronics Cooling in Buoyancy-Induced Convection," *J. Electron. Packag.*, **124**, pp. 155–163.
- [2] Gargini, P., 2015, *ITRS Overview-Past, Present and Future*.
- [3] Kahng, A. B., and Carballo, J., 2015, "ITRS2.0 System Integration Focus Team," (July).
- [4] Khalili Sadaghiani, A., Saadi, N. S., Semsari Parapari, S., Karabacak, T., Keskinöz, M., and Koşar, A., 2017, "Boiling Heat Transfer Performance Enhancement Using Micro and Nano Structured Surfaces for High Heat Flux Electronics Cooling Systems," *Appl. Therm. Eng.*, **127**, pp. 484–498.
- [5] Jung, K. W., Kharangate, C. R., Lee, H., Palko, J., Zhou, F., Asheghi, M., Dede, E. M., and Goodson, K. E., 2017, "Microchannel Cooling Strategies for High Heat Flux ( 1 kW / Cm <sup>2</sup> ) Power Electronic Applications," *Therm. Thermomechanical Phenom. Electron. Syst.*
- [6] Onstad, A. J., Moffat, R. J., Elkins, C. J., and Eaton, J. K., 2009, *Additions to Compact Heat Exchanger Technology: Jet Impingement Cooling and Flow and Heat Transfer in Metal Foam-Fins*.
- [7] Boomsma, K., Poulikakos, D., and Zwick, F., 2003, "Metal Foams as Compact High Performance Heat Exchangers," *Mech. Mater.*, **35**(12), pp. 1161–1176.
- [8] Singh, P. K., Tan, S. H. F., Teo, C. J., and Lee, P. S., 2013, "Flow and Heat Transfer in Branched Wavy Microchannels," *ASME Paper no. MNHMT2013-22058*.
- [9] Ashman, S., and Kandlikar, S. G., 2006, "A Review of Manufacturing Processes for Microchannel Heat Exchanger Fabrication," *ASME 4th Int. Conf. Nanochannels, Microchannels, Minichannels, Parts A B*, **2006**, pp. 855–860.
- [10] Bunker, R. S., Bailey, J. C., Lee, C., and Stevens, C. W., 2004, "In-Wall Network (Mesh) Cooling Augmentation of Gas Turbine Airfoils," *ASME Paper No. GT2004-54260*, pp. 1–12.
- [11] Liang, G., 2009, "Turbine Airfoil with Near-Wall Mini Serpentine Cooling Channels."
- [12] "Powder Bed AM," Lawrence Livermore Natl. Lab. [Online]. Available: [acamm.llnl.gov](http://acamm.llnl.gov).
- [13] Kleszczynski, S., Ladewig, A., Friedberger, K., Jacobsmühlen, J. zur, Merhof, D., and G. Witt, 2015, "Position Dependency of Surface Roughness in Parts From Laser Beam Melting Systems," *SFF Symp. Proc.*, pp. 360–370.
- [14] Alkahari, M. R., Furumoto, T., Ueda, T., Hosokawa, A., Tanaka, R., and Abdul Aziz, M. S., 2012, "Thermal Conductivity of Metal Powder and Consolidated Material Fabricated via Selective Laser Melting," *Key Eng. Mater.*, **523–524**, pp. 244–249.
- [15] Snyder, J. C., Stimpson, C. K., Thole, K. A., and Mongillo, D., 2016, "Build Direction Effects on Additively Manufactured Channels," *J. Turbomach*, **138**(5), p. 51006.
- [16] Stimpson, C. K., Snyder, J. C., Thole, K. A., and Mongillo, D., 2016, "Roughness Effects on Flow and Heat Transfer for Additively Manufactured Channels," *J. Turbomach*, **138**(5), p. 51008.
- [17] Ostanek, J. K., and Thole, K. A., 2012, "Wake Development in Staggered Short Cylinder Arrays within a Channel," *Exp. Fluids*.
- [18] Lawson, S. A., Thrift, A. A., Thole, K. A., and Kohli, A., 2011, "Heat Transfer from Multiple Row

- Arrays of Low Aspect Ratio Pin Fins,” *Int. J. Heat Mass Transf.*, **54**(2011), pp. 4099–4109.
- [19] Wright, L. M., Fu, W. L., and Han, J. C., 2004, “Thermal Performance of Angled, V-Shaped, and W-Shaped Rib Turbulators in Rotating Rectangular Cooling Channels (AR=4:1),” *J. Turbomach.*, **124**(4), pp. 604–614.
- [20] Belegundu, A., and Chandrupatla, T., 2011, *Optimization Concepts and Applications in Engineering*, Cambridge University Press, New York, NY, USA.
- [21] Martinelli, L., and Jameson, A., 2012, “Computational Aerodynamics: Solvers and Shape Optimization,” *J. Heat Transfer*, **135**(1), p. 11002.
- [22] Gibson, N., 2011, *Gradient-Based Methods for Optimization . Part I .*
- [23] Canonsburg, A. D., 2015, “ANSYS Fluent Advanced Add-On Modules,” **15317**(January), pp. 724–746.
- [24] Yong, J. Q., and Teo, C. J., 2014, “Mixing and Heat Transfer Enhancement in Microchannels Containing Converging-Diverging Passages,” *J. Heat Transfer*, **136**(4), p. 41704.
- [25] Sui, Y., Teo, C. J., Lee, P. S., Chew, Y. T., and Shu, C., 2010, “Fluid Flow and Heat Transfer in Wavy Microchannels,” *Int. J. Heat Mass Transf.*, **53**(13–14), pp. 2760–2772.
- [26] Guzmán, A. M., Cárdenas, M. J., Urzúa, F. A., and Araya, P. E., 2009, “Heat Transfer Enhancement by Flow Bifurcations in Asymmetric Wavy Wall Channels,” *Int. J. Heat Mass Transf.*, **52**(15–16), pp. 3778–3789.
- [27] Khaing, M. W., Fuh, J. Y. H., and Lu, L., 2001, “Direct Metal Laser Sintering for Rapid Tooling: Processing and Characterisation of EOS Parts,” *J. Mater. Process. Technol.*, **113**(1–3), pp. 269–272.
- [28] Ning, Y., Wong, Y. S., Fuh, J. Y. H., and Loh, H. T., 2006, “An Approach to Minimize Build Errors in Direct Metal Laser Sintering,” *IEEE Trans. Autom. Sci. Eng.*, **3**(1), pp. 73–80.
- [29] Delgado, J., Ciurana, J., and Rodríguez, C. A., 2012, “Influence of Process Parameters on Part Quality and Mechanical Properties for DMLS and SLM with Iron-Based Materials,” *Int. J. Adv. Manuf. Technol.*, **60**(5–8), pp. 601–610.
- [30] Kandlikar, S. G., Schmitt, D., Carrano, A. L., and Taylor, J. B., 2005, “Characterization of Surface Roughness Effects on Pressure Drop in Single-Phase Flow in Minichannels,” *Phys. Fluids*, **17**(2005), p. 100606.
- [31] Huang, K., Wan, J. W., Chen, C. X., Li, Y. Q., Mao, D. F., and Zhang, M. Y., 2013, “Experimental Investigation on Friction Factor in Pipes with Large Roughness,” *Exp. Therm. Fluid Sci.*, **50**, pp. 147–153.
- [32] Dai, B., Li, M., and Ma, Y., 2014, “Effect of Surface Roughness on Liquid Friction and Transition Characteristics in Micro- and Mini-Channels,” *Appl. Therm. Eng.*, **67**(1), pp. 283–293.
- [33] Norris, R. J., 1971, *Some Simple Approximate Heat Transfer Correlations for Turbulent Flow in Ducts with Surface Roughness*, American Society of Mechanical Engineers M4 - Citavi, New York.
- [34] Ventola, L., Robotti, F., Dialameh, M., Calignano, F., Manfredi, D., Chiavazzo, E., and Asinari, P.,

- 2014, "Rough Surfaces with Enhanced Heat Transfer for Electronics Cooling by Direct Metal Laser Sintering," *Int. J. Heat Mass Transf.*, **75**, pp. 58–74.
- [35] Wong, M., Owen, I., Sutcliffe, C. J., and Puri, A., 2009, "Convective Heat Transfer and Pressure Losses across Novel Heat Sinks Fabricated by Selective Laser Melting," *Int J Heat Mass Transf.*, **52**(1–2), pp. 281–288.
- [36] Manglik, R. M., and Bergles, A. E., 1995, "Heat Transfer and Pressure Drop Correlations for the Rectangular Offset Strip Fin Compact Heat Exchanger," *Exp. Therm. Fluid Sci.*, **10**(2), pp. 171–180.
- [37] Pham, M. V., Plourde, F., and Doan, S. K., 2008, "Turbulent Heat and Mass Transfer in Sinusoidal Wavy Channels," *Int. J. Heat Fluid Flow*, **29**(5), pp. 1240–1257.
- [38] Chang, S. W., Lees, A. W., and Chou, T. C., 2009, "Heat Transfer and Pressure Drop in Furrowed Channels with Transverse and Skewed Sinusoidal Wavy Walls," *Int. J. Heat Mass Transf.*, **52**(19–20), pp. 4592–4603.
- [39] Stone, K. M., and Vanka, S. P., 1997, "Numerical Study of Flow and Heat Transfer in Wavy Passages," University of Illinois.
- [40] Snyder, B., Li, K. T., and Wirtz, R. A., 1993, "Heat Transfer Enhancement in a Serpentine Channel," *Int. J. Heat Mass Transf.*, **36**(12), pp. 2965–2976.
- [41] EOS GmbH, "EOSINT M 280 System Data Sheet."
- [42] 2014, "Volume Graphics MAX."
- [43] Weaver, S. A., Barringer, M. D., and Thole, K. A., 2011, "Microchannels With Manufacturing Roughness Levels," *J. Turbomach.*, **133**(4), p. 41014.
- [44] Meriam, "LFE Model 50MJ10-9."
- [45] EOS GmbH, 2014, "EOS NickelAlloy IN718 for EOSINT M 270 Systems," p. 6 T4-Material data sheet M4.
- [46] Kline, S. J., and McClintock, F. A., 1953, "Describing the Uncertainties in Single Sample Experiments," *Mech. Eng.*, **75**(1953), pp. 3–8.
- [47] ANSYS, 2015, "ANSYS FLUENT."
- [48] Pointwise, 2015, "Pointwise."
- [49] Çengel, Y. A., and Cimbala, J. M., 2010, *Fluid Mechanics*, McGraw-Hill Higher Education, Boston.
- [50] Dean, W. R., 1928, "The Stream-Line Motion of Fluid in a Curved Pipe," London, Edinburgh, Dublin *Philos. Mag. J. Sci.*, **5**(30).
- [51] Gnielinski, V., 1975, "New Equations for Heat and Mass Transfer in Turbulent Pipe and Channel Flow," *Int. Chem. Eng.*, **16**(2), pp. 359–368.
- [52] Chyu, M. K., Hsing, Y. C., and Natarajan, V., 1998, "Convective Heat Transfer of Cubic Fin Arrays in a Narrow Channel," *J. Turbomach.*, **12**(2), pp. 362–367.
- [53] Kirsch, K. L., Ostanek, J. K., Thole, K. A., and Kaufman, E., 2014, "Row Removal Heat Transfer Study for Pin Fin Arrays," *ASME Paper No. GT2014-25348*.
- [54] Ostanek, J. K., and Thole, K. A., 2012, "Flowfield Interactions in Low Aspect Ratio Pin-Fin Arrays,"



- J. Turbomach, **134**, p. 051034 (10 pages).
- [55] Kirsch, K. L., and Thole, K. A., 2017, “Heat Transfer and Pressure Loss Measurements in Additively Manufactured Wavy Microchannels,” J. Turbomach, **139**(1), p. 11007.
  - [56] Wang, G., and Vanka, S. P., 1995, “Convective Heat Transfer in Periodic Wavy Passages,” Int. J. Heat Mass Transf., **38**(17), pp. 3219–3230.
  - [57] Ramgadia, A. G., and Saha, A. K., 2013, “Numerical Study of Fully Developed Flow and Heat Transfer in a Wavy Passage,” Int. J. Therm. Sci., **67**, pp. 152–166.
  - [58] Strano, G., Hao, L., Everson, R. M., and Evans, K. E., 2013, “Surface Roughness Analysis, Modelling and Prediction in Selective Laser Melting,” J. Mater. Process. Technol., **213**(4), pp. 589–597.
  - [59] Wegner, A., and Witt, G., 2012, “Correlation of Process Parameters and Part Properties in Laser Sintering Using Response Surface Modeling,” Phys. Procedia, **39**(May 2016), pp. 480–490.
  - [60] Bacchewar, P. B., Singhal, S. K., and Pandey, P. M., 2007, “Statistical Modelling and Optimization of Surface Roughness in the Selective Laser Sintering Process,” Proc. Inst. Mech. Eng. Part B-Journal Eng. Manuf., **221**(1), pp. 35–52.
  - [61] Ealy, B., Calderon, L., Wang, W., Kapat, J., Mingareev, I., Richardson, M., and Valentin, R., 2016, “Characterization of LAM-Fabricated Porous Superalloys for Turbine Components,” J. Eng. Gas Turbines Power, **139**(10), p. 102102 (7 pages).
  - [62] Maurer, M., Sierra, P., and Meng, P., 2016, “Reheat Burner Front Panel Produced By Additive Manufacturing Challenges , Strategies and Engine Validation,” *ASME Paper No. GT2016-57458*, pp. 1–11.
  - [63] Stimpson, C. K., Snyder, J. C., and Thole, K. A., 2016, “Scaling Roughness Effects on Pressure Loss and Heat Transfer of Additively Manufactured Channels,” J. Turbomach, **139**(2), p. 021003 (10 pages).
  - [64] Chi, Z., Liu, H., Zang, S., and Jiao, G., 2015, “Conjugate Heat Transfer Optimization of the Nonuniform Impingement Cooling Structure of a HPT 2nd Stage Vane,” *ASME Paper No. GT2015-42097*.
  - [65] Verstraete, T., Amaral, S., Van den Braembussche, R., and Arts, T., 2010, “Design and Optimization of the Internal Cooling Channels of a High Pressure Turbine Blade—Part II: Optimization,” J. Turbomach., **132**(2), p. 21013.
  - [66] Abdoli, A., and Dulikravich, G. S., 2014, “Multi-Objective Design Optimization of Branching , Multifloor , Counterflow Microheat Exchangers,” J. Heat Transfer, **136**(10), p. 101801 (10 pages).
  - [67] Lu, S., Qiang, Z., Wen, F., and Teng, J., 2015, “Aerodynamic and Heat Transfer Optimization of One Stage Air-Cooled Turbine,” *ASME Paper Number GT2015-42974*.
  - [68] Willeke, S., and Verstraete, T., 2015, “Adjoint Optimization of an Internal Cooling Channel U-Bend,” *ASME Paper No. GT2015-43423*.
  - [69] Morimoto, K., Suzuki, Y., and Kasagi, N., 2010, “Optimal Shape Design of Compact Heat

- Exchangers Based on Adjoint Analysis of Momentum and Heat Transfer,” *J. Therm. Sci. Technol.*, **5**(1), pp. 24–35.
- [70] Wang, C., Montanari, F., and Hill, D. C., 2015, “Application of Adjoint Solver to Optimization of Fin Heat Exchanger,” *ASME Paper No. GT2015-43293*, pp. 1–10.
  - [71] Xue, L., Li, Y., Chen, J., and Wang, S., 2015, “Laser Consolidation - a Novel Additive Manufacturing Process for Making Net-Shape Functional Metallic Components for Gas Turbine,” *ASME Paper No. GT2015-43971*, pp. 1–11.
  - [72] Dede, E. M., Joshi, S. N., and Zhou, F., 2015, “Topology Optimization, Additive Layer Manufacturing, and Experimental Testing of an Air-Cooled Heat Sink,” *J. Mech. Des.*, **137**(11), pp. 1–9.
  - [73] Pietropaoli, M., Ahlfeld, R., Montomoli, F., Caini, A., and D’Ercole, M., 2016, “Design for Additive Manufacturing: Internal Channel Optimization,” *ASME Paper No. GT2016-57318*.
  - [74] Dirker, J., and Meyer, J. P., 2013, “Topology Optimization for an Internal Heat-Conduction Cooling Scheme in a Square Domain for High Heat Flux Applications,” *J. Heat Transfer*, **135**(11), p. 111010.
  - [75] Boger, D. A., 2013, “A Continuous Adjoint Approach To Design Optimization in Multiphase Flow,” Penn State University.
  - [76] AliCat, 2014, “Mass Flow Controller - Operating Manual.”
  - [77] Chyu, M. K., and Moon, H. K., 2009, “Effects of Height-to-Diameter Ratio of Pin Element on Heat Transfer from Staggered Pin-Fin Arrays,” *ASME Paper No. GT2009-59814*.
  - [78] Metzger, D. E., Shepard, W. B., and Haley, S. W., 1986, “Row Resolved Heat Transfer Variations in Pin-Fin Arrays Including Effects of Non-Uniform Arrays and Flow Convergence,” *ASME Paper No. 86-GT-132*.
  - [79] Metzger, D. E., Fan, C. S., and Haley, S. W., 1984, “Effects of Pin Shape and Array Orientation on Heat Transfer and Pressure Loss in Pin Fin Arrays,” *J. Eng. Gas Turbines Power*, **106**(1), p. 252.
  - [80] Simoneau, R. J., and VanFossen, G. J., 1984, “Effect of Location in an Array on Heat Transfer to a Short Cylinder in Crossflow,” *J. Heat Transfer*, **106**(1), p. 42.
  - [81] VanFossen, G. J., 1982, “Heat-Transfer Coefficients for Staggered Arrays of Short Pin Fins,” *J. Eng. Power*, **104**(2), p. 268.
  - [82] Armstrong, J., and Winstanley, D., 1988, “A Review of Staggered Array Pin Fin Heat Transfer for Turbine Cooling Applications,” *J. Turbomach.*, **110**(1), p. 94.
  - [83] Ostanek, J. K., 2015, “Improving Pin-Fin Heat Transfer Predictions Using Artificial Neural Networks,” *ASME Paper No. GT2013-95903*.
  - [84] Lyall, M. E., Thrift, A. A., Thole, K.A., Kohli, A., 2011, “Heat Transfer from Low Aspect Ratio Pin Fins,” *J. Turbomach*, **133**, p. 011001 (10 pages).
  - [85] Siw, S. C., Fradeneck, A. D., Chyu, M. K., and Alvin, M. A., 2015, “The Effects of Different Pin-Fin Arrays on Heat Transfer and Pressure Loss in a Narrow Channel,” *GT2015-43855*, pp. 1–9.
  - [86] Marques, C., and Kelly, K. W., 2004, “Fabrication and Performance of a Pin Fin Micro Heat

- Exchanger,” J. Heat Transfer, **126**(June), p. 434.
- [87] İzci, T., Koz, M., and Kosar, A., 2015, “The Effect of Micro Pin-Fin Shape on Thermal and Hydraulic Performance of Micro Pin-Fin Heat Sinks,” Heat Transf. Eng., **36**(May), pp. 1447–1457.
  - [88] Jasperson, B. a., Turner, K. T., and Pfefferkorn, F. E., 2010, “Comparison of Micro-Pin-Fin and Microchannel Heat Sinks Considering Thermal-Hydraulic Performance and Manufacturability,” IEEE Trans. Components Packag. Technol., **33**(1), pp. 148–160.
  - [89] Heo, K. Y., Kihm, K. D., and Lee, J. S., 2014, “Fabrication and Experiment of Micro-Pin-Finned Microchannels to Study Surface Roughness Effects on Convective Heat Transfer,” J. Micromechanics Microengineering, **24**(12), p. 125025.
  - [90] Chang, S. W., and Lees, A. W., 2010, “Endwall Heat Transfer and Pressure Drop in Scale-Roughened Pin-Fin Channels,” Int. J. Therm. Sci., **49**(4), pp. 702–713.
  - [91] Cormier, Y., Dupuis, P., Farjam, A., Corbeil, A., and Jodoin, B., 2014, “Additive Manufacturing of Pyramidal Pin Fins: Height and Fin Density Effects under Forced Convection,” Int. J. Heat Mass Transf., **75**, pp. 235–244.
  - [92] Dupuis, P., Cormier, Y., Fenech, M., and Jodoin, B., 2016, “Heat Transfer and Flow Structure Characterization for Pin Fins Produced by Cold Spray Additive Manufacturing,” Int. J. Heat Mass Transf., **98**, pp. 650–661.
  - [93] Dupuis, P., Cormier, Y., Fenech, M., Corbeil, A., and Jodoin, B., 2016, “Flow Structure Identification and Analysis in Fin Arrays Produced by Cold Spray Additive Manufacturing,” Int. J. Heat Mass Transf., **93**, pp. 301–313.
  - [94] Yadroitsev, I., and Smurov, I., 2011, “Surface Morphology in Selective Laser Melting of Metal Powders,” Phys. Procedia, **12**(1), pp. 264–270.
  - [95] Pakkanen, J., Calignano, F., Trevisan, F., Lorusso, M., Ambrosio, E. P., Manfredi, D., and Fino, P., 2016, “Study of Internal Channel Surface Roughnesses Manufactured by Selective Laser Melting in Aluminum and Titanium Alloys,” Metall. Mater. Trans. A, **47**(3837).
  - [96] Jamshidinia, M., and Kovacevic, R., 2015, “The Influence of Heat Accumulation on the Surface Roughness in Powder-Bed Additive Manufacturing,” Surf. Topogr. Metrol. Prop., **3**(1), p. 14003.
  - [97] Incropera, F. P., DeWitt, D. P., Bergman, T. L., and Lavine, A. S., 2007, *Fundamentals of Heat and Mass Transfer*, John Wiley & Sons.
  - [98] Colebrook, C. F., and White, C. M., 1937, “Experiments with Fluid Friction in Roughened Pipes,” Proc. R. Soc. Lond. A. Math. Phys. Sci., **161**(906), pp. 367–381.
  - [99] Ostanek, J. K., 2012, “Flowfield Interactions in Low Aspect Ratio Pin-Fin Arrays,” The Pennsylvania State University.
  - [100] Brigham, B. A., and VanFossen, G. J., 1984, “Length to Diameter Ratio and Row Number Effects in Short Pin Fin Heat Transfer,” J. Eng. Gas Turbines Power, **106**(1), p. 241.
  - [101] Damerow, W. P., Murtaugh, J. C., and Burgraff, 1972, “Experimental and Analytical Investigation of the Coolant Flow Characteristics in Cooled Turbine Airfoils,” NASA CR-120883.

- [102] Jacob, M., 1938, "Heat Transfer and Flow Resistance in Cross Flow of Gases over Tube Banks," *Trans ASME*, **59**, pp. 384–386.
- [103] Herman, C. V., Mayinger, F., and Sekulic, D. P., 1991, "Experimental Verification of Oscillatory Phenomena in Heat Transfer in a Communicating Channels Geometry," *Exp. Heat Transf, Fluid Mech. Thermodyn.*, pp. 904–911.
- [104] Barrot, C., and Colin, S., 2012, "Design of Tree-Shaped Microchannel Networks Submitted to Simultaneous Pressure Driven and Electro-Osmotic Flows," *ASME Paper No. ICNMM2012-73104*.
- [105] Guzman, A. M., Beiza, M. P., Diaz, A. J., Fischer, P. F., and Ramos, J. C., 2013, "Flow and Heat Transfer Characteristics in Micro and Mini Communicating Pressure Driven Channel Flows by Numerical Simulations," *Int. J. Heat Mass Transf.*, **58**(1–2), pp. 568–577.
- [106] Sekulic, D. P., 1989, "Flow Through Communicating Channels Compact Heat Transfer Geometry," *Int. Comm. Heat Mass Transf.*, **16**, pp. 667–679.
- [107] Peng, Y., Liu, W., Chen, W., and Wang, N., 2014, "A Conceptual Structure for Heat Transfer Imitating the Transporting Principle of Plant Leaf," *Int. J. Heat Mass Transf.*, **71**, pp. 79–90.
- [108] Weaver, A. M., Liu, J., and Shih, T. I., 2015, "A Weave Design for Trailing-Edge Cooling," *AIAA-2015-1446*.
- [109] Kirsch, K. L., and Thole, K. A., 2017, "Experimental Investigation of Numerically Optimized Wavy Microchannels Created Through Additive Manufacturing," *Proc. ASME Turbo Expo 2017 Turbomach. Tech. Conf. Expo*.
- [110] Arie, M. A., Shooshtari, A. H., Rao, V. V., Dessiatoun, S. V., and Ohadi, M. M., 2017, "Air-Side Heat Transfer Enhancement Utilizing Design Optimization and an Additive Manufacturing Technique," *J. Heat Transfer*, **139**(3), p. 31901.
- [111] Pucci, E., Cerutti, M., Peano, G., Facchini, B., and Andreini, A., 2017, "Cooling System Optimization of Combustor Liners," *Proceedings of ASME Turbo Expo 2017: Turbomachinery Technical Conference and Exposition*.
- [112] Anwar, A. Bin, and Pham, Q. C., 2017, "Selective Laser Melting of AlSi10Mg: Effects of Scan Direction, Part Placement and Inert Gas Flow Velocity on Tensile Strength," *J. Mater. Process. Technol.*, **240**, pp. 388–396.
- [113] Schurb, J., Hoebel, M., Haehnle, H., Kissel, H., Hoebel, M., Bogdanic, L., and Etter, T., 2016, "Additive Manufacturing of Hot Gas Path Parts and Engine Validate in Heavy Duty GT," *ASME Paper No. GT2016-57262*, pp. 1–10.
- [114] Gee, D. L., and Webb, R. L., 1980, "Forced Convection Heat Transfer in Helically Rib-Roughened Tubes," *Int J Heat Mass Transf.*, **23**, pp. 1127–1136.
- [115] Kirsch, K. L., and Thole, K. A., 2017, "Numerical Optimization, Characterization, and Experimental Investigation of Additively Manufactured Communicating Microchannels," *In Progress*.
- [116] Xu, S., Radford, D., Meyer, M., and Müller, J.-D., 2015, "CAD-Based Adjoint Shape Optimization of a One-Stage Turbine with Geometric Constraints," *ASME Paper No. GT2015-42237*.

- [117] Lyu, Z., and Martins, J., 2013, “RANS-Based Aerodynamic Shape Optimization of a Blended-Wing-Body Aircraft,” Proc. 51st AIAA Aerosp. ..., pp. 1–17.
- [118] Formlabs, 2016, “FormLabs 2.”
- [119] Kirsch, K. L., and Thole, K. A., 2017, “Pressure Loss and Heat Transfer Performance for Additively and Conventionally Manufactured Pin Fin Arrays,” Int. J. Heat Mass Transf., **108**.
- [120] Langhaar, H. L., “Steady Flow in the Transition Length of a Straight Tube,” J. Appl. Mech., **9**, pp. A55–A58.
- [121] Pope, S. B., 2000, *Turbulent Flows*, Cambridge University Press.

## A APPENDIX A: DETAILED DESCRIPTION OF GEOMETRIES

This appendix serves as a supplement to the discussions in sections 2.4, 3.4, 5.4, and 6.4, where the wavy channel geometries were described. More details on the reasoning behind the geometric features of the microchannels will be presented here.

### A.1 Variable cross-section versus constant cross-section

As previously mentioned, the channel curves were created using four  $45^\circ$  arcs. A rectangle of aspect ratio two (height to width) was swept along the curve to create the channel. The rectangle was kept normal to the channel inlet and, as such, created a contraction in channel cross-sectional area that depended on the channel wavelength. Figure 2-2 is reproduced as Figure A-1 to highlight the changes in cross-sectional area. Because of the manner in which the wave was constructed, the longer wavelength channels also had higher amplitudes, which led to a more constricted cross-sectional area.

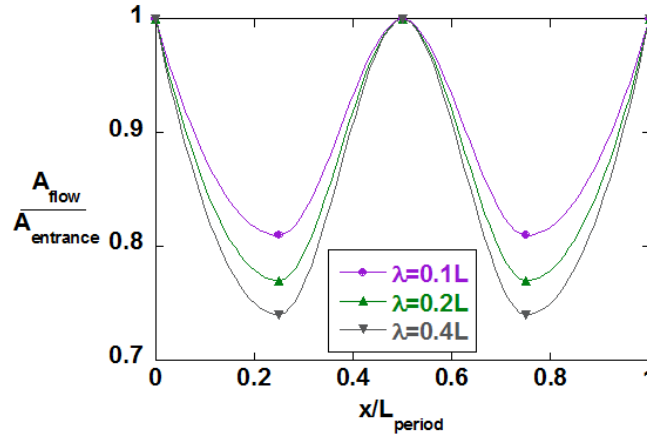


Figure A-1. Change in cross-sectional area for each of the wavelengths from the study in Chapter 2 through one wavelength of each channel. The longer the wavelength, the more significant deviation from the inlet cross-sectional area. This figure is a reproduction of Figure 2-2.

Numerical studies were also performed on wavy channels with a constant cross-sectional area. For the  $\lambda=0.1L$  case, the simulation results predicted a decrease in friction factor augmentation of 4.5% relative to the variable cross-sectional area geometry; the decrease in Nusselt number augmentation was also 4.5%. For the  $\lambda=0.4L$  case, the constant cross-sectional area geometry showed a decrease of 8.5% in friction factor augmentation relative to the variable cross-section geometry; Nusselt number augmentation was 15% under the variable cross-section geometry. Given that two of the optimization goals of this study were to increase the heat transfer, the variable cross-section geometry was chosen as the baseline configuration.

## A.2 Addition of branches between primary channels

Singh et al. [8] was the first study to include branches between primary wavy channels. The results from the Singh et al. study showcased the benefits of introducing a connection between channels. The addition of the branches increased the heat transfer over isolated wavy channels [8]: flow emanating from the branches disrupted the boundary layer on the primary channels' walls. For reference, the design of Singh's wavy channels is provided in this section, and is shown in Figure A-2. The branches were angled at  $45^\circ$  to the horizontal, and were positioned such that high pressure fluid from one channel was drawn into a region of lower pressure in a neighboring channel.



**Figure A-2. Communicating channel design from Singh et al. [8].**

In an initial attempt to manufacture communicating microchannels, we designed our channels to be exactly like those in the study by Singh et al. Simulation results from the isolated channels showed that the location of the branches from Singh et al. would translate well to the flow conditions of interest in the current study; the branches would facilitate flow movement from higher pressure regions of one channel and dump to lower pressure regions in the neighboring channel.

However, upon receiving the results from the CT scan, we found that the branches did not build properly. Because the branches were included in between every primary branch, and because of the build direction that was chosen, the as-manufactured branches were unrecognizable as branches; instead, poorly-defined gaps existed between neighboring channels. A top-down view of the as-manufactured initial branch design is shown in Figure A-3. The solid material between the channels resembled discrete fins as opposed to the boundaries of coherent channels; therefore, the initial design was deemed unsuccessful, and a new design was created.

The new design corrected the mistakes of the initial design. For one, the branches were included in every other period in the streamwise dimension, and every other channel in the spanwise dimension. This pattern ensured that the primary channels themselves would retain their shape, and as a consequence, promote the intended flow features. Additionally, the branches in the new design included fillets. The target flowrate in the study by Singh et al. was well into the laminar regime and, as such, sharp corners at the inlet to branches were not as detrimental to the friction factor as would be the case at higher Reynolds numbers. Therefore, fillets were included at the entrance to the branches, and on one corner at the exit of the branches. The dimensions of the fillets are given in Figure A-4. The fillet radii were chosen visually.

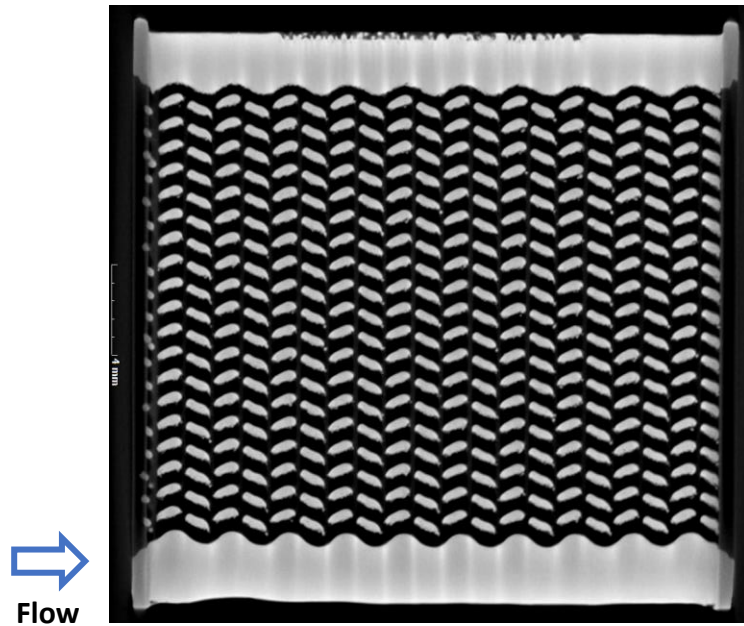


Figure A-3. Top-down view at 50% channel height of the as-manufactured initial communicating wavy channel design.

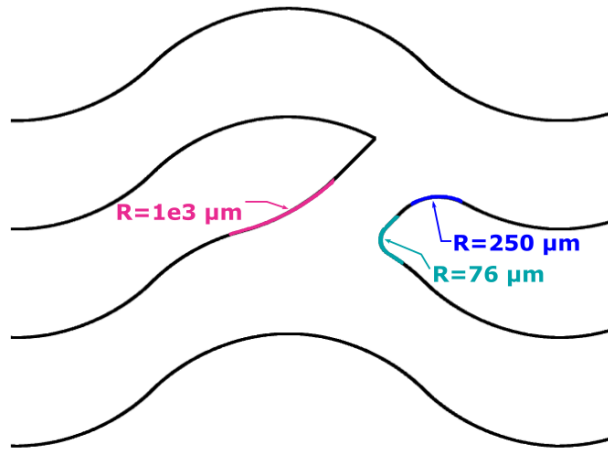


Figure A-4. Fillet radii for the communicating wavy channels. The radii were the same for the  $\lambda=0.4L$  communicating channels.

As confirmation that the branches were included in advantageous locations, Figure A-5 shows contours of normalized static pressure from the isolated channel simulations. The contours show the difference between the local static pressure and the exit pressure, normalized by the pressure difference between channel inlet and outlet. The results from the isolated channel simulations were duplicated to include two neighboring channels. The channel from the communicating channels are included atop the contours from the isolated channels. As can be seen



in the figure, the entrance of the branch is centered on the region of high pressure in one channel; the branch exit indeed dumps fluid into a lower pressure region of its neighboring channel.

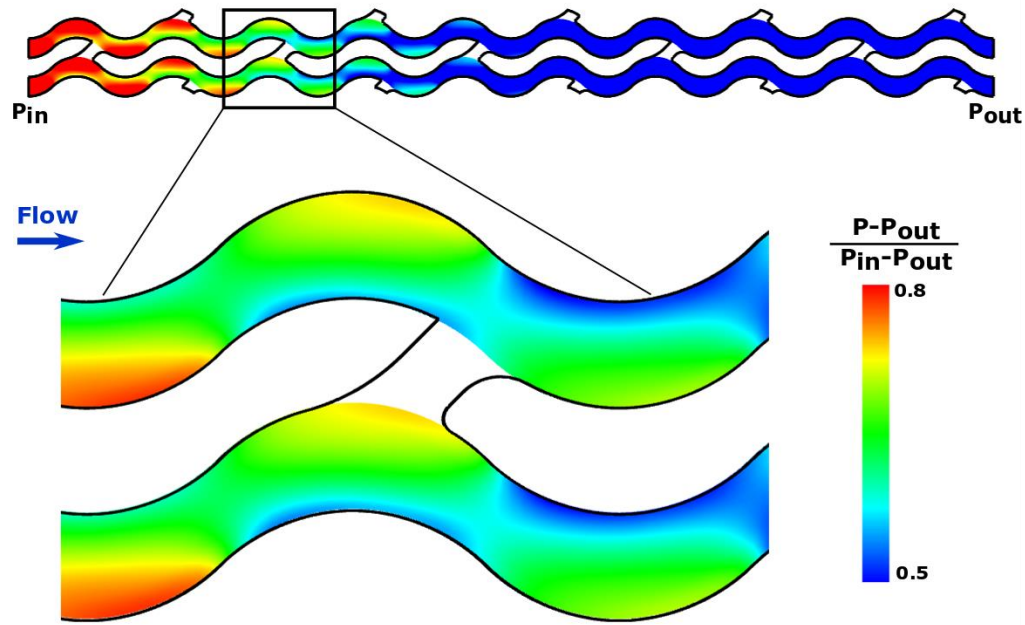


Figure A-5. Contours of normalized static pressure from the isolated wavy channel simulations; contours were duplicated to include two channels. The outline of the communicating wavy channels are laid atop the two isolated channel contours. The inlet to the branch is centered on the high pressure region of one channel, and exits into the lower pressure region of the neighboring channel.

### A.3 Optimized Shape Changes: Peaks and Troughs

The primary focus of the discussion on shape changes in the wavy channels revolved around those located in between the peaks and the troughs of the waves. Certainly, the shape changes in those areas were the most severe; the centripetal force acting on the fluid particles abruptly switched signs in between the peaks and the troughs, and the optimizer targeted those flow patterns. As previously mentioned, the shapes *at* the peaks and the troughs largely mimicked those from the baseline design—when viewed at a distance, the cross-section was rectangular. However, upon zooming into slices at the peaks and the troughs of the optimized designs, further inspection revealed that the cross-sections were not perfectly rectangular, and did, in fact, differ very slightly from the baseline.

Figure A-6 shows a one slice taken at the streamwise middle of the channel, located at a peak in the wave design of the  $\lambda=0.1L$  case. All four of the geometries (baseline, plus three optimized geometries) are presented in the figure and are laid atop one another for reference. These differences among all four shapes were incredibly small, and certainly not large enough for the L-PBF process to resolve. To note, however, the four corners of each of the designs coincide; given

that the optimization procedure was meant to modify the shape of the geometry, as opposed to its topology, the four outside corners of the geometry did not move, even when inspected at extremely zoomed-in views.

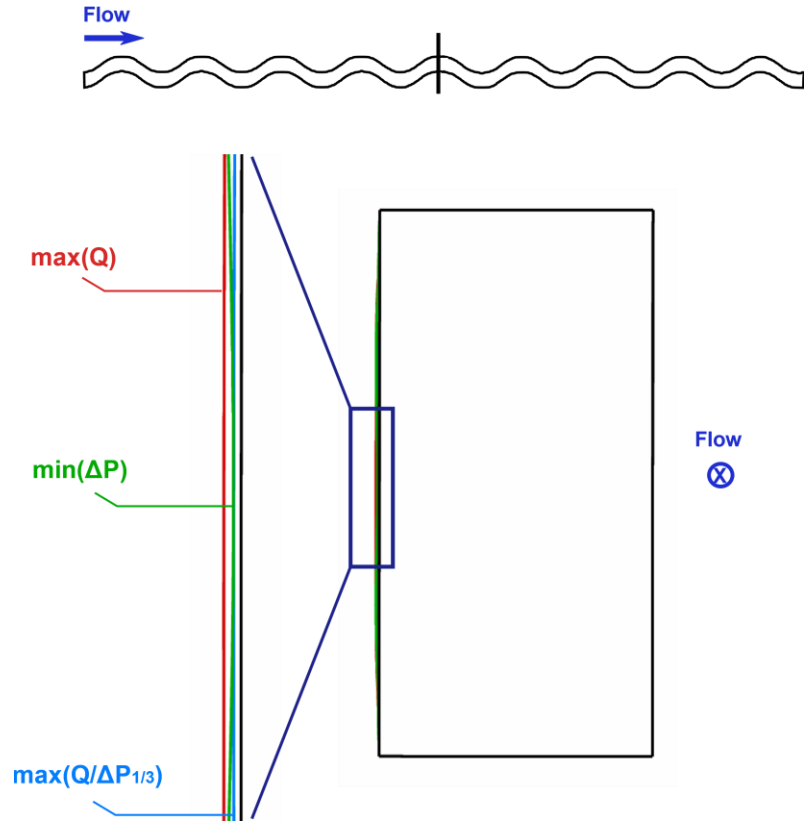


Figure A-6. Change in shape among all three optimized cases, plus the baseline, for the  $\lambda=0.1L$  wavy channel design. Slice location was taken at the peak of the wave; the optimized designs show slight deviations from the baseline's pure rectangular cross-sectional area.

#### A.4 Nondestructive Evaluation

The setup for the CT scan resulted in a resolution of  $35\ \mu\text{m}$ . The resolution is set by a number of factors, two of which are the material of the part and the size of the desired scan area. A resolution of  $35\ \mu\text{m}$  (3.5% of channel height), was deemed to be sufficient to capture, at the very least, larger roughness features. No higher-resolution evaluations, such as Optical Profilometry or Scanning Electron Microscopy, of the internal surface roughness were performed for any test coupons in the current studies; no test coupons were cut open to more closely inspect the internal surface roughness. Ongoing research in the START Lab is investigating the effects of large scale versus small scale roughness on the friction factor and heat transfer performance of microchannels; an in-depth analysis of the surface morphology and roughness features' effects on performance were not the focus of the current studies.

## B APPENDIX B: FURTHER DISCUSSION ON NUMERICAL MODEL AND ADJOINT METHOD

This appendix serves as a supplement to the discussions in sections 5.5, 5.6, and 6.5, which outlined the numerical method and described some of the optimized results. Further details on the adjoint method will be given here, as well as a more in-depth discussion of the numerical setup and numerical results.

### B.1 Adjoint Method

The adjoint solver used in the current studies was developed using a discrete approach, as opposed to a continuous approach. In the discrete approach, the adjoint equations are based on the discretized form of the governing equations. Consequently, the adjoint equations are tightly tied to the chosen flow solver [23], which underscores the importance of choosing a solver that can reasonably capture important flow structures. For reference, in the continuous approach, the adjoint partial differential equations and the adjoint boundary conditions are derived explicitly [23]. Once derived, the adjoint equations can then be discretized. As such, the adjoint equations derived using a continuous approach are much less sensitive to the chosen flow solver. However, the added complexity of the continuous approach was deemed too great by Ansys, and the discrete adjoint solver was implemented for sensitivity analyses.

Modifications to the current studies' geometries were based on a gradient algorithm. Mesh nodes were moved per the relation shown in Equation 1-1;  $x_j^n$  is the  $j^{\text{th}}$  coordinate of the  $n^{\text{th}}$  node in the mesh,  $\mathbf{J}$  is the observable, and  $\lambda$  is an arbitrary scaling factor determined by both the sensitivities calculated from the adjoint equations and the degree to which the user prescribes a change in the observable (see Section B.2 for more information on the user's role in the shape change) [23]. The sign of  $\lambda$  depends on whether the objective is to be increased or decreased.

$$\delta x_j^n = \lambda \cdot \frac{\partial \mathbf{J}}{\partial x_j^n} \quad \mathbf{1-1}$$

Problems that contain many degrees of freedom, and/or problems that contain turbulent flow can produce noisy values for the term  $\partial \mathbf{J} / \partial x_j^n$  [23]. In these situations, computing the change in position for node  $x_j^n$  can result in surfaces that contain many inflections that would not be physically realizable and/or would result in poor-quality meshes. Mesh morphing, therefore, is implemented not only to smooth the resultant mesh, but also to smooth the sensitivity field generated by the solution of the adjoint equations.

The mesh morphing approach was designed to provide both global and local deformations that yield smooth shapes. The global deformation scheme ensures that the deformation field

maintains continuity in the optimized shape, while the local deformation scheme allows for locally sharper deformations if required to satisfy the objective function. A full mathematical description of these two different smoothing schemes can be found in [23].

## **B.2 Implicit constraints on optimization method**

Once the adjoint equations have been solved to convergence, the user determines to what extent the geometry should be modified. In the design tool within the optimization toolbox, the user can choose by how much the objective function should be changed. The amount of change can be imposed as a percentage of the current value of the objective function, or simply as a prescribed, scalar value. However, if the change to the objective function is too great, the shape change generated by the sensitivity analysis may result in a poor-quality mesh, which would cause an inability to converge the subsequent flow solution. While the two deformation smoothing schemes mentioned in Section B.1 are applied to all shape changes, they are most effective for relatively small mesh movements: the topological definition of the initial geometry is fixed [23].

An example of too aggressive an objective change can be seen in Figure B-1. The baseline geometry was the  $\lambda=0.1L$  isolated wavy channel case; the objective was to maximize heat transfer. The channel outlines shown are from the first design iteration; that is, the shape changes were the result of the first solution of the adjoint equations following the first flow solution of the baseline design. Channel outlines at one slice location are shown in the figure; the different outlines represent different imposed changes to the objective function. The baseline design is included for reference. All three of the colored outlines follow a similar trend, which is expected: the shapes were changed based on the results from the sensitivity analysis. However, with more aggressive prescribed changes to the objective functions, the shape changes started drastically changing the channel architecture. For example, where the objective function was to be increased by 20%, the left wall (from the reader's point of view) at mid-height shows an upward curvature.

The resultant meshes from both the 10% and 20% prescribed increase in heat transfer did not yield converged flow solutions. These two cases showed a translation of the four corners of the optimized shapes relative to the baseline, which may have contributed to the fact that the flow solution could not converge. The shape change that resulted from the 7% increase in heat transfer did result in a converged flow solution, and was therefore used in for subsequent design iterations.

Especially at the beginning of the optimization procedure (early in the design iterations), the limits of the shape changes were pushed in order to generate the largest shape change. However, with further design iterations, the prescribed change to the objective function was slowly diminished. Smaller prescribed changes to the objective function ensured incremental changes to the geometry that would yield converged flow solutions.

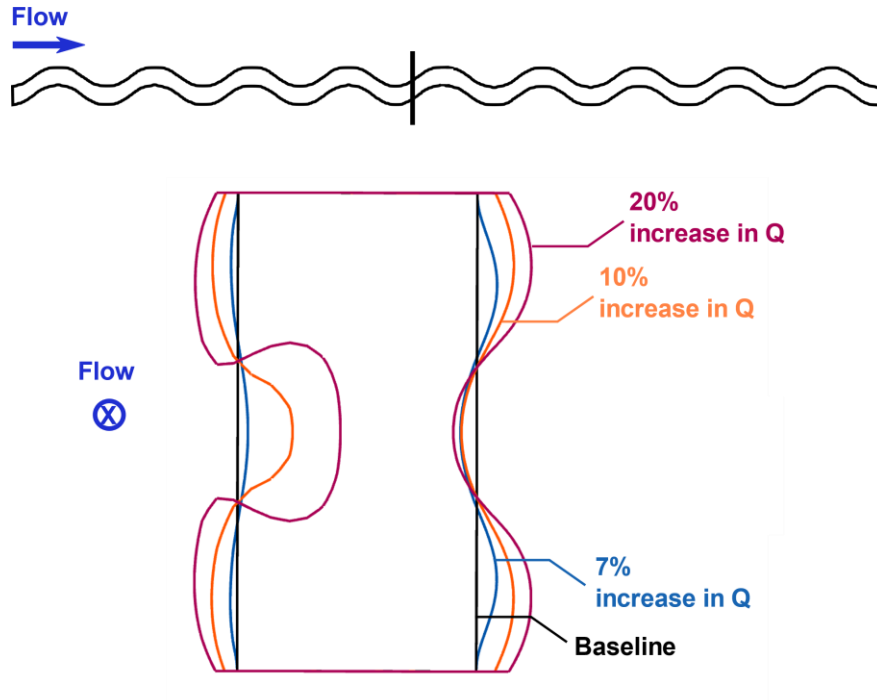


Figure B-1. Shape changes as dictated by different imposed changes to the objective function. The baseline design is shown for comparison.

### B.3 Side wall boundary conditions

In the current studies, the side walls of the fluid domain were modeled as adiabatic. However, an argument for a constant temperature boundary condition on the side walls can easily be made; given the high fin efficiency of these microchannels, the side walls may be considered to be at the same temperature as the heated top and bottom walls. To understand the potential difference in results, the previously-described optimization procedure was applied to a simulation with side walls held at the same constant temperature as the top and bottom endwalls. The optimization procedure was run to completion; that is, the design iterations continued until no further changes to the shape took place. Seven design iterations were performed for the geometry with the adiabatic side walls, while three iterations were run for the geometry with the constant temperature side walls.

The objective function for this exploratory simulation was to maximize the heat transfer. In the case with the adiabatic walls, the increase in heat transfer from the optimized design over the baseline design was 26% (Table 5-1); with the constant temperature side walls, the final increase in heat transfer was 7% over the baseline.

Figure B-2 shows one slice each from the two different side wall boundary conditions. On the left side of the figure is the constant temperature side wall boundary condition, and on the right side is the adiabatic side wall boundary condition. The slices are colored by non-dimensional

temperature, defined in the same way as in previous chapters. The non-dimensional temperature is significantly higher in the constant temperature boundary condition case than in the adiabatic boundary condition case; the two extra surfaces contributing to the heat transfer expectedly increased the non-dimensional temperature. However, the shapes between the two slices are remarkably similar. The right-hand wall bowed outward significantly at the channel mid-height in both cases, with a slight outward bow also seen on the left-hand wall.

The slice location shown in Figure B-3 is at the peak in the channel, just beyond the location shown in Figure B-2, and shows normalized axial velocity with secondary velocity vectors overlaid. The flow patterns between the two different boundary conditions are very similar: velocity vectors point nearly directly upward (near the right walls) or directly downward (near the left walls), acting to force fluid toward the top and bottom endwalls. The magnitude of normalized velocity is also similar between the two boundary conditions.

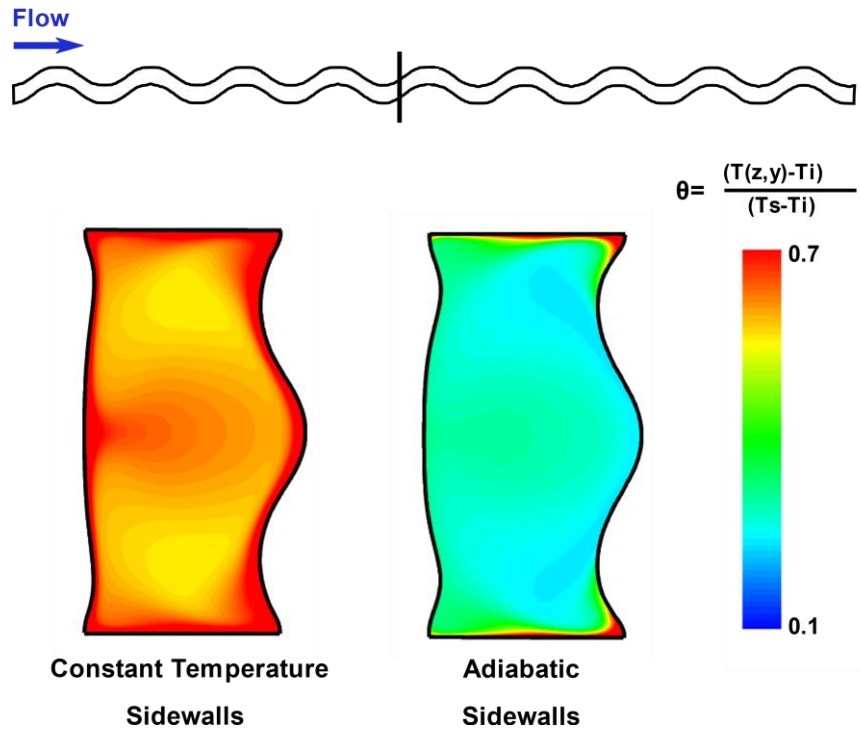


Figure B-2. Comparison of shape changes at one slice location for different side wall boundary conditions. Contours are colored by non-dimensional temperature.

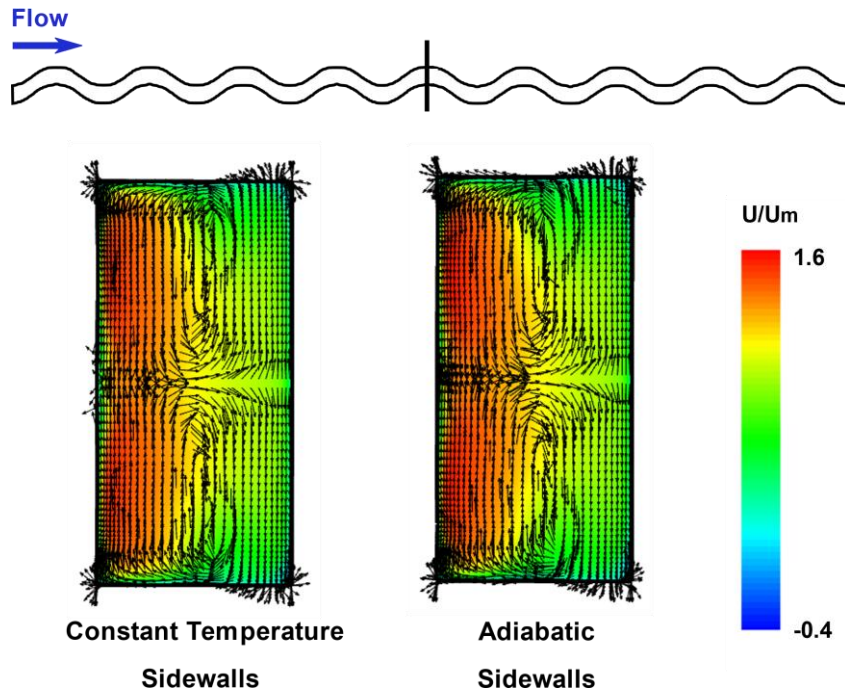


Figure B-3. Comparison of flow structures at one peak in the wavy channel design. Contours are colored by normalized axial velocity, and secondary velocity vectors are overlaid.

Even with the constant temperature side wall boundary condition, the goal of the optimizer appeared to focus on the flow structures and generating stronger vortices. Despite the different boundary conditions, and the undoubtedly different local temperature distributions, the shape changes remained of the same ilk. The optimization procedure was based on the flowfield calculated by the various flow solutions. Maximizing heat transfer, therefore, appeared to be less about the boundary conditions, and more about the flow structures induced by the geometry, which is encouraging for future applications of this optimization method. Assuming the dominant flow structures are captured accurately by the flow solver, the inability to impose the exact experimental boundary conditions (solid domain, conjugate heat transfer, etc.) may not have too large an effect on the optimized geometries.

## **VITA**

### **Kathryn L. Kirsch**

Kathryn was born and raised in Maple Glen, PA, a small town just outside of Philadelphia. In 2007, she graduated from Mount Saint Joseph Academy, an all-girls high school in Philadelphia, and began her studies at Penn State. In the summers of her undergraduate years, Kathryn worked four internships—one rotation each at General Electric Transportation and Pratt & Whitney, and two rotations at Knolls Atomic Power Laboratory. She was also active in undergraduate research projects. She worked under Dr. Mirna Urquidi-Macdonald from 2008-2010, and published two conference papers on their work together. In her senior year, Kathryn worked under Dr. Seungjin Kim in the Advanced Multiphase Flow Lab (AMFL). In August of 2011, she began her graduate work in the Experimental and Computational Convection Laboratory (ExCCL) under the direction of Professor Karen A. Thole.

Kathryn graduated with her M.S. degree in Mechanical Engineering in 2013, after which she moved to Karlsruhe, Germany. She worked at the Institut für Thermische Strömungsmaschinen at the Karlsruher Institut für Technologie under the direction of Professor Hans Jorg Bauer for six months, where she gained an invaluable network of peers, in addition to further experience as an experimentalist. When she returned to Penn State, she started her Ph.D. in the Steady Thermal Aero Research Turbine Laboratory (START), where she was funded by the National Science Foundation Graduate Research Fellowship.

As a graduate student, Kathryn became involved in alumni engagement within the College of Engineering. She became a member of the Penn State Engineering Alumni Society (PSEAS) in 2012. Shortly after, she founded the Engineering Young Alumni Advisory Board (EYAAB), Penn State's first young alumni engagement group. She also served on the Student Advisory Committee within her technical community, the American Society of Mechanical Engineers (ASME) Gas Turbine Segment. Upon graduation, Kathryn will remain working in the START Lab as a post-doctoral researcher for another year.